Mechanisms behind the fate of early chromosomal and transcriptional heterogeneities in the mouse embryo

Shruti Singla

King's College
University of Cambridge

The dissertation is submitted for the degree of Doctor of Philosophy (PhD)

August 2019

Declaration

This dissertation is the result of my own work and includes nothing which is the outcome of work done in collaboration except where specifically indicated in the text. This dissertation does not exceed the prescribed word limit as set by the Degree Committee.

Shruti Singla

Acknowledgements

I would like to express my deepest gratitude to my supervisor, Prof. Magdalena-Zernicka Goetz, for her persistent guidance, patience, and providing an excellent atmosphere for doing research. I am grateful to her for her professional acumen and a fine sense of perfection.

I am grateful to everyone in the Zernicka-Goetz lab, the past and present members, for timely valuable suggestions, cooperation, and assistance. In particular, I would like to thank following colleagues: Meng Zhu, for her relevant advice and assistance with experiments throughout my research and being an indispensable best friend; Agnieszka Jedrusik for her valuable suggestions related to mouse embryology and being an exceptional friend; Sarah Graham for training me during the first year of my Ph. D; Christos Kyprianou and Antonia Weberling for assistance with the post-implantation embryo recovery; and Marta Shahbazi for help with my science communication skills (writing and presentation) right from the start of my Ph. D. I am also thankful to Prof. David Glover for stimulating discussions and insightful comments. I would also like to thank everyone at the Gurdon Animal Facility and PDN staff, who are as much instrumental in making this study possible. I also wish to thank Bill Mansfield for assistance with embryo transfers.

I express my sincerest gratitude to my parents, Naresh and Sona, for their never-ending love & support. Without their blessings and encouragement, I could never have reached this level in my career and life. I dedicate my thesis to them. I also wish to thank my dear friend Rajat for his unflagging support throughout.

I am enormously thankful to Wellcome Trust for selecting me and providing me this lifetime opportunity. Lastly, I thank Welcome Trust and Cambridge Trust for providing me generous financial support.

Contents

List of Figures

List of Tables

List of Abbreviations

TE	Trophectoderm	BafA1	Bafilomycin A1
ICM	Inner cell mass	2i	Two-inhibitor
PE	Primitive endoderm	ExE	Extra-embryonic ectoderm
EPI	Epiblast	UPD	Uniparental disomy
ERK	Extracellular signal–regulated kinase	SAC	Spindle assembly checkpoint
PMS	Pregnant mares' serum gonadotrophin	FISH	Fluorescent in-situ hybridization
RNA	Ribonucleic acid	VE	Visceral endoderm
GSK3β	Glycogen synthase kinase 3-β	KO	Knockout
DNA	Deoxyribonucleic acid	IVF	*In vitro* fertilization
cDNA	Complementary DNA	ANOVA	Analysis of variance
mRNA	messenger RNA	ROI	Region of interest
siRNA	Small interfering RNA	E3.5	Embryonic day 3.5
DIC	Differential Interference Contrast	E4.5	Embryonic day 4.5
mESCs	Mouse embryonic stem cells	LE	Luminal epithelium
hCG	Human chorionic gonadotrophin	TF	Transcription factor
GFP	Green fluorescent protein	ROS	Reactive Oxygen Species
RFP	Red fluorescent protein	NGS	Next generation sequencing
SNP	Single Nucleotide Polymorphisms	pRN3P	pBluescriptRN3 plasmid
DMEM	Dulbecco's Modified Eagle Medium	PGT-A	Pre-implantation genetic testing for aneuploidy
PGS	Pre-implantation genetic screening	FGF	Fibroblast growth factor
MAPK	Mitogen-activated protein kinase	PBS	Phosphate Buffer Solution
DMSO	Dimethyl sulfoxide	PBST	PBS with 0.1% Tween
PCR	Polymerase chain reaction	PFA	Paraformaldehyde
qRT-PCR	Quantitative real-time PCR	ZGA	Zygotic genome activation
ESR	Environmental stress response	BSA	Bovine Serum Albumin
DAPI	4',6-diamidon-2-phenylindole	LIF	Leukaemia inhibitory factor
CPM	Confined placental mosaicism	F-actin	Fibrillar actin
aCGH	comparative genomic hybridization	ECM	Extra-cellular matrix
PCA	Principle component analysis	HSP	Heat shock protein
IVC1	*In vitro* implantation medium		

List of Genes

Amot	Angiomotin
Cdx2	Caudal type homeobox TF 2
Nanog	Nanog homeobox
Oct4	Octamer-binding TF 4
Sox2	SRY (sex determining region Y)-box 2
Sox21	SRY (sex determining region Y)-box 21
Sox17	SRY (sex determining region Y)-box 17
aPKC	Atypical protein kinase C
Par6	Partitioning defective 6 homolog alpha
H3R26me	H3 methylation on arginine residue 26
Carm1	Coactivator Associated Arginine Methyltransferase 1
Gapdh	Glyceraldehyde-3-Phosphate Dehydrogenase
Gata4	GATA Binding Protein 4
Lats1/2	Large Tumor Suppressor Kinase 1 and 2
Yap	Yes Associated Protein 1
Lc3b	Microtubule-associated proteins 1A/1B light chain 3B
Tdgf1	Teratocarcinoma-derived growth factor 1
Klf2	Kruppel-like factor 2
Slc25a36	Solute carrier family 25, member 36
p21	Cyclin-dependent kinase inhibitor 1A
Atg5	Autophagy Related 5
p62	Ubiquitin-binding protein p62 or Sequestosome-1
Podxl	Podocalyxin
Fgfr2	Fibroblast growth factor receptor 2
Tead4	Transcriptional enhancer factor TEF-3
Taz	Tafazzin
UBP6	Ubiquitin carboxyl-terminal hydrolase 6
Pdgfrα	Platelet Derived Growth Factor Receptor Alpha
E-cadherin	Cadherin 1, type 1
Mps1	Monopolar spindle 1-like 1
CENPA	Centromere Protein A
USP10	Ubiquitin Specific Peptidase 10

Italics - Reference to gene or mRNA

Standard - Reference to protein

1 Summary

A series of events during the first four days of mouse embryo development leads to the formation of a blastocyst. The blastocyst consists of neatly segregated three lineages: the epiblast (EPI), which will form the fetus, the extra-embryonic primitive endoderm and the outer layer of the extra-embryonic trophectoderm (TE). This organization prepares the embryo for implantation and subsequent development. This study aims to explore two broad questions: 1) what mechanisms dictate the fate of the progenies of the chromosomally abnormal cells generated during the 4-8 cell stage division; 2) how the transcriptional heterogeneities between the blastomeres of the 4-cell stage embryo affect subsequent lineage segregation.

A high incidence of aneuploidy in the early cleavage divisions is considered the principal cause for low human fecundity and developmental defects. However, there is a dramatic decline in the prevalence of aneuploidy as gestation progresses. To understand the fate of aneuploid cells, a mouse model of chromosome mosaicism was used. *In vitro* culture system and live imaging demonstrated that aneuploid cells were eliminated from the EPI by apoptosis both during pre- and peri-implantation development. Also, aneuploid cells displayed chronic proteotoxic stress. Subsequently, p53-mediated autophagy eliminated aneuploid cells from the EPI. Unlike aneuploid embryos, 1:1 diploid-aneuploid mosaic embryos show developmental potential equivalent to diploids. Their peri-implantation development was followed, and it was found that while aneuploid cells in the EPI underwent apoptosis, the diploid cells over-proliferated to regulate the overall EPI size. These results elucidate the cellular and molecular mechanisms used by mouse embryo to refine the EPI cell population and ensure only the chromosomally fit cells proceed through the development of the fetus.

The second part of the study investigates into the early molecular players that bias cell fate decisions. *Sox21* was earlier identified as the most heterogeneous gene at the 4-cell stage that can influence cell fate decision. The deep sequencing of Sox21 knockout and wild-type embryos was carried out at the 4-cell stage and compared. *Klf2* and *Tdgf1* were found to be important downstream targets of Sox21 that influence lineage segregation. Depletion of both these genes predisposed cells to the TE lineage. Co-overexpression of both these genes rescued the effect of Sox21 knockdown on cell fate. These results demonstrate the mechanism by which *Sox21* heterogeneity, from as early as the 4-cell stage, biases cell fate.

Together, these findings indicate the fundamental mechanisms used by mouse embryo to ensure developmental plasticity.

2 Introduction: An overview of early mouse development

2.1 Pre-implantation mouse embryo development: Zygote to blastocyst

In mammals, the embryo development takes place inside the body of the mother. In the mouse, gestation period is usually 20 days. Pre-implantation stage of development begins after fertilization in the ampulla region of the oviduct and ends with the blastocyst in the uterus. This process occurs over the first four and a half days post-fertilization. During first few cleavage divisions, embryo passes down the oviduct and moves into the uterus at around embryonic day 3.0 (E3.0). The early blastocyst (E3.5) marks the first fate commitment and contains two lineages: the outer layer of trophectoderm (TE) and the inner cell mass (ICM) (Figure 2.1). As the pre-implantation development completes, the ICM segregates into the epiblast (EPI) and the primitive endoderm (PE) lineages in the late blastocyst (E4.5) (Figure 2.1). The TE will give rise to the embryonic component of the future placenta, the EPI will generate the future fetus, and the PE will form the future yolk sac (Bedzhov *et al*., 2014a). The extra-embryonic membranes and placenta allow the embryo to tap maternal resources throughout gestation. The correct specification and organization of embryonic (EPI) and extra-embryonic (TE and PE) lineages is essential for successful implantation and further development of the embryo.

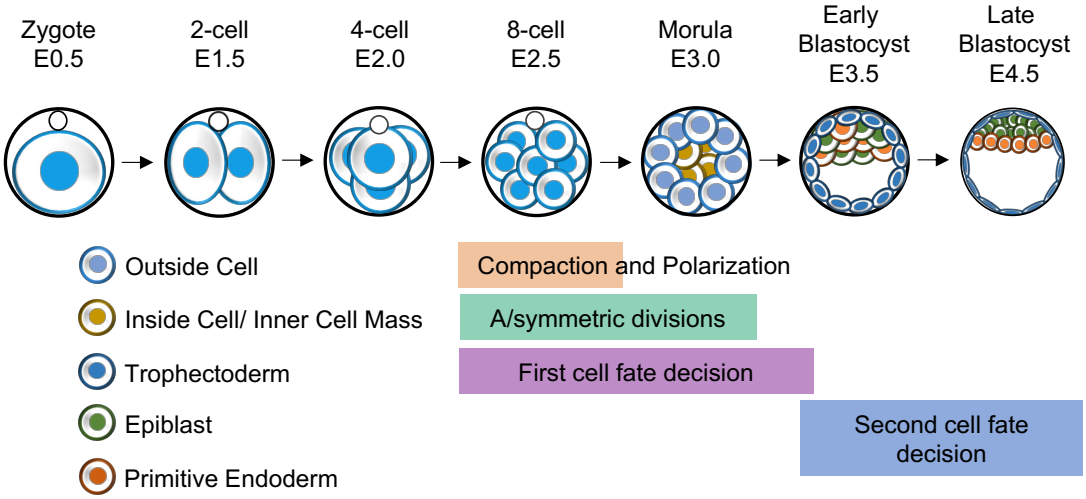

Figure 2.1 Overview of pre-implantation mouse development. Schematic representation of the first 4.5 days of embryo development, from fertilization (zygote) to the blastocyst. As the pre-implantation development completes, the embryo consists of three distinct lineages: the embryonic epiblast (EPI), the trophectoderm (TE) and the primitive endoderm (PE). These lineages are specified by two cell fate decisions. The first fate decision segregates TE and inner cell mass (ICM) which is completed by E3.5. The second fate decision segregates EPI and PE from ICM which is completed by E4.5. The embryo then hatches out of the *zona pellucida* and implants into the uterus.

2.1.1 Zygotic genome activation (ZGA) and early cleavage divisions

Post-fertilization, the zygote divides sequentially without any change in the total cytoplasmic volume of the embryo until implantation (Aiken *et al*., 2004). The resulting daughter cells become smaller and the average nucleo-cytoplasmic ratio increases (Aiken *et al*., 2004). The zygote and the two blastomeres of the 2-cell stage embryo are totipotent, i.e., have the ability to develop as a whole organism (Wu *et al*., 2017). These stages of mouse embryo rely on a maternal pool of mRNA transcripts and proteins stored in the oocyte before fertilization. As the zygotic genome activates, the majority of maternal mRNA transcripts are degraded (Hamatani *et al*., 2004), and zygotic genome begins to transcribe. This occurs in two phases: a minor transcription at the late zygote stage (minor ZGA) and a second major transcription at the 2-cell stage (major ZGA) (Hamatani *et al*., 2004; Wang *et al*., 2004a).

At the 8-cell stage (E2.5), the first major morphological event of the mouse embryo development takes place, known as compaction. This includes flattening of the blastomeres, resulting in a tightly packed embryo with the loss of distinctive cell boundaries. The outer cell-contact-free surface marks the apical side and the inner cell-contact surface marks the basal side of each blastomere in the compacted embryo. There are three critical drivers of compaction: an increase in E-cadherin mediated cell-to-cell adhesion (Hyafil *et al*., 1980), an actomyosin apical polarization mediated increase in the surface tension (Maitre *et al*., 2015), and the formation of filopodia on the membrane (Fierro-Gonzalez *et al*., 2013). Soon after compaction, there is a complete reorganization of the cytoplasm and cytoskeleton and each cell establishes an apical-basal polarity (Johnson and McConnell, 2004; Zhu *et al*., 2017). The cell nuclei and E-cadherin relocate basally (Reeve and Kelly, 1983; Yamanaka *et al*., 2006). The F-actin, microvilli, microtubules, and highly conserved apical proteins including aPKC and Par6 enrich on the apical side (Ducibella and Anderson, 1975; Johnson and Maro, 1984; Johnson and McConnell, 2004; Yamanaka *et al*., 2006). This is regulated by Rho-mediated actomyosin apical polarization through PLC–PKC signalling (Zhu *et al*., 2017).

Both compaction and polarization are critical for further embryo development. In the embryos lacking both maternal and zygotic E-cadherin, a larger proportion of cells showed the expression of TE markers, compared to in wild type (Stephenson *et al*., 2010). This shows that compaction is important to restrict the TE fate and maintain a normal ratio of TE and ICM blastomeres in blastocysts. In the embryos lacking apical-basal polarity, TE lineage formation is suppressed at the blastocyst stage. This again highlights the significance of polarization for the first lineage segregation (Kono *et al*., 2014; Korotkevich *et al*., 2017). Although both compaction and polarization occur at the 8-cell stage, they are independent processes as one can occur without the other (Pratt *et al*., 1982; O'Sullivan *et al*., 1993).

2.1.2 The first cell fate decision

The next two major waves of cell divisions generate distinct inside and outside cells: the 8- to 16-cell transition and the 16- to 32-cell transition via differential inheritance of the apical domains. An 8-cell/16-cell blastomere can divide symmetrically or asymmetrically (Johnson and McConnell, 2004). Symmetric division leads to equal inheritance of the apical polarized domain from the mother blastomere into both the daughter blastomeres. This gives two polar cells that stay on the outside of the embryo. Asymmetric division leads to complete inheritance of the apical polarized domain from the mother blastomere into one of the daughter blastomeres. This gives a polar cell that stays on the outside of the embryo. The other daughter blastomere retains the basal domain, giving a non-polar cell that goes to the inside of the embryo. Some embryos also undergo a third minor wave of asymmetric cell division: 32- to 64-cell transition (Morris *et al*., 2010). Besides asymmetric cell division, the inside cells can also be generated by the process of cell internalization driven by the differences in actomyosin contractility (McDole *et al*., 2011; Anani *et al*., 2014; Samarage *et al.,* 2015). Ultimately, the inside non-polar cells will form the pluripotent ICM and the outside polar cells will give the TE (Johnson and McConnell, 2004).

Along with the differential polarity and position in the embryo, it is equally important that lineage specific transcription factors (TFs) are activated in TE and ICM precursors. Unlike 8-cell stage, where all the cells express Cdx2 and Oct4, only outside cells express Cdx2 in the morula and only inside cells express the pluripotency factor Oct4 in the early blastocyst (Niwa *et al*., 2005). $Cdx2^{-/-}$ embryos fail to maintain TE differentiation and fail to implant (Strumpf *et al*., 2005). Also, Cdx2 is required to repress the ICM transcriptional network in the outside cells (Strumpf *et al*., 2005).

Recently, the link between cell polarity and cell position has been elucidated to drive cell fate acquisition. Subsequent to the asymmetric cell division, the cells that acquire apical domain have lower surface tension (Maitre *et al*., 2016). This forces the nonpolar cells with higher surface tension to stay inside the polar cells (Samarage *et al.,* 2015; Maitre *et al*., 2016). Also, the apical domain is sufficient to upregulate the Cdx2 expression and drive the outer polar cells to the TE lineage (Korotkevich *et al*., 2017).

How is the segregation of Cdx2 expression to the outside cells established? This is regulated by the transcription factor Tead4 and Hippo signaling pathway. $Tead4^{-/-}$ embryos fail to maintain the expression of Cdx2 beyond morula stage (Nishioka *et al*., 2008). Tead4 is widely expressed in both TE and ICM lineages (Nishioka *et al*., 2008) but is active only in the outside cells. Tead4 activity is regulated by the two homologous transcriptional co-activators Yap and

Taz. When un-phosphorylated, Yap/Taz go to the nucleus and activate Tead4 which in turn activates Cdx2 (Nishioka *et al*., 2009). Yap/Taz phosphorylation is under the control of a Hippo pathway kinase Lats1/2. In the inside cell of a 16-cell stage embryo, active Lats1/2 phosphorylates Yap/Taz, thereby localizing them to the cytoplasm. This prevents the expression of Cdx2 in the inside cells (Nishioka *et al*., 2009). So, differential phosphorylation and localization of Yap/Taz in outside and inside cells is critical for the specific activation of TE fate programme. Hippo signaling has also been shown to promote pluripotency gene network in inside cells, independent of Cdx2 (Wicklow *et al*., 2014).

Yap/Taz differential localization to inside and outside cells is regulated by the differential inside-outside activity of the junction-associated Hippo pathway component Angiomotin (Amot). In the inside cells, Amot is distributed uniformly across the membrane to the adherens junctions (AJs) and gets phosphorylated. When phosphorylated, it interacts with Lats and activates Hippo pathway (Yap/Taz) (Hirate *et al*., 2013; Leung and Zernicka-Goetz, 2013). In the outside cells, apical polarity determinants sequester Amot from basal AJs to the apical domain and Yap/Taz stay un-phosphorylated. Overall, the presence of the apical domain recruits Amot and Lats to the apical domain and inhibit their activity. This allows Yap/Taz to enter the nucleus and switch on the TE fate programme. Hippo signaling also antagonizes apical domain to ensure robust lineage segregation (Frum *et al*., 2018).

2.1.3 The blastocyst formation and the second cell fate decision

At the 32-cell stage, the TE differentiation is complete, the epithelial junctional complexes mature, and the first epithelial cell layer of the mouse embryo is obtained. This layer now separates the inner cells from the maternal environment by forming zonular tight junctions (TJs) between them (Ducibella *et al*., 1975). Simultaneously, Na+/K+ ATPase pumps polarize within the basal part of the TE, leading to the fluid accumulation and blastocyst cavitation. Besides passive water diffusion across an osmosis gradient, aquaporin water channels in the TE membrane also mediate active water transport (Barcroft *et al*., 2003). The functional TJ permeability seal is prerequisite for the formation of this blastocyst cavity, known as blastocoel (Sheth *et al*., 2000). As the development progresses, the embryonic-abembryonic (em-ab) axis of the blastocyst is formed. By E3.5, distinct TE and ICM lineages are obtained with inner cells pushed on one side of the blastocyst (the embryonic pole) and the blastocoel on the other side (the abembryonic pole) (Bischoff *et al*., 2008). The part of the TE surrounding ICM is known as the polar TE and the other part is known as mural TE. As the cavity further expands, the ICM cells give rise to two distinct lineages – EPI and PE. By E4.5, the epithelial PE layer surrounds the pluripotent apolar EPI cells and faces the blastocoel (Figure 2.1).

Nanog and Gata6 are some of the earliest transcription factors (markers) of EPI and PE respectively. They start to be expressed from 8-cell stage in almost all the cells together and become mutually exclusive during 32- to 64-cell transition (Plusa *et al*., 2008). By E3.5, EPI and PE precursor cells are present in a mosaic 'salt and pepper'-like fashion in the ICM (Chazaud *et al*., 2006). Then, they separate into spatially distinct lineages via active cell migration, positional induction and apoptosis of misplaced cells (Plusa *et al*., 2008; Melihac *et al*., 2009). Blastocysts display an increase in apoptosis during cavity expansion and rarely before that. It is seen predominantly in the ICM (10-20%), with lower levels in the TE (<3%) (Hardy, 1997). While mouse embryos usually do not display apoptosis before the blastocyst stage, Fabian *et al.* (2005) observed some apoptotic morphological changes at the 8-16-cell stages of *in vitro* produced mouse embryos. The role of apoptosis is hypothesized to eliminate cells with inappropriate/conflicting developmental potential or with underlying abnormalities such as DNA damage or aneuploidy (Fabian *et al*., 2005). Finally, both the lineages are sorted and express their respective mature markers – Sox2, Nanog for EPI (Chambers *et al*., 2003; Avilion *et al*., 2003) and Gata6, Sox17, Gata4, Pdgfrα for PE (Molkentin *et al*., 1997; Koutsourakis *et al*., 1999; Plusa *et al*., 2008; Niakan *et al*., 2010).

Mechanisms responsible for the lineage segregation of ICM into PE and EPI are not very well understood. However, there are three crucial drivers of this specification: Nanog and Gata6 mutual repression, Fgf-ERK signaling and the timing of internalization. In the ICM, EPI precursor cells secrete Fgf4 ligand, PE precursor cells express FGF-receptor 2 (Fgfr2), and all ICM cells express FGF-receptor 1 (Fgfr1; key receptor) (Kang *et al*., 2017; Molotkov *et al*., 2017). This Fgf signaling is crucial to specify PE by inhibiting Nanog and allowing Gata6 expression (Kang *et al*., 2017; Molotkov *et al*., 2017). Since inside cells are obtained from three waves of asymmetric cell division, they are predisposed to the EPI or PE fate depending on the wave of origin. The inside cells internalized in the 8-16 cell division were biased to forming future EPI cells and switch on Fgf4 while those internalized in the 16-32 cell division and the 32-64 cell division were strongly biased towards forming PE and inherit higher Fgfr2 levels (Morris *et al*., 2010). For an embryo to successfully develop post-implantation, it is crucial to have a minimum of four cells in the EPI and a correct balance of EPI and PE (Morris *et al*., 2012a). The number of cells internalized during these waves of asymmetric divisions and consequently the amounts of Fgf4 and Fgfr2 in the ICM provides a window of flexibility to ensure this (Morris *et al*., 2012a; Krupa *et al*., 2014).

Mouse embryonic stem cells (mESCs) can be derived from the EPI of the E4.5 embryo (Martin, 1981) and are transcriptionally equivalent to them (Boroviak *et al*., 2014). Since mESCs can be self-renewed indefinitely, they offer an excellent tool to study developmental biology.

Similar to EPI which can contribute to all tissues of the fetus, this ground-state pluripotency can be homogeneously maintained in the mESCs using specific culture conditions. These conditions, known as 2iLIF include: leukaemia inhibitory factor (LIF) and two small molecule inhibitors (2i) (Ying *et al*., 2008). One of the inhibitors blocks MAPK/ERK signaling and the other, known as Chiron, promotes Wnt signaling by inhibiting GSK3β (Ying *et al*., 2008).

2.1.4 Developmental plasticity

Several studies indicate the regulative nature of early cleavage mouse embryos. The early mouse embryos can adapt to experimental perturbations such as the removal, addition or rearrangement of blastomeres, giving rise to fully functional blastocysts or even live pups (Tarkowski, 1959; Tarkowski, 1961; Hillman *et al*., 1972; Suwinska *et al*., 2008). Even removing animal or vegetal poles as early as zygote stage results into a viable offspring (Zernicka-Goetz, 1998). As the development progresses, the blastomeres restrict their developmental potency and this flexibility diminishes. This raises the question - at which developmental stage do blastomeres completely lose this flexibility? The 8- to 16-cell division marks the first wave of lineage segregation resulting into a 16-cell stage compact embryo comprising of inside and outside cells (Figure 2.1). These two populations of cells differ in their position within the embryo, properties including polarity status and gene regulation, and potency to contribute to TE/ICM. In an unperturbed normal development, the daughter outside cells activate a TE fate programme, some daughter outside cells contribute to the ICM and all the daughter inside cells take on an ICM fate. In the absence of outer cells, inner cells can generate TE cells and conversely, in the absence of inner cells, outer cells can generate ICM cells (Ziomek and Johnson, 1982; Johnson and Ziomek, 1983). The aggregated 16-cell embryos derived from 16 inner-only blastomeres or 16 outer-only blastomeres can both develop into blastocysts and give normal mice after implantation (Suwinska *et al*., 2008). The 16- to 32-cell division marks the second wave of lineage segregation resulting into a 32-cell stage morula comprising of two distinct lineages – TE (outer cells) and ICM (inner cells) (Figure 2.1). At the 32-cell stage, the aggregates of outer-only cells formed trophoblastic vesicles and the aggregates of inner-only cells formed blastocysts that failed to implant (Suwinska *et al*., 2008). Overall, this indicates that blastomeres become irreversibly committed to a developmental fate by the 32-cell stage. However, the regulative capability of the mouse embryo as a whole is not lost until later in development. A 32-cell stage, the embryo can result into a viable mouse after segregation and random reaggregation of blastomeres, as the cells sort themselves out into their original inner-outer positions (Suwinska *et al*., 2008).

This does not necessarily imply that all blastomeres in the early cleavage embryos (2-cell/4-cell/8-cell) are equivalent. There is an increasing amount of recent studies indicating that the

regulative capacities of blastomeres of embryos even as early as 2-cell are to a certain degree limited. They hypothesize the presence of a natural early developmental bias within blastomeres of these early cleavage embryos during normal development. This will be discussed in detail in Chapter 6.

2.2 Implantation of the embryo

By end of pre-implantation, all three lineages are established, and the blastocyst hatches from the *zona pellucida* (a glycoprotein membrane surrounding the embryo throughout the pre-implantation development). At this point, both embryo and maternal tissues are ready to allow the invasion of the blastocyst into the uterine wall. Regulated level of estrogen and progesterone prime the uterus to receive the embryo (Ma *et al*., 2003). The uterine lumen narrows to position the embryo in a crypt in the luminal epithelium (LE). Pinopodes, projections on the LE, most likely mediate the initial TE and LE contact and flatten down as the attachment becomes more stable (Aplin and Ruane, 2017). Various cell adhesion molecules and integrins, expressed by both the TE and LE, stabilize the embryo attachment (Basak *et al.*, 2002). Post-attachment, the LE cells at the implantation site undergo cell death or entosis (Parr *et al.*, 1987; Li *et al.*, 2015) and the mural TE differentiates into TE giant cells (TGCs). As the TGCs invade the uterine stromal tissue, they secrete factors that initiate decidualization of the stromal cells (Bany and Cross, 2006). TGCs induce vasculature remodeling and angiogenesis at the site of implantation to facilitate nutrient, waste and gas exchange between the embryo and the mother (Cross *et al.*, 2002).

2.3 Post-implantation development: Egg cylinder morphogenesis

A drastic change in the shape and size of the embryo takes place within 24 hours following the initiation of implantation (E5.0). Both embryonic and extra-embryonic tissues undergo a burst of cell proliferation and the blastocyst transforms into the elongating egg cylinder (Bedzhov *et al*., 2014a). The apolar EPI transforms into a polarized epithelium with a lumen at its centre (the apical side of the EPI cells) and occupies the distal part of the embryo (Figure 2.2). Simultaneously, the EPI undertakes extensive change in gene expression (Nichols and Smith, 2009) and epigenetic signature (Heard, 2004). The polar TE proliferates to form the extra-embryonic ectoderm tissue (ExE) and the ectoplacental cone (EPC). The ExE sits above the cup-shaped EPI and the EPC sits above the ExE (Figure 2.2). The ExE is the source of the TE stem cells (TSCs) and will give rise to the future placenta. The PE proliferates to form the parietal endoderm (PaE) and the visceral endoderm (VE) (Bedzhov *et al*., 2014a). The epithelial VE forms a monolayer around the ExE and the cup-shaped EPI and the PaE lines the blastocoelic surface of the mural TE (Figure 2.2). The VE will give rise to the future yolk-

sac. Overall, the embryo adopts a cylindrical shape with pro-amniotic cavity running through its centre (Figure 2.2), laying the foundation for the developing body.

As the blastocyst implants, TE and PE secrete extracellular matrix (ECM) signalling components and assemble a basement membrane around the EPI. The β1-integrin receptors on the surface of the EPI sense these ECM components, such as laminin, which leads to EPI cell apical-basal polarization (Bedzhov and Zernicka-Goetz, 2014). As EPI cells polarize, actin filaments and the Golgi apparatus move apically, and nucleus localizes basally. This reorganization of actomyosin leads to apical constriction where all the EPI cells meet, resulting into the formation of a 'rosette-like' structure (Figure 2.2). This apical domain of EPI expresses the negatively charged sialomucin protein, podocalyxin (Podxl) in the centre of the rosette. As a result of the charge repulsion of the apical membranes, a small lumen is formed in the centre of the EPI (Bedzhov and Zernicka-Goetz, 2014). Simultaneously, another cavity, also lined by Podxl, emerges in the centre of the ExE (on the apical side) (Bedzhov and Zernicka-Goetz, 2014). As the lumen in the centre of the EPI expands, the egg cylinder elongates and it merges with the cavity in the ExE, giving a mature pro-amniotic cavity by E5.75 (Figure 2.2).

Studies using knockouts for laminin genes and β1-integrin receptor highlight the role of the basement membrane during mouse embryo post-implantation development. The homozygous loss of the β1-integrin receptor leads to EPI defect (Stephens *et al*., 1995). Individual knockouts for laminin subunits, Lama1$^{-/-}$, Lamb1$^{-/-}$ and Lamc1$^{-/-}$, result in early embryonic lethality (Smyth *et al*., 1999; Miner *et al*., 2004). Evidently, the basement membrane creates a niche for the polarization and maturation of EPI. Remarkably, this function of the basement membrane and the EPI post-implantation morphogenesis can be mimicked *in vitro* in the absence of TE by embedding ICMs in ECM gels (Bedzhov and Zernicka-Goetz, 2014).

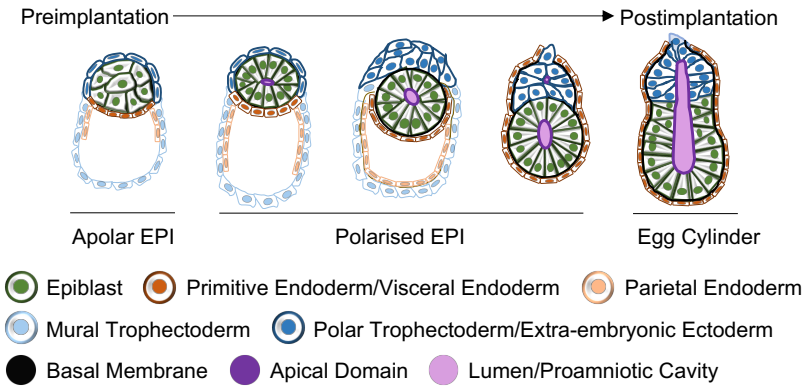

Figure 2.2. A model for the peri-implantation morphogenesis in mouse (Adapted from Bedzhov and Zernicka-Goetz, 2014)**.** As the late blastocyst (E4.5) implants into the uterus, it rapidly proliferates and transforms into an egg cylinder (E5.75). EPI organizes into a polarized rosette and opens a central lumen on the apical side.

3 Introduction I: Aneuploidy in mammalian systems

3.1 Comparison between mouse and human early embryo development

In humans, the pre-implantation stages are morphologically similar to mouse and end with the formation of the blastocyst in the uterus. However, the timing of developmental events differs between mouse and human. In humans, the major ZGA occurs at 4-8 cell stage, followed by compaction at 16-cell stage (Cockburn and Rossant, 2010). The blastocoel begins to form at day 5 and the late blastocyst is obtained by day 6 (Niakan *et al*., 2012). Primary lineage regulators are similar between mouse and human including TFs such as Oct4, Sox2, Nanog, Cdx2, Gata3, Sox17, Gata4 and Gata6 (Cockburn and Rossant, 2010; Niakan *et al*., 2012; Stirparo *et al*., 2018). On the mechanistic level, Cdx2 seems to suppress Oct4 in TE in humans too (Cockburn and Rossant, 2010). However, there are some deviations between human and mouse with respect to mechanisms of lineage specification, gene expression patterns, epigenetics and genomic instability (Niakan *et al*., 2012). The time of lineage restriction in relation to the initiation of blastocyst formation is later in humans (Cockburn and Rossant, 2010). Human EPI cells lack the expression of several genes active in mouse EPI and ESC, such as *Esrrb*, *Fbxo15*, *Nrob1* and *Klf2* (Stirparo *et al*., 2018). Also, human pre-implantation embryos are highly susceptible to developmental arrest and aneuploidy (Niakan *et al*., 2012). As the pre-implantation development completes, human blastocyst contains all three lineages: TE, EPI and PE. Then, the blastocyst hatches out of the *zona* and implants at day 7.

Post-implantation, EPI and hypoblast (equivalent of mouse VE) segregate and blastocysts attach on the polar TE side (Deglincerti *et al*., 2016). The embryos form a bilaminar disc of two layers – the EPI and the hypoblast. The EPI cells line the pro-amniotic cavity and the hypoblast cells line the yolk sac with the bilaminar disc in between. Similar to mouse egg cylinder, EPI cells became radially organized around a small central lumen and undergo lumenogenesis by EPI polarization and charge repulsion, not by apoptosis (Deglincerti *et al*., 2016; Shahbazi *et al*., 2016).

Given the logistical, ethical and financial challenges of working with human, overall mouse offers a relevant model for the study of mammalian pre- and post-implantation development.

3.2 The role of aneuploidy in human pregnancy

Humans have relatively low fecundity. The maximal chance of conceiving a clinically recognized pregnancy in one menstrual cycle is 30-40% (Macklon *et al*., 2002). Studies using hysterectomy specimens, clinical miscarriage data and using the elevated hCG (human chorionic gonadotropin) levels in urine specimens as a marker for early pregnancy indicate that 30% pregnancies are lost before implantation, 30% are lost before the missed period (i.e. pre-clinical) and 10% as spontaneous miscarriages (Hertig *et al*., 1959; Macklon *et al*., 2002). With the introduction of human *in vitro* fertilization (IVF) and advances in cytogenetic techniques, chromosomal abnormalities in oocytes and embryos, such as aneuploidy, are considered as the most likely cause of this high rate of pregnancy loss (Macklon *et al*., 2002; Hodes-Wertz *et al*., 2012). Aneuploidy is defined as the presence of an abnormal number of chromosomes. It can occur either by chromosomal gain (trisomy) or loss (monosomy), known as 'whole chromosomal aneuploidy' or due to rearrangements of chromosomal parts by their deletions, amplifications or translocations, known as 'segmental aneuploidy' (Storchova, 2012). Aneuploidy of a cell population can be of two types: (I) uniform aneuploidy (each cell of the population contains the same chromosomal abnormality); (II) mosaic aneuploidy (differing chromosome constitutions in different cells of the population). In humans, aneuploidy is widely associated with several diseases including cancer and reproductive health problems, in particular subfertility, miscarriage, and neonatal developmental defects.

Since the 1970s, large cytogenetic studies were published correlating early pregnancy loss and genetic abnormalities. These studied revealed that >50% of first trimester spontaneous miscarriage samples were chromosomally abnormal (Boué *et al*., 1975; Hassold *et al*., 1980; Fritz *et al*., 2001). Following the success of IVF (Steptoe and Edwards, 1978), it was possible to evaluate the potential role of aneuploidy in human embryos before implantation. There is a considerable heterogeneity in the reported prevalence of mosaicism in human pre-implantation embryos, ranging from 15% (Harper *et al*., 1995) to more than 90% (Bielanska *et al*., 2002; Vanneste *et al*., 2009). This variation can be attributed to several factors including the developmental stage of embryos used, the lineage of the embryos used, the number of cells tested, the cytogenetic method to detect ploidy status and the number of chromosomes analyzed. Earlier studies used chromosome spreading (Zenzes *et al*., 1992), followed by fluorescent in-situ hybridization (FISH) (Delhanty *et al*., 1993; Magli *et al*., 2000; Baart *et al*., 2007; Munńe *et al*., 2010) to detect aneuploidy. The major limitation of FISH is that only a limited number of chromosomes can be analyzed at one time. Consequently, several protocols have been developed to detect aneuploidy: real-time polymerase chain reaction (qRT-PCR) (Treff and Scott, 2013; Zimmerman *et al*., 2016), single nucleotide polymorphism (SNP) microarray (Treff *et al*., 2010; Handyside, 2011), comparative genomic hybridization (aCGH)

microarray (Wells and Delhanty, 2000; Voullaire *et al*., 2002) and more recently, next generation sequencing (NGS) (Fiorentino *et al*., 2014; Zheng *et al*., 2015). These molecular biology techniques enable all chromosomes to be evaluated rapidly and at high resolution. Overall, majority of studies conclude that mosaic aneuploidy is prevalent in >70% of human IVF pre-implantation embryos, of which 60% are diploid-aneuploid mosaic (van Echten-Arends *et al*., 2011; Mertzanidou *et al*., 2013). How closely these rates reflect the situation *in vivo* is not known. As human gestation proceeds, the prevalence of chromosomal abnormalities continues to decrease, reaching to only 0.6% in live births (Jacobs *et al*.,1974).

Chromosomal abnormality has been found in pre-implantation embryos from other non-human species as well, such as *in vivo* pig (4.7% - 14.3%) (Hornak *et al*., 2012), *in vitro* produced pig (45.9% - 37%) (Ulloa Ullo *et al*., 2008; Hornak *et al.,* 2015), *in vitro* produced rhesus macaque (73.5% - 49%) (Dupont *et al*., 2010; Daughtry *et al*., 2019), *in vivo* produced rabbit (56%) (Shi *et al*., 2004), *in vitro* produced rabbit (62.5 - 83%) (Shi *et al*., 2004; Curlej *et al*., 2010), *in vivo* produced sheep (19.6%) (Coppola *et al*., 2007), *in vitro* produced sheep (65.3%) (Coppola *et al*., 2007), *in vivo* produced cows (20%) (Iwasaki *et al*., 1992) and *in vitro* produced cows (27% - 40%) (Iwasaki *et al*., 1992; Viuff *et al*., 2000; Turner *et al*., 2019). These studies also suggest that *in vitro* production of embryos can also increase the incidence of chromosomal abnormality as compared to *in vivo* production. This could be attributed to factors such as IVF culture conditions (Wang *et al*., 2001) and ovarian hyperstimulation (Baart *et al*., 2007).

3.2.1 Origin of mosaic aneuploidy in human embryos

Aneuploidy in early human embryos can originate due to errors either in meiosis or mitosis, or in both. Whole-embryo same chromosome aneuploidy arises secondary to errors of meiosis and increases steadily with advanced maternal age (Hassold and Hunt, 2001). Mosaic aneuploidy is likely to arise secondary to errors of mitosis during the first few cleavage divisions post-fertilization (van Echten-Arends *et al*., 2011) and can be independent of maternal age (Baart *et al*., 2006; Munńe, 2006; Vanneste *et al*., 2009). The underlying mechanisms that give rise to these errors remain mostly unclear.

Three main mechanisms have been proposed that can lead to mosaic aneuploidy during embryonic development: non-disjunction, anaphase lagging and endoreplication (Mantikou *et al*., 2012). Non-disjunction is the premature separation of chromatids during anaphase where the two sister chromatids fail to separate. This results in a daughter cell with a monosomy and another daughter cell with a trisomy. Anaphase lagging is the failure of a single chromatid to be incorporated in either nucleus of the daughter cells. This results in a daughter cell with a monosomy and another daughter cell with a disomy. If the lagging chromosome gets randomly

inherited by one of the daughter cells but fails to join the main nucleus, it can get encapsulated in a separate micronucleus, which can catalyze further mosaicism (Vázquez-Diez *et al*. 2016). Endoreplication is the replication of a chromosome without division. This results in a cell with a trisomy of that chromosome. Several studies indicate anaphase lagging as the main source of mosaicism in human pre-implantation development (Coonen *et al*., 2004; Daphnis *et al*., 2005; Capalbo *et al*., 2013).

Several molecular factors could contribute to mosaic aneuploidy during embryonic development. Cleavage stage human embryos have been shown to over-express cell cycle drivers and under-express cell cycle checkpoints, making them prone to chromosome segregation errors (Kiessling *et al*., 2010). Since human embryos activate their genome only at the 4- to 8-cell stage, the first cell divisions are highly dependent on the mRNAs and proteins supplied by the oocyte. If the maternal resources are defective, it can affect microtubule kinetics, cell cycle checkpoints, DNA repair proteins, chromosome cohesion, telomere shortening and mitochondrial function, thereby leading to mitotic errors in early human embryos (Mantikou *et al*., 2012; Vera-Rodriguez *et al.,* 2015). The considerable time between the initiation of meiosis and fertilization is likely to contribute to the defective maternal RNA and protein pool (Mantikou *et al*., 2012). Minor dysregulation of maternal genes that have the ability to alter mitotic fidelity can also lead to aneuploidy in human embryos (McCoy *et al*. 2015a). Besides maternal factors, mitotic mosaicism can also arise due to paternal factors. Since the centrosome is inherited from the sperm, dispermy or the disruption of sperm centrosome can result in mosaicism (Palermo *et al*., 1994, 1997). Severe male factor infertility can also lead to aneuploidy (Silber *et al*., 2003; Magli *et al*., 2009).

3.2.2 Aneuploidy screening techniques to improve IVF outcomes

Since high frequency of aneuploidy in pre-implantation embryos is widely associated with low IVF success rate, the reliable recognition of euploid embryos for transfer could in theory improve IVF outcome. Many techniques to identify embryos with a high developmental potential have been pioneered. Non-invasive methods include monitoring embryo throughout development using time-lapse imaging and morphology assessment. The features of cell number, symmetry of blastomere size and shape, level of fragmentation, degree of compaction, degree of the blastocyst cavity expansion, organization of cell in ICM and TE and hatching may be evaluated to determine embryo viability (Machtinger and Racowsky, 2013). Several studies report that measuring the duration of the first cytokinesis and the time between the 2^{nd} and 3^{rd} mitotic divisions, time to 5^{th} and 8^{th} cell, time to start of bastulation, distorted cytoplasm movement, multinucleation in 3^{rd} cell cycle, direct cleavage and reverse cleavage could be used to predict blastocyst fate (Wong *et al*., 2010; Hashimoto *et al*., 2012; Desai *et*

al., 2014; Basile *et al*., 2015; Yang *et al*., 2018). However, there is not enough evidence associating morphokinetics, embryo viability and ploidy status. Alternatively, advanced metabolic and proteomic profiling of the spent media (media that was used for embryo culture) have also been explored to potentially diagnose the embryo viability (Seli *et al*., 2010; Picton *et al*., 2010; Mains *et al*., 2011; Cortezzi *et al.,* 2011; McReynolds *et al.,* 2011).

In contrast to the non-invasive approaches used, pre-implantation genetic screening (PGS) is an invasive test to assay the chromosomal status of embryos (Wilton, 2002). All the biopsied embryos are typically vitrified until testing is complete and the known euploid embryos are then thawed and transferred in the next cycle. There are currently three sources of biopsy that can be used for PGS: polar bodies from oocytes and zygotes; one/two blastomeres from cleavage-stage embryos and 5-10 TE cells from blastocysts. Several robust genetic screening technologies are utilized in clinics for PGS: FISH, aCGH, SNP arrays, qRT-PCR and NGS. Each biopsy technique and genetic diagnostic technology has its own advantages and disadvantages (reviewed in Griffin and Ogur, 2018). It is essential to clearly understand these pros and cons to optimize the chances of achieving a viable pregnancy and the birth of a healthy baby. The most widely accepted practice involves the aCGH, or more recently, NGS-based genetic analysis of biopsied TE cells of blastocysts (Yang *et al*., 2012; Wells *et al*., 2014; Coates *et al*., 2017). Numerous reports have demonstrated PGS efficacy in improving IVF outcomes, while reducing the risk of miscarriage and multiple pregnancy rate (Griffin and Ogur, 2018). However, there are several challenges associated with the pre-implantation genetic testing for aneuploidy (PGT-A). The main issue is the reliable detection of mosaicism in the sample. A second issue is that being an invasive procedure - it poses potential risk on the subsequent embryo development and viability. A third issue is that the TE biopsy might not be directly reflective of the future fetus, which is derived from the ICM. Such considerations have led to the investigation of alternative non- (or minimally) invasive means of PGT-A. Several studies explore the potential of cell-free embryonic DNA in the spent medium (Shamonki *et al*., 2016; Xu *et al*., 2016) and/or in the fluid of the blastocoel cavity, known as, blastocoelic fluid (BF) (Gianaroli *et al*., 2014; Magli *et al*., 2016) to diagnose the embryo chromosome status (Kuznyetsov *et al*., 2018). Although still controversial, higher mitochondrial DNA content in spent medium of blastocysts has also been demonstrated as a biomarker associated with aneuploidy, lower implantation rates and reduced embryo viability (Diez-Juan *et al.,* 2015; Fragouli *et al.,* 2015a, 2017a). Although promising, use of cell-free DNA requires further validation and improvements before it is used in clinics as an alternative to embryo biopsy to examine the embryo ploidy status. A recent study emphasizes the application of invasive and non-invasive aneuploidy detection methods in synergy for enhanced diagnostics (Ben-Nagi *et al*., 2019).

3.3 The fate of aneuploid cells

Since mosaic aneuploidy is highly prevalent in human pre-implantation embryos, it is essential to understand its impact on the embryo development and implications for embryo selection in IVF. There is a reduction in mosaicism as the human development progresses. Several studies report that this decline in mosaicism starts as early as the pre-implantation stage of development from cleavage-stage stage to the blastocyst stage (Almeida and Bolton, 1996; Bielanska *et al*., 2002; McCoy *et al*. 2015b). What mediates this shift away from mosaicism towards euploidy remains unknown. It could either result from developmental failure of the mosaic embryo or through the regulation of aneuploid cells during development. Multiple studies report that embryos displaying high levels of aneuploidy during early cleavage-divisions have low rates of blastocyst formation or high rates of implantation failure (Bielanska *et al*., 2002; Santos *et al*., 2010; Fragouli *et al*., 2015b). However, there is also increasing evidence that some mosaic human embryos have the potential to develop into viable euploid births (Greco *et al*., 2015; Fragouli *et al*., 2017b; Spinella *et al*., 2018; Rubino *et al*., 2018). Perhaps the developmental ability of a mosaic embryo could depend on the ratio of diploid and aneuploid cells. If indeed some mosaic embryos have full developmental potential it is important to understand what mechanisms regulate aneuploidies during embryo development. Following three mechanisms have been proposed to explain the fate of aneuploid cells:

- Self-correction

This hypothesis proposes that aneuploid cells can self-correct aneuploidy by a mitotic error including monosomy rescue (duplication of the single chromosome) or trisomy rescue (loss of the extra chromosome). While some studies favor this hypothesis (Munńe *et al*., 2005; Barbash-Hazan *et al*., 2009), there is no direct evidence in human embryos. Some recent studies report the generation of euploid induced pluripotent stem cells from cells of a Down syndrome mouse model or from human trisomic patient fibroblasts or from amniotic fluid-derived cells from trisomy 21 patients, possibly via the loss of the extra chromosome (Hirota *et al*., 2017; Inoue *et al*., 2019). In human embryos, one way to detect self-correction is to assess the incidence of uniparental disomy (UPD). UPD is the inheritance of both copies of the chromosome from the same parent. All monosomy rescues and one-third of trisomy rescues will result in UPD. There are a few studies that report the occurrence of UPD in early human embryos, although the incidence is rare (Vanneste *et al*., 2009; McCoy *et al*., 2015b).

- Preferential allocation to the trophectoderm lineage

This hypothesis proposes that aneuploid cells actively segregate to the TE layer (precursor of the future placental tissue) while euploid cells get incorporated into the future fetal lineage as the embryo develops. This hypothesis gives one possible explanation for the observation of

confined placental mosaicism (CPM). CPM was first described in 1983, where chromosome mosaicism was found only in placental chorionic cells and not in cells derived from the embryo proper (Kalousek and Dill, 1983; Baffero *et al*., 2012). There are animal studies in support of this hypothesis (James *et al*., 1995, Viuff *et al*., 2002; MacKay and West, 2005). In tetraploid-diploid mice chimeras and bovine mixoploids, polyploid cells display higher distribution frequency in TE lineage compared to in the ICM. However, detailed karyotypic analyses of human blastocysts to characterize the chromosome constitution of TE and ICM cells found no evidence of preferential segregation of abnormalities to the TE lineage (Johnson *et al*., 2010, Northrop *et al*., 2010; Capalbo *et al*., 2014).

- Clonal depletion

This hypothesis proposes that in a diploid-aneuploid mosaic embryo, the aneuploid cells become progressively eliminated either by apoptosis or senescence or blastomere exclusion. While some studies favor this hypothesis (Ambartsumyan and Clark, 2008; Santos *et al*., 2010; Zhan *et al*., 2016), there is no direct evidence in human embryos. In maize and rice, trisomic plants grow significantly more poorly than their wild-type counterparts (McClintock 1929; Singh *et al*., 1996). Studies using aneuploid yeast strains and mammalian cell lines have revealed that aneuploid cells show impaired proliferation compared to euploid cells (Torres *et al*., 2007; Thompson and Compton, 2008; Williams *et al*., 2008; Li *et al*., 2010; Pfau *et al*., 2016). There are some studies that provide direct evidence supporting this hypothesis using mouse mosaic embryos, as discussed in the next section and explored further in the thesis. This hypothesis gives another possible explanation for the observation of CPM, if aneuploid cells undergo clonal depletion in specifically ICM lineage.

Overall, there is insufficient evidence to support any of these processes in human embryos.

3.3.1 The fate of aneuploid cells in mouse embryos

In order to determine the precise fate of aneuploid cells, it is important to follow them in real-time as the whole embryo develops. This is particularly challenging with human embryos since it will require non-invasive identification and fluorescent labeling of aneuploid cells within the embryo. For decades, mouse embryos offer a useful system to get insights into early mammalian development. Consequently, there are a few publications using mouse as a model to investigate the effect of aneuploidy on early embryo development. However, unlike in human embryos, pre-implantation aneuploidy rates in the mouse embryos are reported as low, typically between 1 and 4% (Glenister *et al*., 1987; Liu *et al*., 2008). One possible explanation for this difference between the aneuploidy rates between human and mouse pre-implantation embryos is the difference in their respective zygotic genome activation (ZGA)

timings. Until ZGA occurs, the embryo is entirely dependent on a pool of mRNAs and proteins provided by the oocyte. It could be hypothesized that later the ZGA occurs post-fertilization, greater is the window of opportunity where mitotic instability increases due to defective or insufficient maternal resources. In mice, ZGA occurs at the 2-cell stage while it occurs later at the 4-8 cell stage division in the humans. Similar correlation could be seen in other mammalian systems (Carbone and Chavez, 2015): in porcine embryos ZGA occurs at the 4-cell stage and aneuploidy rates are 4.7% - 14.3%, in rhesus macaque *in vitro* produced embryos ZGA occurs at the 6-8 cell stage and aneuploidy rates are 49% - 73.5%, and in rabbit embryos ZGA occurs at the 8-16 cell stage and aneuploidy rates are 56%. This suggests a possibility that ZGA timing and the rate of aneuploidy in pre-implantation embryos are linked. Another possible reason for the difference in the aneuploidy rates between human and mouse pre-implantation embryos could be because centrosome is maternally inherited in mouse while it is paternally inherited in humans (Carbone and Chavez, 2015). Similar to humans, centrosome is paternally inherited in porcines, rhesus macaques and rabbits as well (Carbone and Chavez, 2015). Due to low pre-implantation aneuploidy rates in the mouse embryos, efforts were made towards the development of mouse models of aneuploidy.

Historically, mouse autosomal trisomies and monosomies were generated by mating normal females with feral males, doubly heterozygous for two different Robertsonian fusion metacentric chromosomes with an arm in common (Epstein *et al*., 1985). All the full trisomies, except trisomy 19, die before birth (mostly early post-implantation), and display growth retardation and congenital malformations (Epstein *et al*., 1985). Interestingly, there seems to exist an indirect correlation between the size of the chromosome present as trisomy and embryo survival. In contrast to trisomic embryos, monosomic embryos die before implantation (Epstein *et al*., 1985). To study the functional consequences of aneuploidy, diploid-aneuploid mosaic chimeras were generated by aggregating aneuploid embryos with diploid embryos at the pre-implantation stage. These mosaic chimeras resulted in viable mice, carrying aneuploid cells in varying proportions in different tissues. Overall, it was seen that aneuploid cells suffer proliferative disadvantage as compared to diploid cells (Epstein *et al*., 1985). Another study used Sycp3-null female mouse model to investigate the fate of aneuploid cells during embryo development (Lightfoot *et al*., 2006). Inactivation of synaptonemal complex protein 3, Sycp3, lead to chromosomal missegregation errors during meiosis, resulting in aneuploid oocytes (Yuan *et al*., 2002). Upon fertilization, the zygote inherited this whole chromosome aneuploidy. These embryos started to show abnormal morphology and increased apoptosis during gastrulation (Lightfoot *et al*., 2006). Furthermore, homozygous knockout embryos for several mitotic checkpoint genes (*BubR1*, *Bub3*, *Mad2*) and kinetochore components (*Cenpa*, *Cenpc*, *Cenpe*) displayed increased chromosome missegregation and early post-implantation lethality

(Kalistis *et al*., 1998; Dobles *et al*., 2000; Howman *et al*., 2000; Kalistis *et al*., 2000; Putkey *et al*., 2002; Wang *et al*., 2004b). Some of these studies provide evidence for extensive apoptosis (Dobles *et al*., 2000; Wang *et al*., 2004b) or ICM-specific impaired proliferation (Dobles *et al*., 2000; Kalistis *et al*., 2000; Putkey *et al*., 2002), following the induction of mitotic abnormalities.

Recently, a novel mouse model of chromosome mosaicism was developed and employed to investigate the pre- to post-implantation fate of aneuploid cells during mosaic embryo development (Bolton *et al*., 2016). Chromosome mis-segregation errors were induced during the 4- to 8-cell stage division using reversine, which inhibits the key spindle assembly checkpoint (SAC) protein, Monopolar spindle 1-like 1 (Mps1) kinase (Santaguida *et al*., 2010). Reversine treatment significantly increased the rate of aneuploidy in early mouse embryos. It was found that reversine-treated embryos died by early post-implantation stage. There was significant reduction in cell numbers in reversine-treated embryos compared to controls already during blastocyst maturation (E3.5 to E4.5). No evidence of preferential allocation of reversine-treated cells to the TE lineage was found. To generate a model of diploid-aneuploid mosaicism, chimeras containing reversine-treated and control cells were created. Live tracking of reversine-treated cells in these chimeras during blastocyst maturation revealed that different mechanisms regulate them in different lineages: apoptosis in ICM, and increased cell cycle length and senescence in TE (Bolton *et al*., 2016). Unlike reversine-treated embryos, control-reversine chimeras gave live and mostly diploid pups when transferred into foster mothers (Bolton *et al*., 2016). This model will be used further in this thesis to investigate the potential mechanisms accounting for the ultimate fate of the aneuploid cells.

3.4 Cellular responses to aneuploidy

Aneuploidy causes growth retardation and developmental defects in various species including sea urchins, *Drosophila*, plants, *C. elegans*, yeast, mice and humans (Siegel and Amon, 2012). The first question that comes up when studying the basis for the reduced fitness caused by aneuploidy is – Is it due to gain/loss of DNA per se or due to changes in gene expression (RNAs and proteins) levels? Studies that address these questions have been carried out in non-embryonic cellular systems, but they can still be very relevant to understanding the effect of aneuploidy on fundamental cell physiology in mammalian embryos.

Using budding yeast cells, it was demonstrated that the introduction of large-size (upto 1.6 Mb) human or mouse DNA did not significantly impair proliferation (Torres *et al*., 2007). This implied that the phenotype associated with aneuploidy is not due to the mere presence of additional DNA or lack of DNA. This encouraged studies that looked into the changes in transcriptome and proteome of the cells bearing aneuploidy. Studies across various systems

including haploid and budding yeast (Torres *et al*., 2007; Pavelka *et al*., 2010), engineered mammalian cell lines (Williams *et al*., 2008; Stingele *et al*., 2012), and patient-derived cell lines and tissue samples (Mao *et al*., 2005; Halevy *et al*., 2016; Zhao *et al*., 2017) demonstrate that mRNA expression levels mostly scale with the altered chromosome copy numbers (Figure 3.1). Transcriptional dosage compensation can occur for some aneuploid chromosomes in rare cases (Figure 3.1) including for X chromosome in mammals (Payer and Lee, 2008), for both sex chromosomes and autosomes in *Drosophila* (Zhang *et al*., 2010) and for autosomes in some plants (Makarevitch *et al.,* 2008; Zhang *et al*., 2017). The extent of transcriptional dosage compensation for autosomes in yeast is unresolved (Gasch *et al*., 2016; Torres *et al*., 2016). Besides the direct dosage effect on the expression of genes on the chromosome altered, the expression for genes on other chromosomes can also be indirectly affected (Huettel *et al*., 2008; Letourneau *et al*., 2014) (Figure 3.1). This could either be because these genes are downstream targets of TFs on the affected chromosome (Rancati *et al*., 2008) or via micro-RNA deregulation (Dürrbaum *et al*., 2018) or because aneuploidy can cause epigenetic instability (Mulla *et al*., 2017). Similar to mRNA, protein levels also scale with the altered chromosome copy numbers in budding yeast and human cells (Pavelka *et al*., 2010; Stingele *et al*., 2012; Dephoure *et al*., 2014; Liu *et al*., 2017) (Figure 3.1). However, about 25% of all proteins undergo dosage compensation to euploid levels, despite the transcriptional imbalance (Stingele *et al*., 2012; Dephoure *et al*., 2014; Liu *et al*., 2017) (Figure 3.1). Majority of these proteins are components of macromolecular complexes and kinases (Stingele *et al*., 2012; Dephoure *et al*., 2014). They undergo extensive dosage compensation via protein degradation and not via translation inefficiency (Dephoure *et al*., 2014; Ishikawa *et al*., 2017).

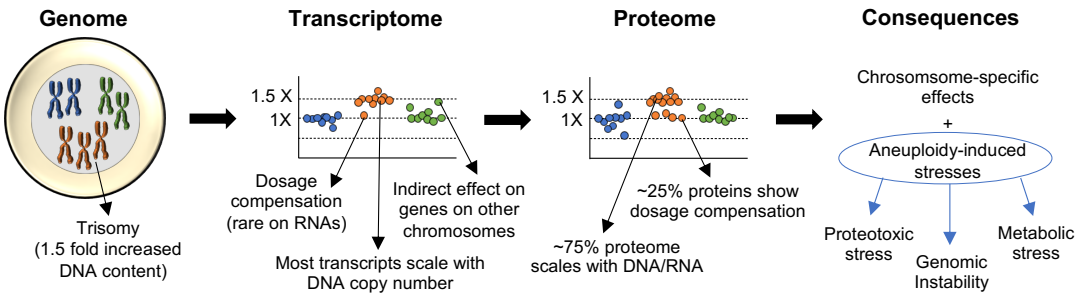

Figure 3.1. Cellular consequences of aneuploidy (Adapted from Soto *et al*., 2019). Aneuploidy (trisomic for orange chromosome here) results in scaled changes to the RNA expression of majority of genes. In rare cases, few genes can undergo dosage compensation on RNA level. Aneuploidy can also indirectly alter the expression of genes on other chromosomes. These changes in RNA, scale to changes in protein expression for most of the proteins. However, about 25% of the proteins undergo dosage compensation. Subsequently, chromosome-specific effects can be observed in aneuploid cells. Additionally, this protein imbalance and other aspects of aneuploidy induce several physiological

stresses involving proteotoxic stress and energy stress. DNA damage due to chromosome missegregation and some of the aneuploidy-induced stresses can further lead to genomic instability.

Besides chromosome-specific effects, a chromosome-independent common transcriptional response is associated with aneuploidy. In aneuploid yeast cells, the genes expression pattern resembles the environmental stress response (ESR) (Torres *et al*., 2007; Sheltzer *et al*., 2012). The ESR is triggered in response to several exogenous stresses such as starvation, osmotic shock, oxidative stress and heat shock. In ESR, genes related to RNA processing and ribosomes are repressed, and genes involved in protein folding and degradation, DNA damage repair, defense against reactive oxygen species (ROS) and energy generation are upregulated (Gasch *et al*., 2000). In aneuploid mammalian cells, a similar transcriptional pattern was identified where genes involved in metabolism, protein processing, inflammation, and Golgi and lysosome-related pathways were upregulated, and genes involved in cell cycle regulation, DNA and RNA metabolism, and ribosome-related pathways were downregulated (Sheltzer *et al*., 2012; Stingele *et al*., 2012; Dürrbaum *et al*., 2014). This indicated that aneuploidy induces a general stress state. Several processes in a cell depend on the correct stoichiometric balance of different proteins such as metabolic homeostasis, DNA replication and mitosis. Unbalanced gene expression in aneuploid cells leads to protein stoichiometry imbalances that could induce several stresses (Figure 3.1) including proteotoxic stress, metabolic stress, replication stress and mitosis stress (reviewed in Zhu *et al*., 2018). The extent and the type of stress could depend on the cell type, the karyotype and the ploidy level.

Since chromosome alterations lead to unbalanced gene expression in aneuploid cells, there is additional burden on the cellular systems to fold excess proteins or degrade misfolded/unbalanced/damaged proteins in order to maintain protein homeostasis. This could result in accumulation of misfolded/unfolded proteins and enhanced **proteotoxic stress** in aneuploid cells. Evidently, there are several studies that show aneuploidy affects all protein quality control pathways. Budding yeast strains and human cells carrying additional chromosomes are defective in protein folding, as shown by impaired HSP90 chaperone induction (Oromendia *et al*., 2012; Donnelly *et al*., 2014; Aivazidis *et al*., 2017). Aneuploid mammalian cells showed increased sensitivity to protein folding inhibitor 17-AAG (Tang *et al*., 2011). Both protein degradation pathways, ubiquitin- proteasome system and autophagy have been shown affected in aneuploid cells. Aneuploid yeast and human cells showed increased sensitivity to the proteasome inhibitor MG132 (Torres et al., 2007; Ohashi et al., 2015). The loss-of-function mutation in *UBP6*, gene encoding a deubiquitinating enzyme that allows proteasome substrates to escape degradation, improved the proliferation of aneuploid yeast cells and reduced protein aggregate burden (Dephoure *et al*., 2014). Activation of lysosomal-

mediated autophagy has also been detected in aneuploid cells (Stingele *et al*., 2012; Ohashi *et al*., 2015). Aneuploid mammalian cells showed increased sensitivity to autophagy inhibitor chloroquine (Tang *et al*., 2011). Depletion of deubiquitinase *UBP3* gene in aneuploid yeast cells and of *USP10* in human cells, impaired their fitness due to impaired protein degradation (Dodgson *et al*., 2016). This shows that the increased load on protein quality control pathways is an attempt by aneuploid cells to restore protein homeostasis and their viability. Additionally, several studies demonstrated increased energy demands and metabolic alterations in aneuploid cells (Torres *et al*., 2007; Williams *et al*., 2008; Li *et al*., 2010). Aneuploid mammalian cells showed increased sensitivity to energy stress-inducer AICAR, indicating enhanced **metabolic stress** (Tang *et al*., 2011). In addition to above-mentioned aneuploidy-induced stresses, some aneuploid cells activate p53 pathway, potentially resulting in their cell cycle-arrest or apoptosis (Li *et al*., 2010; Thompson and Compton, 2010). Several different mechanisms have been proposed to account for p53 activation in response to aneuploidy including DNA damage (Janssen *et al*., 2011), activation of the stress kinase p38 (Thompson and Compton, 2010), and elevated ROS (Li *et al*., 2010).

Overall, exactly how different types of aneuploidy-induced stresses interact and generate molecular signals that lead to the observed phenotypes is only partially understood. Mechanistic response of mouse embryos to aneuploidy will be explored further in this thesis. To this end, the mouse model for chromosome mosaicism, previously developed by the Zernicka-Goetz lab (Bolton *et al*., 2016) will be used. Some unpublished work has been done in this direction by Helen Bolton in the Zernicka-Goetz lab, as demonstrated in her PhD thesis. Using the same model, reversine-treated (aneuploid) pre-implantation embryos were examined for elevated levels of ROS, altered metabolism, replication stress and DNA damage, relative to control (diploid) embryos.

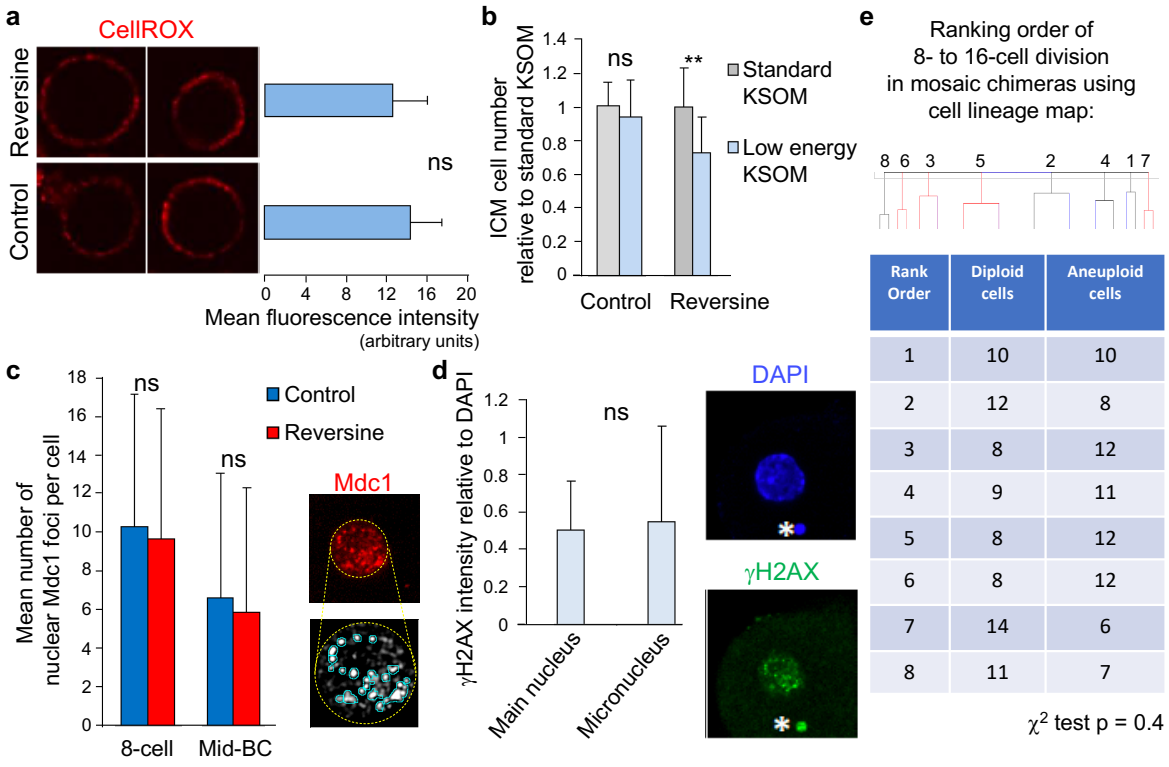

Figure 3.2. Cellular responses in reversine-treated mouse embryos (Adapted from Helen Bolton's PhD Thesis unpublished data)**.** (**a**) Mean ROS intensity levels were calculated for all embryos at the late blastocyst stage using CellROX in each group (control and reversine-treated). (**b**) Control and reversine-treated embryos were cultured in standard KSOM or low energy KSOM. ICM cell number were assessed at the late blastocyst stage. (**p < 0.01). (**c**) Mdc1 foci in nucleus were quantified for control and reversine-treated embryos at the 8-cell or the mid-blastocyst stage. (**d**) γH2AX signal intensity, normalized against DAPI signal, was compared between the paired main and micronucleus (denoted by asterisks) in reversine-treated cells. (**e**) Representative lineage tree of a chimeric embryo comprising of four control (black branches) and four reversine-treated (red branches) cells at the 8-cell stage. The sequence of division from the 8- to 16-cell stage was ranked in order and related to cell origin (reversine or control blastomere) for 1:1 control-reversine chimeric embryos.
For all graphs, ns = not significantly different, data = mean ± s.d. and Student's t-test was used.

To assay the ROS levels, cell-permeable fluoregenic probe, CellROX (Invitrogen) was used. It becomes fluorescent upon oxidation by ROS. There were no significant differences in signal intensity, and thus measurable ROS levels, between control and reversine-treated late blastocysts (Figure 3.2a). To investigate the metabolic differences between control and reversine-treated embryos, they were cultured in either standard or low energy KSOM from the early 8-cell stage onwards, and their development was compared. Standard KSOM media is the current optimal culture media for mouse embryo pre-implantation development (Nagy *et al*., 2003). The constituents of the low-energy KSOM were identical to standard KSOM with lower glucose concentration and no supplementation with L-glutamine, essential or non-

essential amino acids. There was a significant depletion in ICM lineage cell number in reversine-treated late blastocysts incubated in low-energy KSOM compared to in standard KSOM (Figure 3.2b). This effect did not occur in the control blastocysts (Figure 3.2b). This suggested that the pre-implantation embryos may have increased energy consumption upon aneuploidy induction. Next, to investigate if chromosome segregation after reversine treatment resulted in DNA damage, DNA damage response markers, γH2AX and Mdc1 (Bartek and Lucas, 2007) were used. There were no significant differences in nuclear Mdc1 foci between control and reversine-treated embryos at the 8-cell stage or the mid-blastocyst stage (Figure 3.2c). Also, the mean γH2AX levels were identical between the main and micronucleus within the same reversine-treated cell (Figure 3.2d). Thus, there was no DNA damage in the embryos or in the resulting micronuclei after chromosome missegregation induction. Lastly, to investigate if aneuploidy induction causes replication stress in pre-implantation mouse embryos, cell-cycle lengths were assessed. This is because replication stress leads to delay or complete arrest of the cell cycle (Passerini *et al*., 2016). 1:1 control-reversine chimeras were live imaged during the 8- to 16-cell stage division. The order of cell division was ranked from first through to last for each embryo and related to cell history (diploid or aneuploid). If reversine-treated blastomeres underwent replication stress, then their distribution would be skewed towards the lower ranks. There were no significant differences in order of cell division between control and reversine-treated blastomeres (Figure 3.2e). Thus, there was no evidence of replication stress in the embryos after chromosome missegregation induction.

3.5 Project Aims

Aneuploidy is considered a major cause of human reproductive health problems and developmental disabilities. A large proportion of cleavage-stage human embryos created through *in vitro* fertilization (IVF) display mosaicism. However, the incidence of aneuploidy declines as gestation progresses, with the steepest drop occurring as the embryo completes implantation. What accounts for the reduced frequency of aneuploid cells during development, is not well known. The first aim of this chapter was to investigate the cellular fate of aneuploid cells, with a specific focus on peri-and early post-implantation development. Secondly, since some diploid-aneuploid mosaic embryos can have full developmental potential, these embryos will be studied during peri-implantation to understand what mechanisms confer their viability. Thirdly, the molecular mechanisms that mediate the elimination of aneuploid cells from the embryonic lineage (pre- to post-implantation stages of development) will be investigated. For all the above-mentioned aims, the mouse model for chromosome mosaicism, previously developed by the Zernicka-Goetz lab (Bolton *et al*., 2016), will be employed. Lastly, a mouse embryonic stem cell-based model for chromosome mosaicism will be developed.

4 Results I: Elucidating mechanisms that dictate the elimination of aneuploid cells from the mouse epiblast

4.1 Elimination of aneuploid cells from the mouse epiblast during pre-implantation development via apoptosis

It was previously shown that reversine treatment leads to an increased rate of chromosomal missegregation errors in cleavage-stage mouse embryos by bypassing the SAC (Bolton *et al*., 2016). The rate of aneuploidy in reversine-treated embryos was significantly higher than in controls (DMSO-treated embryos). It was found that there were no differences between reversine-treated embryos and controls in terms of morphology, expression of lineage-specific TFs and relative allocation of cells to the ICM and TE lineages until the end of pre-implantation stage of development (E4.5). However, there was divergence in cell numbers between the early to late blastocyst stage (E3.5 to E4.5). Reversine-treated embryos comprised of fewer cells than controls in all three lineages (EPI, PE and TE) at the late blastocyst stage (Bolton *et al*., 2016). This section of my thesis will investigate what accounts for this depletion in cell number between the early to late blastocyst stage in the reversine-treated embryos. I will focus on the EPI lineage throughout this chapter since this lineage will eventually give rise to fetus.

4.1.1 Evaluating the ploidy status of cleavage-stage mouse embryos after reversine treatment

Before using the Bolton *et al.* (2016) model of chromosome mosaicism, the first step was to confirm if reversine treatment induces aneuploidy in cleavage-stage mouse embryos in my hands. Since FISH technique has several limitations (Griffin and Ogur, 2018) and single-cell genome sequencing is highly expensive and often not available to us, it was necessary to develop a reliable protocol to evaluate the chromosome status of cells within the mouse embryo. Two approaches were investigated: evaluation of centromere number and chromosome spreading.

- Evaluation of centromere number

Since every chromosome contains one centromere in the mouse, the centromere number could indicate the ploidy status for that chromosome. The localization of centromere protein, CENPA was investigated. To this end, 2-cell embryos were injected with mRNA encoding a Zsgreen tagged CENPA (CENPA-Zsgreen). They were fixed and immunostained with anti-CENPA. *CENPA-Zsgreen* mRNA upon translation co-localized with anti-CENPA (Figure 4.1). CENPA-Zsgreen in theory would allow the detection of aneuploid cells in embryos during live imaging. However, it was not possible to count the centromeres accurately due to their close proximity and overlapping signals. Therefore, this approach was abandoned.

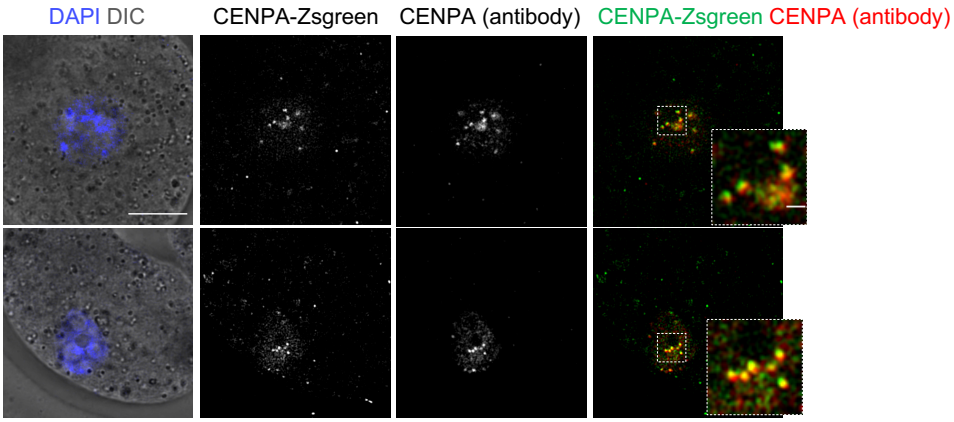

Figure 4.1. Ploidy assessment using evaluation of centromeres. Labelling of endogenous centromeres with CENPA-Zsgreen and anti-CENPA staining in mouse embryo blastomeres. Scale bar, 10 μm. Squares indicate the magnified region, scale bar, 1 μm. n = 8 embryos.

- Chromosome spreading

Alternatively, the classical cytogenetic technique of generating chromosome spreads was attempted. Several variations at every step in the procedure were tried to optimize the protocol for mouse embryos: metaphase arrest (colcemid or colchicine, dose and length of exposure), hypotonic treatment (KCl or NaCl or sodium citrate, dose, incubation time and temperature), fixation (composition of fixative) and spreading technique (dropping onto slide approach and mounting). Finally, the protocol that produced good quality spreads was – 0.1 μg/ml colcemid for 12 hours to arrest cells in metaphase, 10 minute hypotonic treatment at room temperature in 1% sodium citrate (pre-heated at 37^0C), 30 minute fixation in 3:1 methanol: glacial acetic acid, mouth pipet embryos on slides, air dry slides for 1 minute and mount with DAPI. In the cases where metaphase was achieved, only those were included for analysis and counting in which chromosomes were adequately spread instead of clumping over each other (Figure 4.2a). Luckily, spreads for different blastomeres within the same embryo clustered separately (Figure 4.2a). Where spreads for different blastomeres were too close to each other without a clear boundary, they were excluded from the analysis. This protocol was then used to evaluate the effectiveness of reversine treatment.

Embryos were treated with 0.5 μM reversine or with an equivalent concentration of DMSO (controls) during the 4-8 cell stage division. After treatment, embryos were arrested in metaphase during the 8-16 cell stage division and chromosome spreads were performed. Significantly higher rates of aneuploidy were found in reversine-treated blastomeres than in controls (Figure 4.2b). Thus, it was confirmed that reversine-treatment induces aneuploidy in cleavage-stage mouse embryos, in agreement with previous results (Bolton *et al*., 2016).

Using fluorescent *in situ* hybridization and single-cell genome sequencing it was demonstrated that reversine treatment generates a mosaic of different aneuploidies and some diploid cells (Bolton *et al*., 2016). Using metaphase spreads, both hyperploidy and hypoploidy was seen after reversine treatment, although more hypoploidy was detected compared to hyperploidy (Figure 4.2c). However, for simplicity reversine-treated cells will be referred to as aneuploid and controls as diploid throughout this chapter from hereon.

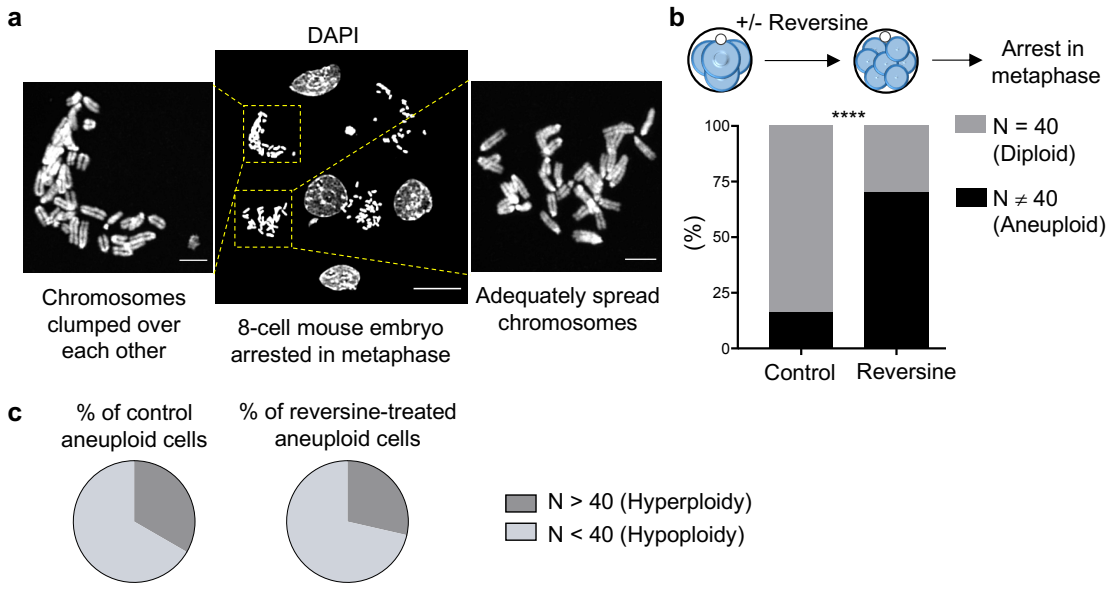

Figure 4.2. Ploidy assessment using chromosome spreads of mouse embryos. (**a**) A representative image of chromosome spread for a reversine-treated 8-cell mouse embryo. Scale bar, 30 µm. Squares indicate the magnified region (individual blastomeres), scale bars, 5 µm. In the example on right, chromosomes are well-spread and suitable for counting. In the example on left, chromosomes are clumping over each other and therefore excluded from analysis. All the three images are maximum projections. (**b**) Number of chromosomes per cell (N) were counted for mouse embryos. Control n = 38 cells, reversine-treated n = 30 cells. Fisher's exact test was used and ****p < 0.0001. (**c**) Distributions of control cells and reversine-treated cells that were categorised aneuploid in (**b**) according to the number of chromosomes per cell (N).

It is worth noting here that the frequency of aneuploidy could differ between mice of different genetic backgrounds and biological ages (Gearhart *et al*., 1986). Since reversine does not induce aneuploidy in 100% of the treated cells, it is important to use a young control mouse with the lowest frequency of aneuploidy. Also, since reversine induces a range of ploidies (Bolton *et al*., 2016) (Figure 4.2b-c), it will be important to develop a method to recognise aneuploid cells (if possible, also recognise the type of aneuploidy) with live imaging for future experiments. Following aneuploid cells in real-time as the whole embryo develops, will allow determination of the precise fate of aneuploid cells. These and other concerns associated with

using reversine as a method to induce aneuploidy in the early mouse embryos have been discussed in detail in Section 5.1.

4.1.2 Time-lapse imaging of aneuploid and diploid-aneuploid chimeric embryos

It was previously shown that the preferential depletion in aneuploid cell number in the EPI lineage during blastocyst maturation in the diploid-aneuploid embryos was due to increased apoptosis compared to diploid cells (Bolton *et al*., 2016). It was investigated if same holds true in aneuploid embryos (whole reversine-treated embryos) and was confirmed again in diploid-aneuploid embryos (embryos containing reversine-treated and control blastomeres).

To determine the fate of aneuploid cells in the mouse embryo, two types of chimeric embryos were generated at the 8-cell stage: aneuploid(red fluorescent)-diploid(non-fluorescent) chimera and aneuploid(red fluorescent)-aneuploid(non-fluorescent) chimera (Figure 4.3a). To generate these chimeras, four red fluorescent and four non-fluorescent cells isolated from the respective 8-cell stage embryos were aggregated. Both aneuploid and diploid cells were generated by reversine or DMSO treatment at the 4-8 cell stage, respectively. Membrane-associated red fluorescent marker expressing cells were obtained using mT/mG transgenic embryos (Muzumdar *et al*., 2007). This enabled visualization of individual membrane throughout the period of imaging and recognition of apoptosis by membrane blebbing (Kerr *et al*., 1972; Porter and Jänicke, 1999). The red fluorescent clones were monitored by time-lapse imaging during blastocyst maturation in these chimeras and compared with diploid mT/mG embryos. To analyse ICM apoptosis rates, the incidence of membrane blebbing (Figure 4.3b) was quantified with time in ICMs for both types of chimeras and diploid embryos. It was found that aneuploid cells in both aneuploid-diploid (Figure 4.3c,e) and aneuploid-aneuploid (Figure 4.3d,f) chimeric ICMs underwent apoptosis at significantly higher rate and at overall higher level than diploid cells in diploid ICMs during blastocyst maturation (E3.5 to E4.5 transition). For future experiments, it will be beneficial to use a live marker of cell death, such as caspase sensor (Bardet *et al*., 2008), to analyse apoptosis rates.

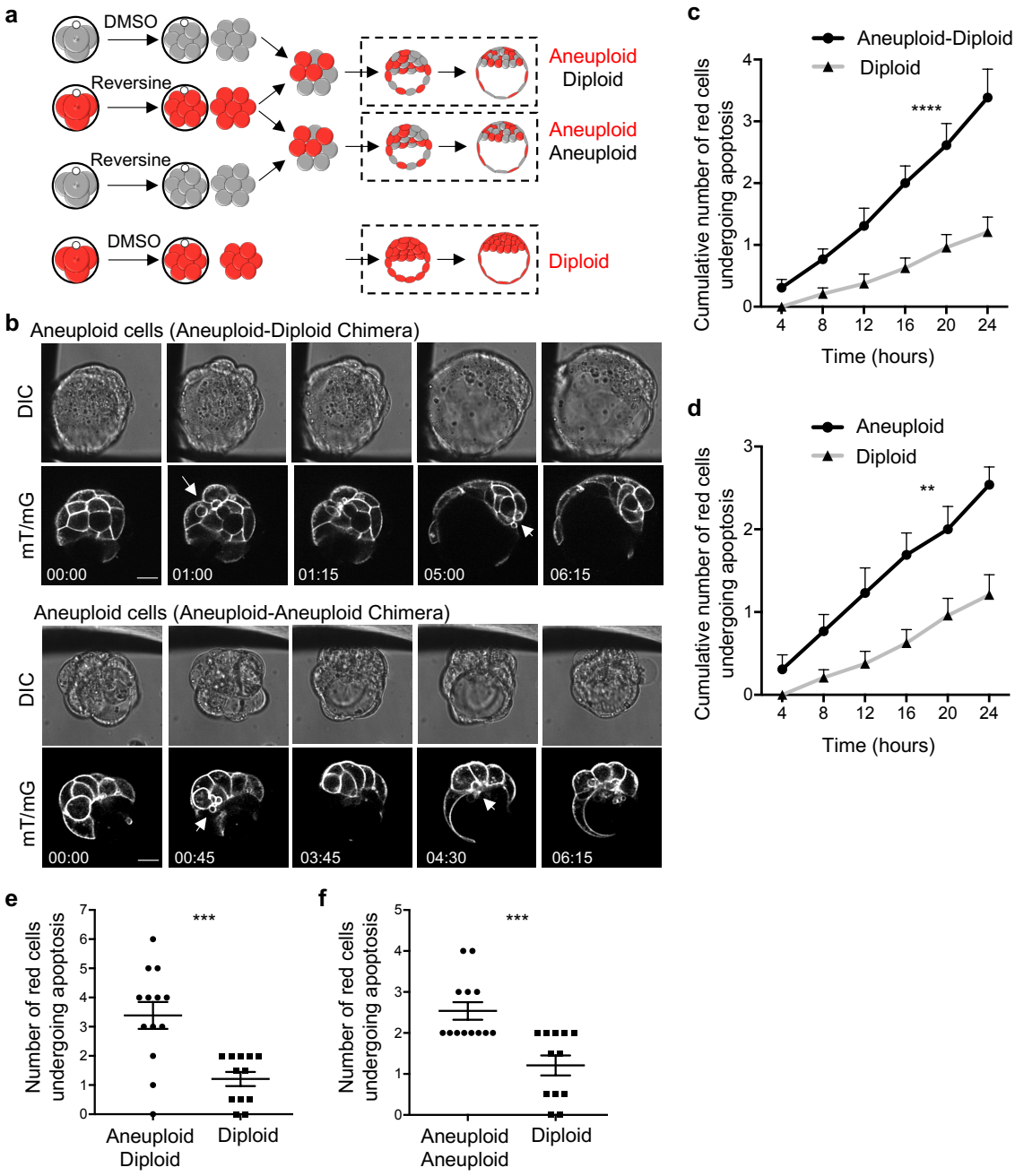

Figure 4.3. Apoptosis of aneuploid cells during pre-implantation development of aneuploid-diploid and aneuploid chimeras. (**a**) 8-cell chimeras, aneuploid-diploid and aneuploid-aneuploid, each containing a 1:1 ratio of blastomeres from membrane-targeted red fluorescent (mT/mG) and non-fluorescent transgenics was generated. Diploid 8-cell mT/mG embryos were also obtained. For all three types of embryos. mT/mG cells (red fluorescent) were imaged during blastocyst maturation. (**b**) Here are shown the sequential representative images from a time-lapse series of aneuploid cells (membrane fluorescent) in an aneuploid-diploid chimera (top panel) and in an aneuploid chimera (bottom panel), undergoing apoptosis (hour:minute). Scale bars, 20 μm. Comparison of the rate of apoptosis of red fluorescent cells in the ICM between (**c**) the aneuploid(red fluorescent)-diploid(non-fluorescent) chimera and diploid red fluorescent embryos and between (**d**) the aneuploid(red fluorescent)-aneuploid(non-fluorescent) chimera and diploid red fluorescent embryos. For both (**c**) and (**d**), linear regression

determined the slopes to be significantly different from each other. Comparison of the level of apoptosis of red fluorescent cells in the ICM between (**e**) the aneuploid(red fluorescent)-diploid(non-fluorescent) chimera and diploid red fluorescent embryos and between (**f**) the aneuploid(red fluorescent)-aneuploid(non-fluorescent) chimera and diploid red fluorescent embryos. For (**e**) Student's t-test with Welch's correction was used and for (**f**) Student's t-test was used. For (**c**), (**d**), (**e**) and (**f**), Aneuploid-diploid n = 13 chimeras, aneuploid n = 13 chimeras and diploid n = 12 mT/mG. For diploid embryos, the quantification related to number of dying cells was divided by half for each embryo for each time-interval for the final analysis (plotting graphs and statistics).
All data are mean ± s.e.m. and **p < 0.01, ***p < 0.001 and ****p < 0.0001.

4.1.3 Inhibition of apoptosis in aneuploid embryos during blastocyst maturation

As an alternative method to investigate the role of apoptosis in the reduction of cell number in aneuploid EPI, the effect of apoptosis inhibition was examined. To this end, apoptosis was inhibited via treatment with the pan-caspase inhibitor ZVAD because caspases are crucial mediators of apoptosis (Cohen, 1997). Aneuploid (reversine-treated) and diploid (controls) embryos were cultured in a KSOM medium containing 20 μM ZVAD during blastocyst maturation. Aneuploid and diploid embryos were also cultured in equivalent concentration of DMSO as control. All four types of embryos were imaged during blastocyst maturation in the presence of SYTOX (Life Technologies). SYTOX is a fluorescent cell death reporter and thus, allowed the visualization of dying cells (Figure 4.4). To analyse cell death rates, SYTOX-positive cells were quantified with time in ICMs for all four types of embryos. It was found that ZVAD treatment significantly reduced the number of dying cells in the ICM of aneuploid embryos (Figure 4.5a). There was some reduction in the number of dying cells in the ICM of diploid embryos as well, but not significant (Figure 4.5a). Consequently, the reduction in EPI cell number in aneuploid late blastocysts compared to diploid late blastocysts as seen in Bolton *et al*. (2016), was alleviated after ZVAD treatment (Figure 4.5b). However, there were still some dying cells (SYTOX-positive) remaining in both diploid and aneuploid embryos after ZVAD treatment (Figure 4.5a). This implied that either this cell death was not mediated by caspases or ZVAD was not effective in removing caspase 100%. This was investigated by checking for cleaved capsase-3-positive cells in ZVAD-treated aneuploid late blastocysts using immunostaining. Some of the ZVAD-treated aneuploid embryos were positive for cleaved caspase-3 (Figure 4.5c), indicating that the apoptotic cell death was not completely alleviated after ZVAD treatment. Together these results indicate that caspase-mediated apoptosis eliminates aneuploid cells from the EPI during blastocyst maturation.

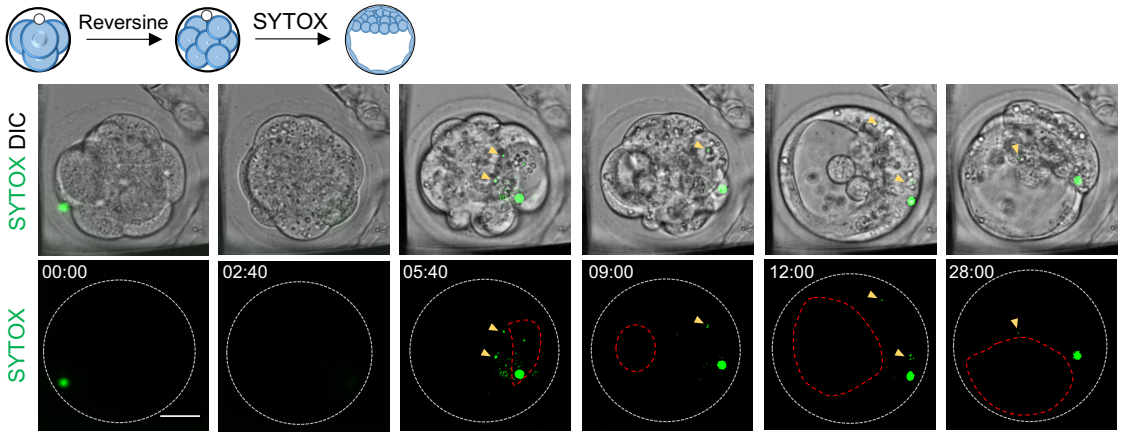

Figure 4.4. Cell death during pre-implantation development of an aneuploid embryo. Reversine-treated embryo was imaged in the presence of SYTOX to label dying cells until the late blastocyst stage. Sequential representative images from a time-lapse recording show dying reversine-treated cells (arrows) from the early blastocyst stage onwards (hour:minute). Red line marks the site of the cavity. Scale bar, 30 μm.

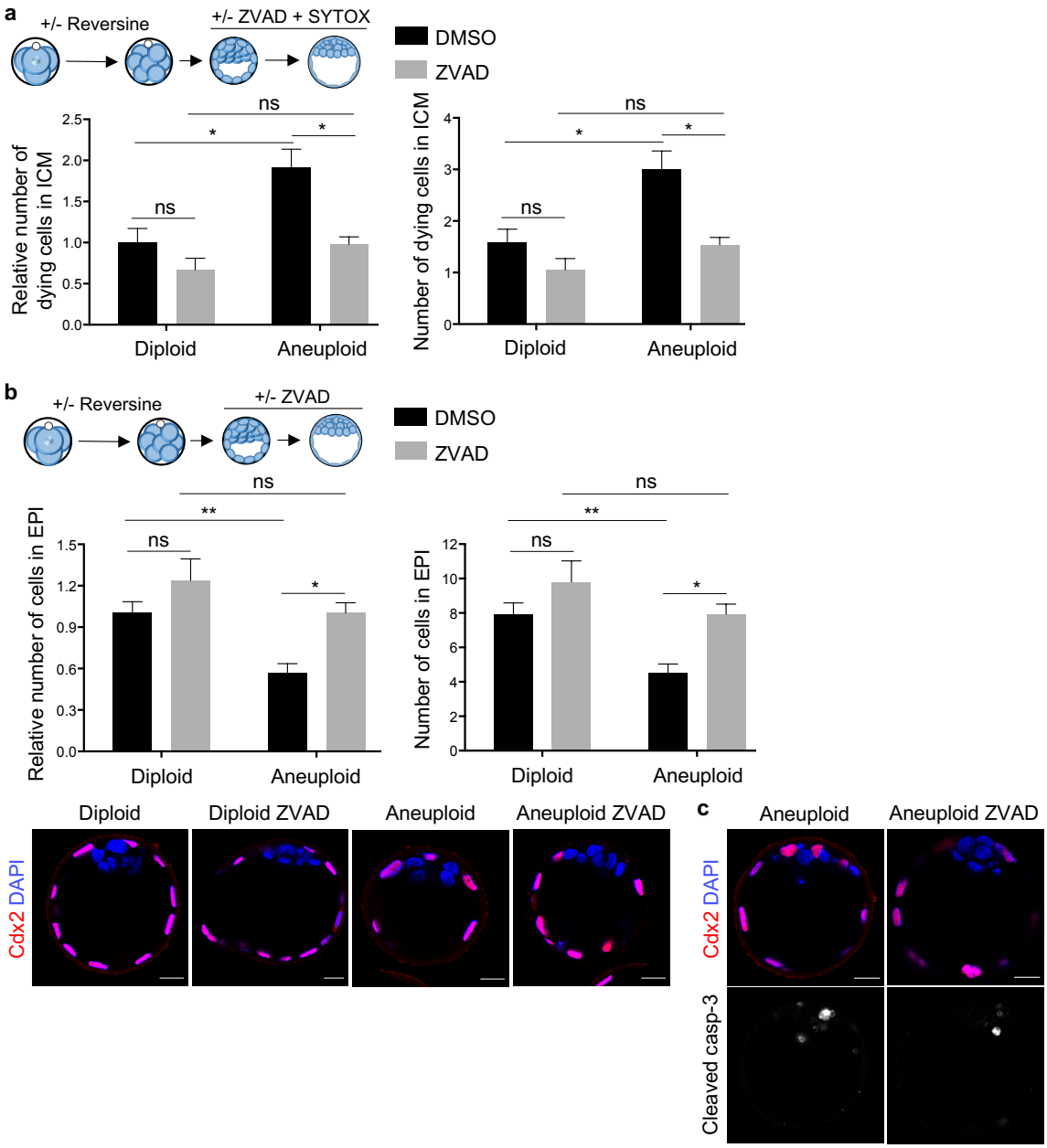

Figure 4.5. Elimination of aneuploid cells from the EPI of aneuploid embryos during blastocyst maturation via apoptosis. (**a**) Diploid and aneuploid (reversine-treated) embryos were imaged in the presence of ZVAD or DMSO and SYTOX from the early blastocyst to the late blastocyst stage (24 hours). Number of cells dying in ICM (SYTOX-positive) were assessed. They have been plotted relative to number of cells dying in ICM in controls (DMSO-treated diploids) and independently. Diploid n = 14 embryos, aneuploid n = 13 embryos, diploid ZVAD n = 20 embryos, aneuploid ZVAD n = 13 embryos. (**b**) Diploid and aneuploid embryos were cultured in the presence of ZVAD or DMSO during blastocyst maturation. They were immunostained for Cdx2 and DAPI at the late blastocyst stage. Scale bars, 20 μm. Number of cells in the EPI were assessed. They have been plotted relative to EPI cell number in controls (DMSO-treated diploids) and independently. Diploid n = 26 embryos, aneuploid n = 27 embryos, diploid ZVAD n = 13 embryos, aneuploid ZVAD n = 12 embryos. (**c**) Aneuploid embryos cultured in the presence of ZVAD or DMSO during blastocyst maturation. They were immunostained

for cleaved caspase-3, Cdx2 and DAPI at the late blastocyst stage. Scale bars, 20 μm. For graphs (**a**) and (**b**), Kruskal-Wallis test was used, ns = not significantly different, *p < 0.05, **p < 0.01 and all data are mean ± s.e.m.

4.2 Elimination of aneuploid cells from the mouse epiblast during peri-implantation development via apoptosis

It was previously shown that up to 44% of aneuploid cells were preferentially eliminated from the embryonic lineage of diploid-aneuploid mosaic embryos as the pre-implantation blastocyst matures (Bolton *et al.*, 2016). Upon transfer of these diploid-aneuploid embryos to foster mothers and post-implantation recovery (E7.5), there was a dramatic decline of aneuploid cells in the embryonic lineage. Consistently, whole aneuploid embryos resulted in complete post-implantation lethality. However, the mechanisms that eliminate aneuploid cells from the embryonic lineage as embryos implant remain unknown. So, this section investigates what determines the fate of aneuploid cells within the embryonic lineage beyond the blastocyst stage in the aneuploid embryos and diploid-aneuploid embryos. The implantation period of development is particularly important to study because the embryonic lineage of cells undergoes extensive proliferation and reorganization in shape, gene expression, epigenetic signatures, and metabolism, laying the foundation for the developing body. In addition, it was also shown that unlike aneuploid embryos, 1:1 diploid-aneuploid embryos had full post-implantation developmental potential (Bolton *et al.*, 2016). So, this section will also address what confers diploid-aneuploid embryos this developmental plasticity.

4.2.1 Apoptosis of aneuploid embryo ICMs during peri-implantation *in vitro*

Despite its importance, implantation period of development (peri-implantation) remains enigmatic because the embryo invades the uterine wall upon implantation, making it extremely difficult to recover. To recapitulate the ICM development from pre- to post-implantation stages without interruption, *in vitro*, several protocols were attempted (they have been discussed in detail in section 5.2). Finally, a new simplified method was established.

Aneuploid embryos (reversine-treated) and diploid embryos (controls) were cultured until the late blastocyst stage (E4.5). Then, the TE layer was removed through immunosurgery (Solter and Knowles, 1975), to focus on the fate of cells within the ICM lineage. The ICMs were then embedded in Matrigel drops. Matrigel, derived from Engelbreth-Holm Swarm (EHS) mouse sarcoma, was used to provide the ECM components to mimic the basal membrane function *in vitro*. *In vivo*, this basal membrane is assembled by TE and PE cells and is essential for EPI polarization and maturation during peri-implantation stages (Bedzhov and Zernicka-Goetz, 2014). To recapitulate ICM development beyond blastocyst stage of development, the

embedded embryo ICMs were cultured in previously described *in vitro* implantation medium (IVC1) (Morris *et al*., 2012b) for three days. The schematic for the above-mentioned protocol is shown in Figure 4.6a.

Using time-lapse imaging throughout this 72-hour period, it was found that the diploid ICMs followed the normal sequence of events of peri-implantation development: EPI rearrangement into a rosette and opening of the lumen in the centre, as described before (Bedzhov and Zernicka-Goetz, 2014) (Figure 4.6b). Nucleus-associated green fluorescent marker expressing embryos from Histone H2B-GFP transgenic mice were used (Hadjantonakis and Papaioannou, 2004). Diploid ICMs developed into organized structures with characteristic post-implantation morphology, in which the PE (marked by Gata4) surrounded the epithelial EPI (marked by Oct4) that formed a lumen in its center (lined by podocalyxin) (Figure 4.6c). To score the developmental efficiency of the assay (efficiency of the ICMs to develop into organized structures), ICMs were analysed after 72-hour *in vitro* culture for three characteristic features: a layer of PE surrounding the epithelial EPI (marked by Oct4) with a lumen in its center (lined by Podxl) (Figure 4.6c). Due to technical difficulty, the developmental efficiency of diploid ICMs was 30%. Aneuploid ICMs (reversine-treated) also developed the same post-implantation morphology after 72-hour *in vitro* culture (Figure 4.6c), but their developmental efficiency was 53% lower than that of diploid embryos (Figure 4.6d). Importantly, the organized aneuploid structures had significantly fewer cells in EPI than diploid organized structures (Figure 4.6e).

To determine how aneuploid cells were eliminated from aneuploid embryo EPI between the pre- to post-implantation stages of development, time-lapse imaging of aneuploid ICMs was performed during *in vitro* culture in IVC1. Nucleus-associated green fluorescent marker expressing embryos from Histone H2B-GFP transgenic mice were used (Hadjantonakis and Papaioannou, 2004). The morphological features characteristic of apoptosis (Kerr *et al*., 1972; Porter and Jänicke, 1999) were observed in the aneuploid cells that included nuclear condensation and disintegration into blebs (Figure 4.7a). Consistently, the organized structures obtained after 72-hour *in vitro* culture of aneuploid ICMs were highly cleaved caspase-3 positive (Figure 4.7b). Active caspase-3 (cleaved) is extensively involved in the execution and efficient completion of apoptosis, and the formation of apoptotic bodies (Porter and Jänicke, 1999).

These results overall indicate the involvement of programmed cell death in the elimination of aneuploid cells from aneuploid embryonic lineage during peri-implantation stage of development. Despite this depletion, aneuploid embryos established and segregated both EPI

and extra-embryonic PE lineages correctly and developed with correct morphology as diploids during peri-implantation stages, similar to their behavior during pre-implantation stages of development (Bolton *et al*., 2016).

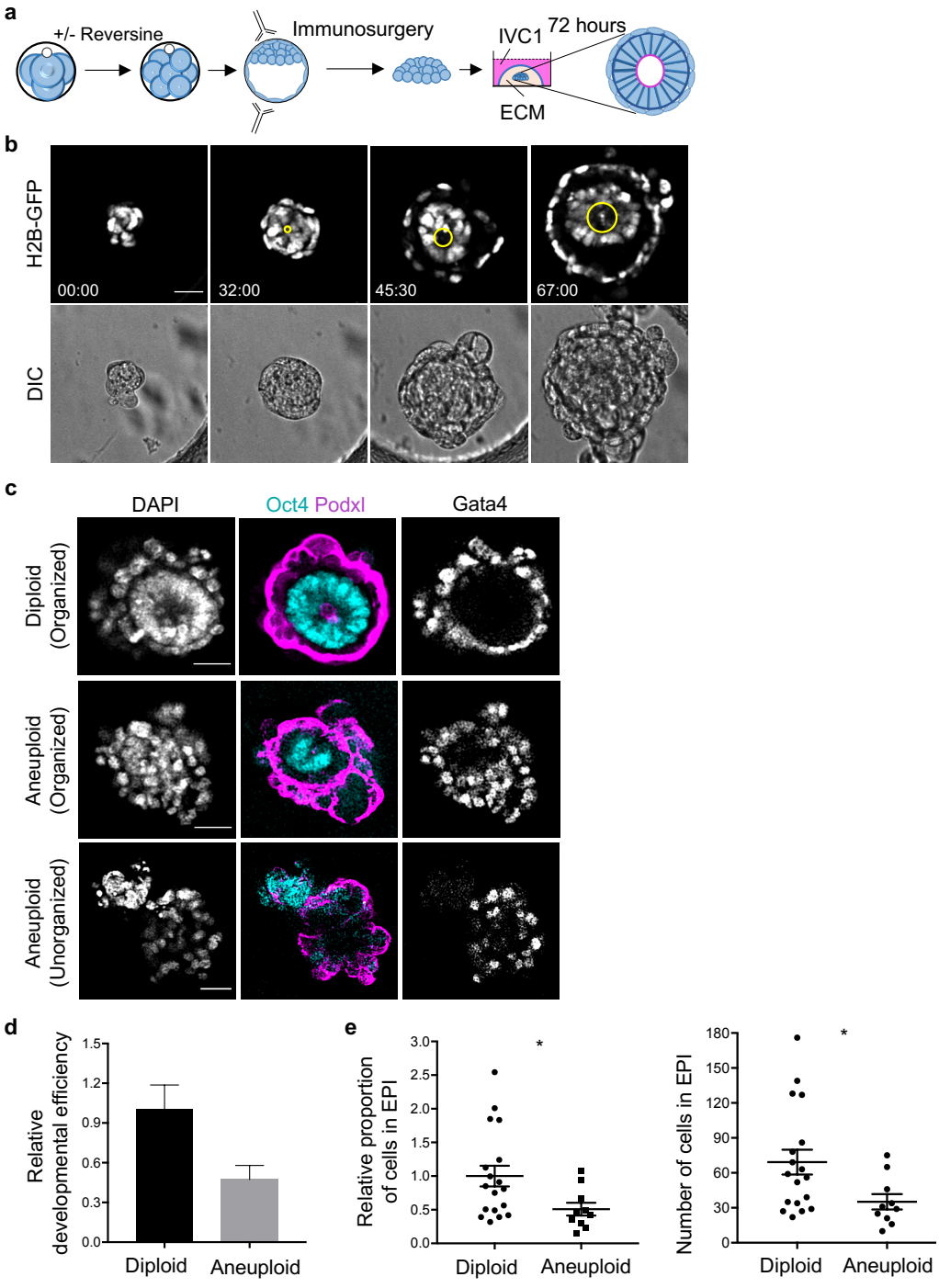

Figure 4.6. Elimination of aneuploid cells from the EPI of aneuploid embryos during peri-implantation stage of development. (**a**) Schematic for the experimental design where diploid (control) and aneuploid (reversine-treated) embryos were cultured until the late blastocyst stage. Immunosurgery was performed to remove the outer TE layer and the ICMs were embedded in extra-cellular matrix proteins (provided by Matrigel). They were cultured in IVC1 medium for 72 hours to allow the

development of apolar EPI into an epithelial EPI surrounded by a layer of PE cells and enclosing a lumen. (**b**) Sequential representative images of a time-lapse series of a control embryo ICM, obtained using Histone H2B-GFP transgenic embryos, cultured according to schematic shown in (**a**) (hour:minute). Yellow line marks the site of the emerging lumen. Scale bar, 30 μm. (**c**) Diploid and aneuploid ICMs were cultured according to schematic shown in (**a**) for 72 hours and immunostained for DAPI, Oct4 (to mark EPI), Gata4 (to mark PE) and Podxl (podocalyxin to mark the lumen). Scale bars, 30 μm. (**d**) Relative efficiency of ICMs (relative to diploids) to form an organised structure assessed according to (**c**) was evaluated for aneuploid and diploid embryos. To score the developmental efficiency of the assay, ICMs were analysed for three characteristic features: a layer of PE surrounding the epithelial EPI (marked by Oct4) with a lumen in its center (lined by Podxl). n = 3 experiments. Diploid n = 34 embryos, aneuploid n = 36 embryos. (**e**) Number of cells in the EPI (Oct4-positive) were analyzed for the organized structures obtained for diploid and aneuploid embryos cultured according to schematic shown in (**a**). They have been plotted relative to EPI cell number in diploids and independently. Student's t-test with Welch's correction was used. *p < 0.05. For (**c**) and (**e**), Diploid n = 18 embryos, aneuploid n = 10 embryos. For graphs (**d**) and (**e**), all data are mean ± s.e.m.

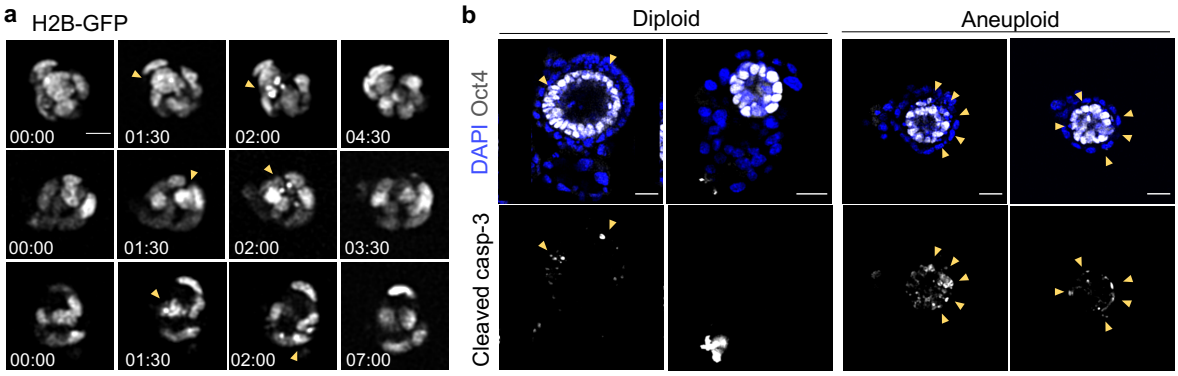

Figure 4.7. Apoptosis of aneuploid cells from the EPI of aneuploid embryos during peri-implantation stage of development. (**a**) Sequential representative images of three examples of time-lapse series of Histone H2B-GFP aneuploid embryos ICMs cultured according to schematic shown in Figure 4.6a (hour:minute). Yellow arrows mark the apoptotic cells. Scale bar, 15 μm. (**b**) Diploid and aneuploid ICMs were cultured according to schematic shown in Figure 4.6a for 72 hours and immunostained for DAPI, Oct4 (to mark the EPI) and cleaved caspase-3 (to label apoptosis). Yellow arrows mark the cleaved caspase-3 positive cells in the EPI. Scale bars, 30 μm. Diploid n = 15 embryos, aneuploid n = 20 embryos.

4.2.2 Elimination of aneuploid cells from diploid-aneuploid embryo ICMs during peri-implantation *in vitro*

Next step was to investigate whether aneuploid cells followed similar fate in diploid-aneuploid mosaic embryos during peri-implantation stage of development as in aneuploid (whole reversine-treated) embryos. To visualize the ICM development of diploid-aneuploid embryos during peri-implantation stages *in vitro*, same protocol was followed as described in section

4.2.1. Briefly, four diploid cells and four aneuploid cells were isolated from the respective 8-cell stage embryos and aggregated together to generate an 8-cell 1:1 diploid-aneuploid chimera. To distinguish diploid and aneuploid cells in such mosaics, chimeras were generated in which diploid clones expressed a membrane-targeted red fluorescent (mT/mG) marker, while aneuploid cells were non-fluorescent. Control diploid-diploid chimeras were also generated using the same approach. Both the chimeras were allowed to develop to the late blastocyst stage. Then, the TE layer was removed through immunosurgery. The resulting chimeric ICMs were embedded in Matrigel and cultured in IVC1 medium for three days to recapitulate ICM development during the peri-implantation stages of development. The schematic for the above-mentioned protocol is shown in Figure 4.8a.

It was found that both diploid-diploid and diploid-aneuploid chimeras developed into organized structures with characteristic post-implantation morphology, in which the PE surrounded the epithelial EPI (marked by Oct4) that formed a lumen in its center (lined by Podxl) (Figure 4.8b). Unlike aneuploid embryos (Figure 4.6d), the efficiency of development into these organized structures in 72-hour IVC1 culture was similar for 1:1 diploid-aneuploid chimeras compared to diploid-diploid chimeras (Figure 4.8c). The composition of these organized structures, i.e. the distribution of red fluorescent and non-fluorescent cells in both EPI (Oct4-positive) and PE (DAPI-positive and Oct4-negative) lineages, was then characterized for both diploid-diploid and diploid-aneuploid chimeras. On average, the diploid(red fluorescent)-diploid(non-fluorescent) chimeras contained 64.9% non-fluorescent cells in the EPI and 65.9% non-fluorescent cells in the PE (Figure 4.8b). When the same clone of cells was aneuploid, as in the diploid(red fluorescent)-aneuploid(non-fluorescent) chimeras, the contribution of non-fluorescent cells decreased to 30.3% in the EPI and to 38.2% in the PE, on average (Figure 4.8b). The frequency distribution of the composition of these organized structures, i.e. what % of chimeras carried a particular % of non-fluorescent cells, was then characterized for both diploid-diploid and diploid-aneuploid chimeras for both EPI and PE lineages. There was a significant difference between the frequency distributions of the non-fluorescent cells in diploid(red fluorescent)-diploid(non-fluorescent) and diploid(red fluorescent)-aneuploid(non-fluorescent) chimeras for both EPI and PE lineages (Figure 4.8d,e). Strikingly, 47.4% of diploid(red fluorescent)-aneuploid(non-fluorescent) chimeras completely lacked non-fluorescent aneuploid cells in the EPI lineage (Figure 4.8d). In contrast, only 19% of the diploid-diploid chimeras showed complete loss of non-fluorescent cells in the EPI lineage (Figure 4.8d). Similarly, 31.6% of diploid(red fluorescent)-aneuploid(non-fluorescent) chimeras completely lacked non-fluorescent aneuploid cells in the PE lineage, whereas only 10% of the diploid-diploid chimeric PE lacked non-fluorescent cells (Figure 4.8e).

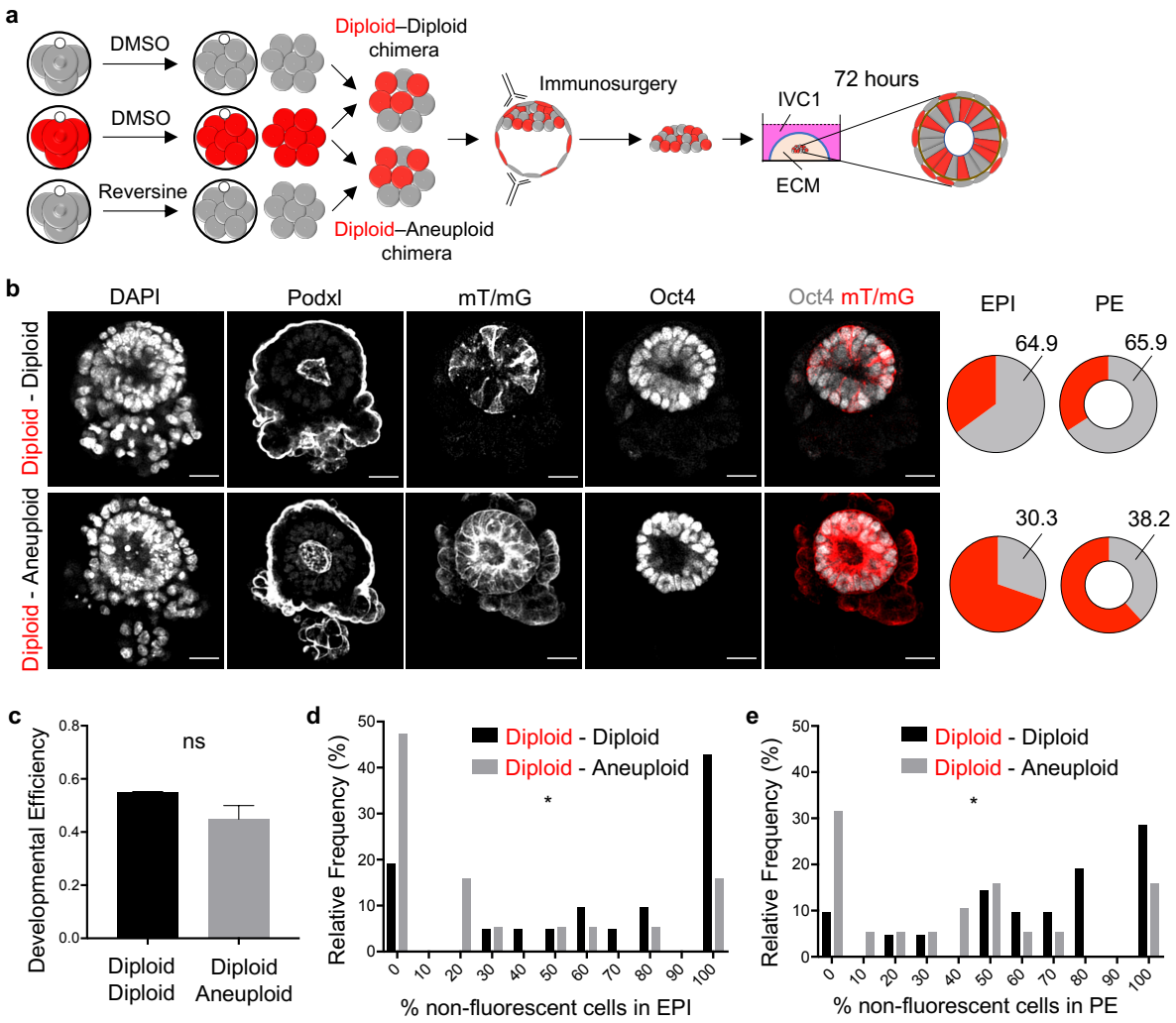

Figure 4.8. Elimination of aneuploid cells from the aneuploid-diploid chimeric mosaic EPI and PE during peri-implantation development *in vitro*. (**a**) Schematic for the experimental design where 8-cell chimeras containing a 1:1 ratio of red fluorescent and non-fluorescent blastomeres were generated at the 8-cell stage. mT/mG transgenic embryos were used for red fluorescent cells. For diploid-aneuploid chimeras, non-fluorescent cells were aneuploid (reversine-treated) and red fluorescent cells diploid. At the late blastocyst stage, immunosurgery was performed to get rid of the outer TE layer. The chimeras were embedded in Matrigel and cultured in IVC1 medium for 72 hours. (**b**) After 72-hour *in vitro* culture, chimeras were assessed for the composition of the EPI (Oct4-positive) and PE (DAPI-positive and Oct4-negative), i.e. the average distribution of both red fluorescent and non-fluorescent cells. In the examples shown, the diploid-diploid chimera contained both red fluorescent and non-fluorescent cells in the EPI. In contrast, most of the diploid-aneuploid chimera originated from the red fluorescent diploid clone. Scale bars, 30 μm. (**c**) The efficiency of chimeras to form an epithelial EPI (marked by Oct4 in (**b**)) surrounded by a layer of PE and enclosing a lumen (marked by Podxl in (**b**)) after 72-hour *in vitro* culture was assessed. n = 3 experiments, Mann-Whitney test was used, ns = not significantly different and all data are mean ± s.e.m. Frequency distributions of non-fluorescent cells within the EPI (**d**) and PE (**e**) of diploid(red-fluorescent)-diploid(non-fluorescent) and of diploid(red fluorescent)-aneuploid(non-fluorescent) chimeras. For graphs (**d**) and (**e**), Kolmogorov-Smirnov test

was used to compare the frequency distributions for two types of chimeras, and *p < 0.05. For (**b**), (**c**), (**d**) and (**e**), diploid-diploid n = 21 chimeras and diploid-aneuploid n = 19 chimeras.

Next step was to investigate whether the above-mentioned depletion of aneuploid cells from the EPI of the diploid-aneuploid mosaic embryos during peri-implantation stage of development was dependent on the fluorescent marker used to track them or on the genetic background. To this end, the combination was reversed, i.e., four red fluorescent (mT/mG) aneuploid cells and four non-fluorescent diploid cells were aggregated to generate the diploid-aneuploid chimera. Control diploid-diploid chimeras were also generated using the same approach. Both diploid(non-fluorescent)-diploid(red fluorescent) and diploid(non-fluorescent)-aneuploid(red fluorescent) chimeras were allowed to develop according to previously mentioned protocol for three days in Matrigel and IVC1 after immunosurgery (Figure 4.9a). Same as before, the diploid-aneuploid chimeras developed into organized structures with characteristic post-implantation morphology, in which the PE surrounded the EPI (marked by Oct4) that formed a lumen in its center (lined by Podxl) (Figure 4.9b). The composition of these organized structures was then characterized for both chimeras in the EPI. On average, the diploid(red fluorescent)-diploid(non-fluorescent) chimeras contained 35.1% red fluorescent cells in the EPI (Figure 4.9c). When the same clone of cells was aneuploid, as in the diploid(non-fluorescent)-aneuploid(red fluorescent) chimeras, the contribution of red fluorescent cells decreased to 15.4% in the EPI, on average (Figure 4.9c). Also, 70% of diploid(non-fluorescent)-aneuploid(red fluorescent) chimeras completely lacked red fluorescent aneuploid cells in the EPI (Figure 4.9d). In contrast, 42.9% of the diploid-diploid chimeras showed complete loss of red fluorescent cells in the EPI (Figure 4.9d). However, the frequency distributions of the red fluorescent cells in diploid(non-fluorescent)-diploid(red fluorescent) and diploid(non-fluorescent)-aneuploid(red fluorescent) chimeras in EPI were not significantly different (Figure 4.9d). This could be attributed to differential preference for non-fluorescent clone already in the diploid-diploid chimeric EPI, which likely reflects the effect of different genetic backgrounds of the transgenic embryos used. When all the diploid-aneuploid mosaic chimeras were analysed together, irrespective of the fluorescent marker or genetic background, it was found that these chimeras contained a significantly higher frequency of diploid cells than aneuploid cells in the EPI (Figure 4.9e). On average, diploid-aneuploid chimeras were composed of 77% diploid cells and 23% aneuploid cells in the EPI by the early post-implantation stage, starting from 50% diploid cells and 50% aneuploid cells distribution at the 8-cell stage (Figure 4.9e).

To test the effect of embryo size on the peri-implantation development of diploid-aneuploid ICMs, double size diploid-aneuploid mosaic chimeras were generated. The whole 8-cell red

fluorescent (mT/mG) diploid was aggregated with whole 8-cell non-fluorescent aneuploid embryo to generate a 16-cell diploid-aneuploid chimera at the 8-cell stage. Control double size diploid-diploid chimeras were also generated using the same approach. Both the chimeras were embedded in Matrigel after immunosurgery and allowed to develop for three days in IVC1 medium (Figure 4.10a). It was found the both double size diploid-diploid chimeras and diploid-aneuploid chimeras developed characteristic post-implantation organization (Figure 4.10b). These chimeras also showed a dramatic decline in the presence of aneuploid cells in the EPI. On average, the diploid(red fluorescent)-diploid(non-fluorescent) chimeras contained 61% non-fluorescent cells in the EPI (Figure 4.10b). When the same clone of cells was aneuploid, as in the diploid(red fluorescent)-aneuploid(non-fluorescent) chimeras, the contribution of non-fluorescent cells decreased to 22.1% in the EPI, on average (Figure 4.10b). There was a significant difference between the frequency distributions of the non-fluorescent cells in diploid(red fluorescent)-diploid(non-fluorescent) and diploid(red fluorescent)-aneuploid(non-fluorescent) EPI (Figure 4.10c). 53.3% of diploid(red fluorescent)-aneuploid(non-fluorescent) chimeras completely lacked non-fluorescent aneuploid cells in the EPI (Figure 4.10c). In contrast, 25% of the diploid-diploid chimeras lacked non-fluorescent cells in the EPI (Figure 4.10c). Next, to determine if ECM components secreted from the PE cells were sufficient for EPI maturation during implantation (Bedzhov and Zernicka-Goetz, 2014), these chimeras were cultured without Matrigel in IVC1 for three days after immunosurgery (Figure 4.10d). In agreement with the above observations, it was found the both double size diploid-diploid chimeras and diploid-aneuploid chimeras developed characteristic post-implantation organization at equivalent rates (Figure 4.10e,f). These chimeras also showed a dramatic decline in the presence of aneuploid cells in the EPI and the PE. On average, the diploid(red fluorescent)-diploid(non-fluorescent) chimeras contained 69% non-fluorescent cells in the EPI and 74.9% non-fluorescent cells in the PE (Figure 4.10e). When the same clone of cells was aneuploid, as in the diploid(red fluorescent)-aneuploid(non-fluorescent) chimeras, the contribution of non-fluorescent cells decreased to 33.3% in the EPI and to 37.5% in the PE, on average (Figure 4.10e). There was a significant difference between the frequency distributions of the non-fluorescent cells in diploid(red fluorescent)-diploid(non-fluorescent) and diploid(red fluorescent)-aneuploid(non-fluorescent) chimeras for both EPI and PE (Figure 4.10g,h). 53.3% of diploid(red fluorescent)-aneuploid(non-fluorescent) chimeras completely lacked non-fluorescent aneuploid cells in the EPI (Figure 4.10g). In contrast, only 15.4% of the diploid-diploid chimeras lacked non-fluorescent cells in the EPI (Figure 4.10g). Similarly, 23.3% of diploid(red fluorescent)-aneuploid(non-fluorescent) chimeras completely lacked non-fluorescent aneuploid cells in the PE, whereas all of the diploid-diploid chimeras contained non-fluorescent cells in the PE (Figure 4.10h).

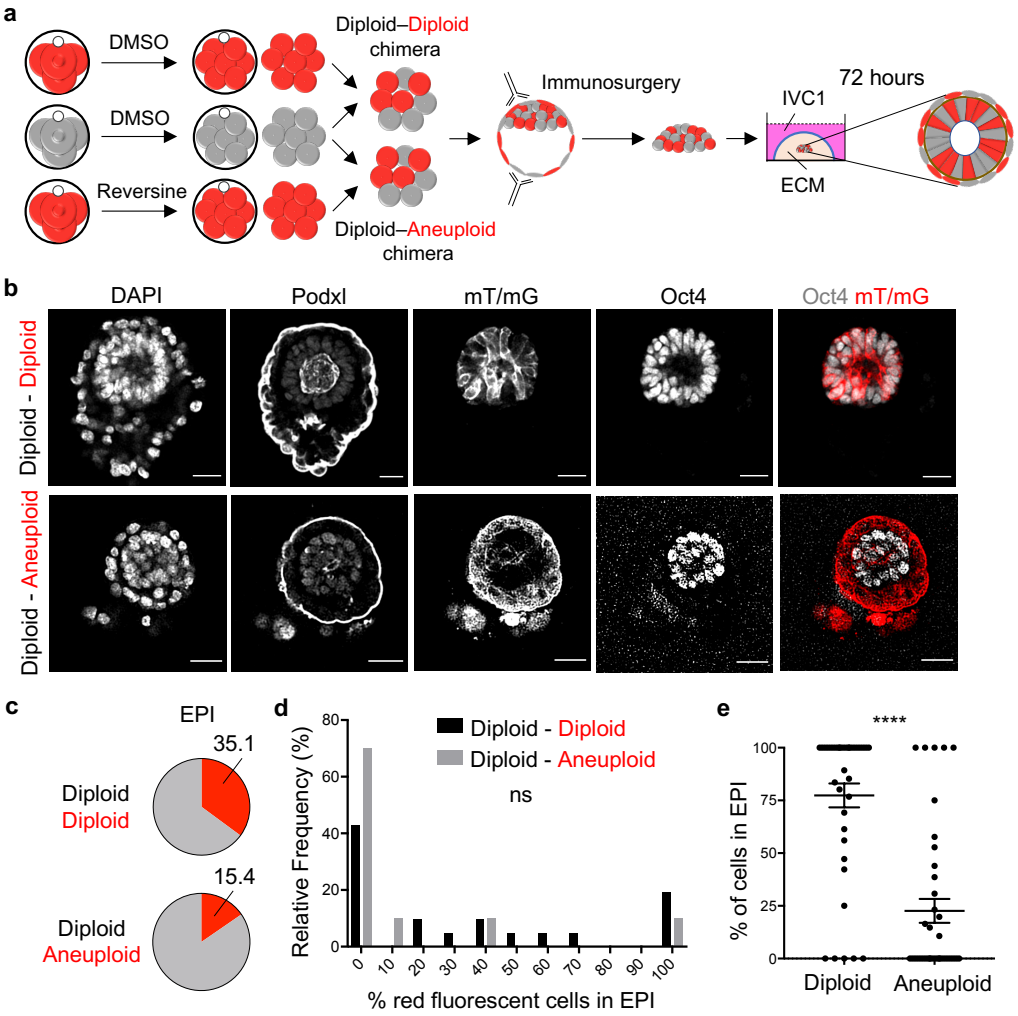

Figure 4.9. Elimination of red fluorescent aneuploid cells from the aneuploid-diploid chimeric mosaic EPI during peri-implantation development *in vitro*. (**a**) Schematic for the experimental design where 8-cell chimeras containing a 1:1 ratio of red fluorescent and non-fluorescent blastomeres were generated at the 8-cell stage. mT/mG transgenic embryos were used for red fluorescent cells. For diploid-aneuploid chimeras, red fluorescent cells were aneuploid (reversine-treated) and non-fluorescent cells diploid. At the late blastocyst stage, immunosurgery was performed to get rid of the outer TE layer. The chimeras were embedded in Matrigel and cultured in IVC1 medium for 72 hours. (**b**) In the examples shown, the diploid-diploid chimera contained both red fluorescent and non-fluorescent cells in the EPI. In contrast, entire diploid-aneuploid chimera EPI lacked the red fluorescent aneuploid clone. Scale bars, 30 μm. (**c**) After 72-hour *in vitro* culture, chimeras were assessed for the composition of the EPI (Oct4-positive cells), i.e. the average distribution of both red fluorescent and non-fluorescent cells. (**d**) Frequency distributions of red fluorescent cells within the EPI of control diploid(non-fluorescent)-diploid(red fluorescent) chimeras and of diploid(non-fluorescent)-aneuploid(red fluorescent) chimeras. Kolmogorov-Smirnov test was used to compare the frequency distributions for two types of chimeras, and ns = not significantly different. For (**b**), (**c**) and (**d**), diploid-diploid n = 21 chimeras and diploid-aneuploid n = 20 chimeras. (**e**) Comparison between the contribution

of diploid and aneuploid clones to the EPI of diploid-aneuploid mosaic chimeras, n = 39 chimeras. Mann-Whitney test was used, ****p < 0.0001 and all data are mean ± s.e.m.

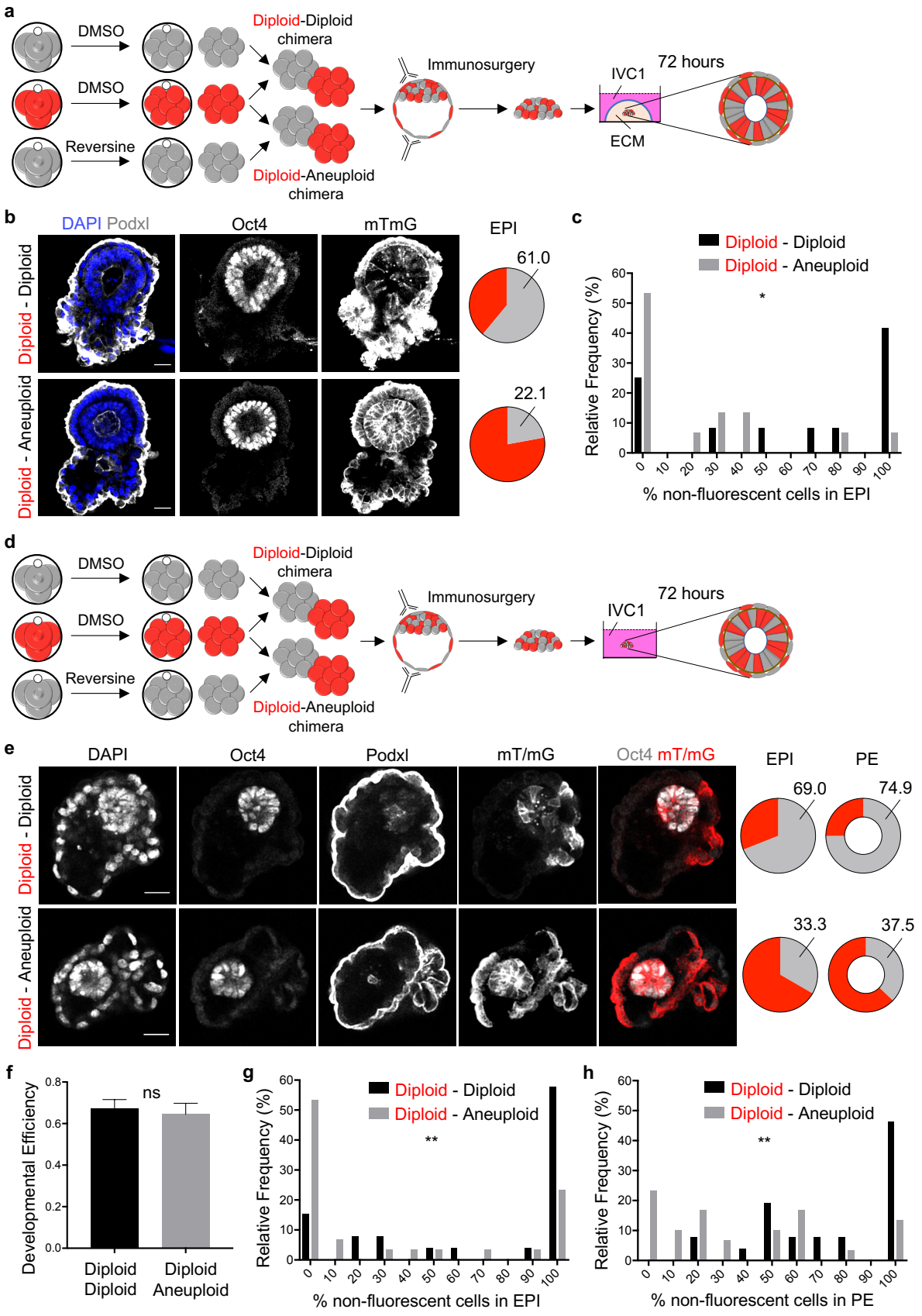

Figure 4.10. Elimination of aneuploid cells from the double size aneuploid-diploid chimeric mosaic EPI during peri-implantation development *in vitro*. (**a**) Schematic for the experimental design where 16-cell chimeras containing a 1:1 ratio of red fluorescent and non-fluorescent blastomeres were generated at the 8-cell stage. mT/mG transgenic embryos were used for red fluorescent cells. For diploid-aneuploid chimeras, red fluorescent cells were diploid and non-fluorescent cells aneuploid (reversine-treated). At the late blastocyst stage, immunosurgery was performed to get rid of the outer TE layer. The chimeras were embedded in Matrigel and cultured in IVC1 medium for 72 hours. (**b**) After 72-hour *in vitro* culture, chimeras were assessed for the composition of the EPI (Oct4-positive cells), i.e. the average distribution of both red fluorescent and non-fluorescent cells. In the examples shown, the diploid-diploid chimera contained both red fluorescent and non-fluorescent cells in the EPI. In contrast, most of the diploid-aneuploid chimera EPI originated from the red fluorescent diploid clone. Scale bars, 30 μm. (**c**) Frequency distributions of non-fluorescent cells within the EPIof control diploid(red fluorescent)-diploid(non-fluorescent) chimeras and of diploid(red fluorescent)-aneuploid(non-fluorescent) chimeras. For (**b**) and (**c**), diploid-diploid n = 12 chimeras and diploid-aneuploid n = 15 chimeras. (**d**) Schematic for the experimental design where 16-cell diploid-diploid and diploid-aneuploid chimeras were generated at the 8-cell stage using similar approach as mentioned in (**a**). At the late blastocyst stage, immunosurgery was performed and the chimeric ICMs were cultured in IVC1 medium for 72 hours. (**e**) After 72-hour *in vitro* culture, chimeras were assessed for the composition of the EPI (Oct4-positive cells) and PE (DAPI-positive and Oct4-negative cells). In the examples shown, the diploid-diploid chimera contained both red fluorescent and non-fluorescent cells in the EPI and PE. In contrast, most of the diploid-aneuploid chimera EPI and PE originated from the red fluorescent diploid clone. Scale bars, 30 μm. (**f**) The efficiency of chimeras to form an epithelial EPI (marked by Oct4 in (**e**)) surrounded by a layer of PE cells and enclosing a lumen (marked by Podxl in (**e**)) after 72-hour *in vitro* culture was assessed. n = 3 experiments, Mann-Whitney test was used, ns = not significantly different and all data are mean ± s.e.m. Frequency distributions of non-fluorescent cells within the EPI (**g**) and PE cell layer (**h**) of control diploid(red fluorescent)-diploid(non-fluorescent) chimeras and of diploid(red fluorescent)-aneuploid(non-fluorescent) chimeras. For graphs (**c**), (**g**) and (**h**), Kolmogorov-Smirnov test was used to compare the frequency distributions for two types of chimeras, *$p < 0.05$ and **$p < 0.01$. For (**e**), (**f**), (**g**) and (**h**), diploid-diploid n = 26 chimeras and diploid-aneuploid n = 30 chimeras.

Together, these results indicate that aneuploid cells continue to get eliminated from the EPI during the development of diploid-aneuploid ICMs beyond blastocyst stage *in vitro*.

4.2.3 Elimination of aneuploid cells from diploid-aneuploid embryo epiblast during peri-implantation *in vivo* and *in vitro*

To determine the fate of aneuploid cells in embryos which were allowed to implant *in vivo* and from which TE was not removed, intact diploid-diploid and diploid-aneuploid chimeras were transferred back to foster mothers at the early blastocyst stage. Four red fluorescent (mT/mG)

diploid cells and four non-fluorescent aneuploid cells, isolated from the respective 8-cell stage embryos, were aggregated together to generate the 8-cell diploid-aneuploid chimera. Control diploid-diploid chimeras were also generated using the same approach. The chimeric embryos were recovered 12hours after implantation (at E5.0) and cultured *in vitro* for 36 hours (schematic shown in figure 4.11a). It was found that both diploid-diploid and diploid-aneuploid chimeras developed into organized structures with characteristic post-implantation morphology, in which the TE sat above the epithelial EPI (marked by Oct4) that formed a lumen in its center (lined by Podxl) and a layer of PE cells surrounded both EPI and TE (Figure 4.11b). These chimeras also showed a dramatic decline in the presence of aneuploid cells in the EPI (Oct4-positive cells) lineage. On average, the diploid(red fluorescent)-diploid(non-fluorescent) chimeras contained 49.99% non-fluorescent cells in the EPI (Figure 4.11c). When the same clone of cells was aneuploid, as in the diploid(red fluorescent)-aneuploid(non-fluorescent) chimeras, the contribution of non-fluorescent cells decreased to 19.67% in the EPI, on average (Figure 4.11c). There was a significant difference between the frequency distributions of the non-fluorescent cells in diploid(red fluorescent)-diploid(non-fluorescent) and diploid(red fluorescent)-aneuploid(non-fluorescent) chimeras in EPI (Figure 4.11d). 78.6% of diploid(red fluorescent)-aneuploid(non-fluorescent) chimeras completely lacked non-fluorescent aneuploid cells in the EPI lineage (Figure 4.11d). In contrast, only 14.3% of the diploid-diploid chimeras lacked non-fluorescent cells in the EPI (Figure 4.11d). Similar results were obtained with double size chimeras (schematic shown in Figure 4.11e). On average, the diploid(red fluorescent)-diploid(non-fluorescent) chimeras contained 56.27% non-fluorescent cells in the EPI (Figure 4.11f). When the same clone of cells was aneuploid, as in the diploid(red fluorescent)-aneuploid(non-fluorescent) chimeras, the contribution of non-fluorescent cells decreased to 1.99% in the EPI, on average (Figure 4.11f). There was a significant difference between the frequency distributions of the non-fluorescent cells in diploid(red fluorescent)-diploid(non-fluorescent) and diploid(red fluorescent)-aneuploid(non-fluorescent) chimeras in EPI (Figure 4.11g). 75% of diploid(red fluorescent)-aneuploid(non-fluorescent) chimeras completely lacked non-fluorescent aneuploid cells in the EPI, whereas all of the diploid-diploid chimeras contained non-fluorescent cells in the EPI (Figure 4.11g).

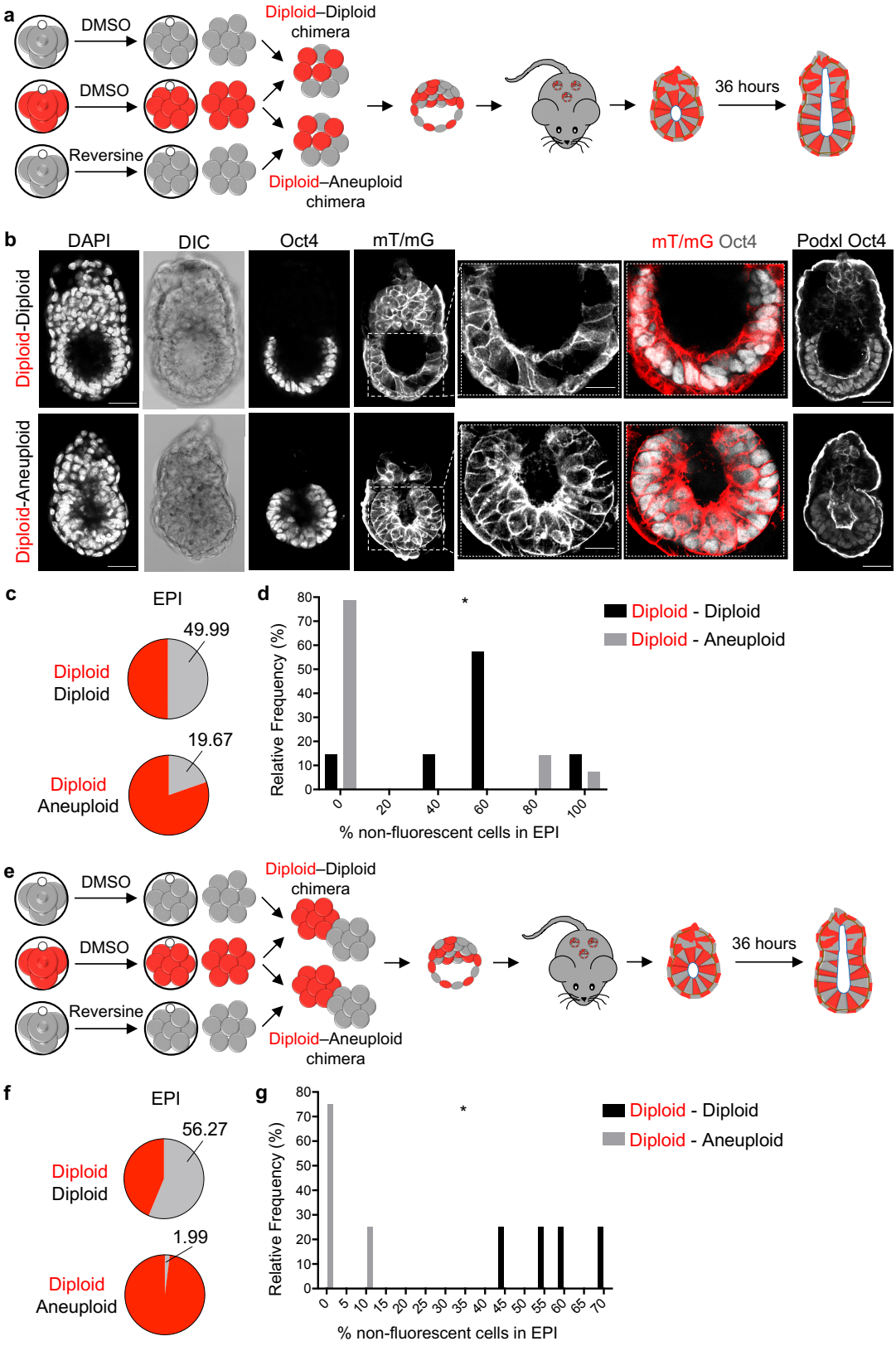

Figure 4.11. Elimination of aneuploid cells from the aneuploid-diploid chimeric EPI during peri-implantation development *in vivo* and *in vitro*. (**a**) Schematic for the experimental design where 8-cell chimeras containing a 1:1 ratio of red fluorescent and non-fluorescent blastomeres were generated at the 8-cell stage. mT/mG transgenic embryos were used for red fluorescent cells. For diploid-

aneuploid chimeras, red fluorescent cells were diploid and non-fluorescent cells aneuploid (reversine-treated). At the early blastocyst stage, chimeras were transferred to a pseudo-pregnant mother and recovered 12 hours after implantation and *in vitro* cultured for 36 hours. (**b**) In the examples shown, the diploid-diploid chimera contained both red fluorescent and non-fluorescent cells in the EPI. In contrast, most of the diploid-aneuploid chimera EPI originated from the red fluorescent diploid clone. Scale bars, 40 μm. Squares indicate the magnified regions, scale bars, 20 μm. (**c**) After culture, chimeras were assessed for the composition of the EPI (Oct4-positive cells), i.e. the average distribution of both red fluorescent and non-fluorescent cells. (**d**) Frequency distribution of non-fluorescent cells in the EPI of diploid(red fluorescent)-diploid(non-fluorescent) and diploid(red fluorescent)-aneuploid(non-fluorescent) chimeras. Kolmogorov-Smirnov test was used to compare the frequency distributions for two types of chimeras and *$p < 0.05$. For (**b**), (**c**) and (**d**), diploid-diploid n = 7 chimeras and diploid-aneuploid n = 14 chimeras. (**e**) The approach in (**a**) was followed for 16-cell chimeras containing a 1:1 ratio of red fluorescent and non-fluorescent cells generated at the 8-cell stage. (**f**) After culture, both the double size chimeras were assessed for the composition of the EPI. (**g**) Frequency distribution of non-fluorescent cells in the EPI of diploid(red fluorescent)-diploid(non-fluorescent) and diploid(red fluorescent)-aneuploid(non-fluorescent) chimeras. Kolmogorov-Smirnov test was used to compare the frequency distributions for two types of chimeras and *$p < 0.05$. For (**f**) and (**g**), diploid-diploid n = 4 chimeras and diploid-aneuploid n = 4 chimeras.

4.2.4 Apoptosis of aneuploid cells in diploid-aneuploid epiblast during peri-implantation

Results shown in sections 4.2.2 and 4.2.3 together indicate that aneuploid cells are preferentially eliminated from the EPI lineage during the development of diploid-aneuploid mosaic embryos from pre- to post-implantation stages of development. To determine how aneuploid cells become eliminated from diploid-aneuploid embryo EPI during peri-implantation stages of development, their time-lapse imaging was performed. Red fluorescent diploid embryos were obtained from mT/mG transgenics and green fluorescent aneuploid (reversine-treated) embryos were obtained from histone H2B-GFP transgenics. Four red fluorescent diploid cells and four green fluorescent aneuploid cells were aggregated together to generate an 8-cell diploid-aneuploid chimera at the 8-cell stage. They were cultured according to the schematic shown in Figure 4.12a. The chimeric ICMs were embedded in Matrigel and live-imaged during 72-hour IVC1 culture. It was found that the green fluorescent aneuploid cells of the diploid-aneuploid chimeric EPI displayed the morphological features characteristic of apoptosis (Kerr *et al*., 1972; Porter and Jänicke, 1999): nuclear condensation and disintegration into blebs (Figure 4.12a). The cellular debris of apoptotic green fluorescent aneuploid cells was then engulfed by the neighboring red fluorescent diploid cells (Figure 4.12a). Similar result was obtained for double-size diploid(red fluorescent)-aneuploid(green fluorescent) chimeric ICMs cultured according to schematic shown in Figure 4.12b in IVC1 culture without Matrigel (Figure 4.12b). Similar result was obtained for diploid(red fluorescent)-

aneuploid(green fluorescent) chimeras in which the TE was not removed when they were recovered from foster mother 12 hours after implantation and *in vitro* cultured (Figure 4.12c).

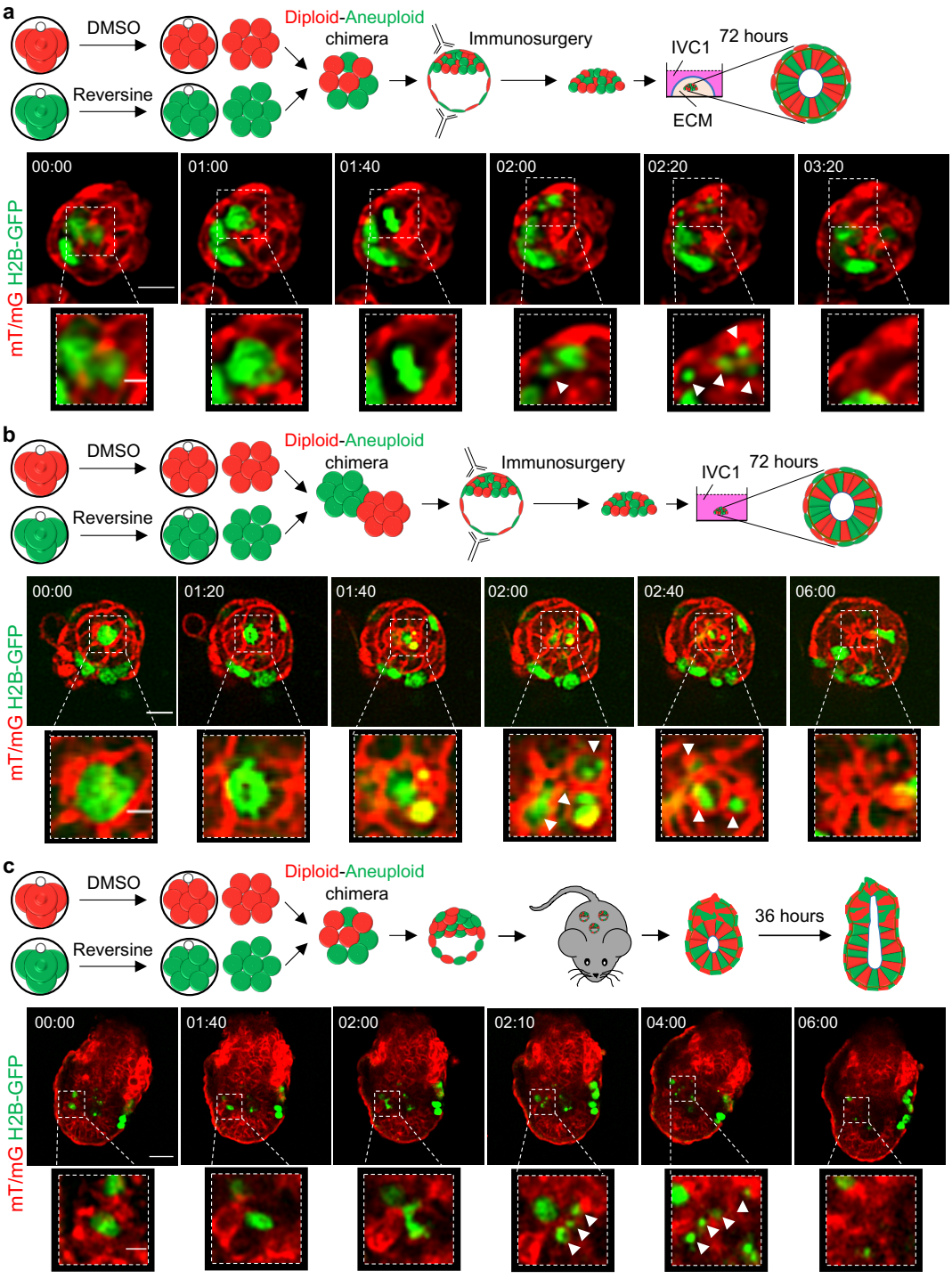

Figure 4.12. Elimination of aneuploid cells from the diploid-aneuploid EPI during peri-implantation stage of development by apoptosis. 1:1 Diploid-aneuploid chimeras were made at the 8-cell stage, in which diploid cells came from mT/mG (red fluorescent membrane) transgenic embryos and aneuploid cells came from Histone H2B-GFP (green fluorescent nucleus) transgenic embryos. They were live-imaged beyond the blastocyst stage using different peri-implantation culture systems

used. Here are shown the sequential representative images from time-lapse series for three diploid-aneuploid chimeras, each showing apoptosis of an aneuploid cell (histone H2B-GFP) (white boxes), while developing from pre- to post-implantation stages of development. White arrows indicate the apoptotic debris. (**a**) 8-cell diploid-aneuploid chimeras were generated at the 8-cell stage. Immunosurgery was performed on them at the late blastocyst stage to remove the outer TE layer. The chimeric ICMs were then embedded in Matrigel and cultured in IVC1 medium for 72 hours, during which they were live-imaged. Scale bar, 20μm. Squares indicate the magnified regions, scale bar, 7μm. Diploid-aneuploid n = 12 chimeras. (**b**) 16-cell diploid-aneuploid chimeras were generated at the 8-cell stage. Immunosurgery was performed on them at the late blastocyst stage. The double-size chimeric ICMs were then cultured in IVC1 medium for 72 hours, during which they were live-imaged. Scale bar, 20μm. Squares indicate the magnified regions, scale bar, 7μm. Diploid-aneuploid n = 22 chimeras. (**c**) 8-cell diploid-aneuploid chimeras were generated at the 8-cell stage. At the early blastocyst stage, these chimeras were transferred to pseudo-pregnant mothers and recovered 12 hours after implantation. Then they were *in vitro* cultured for 36 hours and live-imaged. Scale bar, 40μm. Squares indicate the magnified regions, scale bar, 10μm. Diploid-aneuploid n = 12 chimeras.

Therefore, these results led to the conclusion that aneuploid cells in the diploid-aneuploid mosaic embryos are preferentially depleted from the EPI by apoptosis during the peri-implantation stage of development, and the apoptotic debris was engulfed and gradually cleared by neighboring diploid cells.

4.2.5 Size regulation of diploid-aneuploid epiblast during peri-implantation

In sections 4.2.2 and 4.2.3, it was demonstrated that one clone of cells, aneuploid cells, were significantly eliminated from the EPI lineage during the development of 1:1 diploid-aneuploid mosaic embryos from pre- to post-implantation stages of development. In order to determine the effect of preferential elimination of aneuploid cells from diploid-aneuploid mosaics on the overall mosaic embryo development, the mosaic EPI at the end of implantation was analyzed. Interestingly, it was found that despite the depletion of aneuploid cells, diploid-diploid and diploid(red fluorescent)-aneuploid(non-fluorescent) chimeric ICMs cultured according to schematic shown in Figure 4.8a had a similar average EPI cell number after 72 hours of IVC1 culture (Figure 4.13a). This finding was independent of the fluorescent marker used because diploid-diploid and diploid (non-fluorescent)-aneuploid(red fluorescent) chimeric ICMs cultured according to schematic shown in Figure 4.9a also had average EPI cell number equivalent to controls (Figure 4.13b). Similar result was obtained for double-size diploid(red fluorescent)-aneuploid(non-fluorescent) chimeric ICMs cultured according to schematic shown in Figure 4.10a (Figure 4.13c) and cultured according to schematic shown in Figure 4.10d (Figure 4.13d). The average number of cells in the early post-implantation EPI was also similar in diploid-diploid and diploid-aneuploid chimeras (Figure 4.13e) as well as in double size

chimeras (Figure 4.13f), in which TE was not removed and which were allowed to implant *in vivo* (cultured according to schematics shown in Figures 4.11a and 4.11e respectively). Therefore, these results led to the conclusion that diploid-aneuploid mosaic embryos regulate the overall EPI size to the level of diploid-diploid embryos despite the depletion of aneuploid cells during peri-implantation development.

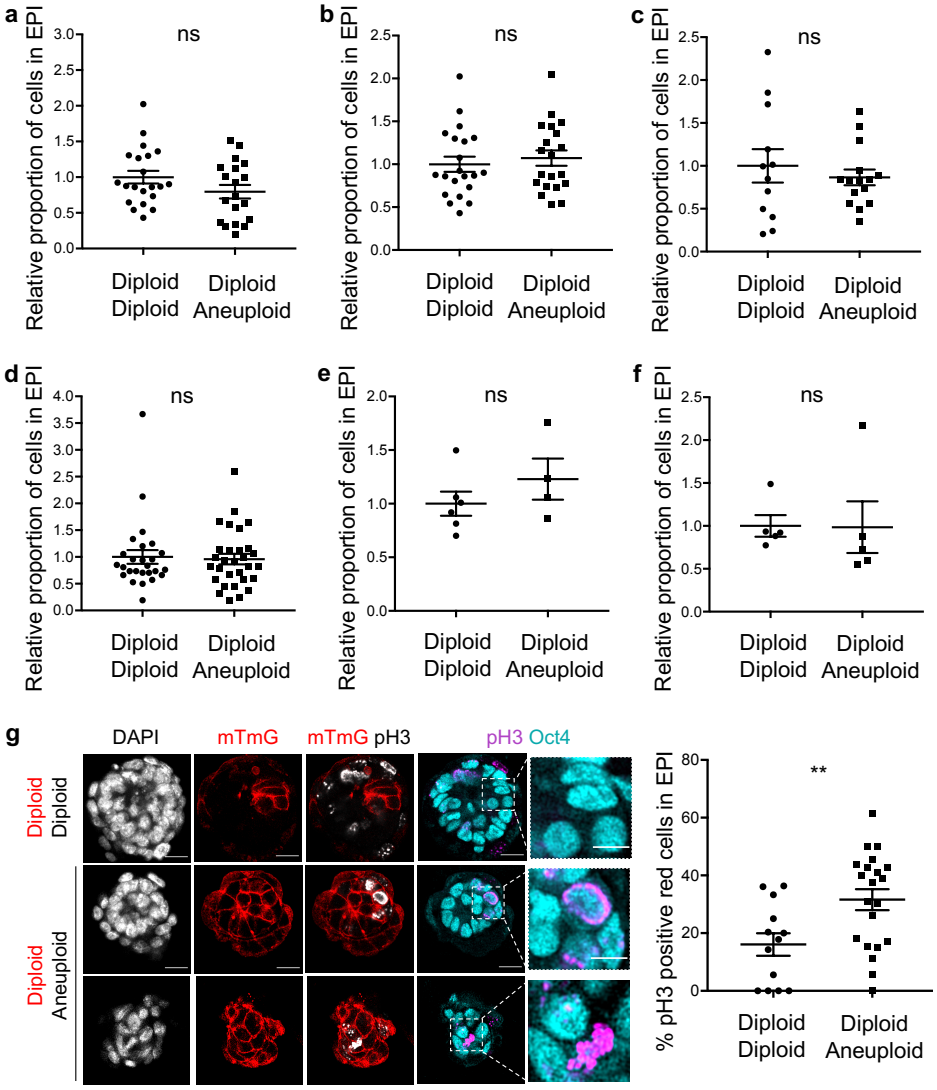

Figure 4.13. Size regulation of the diploid-aneuploid EPI during peri-implantation stage of development. 1:1 Diploid-aneuploid and diploid-diploid chimeras were generated at the 8-cell stage. The two clones of cells used were: red fluorescent membrane (from mT/mG transgenic embryos) cells and non-fluorescent cells. For graphs (**a**), (**b**), (**c**), (**d**), (**e**) and (**f**), relative number of cells in the EPI were analysed for both the chimeras (relative to diploid-diploid chimeras) at the end of the culture for different peri-implantation culture systems used. The chimeras that were used for analysis displayed three characteristic features: a layer of PE surrounding the epithelial EPI (marked by Oct4) with a lumen in its center (lined by Podxl). (**a**) 8-cell diploid(red fluorescent)-aneuploid(non-fluorescent) chimeras were generated at the 8-cell stage. Immunosurgery was performed on them at the late blastocyst stage, to remove the outer TE layer. The chimeric ICMs were then embedded in Matrigel and cultured in IVC1

medium for 72 hours. Student's t-test was used. Diploid-diploid n = 21 chimeras and diploid-aneuploid n = 19 chimeras. (**b**) 8-cell diploid(non-fluorescent)-aneuploid(red fluorescent) chimeras were generated at the 8-cell stage. Same protocol as mentioned in (**a**) was followed with them. Student's t-test was used. Diploid-diploid n = 21 chimeras and diploid-aneuploid n = 20 chimeras. (**c**) 16-cell diploid(red fluorescent)-aneuploid(non-fluorescent) chimeras were generated at the 8-cell stage. Immunosurgery was performed on them at the late blastocyst stage. The double-size chimeric ICMs were then embedded in Matrigel and cultured in IVC1 medium for 72 hours. Student's t-test with Welch's correction was used. Diploid-diploid n = 12 chimeras and diploid-aneuploid n = 15 chimeras. (**d**) 16-cell diploid(red fluorescent)-aneuploid(non-fluorescent) chimeras were generated at the 8-cell stage. Immunosurgery was performed on them at the late blastocyst stage. The double-size chimeric ICMs were then cultured in IVC1 medium for 72 hours. Mann-Whitney test was used. Diploid-diploid n = 26 chimeras and diploid-aneuploid n = 30 chimeras. (**e**) 8-cell diploid(red fluorescent)-aneuploid(non-fluorescent) chimeras were generated at the 8-cell stage. At the early blastocyst stage, these chimeras were transferred to pseudo-pregnant mothers and recovered 12 hours after implantation and then *in vitro* cultured for 36 hours. Mann-Whitney test was used. Diploid-diploid n = 6 chimeras and diploid-aneuploid n = 4 chimeras. (**f**) 16-cell diploid(red fluorescent)-aneuploid(non-fluorescent) chimeras were generated at the 8-cell stage. Same protocol as mentioned in (**e**) was followed with them. Mann-Whitney test was used. Diploid-diploid n = 5 chimeras and diploid-aneuploid n = 5 chimeras. (**g**) 8-cell diploid(red fluorescent)-aneuploid(non-fluorescent) chimeras were generated at the 8-cell stage. Immunosurgery was performed on them at the late blastocyst stage. The chimeric ICMs were then embedded in Matrigel and cultured in IVC1 medium for 48 hours. The percentage of the number of pH3 positive red fluorescent EPI cells of the total red fluorescent EPI cells (mT/mG Oct4-positive) were analysed for each chimera, for both diploid-diploid and diploid-aneuploid chimeras. Scale bars, 20 μm. Squares indicate the magnified regions, scale bars, 10 μm. Student's t-test was used. Diploid-diploid n = 13 chimeras and diploid-aneuploid n = 21 chimeras.
For all the graphs, ns = not significantly different, $^{**}p < 0.01$ and all data are mean ± s.e.m.

Overall regulation of the total number of cells in the EPI despite the depletion of one clone of cells (aneuploid cells) indicated that the other clone of cells (diploid cells) must be undergoing compensatory excessive proliferation during peri-implantation stage of development of 1:1 diploid-aneuploid mosaic embryos. To investigate this, proliferation was assessed in the diploid clone of cells in the diploid-aneuploid chimeric EPI. Both the diploid-diploid and diploid(red fluorescent)-aneuploid(non-fluorescent) chimeric ICMs cultured according to schematic shown in Figure 4.8a, were examined for the mitosis marker phosphorylated histone H3 (Hans and Dimitrov, 2001) and the EPI lineage marker Oct4 after 48 hours IVC1 culture. It was found that the red fluorescent diploid clone showed significantly higher mitosis in the diploid(red fluorescent)-aneuploid(non-fluorescent) chimeric EPI than in the diploid(red fluorescent)-diploid(non-fluorescent) chimeric EPI (Figure 4.13g). Since pH3 does not only mark cells in mitosis phase but also in G2/S phase, it will be better to use DAPI or the cell

cycle reporter FUCCI (Fluorescent Ubiquitination-based Cell Cycle Indicator) (Mort *et al*., 2014) to recognize the cells in mitosis for future experiments. Overall, these results suggest that increased proliferation of the diploid cells compensates for loss of aneuploid cells in the diploid-aneuploid EPI during peri-implantation development, thereby maintaining similar cell number as the diploid-diploid post-implantation EPI.

4.3 p53-autophagy mediated elimination of aneuploid cells from the mouse aneuploid epiblast during pre-implantation development

Results shown in sections 4.1.2 and 4.1.3 revealed that aneuploid cells are eliminated from the ICM by apoptosis during blastocyst maturation (E3.5 to E4.5 transition). Next step was to investigate the mechanisms triggering this apoptosis of aneuploid cells in the ICM. As mentioned in the section 3.4, several potential mechanisms have been proposed underlying the elimination of chromosomally abnormal cells. As demonstrated in section 3.4 and figure 3.2, unpublished work by Helen Bolton in the Zernicka-Goetz lab (PhD thesis) led to the conclusion that reversine-treated (aneuploid) pre-implantation embryos did not show evidence for elevated levels of ROS or replication stress or DNA damage, relative to control (diploid) embryos. Also, there was no evidence for DNA damage in the resulting micronuclei after chromosome missegregation induction (Figure 3.2). This section therefore will investigate what other mechanisms mediate the apoptosis of aneuploid cells in the aneuploid embryos during blastocyst maturation in the ICM lineage. Throughout this section, the aneuploid embryos (whole embryos treated with reversine during the 4- to 8- cell stage) will be compared directly to diploid embryos (equivalent controls).

4.3.1 Equivalent p38 kinase-dependent stress response between aneuploid and diploid embryos in the epiblast lineage

Aneuploid cells have been shown to generate a p38 kinase-dependent stress response that limit their proliferation (Thompson and Compton, 2010; Simões-Sousa *et al*., 2018). To investigate if the activation of canonical p38 pathway could be involved, phospho-p38 levels were compared between aneuploid and diploid blastocysts using immunofluorescence. The resulting nuclear phospho-p38 fluorescence was detected using confocal microscopy and quantified relative to nuclear DAPI fluorescence intensity in the EPI. Aneuploid and diploid embryos were assessed at the late blastocyst stage because the divergence in cell numbers between the two types of embryos is apparent at this stage (Bolton *et al*., 2016). There was no significant difference in the relative phospho-p38 signal intensity between aneuploid and diploid EPI (Figure 4.14). Thus, there were no detectable differences in p38 stress kinase activation between aneuploid and diploid embryos at the late blastocyst stage in EPI.

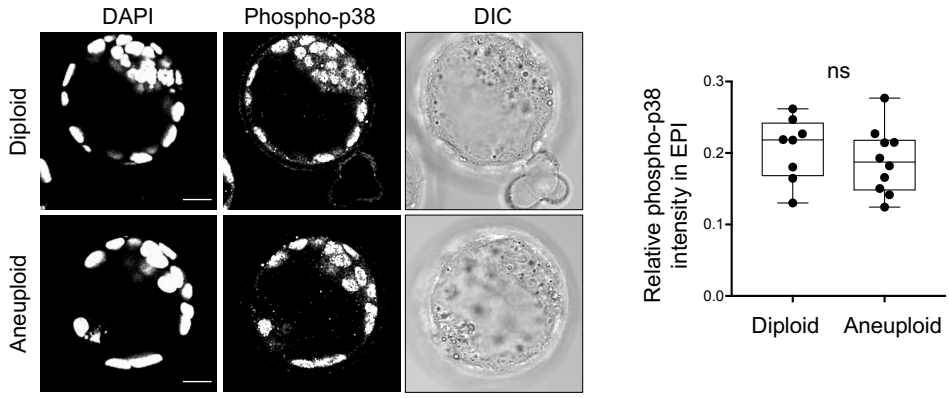

Figure 4.14. Evaluating phospho-p38 levels in the aneuploid late blastocysts. Embryos were treated at the 4-8 cell stage with DMSO (diploid) or reversine (aneuploid). The level of relative nuclear phospho-p38 (relative to DAPI fluorescence intensity) in the EPI between diploid and aneuploid embryos was assessed at the late blastocyst stage. Each dot represents the relative phospho-p38 fluorescence intensity in an embryo. Student's t-test was used and ns = not significantly different. Diploid n = 8 embryos and aneuploid n = 10 embryos. Data are shown as individual data points with Box and Whiskers graph (bottom: 25%; top: 75%; line: median; whiskers: min to max). Scale bars, 20μm.

4.3.2 Chronic misfolding, upregulated autophagy and upregulated p53 pathway in aneuploid pre-implantation embryos

As explained in detail in the section 3.4, the gene imbalances caused by aneuploidy can in turn lead to proteomic imbalances (Oromendia *et al*., 2012; Stingele *et al*., 2012; Ohashi *et al*., 2015). Therefore, next step was to investigate whether reversine-treated aneuploid embryos displayed proteotoxic stress. The heat shock protein 70 (HSP70) represents a group of molecular chaperones instrumental in alleviating misfolded protein stress (Duncan *et al*., 2015). So, HSP70 levels were compared between diploid (control) and aneuploid (reversine-treated) embryos using immunofluorescence. It was found that aneuploid embryos displayed higher HSP70 levels than diploid embryos from the 8-cell stage through to the late blastocyst stage (Figure 4.15a), indicative of chronic misfolding. The relative cytosolic HSP70 fluorescence intensity (relative to nuclear DAPI fluorescence intensity) in the EPI of aneuploid late blastocysts was significantly higher than in diploid blastocysts (Figure 4.15b).

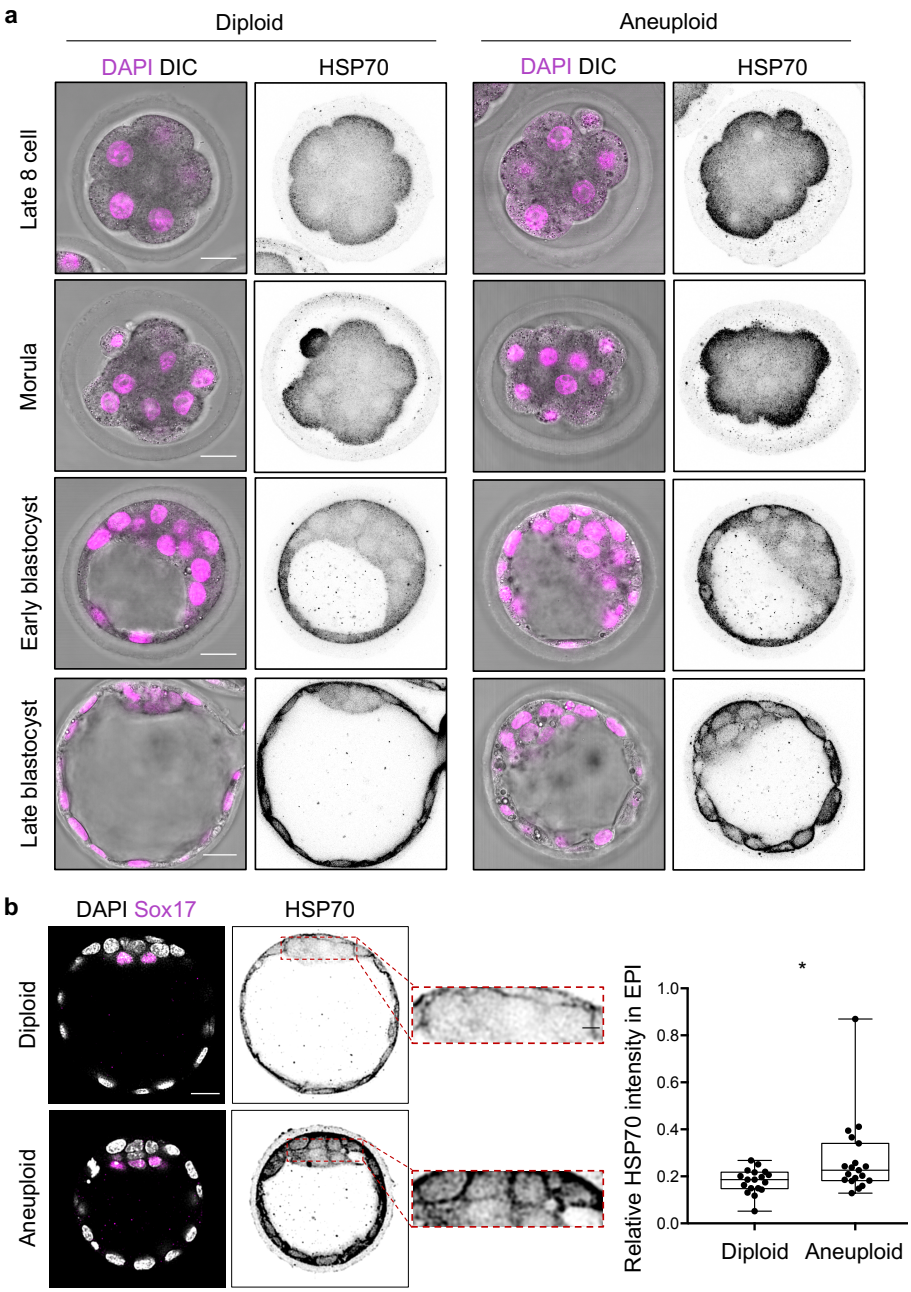

Figure 4.15. Chronic misfolding in the pre-implantation aneuploid embryos. (**a**) HSP70 immunostaining in diploid (controls) and aneuploid (reversine-treated) embryos for the late 8-cell stage, the morula, the early blastocyst and the late blastocyst stages. Scale bars, 20 µm. Diploid: 8-cell n = 12 embryos, morula n = 9 embryos, early blastocyst n = 9 embryos, late blastocyst n = 14 embryos. Aneuploid: 8-cell n = 10 embryos, morula n = 9 embryos, early blastocyst n = 9 embryos, late blastocyst n = 18 embryos. (**b**) The level of relative cytosolic HSP70 (relative to DAPI fluorescence intensity) in the EPI between diploid and aneuploid embryos was assessed at the late blastocyst stage. Each dot represents relative HSP70 levels in an embryo. Embryos were stained with Sox21 (to mark the PE) and cells enclosed between the TE (cells at the periphery of the blastocyst) and PE were assumed to be EPI. Mann-Whitney test was used and *p < 0.05. Diploid n = 18 and aneuploid n = 19 embryos. Data are shown as individual data points with Box and Whiskers graph (bottom: 25%; top: 75%; line: median;

whiskers: min to max). Scale bar, 20μm. Squares indicate the magnified regions, scale bar, 5μm.

The cell responds to an increase in misfolded proteins by upregulating protein quality control mechanisms such as autophagy (Chen *et al*., 2011). Therefore, it was hypothesized that autophagy is upregulated in aneuploid embryos in response to this chronic misfolding. The autophagy pathway has been explained in detail in Figure 4.16. Briefly, autophagy is a non-specific bulk degradation pathway, employed by the cell to degrade cellular components such as damaged organelles and excess/misfolded proteins using lysosomal enzymes. During autophagy, the double-membraned autophagosome forms around the cargo and fuses with lysosomes, finally leading to degradation of the engulfed cargo (Anding and Baehrecke, 2015). The microtubule-associated light-chain 3B (LC3B) and p62/sequestosome 1 are associated with the autophagosome membrane and are two widely used markers of autophagy (Klionsky *et al*., 2016; Niklaus *et al*., 2017) (Figure 4.16). To investigate if the aneuploid embryos activate autophagy, LC3B and p62 levels were compared between diploid (control) and aneuploid (reversine-treated) embryos using immunofluorescence at the late blastocyst stage. The resulting cytoplasmic LC3B and p62 fluorescence was detected using confocal microscopy and the number of puncta per cell were quantified. There was a significant increase in the number of LC3B (Figure 4.17a) and p62 (Figure 4.17b) puncta/cell in the EPI of aneuploid blastocysts compared to diploid blastocysts. These increases in LC3B and p62 puncta were at least in part due to increased levels of their respective transcripts, detected using qRT-PCR at the late blastocyst stage (Figure 4.17c). Since, LC3B is turned over after the fusion of the autophagosome with a lysosome, enhanced LC3B levels in the presence of lysosomal inhibitors indicate autophagic flux (Klionsky *et al*., 2016). To investigate the autophagic flux, lysosomal fusion was inhibited via treatment with the lysosomal inhibitor Bafilomycin A1 (BafA1) (Klionsky *et al*., 2016) (Figure 4.16). Aneuploid (reversine-treated) and diploid (controls) embryos were cultured in KSOM containing 160.6 nM BafA1 during blastocyst maturation. Aneuploid and diploid embryos were also cultured in equivalent concentration of DMSO as control. All four types of embryos were assessed for LC3B accumulation at the late blastocyst stage. BafA1 treatment resulted in a substantial increase in the accumulation of LC3B protein in the EPI for both diploid and aneuploid embryos, with the highest level of accumulation for aneuploid embryos (Figure 4.17d). These results suggest that aneuploid EPI cells upregulate autophagy at the blastocyst stage.

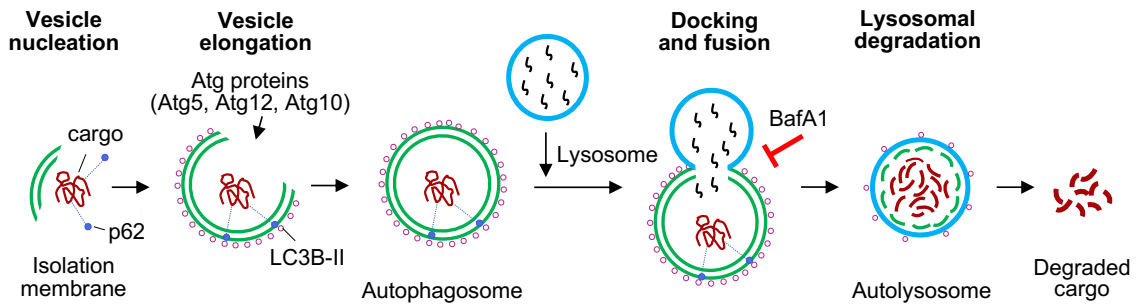

Figure 4.16. Schematic illustrating autophagy (Adapted from Anding and Baehrecke, 2015)**.** Autophagy is a catabolic process that delivers cellular cargo, such as organelles and misfolded proteins, to the lysosome for degradation. Autophagy starts with the nucleation of an isolation membrane (also called a phagophore). The phagophore elongates and sequesters the cargo. Atg proteins are involved in phagophore elongation by mediating two ubiquitin-like processes: (i) Atg5 covalently links to Atg12 via Atg7 and Atg10, and the resulting Atg5-Atg12 complex binds to Atg16; (ii) Atg4 cleaves Atg8 (LC3B) at its carboxyl terminus to give cytosolic LC3B-I, to which the lipid phosphatidylethanolamine binds via Atg7, Atg3 and Atg5-Atg12-Atg16 complex, finally giving LC3B-II (Anding and Baehrecke, 2015). Because of its specific recruitment to autophagosomes, LC3B-II gives a punctate immunostaining (Klionsky *et al*., 2016). The complete closure of the phagophore results in the formation of a double-membrane structure known as the autophagosome. This is followed by the fusion of autophagosome with lysosome to give autolysosomes. In these acidic autolysosomes, the inner membrane and the cargo has been degraded by lysosomal acid hydrolases. The resulting degraded cargo remnants such as the resulting amino acids and free fatty acids, are released back into the cytoplasm. The cargo is tagged with linear ubiquitylation chain which interacts with adaptor proteins such as sequestosome 1/p62. These adaptors carry a LC3-interacting region and mediate the selective capture of the tagged-cargo by the autophagosome (Anding and Baehrecke, 2015). Bafilomycin A1 (BafA1), a V-ATPase inhibitor, is commonly used to block the lysosome acidification and to even block the fusion of autophagosome with lysosome (Klionsky *et al*., 2016).

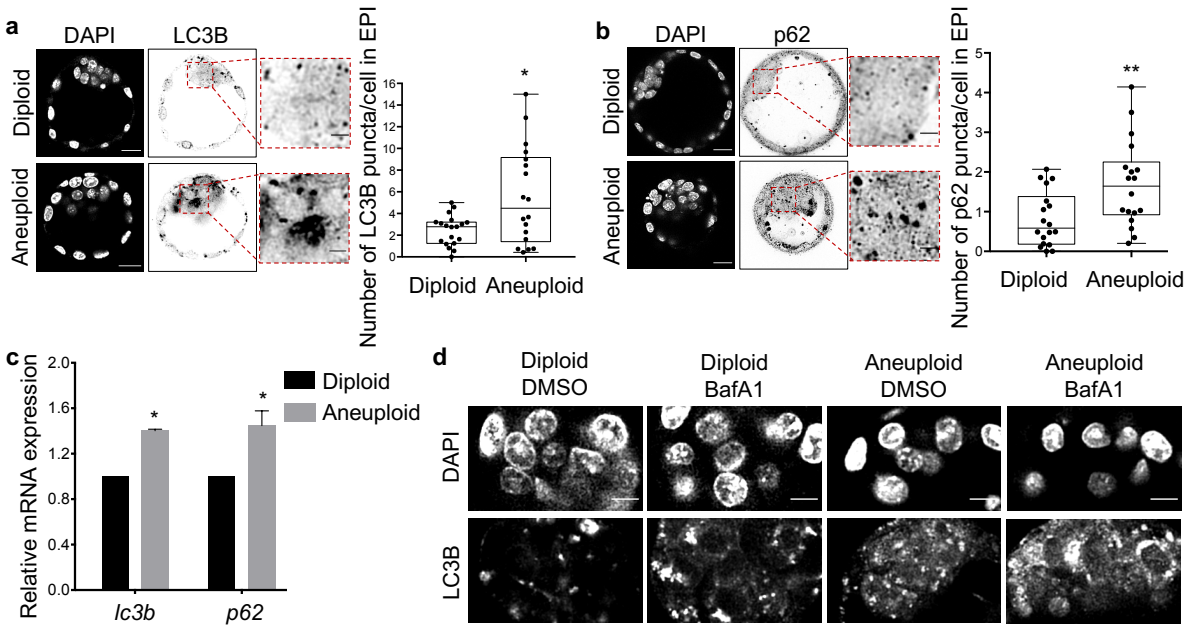

Figure 4.17. Upregulation of autophagy in the pre-implantation aneuploid embryos. Embryos were treated at the 4-8 cell stage with DMSO (diploid) or reversine (aneuploid) and assessed at the late blastocyst stage. The autophagy markers LC3B (**a**) and p62 (**b**) were analysed in the diploid and aneuploid late blastocysts in the EPI using immunofluorescence. Each dot represents the average number of LC3B (**a**) or p62 (**b**) puncta/cell in an embryo. Scale bars, 20 μm. Squares indicate the magnified region. Scale bar, 5 μm. For (**a**), diploid n = 19 embryos and aneuploid n = 18 embryos. Student's t-test with Welch's correction and *p < 0.05. For (**b**), diploid n = 18 embryos and aneuploid n = 18 embryos. Student's t-test and **p < 0.01. For graphs (**a**) and (**b**), data are shown as individual data points as a Box and Whiskers graph (bottom: 25%; top: 75%; line: median; whiskers: min to max). (**c**) mRNA expression for genes involved in autophagy were assessed at the late blastocyst stage (relative to diploid embryos) using qRT-PCR. Diploid n = 69 embryos, aneuploid n = 67 embryos. Mann Whitney test was used and *p < 0.05. All data are mean ± s.e.m. (**d**) Diploid and aneuploid embryos were cultured in the presence of lysosomal inhibitor BafA1 or DMSO and SYTOX from the early blastocyst to the late blastocyst stage (24 hours). They were immunostained for LC3B at the late blastocyst stage to assess the autophagy flux, especially in the EPI. Diploid n = 11 embryos, aneuploid n = 10 embryos, diploid BafA1 n = 9 embryos, aneuploid BafA1 n = 13 embryos. Scale bars, 10 μm.

Studies using human cells and mouse embryos have shown that aneuploidy, arising from chromosome missegregation, activates p53 and that p53 limits the proliferation of aneuploid cells (Li *et al*., 2010; Thompson and Compton, 2010; Janssen *et al*., 2011). The transcriptional factor, p53, is a key player in the cellular response to diverse internal or external stress signals. In turn, p53 can activate diverse cellular processes, including cell cycle arrest, cellular senescence, coordination of various DNA damage repair pathways, differentiation and apoptosis (Aubrey *et al*., 2018). P53 regulates several target genes to control these cellular processes including *puma*, *noxa*, *p21*, *mdm2*, *cyclin G1, bax*, and *bcl-2* (El-Deiry, 1998;

Aubrey *et al*., 2018). To investigate if the activation of p53 pathway could be involved, mRNA levels of *p53* and its target genes (*cyclin G1,* cyclin dependent kinase inhibitor *p21*, and anti-apoptotic *bcl-2*) were compared between aneuploid (reversine-treated) and diploid (control) late blastocysts using qRT-PCR. There was a significant increase in the mRNA levels of *p53*, *p21* and *cyclin G1*, and a significant decrease in *bcl-2* mRNA levels, in aneuploid embryos compared to diploid embryos, indicating an upregulation of the p53 pathway (Figure 4.18).

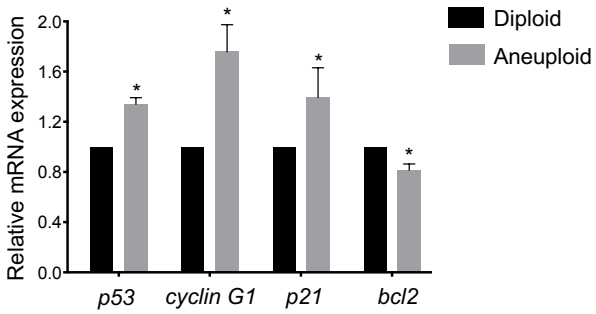

Figure 4.18. Upregulation of p53 pathway in the pre-implantation aneuploid embryos. Embryos were treated at the 4-8 cell stage with DMSO (diploid) or reversine (aneuploid) and assessed at the late blastocyst stage. mRNA expression for genes involved in p53 pathway were assessed at the late blastocyst stage (relative to diploid embryos) using qRT-PCR. Diploid n = 69 embryos, aneuploid n = 67 embryos. Mann Whitney test was used and *$p < 0.05$. All data are mean ± s.e.m.

4.3.3 p53-autophagy cascade eliminates aneuploid cells from the aneuploid ICM during blastocyst maturation

To determine the functional significance of upregulated autophagy and p53 pathway, loss-of-function studies were carried out. To determine the possible role of autophagy in aneuploid embryos, autophagy was disrupted at two different steps of the pathway: (i) knockdown of essential autophagy factor *Atg5* to inhibit the elongation of the autophagosome membrane (Figure 4.16), and (ii) inhibition of lysosome and autophagosome fusion (Figure 4.16). To reduce Atg5, a combination of three Atg5 siRNAs were injected into both the blastomeres of 2-cell stage embryos which were then allowed to develop until the late blastocyst stage. The embryos were then analyzed by qRT-PCR. Atg5 siRNA injection reduced *Atg5* mRNA to 23% relative to embryos injected with control siRNA (Figure 4.19a). Then, to investigate the role of autophagy in the elimination of aneuploid cells from ICM in blastocysts, 2-cell stage embryos with injected with Atg5 siRNA, treated with reversine or DMSO at the 4-8 cell stage and live-imaged in the presence of SYTOX from the early blastocyst to the late blastocyst stage. SYTOX-positive cells were quantified with time in ICMs for all four types of embryos: control siRNA or Atg5 siRNA injected aneuploid embryos and control siRNA or Atg5 siRNA injected diploid embryos. It was found that RNAi-mediated depletion of Atg5 significantly reduced the

number of dying cells in the ICM of aneuploid, but not diploid, embryos (Figure 4.19b). Similarly, lysosomal fusion was inhibited via treatment with the lysosomal inhibitor BafA1 (Figure 4.16). Aneuploid (reversine-treated) and diploid (controls) embryos were cultured in KSOM containing 160.6 nM BafA1 during blastocyst maturation. Aneuploid and diploid embryos were also cultured in equivalent concentration of DMSO as control. All four types of embryos were imaged during blastocyst maturation in the presence of SYTOX. It was found that BafA1 treatment significantly reduced the number of dying cells in the ICM of aneuploid, but not diploid, embryos (Figure 4.19c). Aneuploid and diploid embryos were also treated with 400 nM rapamycin, which induces autophagy via mTOR inhibition (Klionsky *et al*., 2016), during blastocyst maturation in the presence of SYTOX and imaged. In contrast to the effect of autophagy inhibition, rapamycin treatment did not affect the number of dying cells in the ICM of aneuploid or diploid embryos (Figure 4.19d). Together these results indicate that autophagy eliminates specifically aneuploid cells from the ICM during blastocyst maturation.

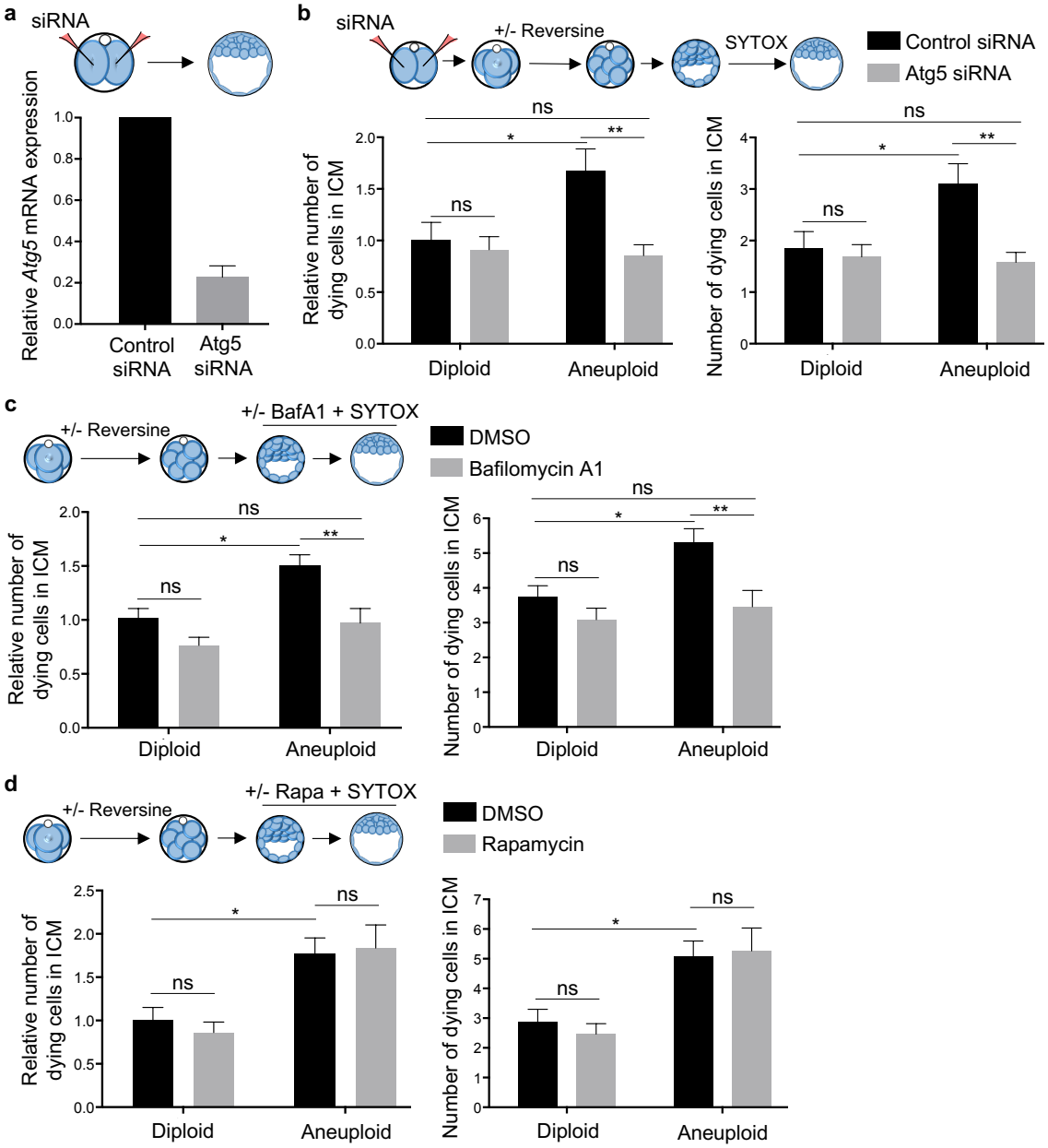

Figure 4.19. Elimination of aneuploid cells from the ICM of aneuploid embryos during blastocyst maturation via autophagy. (**a**) 2-cell stage embryos were injected with siRNA in both the blastomeres. *Atg5* mRNA expression was assessed by qRT-PCR at the late blastocyst stage (relative to control siRNA-injected embryos). Control siRNA n = 30 embryos, Atg5 siRNA n = 21 embryos. (**b**) 2-cell stage embryos were injected with Atg5 siRNA or control siRNA, treated at the 4-8 cell stage with reversine/DMSO, and imaged in the presence of SYTOX during blastocyst maturation (24 hours). Number of cells dying in ICM (SYTOX-positive) were assessed. They have been plotted relative to number of cells dying in ICM in controls (control siRNA-injected diploids) and independently. Diploid n = 20 embryos, aneuploid n = 21 embryos, diploid Atg5 siRNA n = 21 embryos, aneuploid Atg5 siRNA n = 27 embryos. Kruskal-Wallis test was used. (**c**) Diploid and aneuploid (reversine-treated) embryos were imaged in the presence of BafA1 or DMSO and SYTOX from during blastocyst maturation. Number of cells dying in ICM (SYTOX-positive) were assessed. They have been plotted relative to

number of cells dying in ICM in controls (DMSO-treated diploids) and independently. Diploid n = 26 embryos, aneuploid n = 24 embryos, diploid BafA1 n = 23 embryos, aneuploid BafA1 n = 24 embryos. Kruskal-Wallis test was used. (**d**) Diploid and aneuploid embryos were imaged in the presence of Rapamycin (Rapa) or DMSO and SYTOX from during blastocyst maturation. Number of cells dying in ICM (SYTOX-positive) were assessed. They have been plotted relative to number of cells dying in ICM in controls (DMSO-treated diploids) and independently. Diploid n = 15 embryos, aneuploid n = 12 embryos, diploid Rapa n = 15 embryos, aneuploid Rapa n = 15 embryos. One-way ANOVA test was used. For all the graphs, ns = not significantly different, *p < 0.05, **p < 0.01, and all data are mean ± s.e.m.

Next, to determine the role of p53 pathway in aneuploid embryos, p53 pathway was downregulated. To deplete p53, a combination of three p53 siRNAs were injected into both the blastomeres of 2-cell stage embryos which were then allowed to develop until the late blastocyst stage. The embryos were then analyzed by qRT-PCR. p53 siRNA injection reduced *p53* mRNA to 16% and p53 downstream target *cyclin G1* mRNA to 6.3% relative to embryos injected with control siRNA (Figure 4.20a). Then, to investigate the role of p53 pathway in the elimination of aneuploid cells from ICM in blastocysts, 2-cell stage embryos with injected with p53 siRNA, treated with reversine or DMSO at the 4-8 cell stage and imaged in the presence of SYTOX during blastocyst maturation. SYTOX-positive cells were quantified with time in ICMs for all four types of embryos: control siRNA or p53 siRNA injected aneuploid embryos and control siRNA or p53 siRNA injected diploid embryos. It was found that RNAi-mediated depletion of p53 significantly reduced the number of dying cells in the ICM of both diploid and aneuploid embryos (Figure 4.20b). Also, morphologically, while aneuploid embryos are smaller in diameter than diploid embryos and have thicker *zona pellucida* at the late blastocyst stage, p53 siRNA injected aneuploid embryos have similar diameter as diploids and have thinner *zona pellucida* than aneuploid embryos (Figure 4.20c). Overall, this indicated that p53 pathway eliminates aneuploid cells from the ICM during blastocyst maturation, but the elimination of cells by p53 pathway is not specific to the induction of chromosomal abnormality.

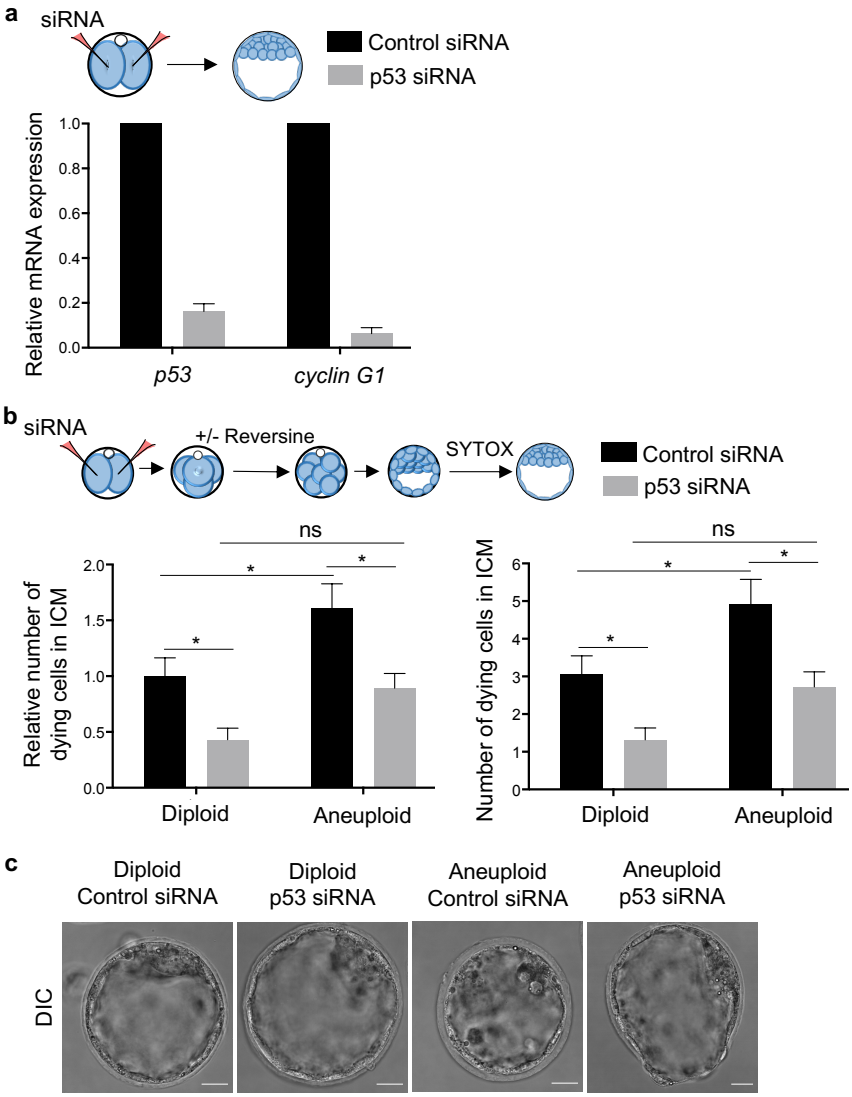

Figure 4.20. Elimination of aneuploid cells from the ICM of aneuploid embryos during blastocyst maturation via p53 pathway. (**a**) 2-cell stage embryos were injected with siRNA in both the blastomeres. *p53* and *cyclin G1* mRNA expression was assessed by qRT-PCR at the late blastocyst stage (relative to control siRNA-injected embryos). Control siRNA n = 20 embryos, p53 siRNA n = 23 embryos. (**b**) 2-cell stage embryos were injected with p53 siRNA or control siRNA, treated at the 4-8 cell stage with reversine/DMSO, and imaged in the presence of SYTOX during blastocyst maturation (24 hours). Number of cells dying in ICM (SYTOX-positive) were assessed. They have been plotted relative to number of cells dying in ICM in controls (control siRNA-injected diploids) and independently. Diploid n = 20 embryos, aneuploid n = 20 embryos, diploid p53 siRNA n = 19 embryos, aneuploid p53 siRNA n = 18 embryos. One-way ANOVA test was used, ns = not significantly different and *$p < 0.05$. For both the graphs, all data are mean ± s.e.m. (**c**) 2-cell stage embryos were injected with p53 siRNA or control siRNA, treated at the 4-8 cell stage with reversine/DMSO, and cultured until the late blastocyst stage. Diploid n = 10 embryos, aneuploid n = 10 embryos, diploid p53 siRNA n = 9 embryos, aneuploid p53 siRNA n = 8 embryos. Scale bars, 20 μm.

Since the above-mentioned results indicate that both p53 pathway and autophagy are required to eliminate aneuploid cells from the ICM during blastocyst maturation, next step was to determine the sequence of signaling between them. To determine whether p53 pathway is required to induce autophagy in aneuploid cells, 2-cell embryos were injected with p53 siRNA in both the blastomeres, then the embryos were treated with reversine or DMSO at the 4-8 cell stage and LC3B accumulation was characterised at the late blastocyst stage using immunostaining. It was found that depletion of p53 pathway reduced the number of LC3B puncta in the EPI of aneuploid embryos, but not diploid embryos (Figure 4.21a). Conversely, to determine whether autophagy is involved in p53 upregulation, 2-cell embryos were injected with Atg5 siRNA in both the blastomeres, then the embryos were treated with reversine at the 4-8 cell stage and mRNA level of *p53* gene was characterised at the late blastocyst stage using using qRT-PCR. It was found that autophagy depletion did not affect the mRNA levels of *p53* in aneuploid embryos (Figure 4.21b). These results indicate that the aneuploidy-induced accumulation of LC3B results from p53 activation and not the other way. Together, these findings suggest that chronic misfolded protein stress stimulates the p53 pathway, which in turn induces autophagy-mediated apoptosis of aneuploid cells in the embryonic lineage lineage of blastocyst-stage mouse embryos (Figure 4.21c).

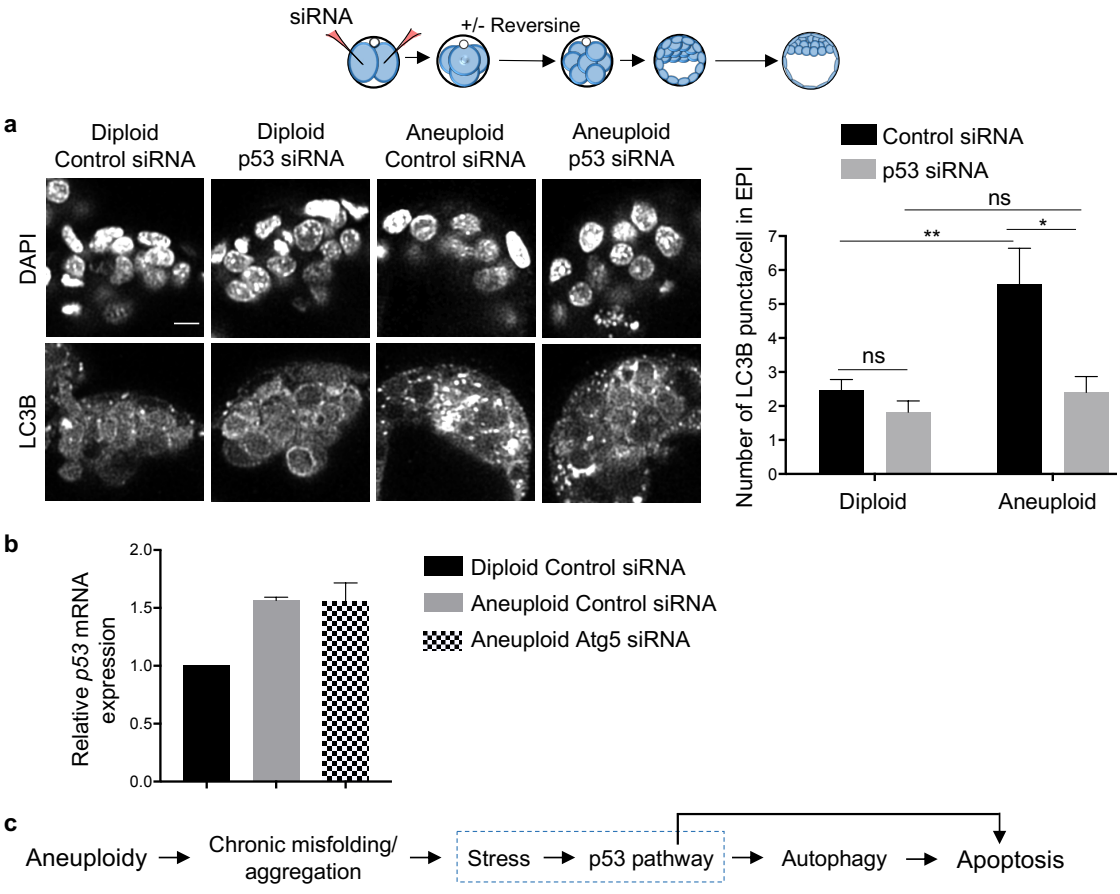

Figure 4.21. p53-autophagy cascade in aneuploid cells in the EPI of aneuploid pre-implantation embryos. (**a**) 2-cell stage embryos were injected with p53 siRNA or control siRNA, treated at the 4-8 cell stage with reversine or DMSO. The level of autophagy (LC3B levels) in the EPI was compared between the four types of embryos at the late blastocyst stage using immunostaining. Diploid n = 19 embryos, aneuploid n = 18 embryos, Diploid p53 siRNA n = 11 embryos, aneuploid p53-siRNA n = 12 embryos. Scale bar, 10 μm. One-way ANOVA test was used, ns = not significantly different, *p < 0.05 and **p < 0.01. (**b**) 2-cell stage embryos were injected with siRNA and treated at the 4-8 cell stage with reversine or DMSO. mRNA expression for *p53* gene was assessed by qRT-PCR at the late blastocyst stage (relative to control siRNA-injected diploids). Diploid n = 20 embryos, aneuploid n = 21 embryos, aneuploid Atg5 siRNA n = 28 embryos. For graphs (**a**) and (**b**), all data are mean ± s.e.m. (**c**) Schematic for the events downstream the induction of aneuploidy, leading to programmed cell death of the cell.

4.4 Autophagy-mediated elimination of aneuploid cells from the mouse aneuploid epiblast during peri-implantation development

Next step was to investigate whether elimination of aneuploid cells from ICM beyond blastocyst stage via apoptosis (as demonstrated in section 4.2.1) was triggered by the same molecular cascade as at the blastocyst stage. To this end, immunosurgery was performed on aneuploid (reversine-treated) and diploid (controls) embryos, ICMs were embedded in Matrigel and cultured in IVC1 medium. Autophagy was assessed using immunofluorescence on these ICMs 48 hours into the IVC1 culture (Figure 4.22). A significant increase in LC3B puncta in aneuploid ICMs compared to diploid ICMs was observed in the EPI lineage, suggesting upregulation of autophagy in aneuploid EPI during peri-implantation stage of development (Figure 4.22).

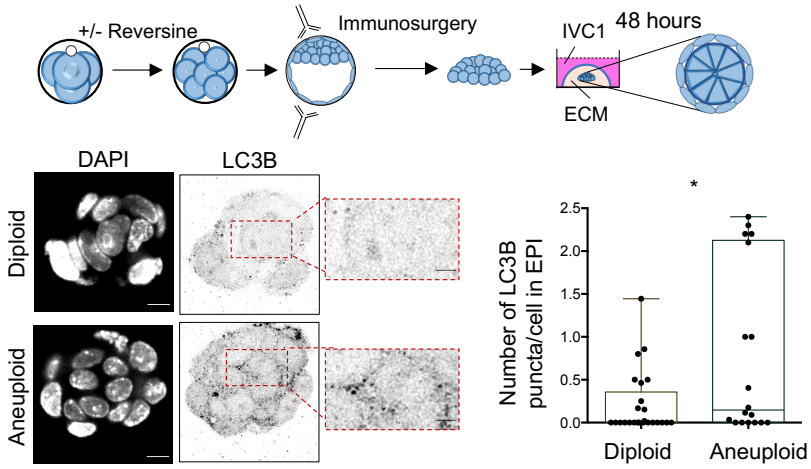

Figure 4.22. Upregulated autophagy in the aneuploid EPI during peri-implantation development *in vitro*. Control (diploid) and reversine-treated (aneuploid) embryos were embedded in Matrigel after immunosurgery at the late blastocyst stage and cultured in IVC1 medium. The level of autophagy in the EPI between diploid and aneuploid ICMs was compared 48 hours after immunosurgery, using LC3B

immunostaining. Scale bars, 7μm. Squares indicate the magnified regions, scale bars, 2μm. Data are shown as individual data points with Box and Whiskers graph (bottom: 25%; top: 75%; line: median; whiskers: min to max). Each dot represents average number of LC3B puncta/cell in an embryo. Mann-Whitney test was used and *$p < 0.05$. Diploid n = 26 embryos and aneuploid n = 22 embryos.

To investigate whether this upregulated autophagy plays a role in the early post-implantation elimination of aneuploid cells (as demonstrated in section 4.2.1), autophagy inhibitor BafA1 (Figure 4.16) was used. Aneuploid embryos were cultured in the presence of BafA1 from the early blastocyst to the late blastocyst stage, immunosurgery was performed, isolated ICMs were embedded in Matrigel and cultured in the presence of BafA1 in IVC1 medium for 72 hours (Figure 4.23a). BafA1-treated aneuploid ICMs developed into organized structures with characteristic post-implantation morphology, in which the PE surrounded the epithelial EPI (marked by Oct4) that formed a lumen in its center (lined by Podxl), similar to diploid and aneuploid ICMs (Figure 4.23b). It was found that the inhibition of autophagy almost doubled the efficiency of development of aneuploid ICMs into organized structures (Figure 4.23b-c). The inhibition of autophagy also led to an increase in the number of EPI cells in the organized aneuploid ICMs after 72-hour IVC1 culture (Figure 4.23d). Accordingly, the size of the EPI of diploid and autophagy-inhibited aneuploid structures was equivalent (Figure 4.23d). These results indicate that elevated autophagy is responsible for low post-implantation developmental efficiency of aneuploid embryos.

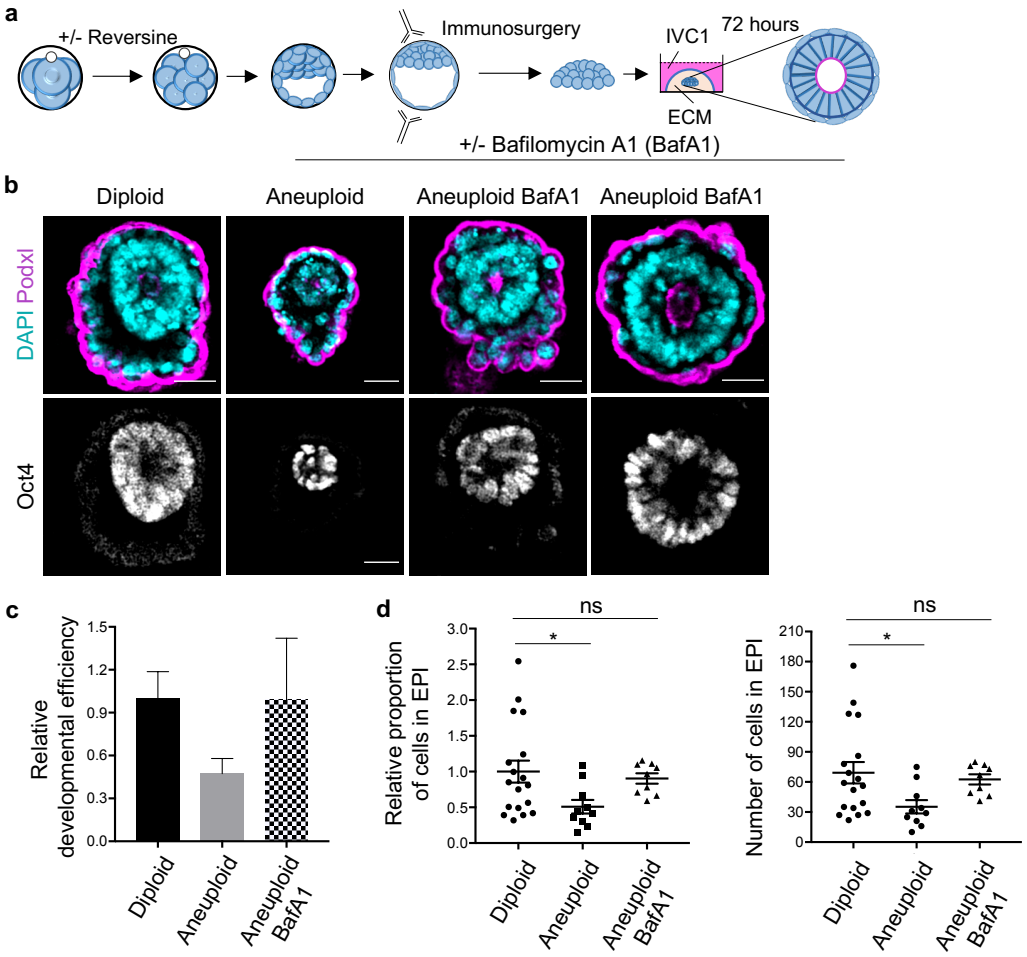

Figure 4.23. Elimination of aneuploid cells from the EPI of aneuploid embryos during peri-implantation stage of development via autophagy. (**a**) Schematic for the experimental design where diploid (control) and aneuploid (reversine-treated) embryos were cultured until the late blastocyst stage. Immunosurgery was performed to remove the outer TE layer and the ICMs were embedded in Matrigel. They were cultured in IVC1 medium for 72 hours in the presence of DMSO/BafA1. (**b**) Diploid and aneuploid ICMs were cultured according to schematic shown in (**a**) for 72 hours and immunostained for DAPI, Oct4 (to mark EPI) and Podxl (podocalyxin to mark the lumen). Scale bars, 30 μm. (**c**) Relative efficiency of ICMs (relative to diploids) to form an organised structure assessed according to (**b**) was evaluated for diploid, aneuploid and aneuploid BafA1 embryos. n = 3 experiments. Diploid n = 34 embryos, aneuploid n = 36 embryos and aneuploid BafA1 = 31 embryos. (**d**) Number of cells in the EPI (Oct4-positive) were analyzed for the organized structures obtained for diploid, aneuploid and aneuploid BafA1 embryos cultured according to schematic shown in (**a**). They have been plotted relative to EPI cell number in diploids and independently. One-way ANOVA test was used, ns = not significantly different and *$p < 0.05$. For (**b**) and (**d**), Diploid n = 18 embryos, aneuploid n = 10 embryos, Aneuploid BafA1 = 9 embryos. For graphs (**c**) and (**d**), all data are mean ± s.e.m. For (**b**), (**c**) and (**d**), the three conditions were run in parallel and the controls for diploid and aneuploid are the same as shown in Figure 4.6c-e.

Next step was to determine whether autophagy indeed led to elimination of aneuploid cells during peri-implantation and to check the ploidy status of the reversine-treated embryos that survive through the peri-implantation stage of development. To this end, DMSO- and reversine-treated embryos were cultured in the presence of BafA1 during blastocyst maturation, immunosurgery was performed, isolated ICMs were embedded in Matrigel and cultured in the presence of BafA1 in IVC1 medium and metaphase spreads were performed to examine their chromosomal integrity (Figure 4.24a). It was found that reversine-treated ICMs that survive through the peri-implantation stage of development exhibit similar ploidy status as controls, i.e., they were mostly diploid (Figure 4.24a). Importantly, reversine-treated embryos after autophagy inhibition displayed significantly higher aneuploidy (Figure 4.24a). Interestingly, while reversine-treated cells exhibited more hypoploidy than hyperploidy immediately after reversine treatment (Figure 4.2c), it was found that reversine-treated ICMs, controls as well as BafA1-treated, that survived through the peri-implantation stage of development exhibited more hyperploidy than hypoploidy (Figure 4.24b). This finding is consistent with the observation that full monosomic mouse embryos die before implantation, while most full trisomic embryos die post-implantation (Epstein *et al*., 1985).

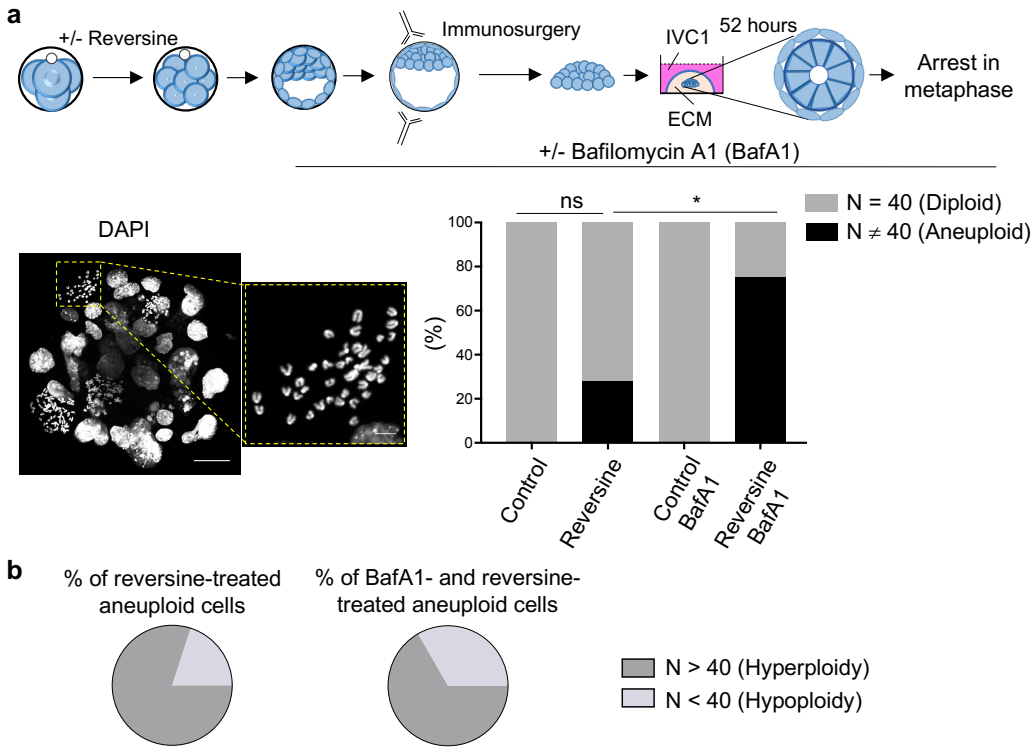

Figure 4.24. Ploidy assessment of the early post-implantation aneuploid ICMs after autophagy inhibition using metaphase spreads. (**a**) Control (diploid) and reversine-treated (aneuploid) embryos were cultured in DMSO or autophagy inhibitor BafA1 during blastocyst maturation. Immunosurgery was performed to get rid of the TE layer at the late blastocyst stage and the ICMs were embedded in Matrigel and cultured in IVC1 medium in the presence of DMSO/BafA1. They were arrested in metaphase, 52

hours into the IVC1 culture. A representative image of chromosome spread for a reversine-treated BafA1 ICM is shown. Scale bar, 30 μm. Square indicates the magnified region (individual blastomere), scale bar, 5 μm. Number of chromosomes per cell (N) were counted for the embryos cultured. Diploid n = 10 cells, aneuploid n = 18 cells, diploid BafA1 n = 10 cells, aneuploid BafA1 n = 8 cells. Fisher's exact test was used, ns = not significantly different and *p < 0.05. (**b**) Distributions of reversine-treated cells and reversine-treated BafA1 cells that were categorised aneuploid in (**a**) according to the number of chromosomes per cell (N).

Overall, the results in this section revealed that elevated autophagy eliminates aneuploid cells from the early blastocyst to the early post-implantation stage of development from the EPI.

4.5 Mouse embryonic stem cell-based model for chromosome mosaicism

Because mouse embryonic stem cells (mESCs) are derived from, and transcriptionally equivalent to, EPI cells (Evans and Kaufman, 1981; Martin, 1981; Boroviak *et al*., 2014), a mESC-based model for mosaicism was generated. Since mESC lines are more amenable to genetic manipulations and biochemical assays than embryos, this *in vitro* model can help study the behavior of aneuploid cells on a deeper molecular and biochemical level. To this end, mESCs were treated with 0.5 μM reversine or with an equivalent concentration of DMSO (controls) during for 16 hours. The increased induction of aneuploidy in reversine-treated mESCs compared to controls (DMSO-treated mESCs) was confirmed by metaphase spreads (Figure 4.25). For simplicity reversine-treated mESCs will be referred to as aneuploid and controls as diploid throughout this section.

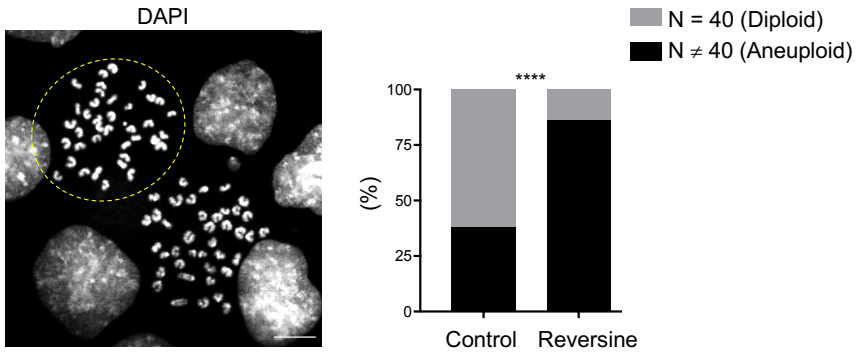

Figure 4.25. Reversine treatment induces aneuploidy in mESCs. A representative image of chromosome spread for reversine-treated mESCs is shown. Scale bar, 10μm. A yellow line marks an aneuploid cell since the number of chromosomes counts to 38. Number of chromosomes per cell (N) were counted. Control n = 92 cells, reversine-treated n = 28 cells. Fisher's exact test was used and ****p < 0.0001.

To generate a mESC-based model for diploid-aneuploid mosaicism, aneuploid (reversine-treated) mESCs were mixed with diploid (control) mESCs in one-to-one ratio (Figure 4.26a). They were then cultured together in a mixture in medium supplemented with 2i and LIF on gelatin-coated plates (Materials and Methods). This medium supports the ground state pluripotency of mESCs, similar to the pre-implantation EPI (Ying *et al*., 2008). To be able to distinguish control and aneuploid clones in the mixture, the aneuploid mESCs expressed green membrane plus red nuclear fluorescence marker (CAG-GFP plus Cherry Histone), while diploid mESCs expressed green nuclear fluorescence marker (Histone H2B-GFP) (Figure 4.26a). As a diploid-diploid control for this experiment, diploid mESCs expressing CAG-GFP plus Cherry Histone and diploid mESCs expressing Histone H2B-GFP were also similarly co-cultured in one-to-one ratio (Figure 4.26a). After four days, various compound structures had assembled in the plates (Figure 4.26b). The composition of these structures was individually characterized, i.e. the distribution of CAG-GFP plus Cherry Histone cells and Histone H2B-GFP cells for both diploid-diploid and diploid-aneuploid co-cultures. On average, the diploid(green)-diploid(red+green) structures contained 49.7% red+green cells (Figure 4.26b). When the same clone of cells was aneuploid, as in the diploid(green)-aneuploid(red+green) structures, the contribution of red+green cells decreased to 41.8%, on average (Figure 4.26b). The frequency distribution of the composition of these organized structures, i.e. what % of structures carried a particular % of red+green cells, was then characterized for both diploid-diploid and diploid-aneuploid co-cultures. 51.7% of diploid(green)-aneuploid(red+green) structures completely lacked red+green aneuploid cells (Figure 4.26c). In contrast, 37.9% of the diploid-diploid structures showed complete loss of red+green cells (Figure 4.26c). These results indicate that although not significant but there is preferential elimination of aneuploid mESCs when cultured with diploid mESCs. There was some evidence of apoptosis in aneuploid cells in diploid-aneuploid co-cultures as investigated by cleaved caspase-3 immunostaining, indicating that apoptosis might be involved in eliminating aneuploid cells in this case (Figure 4.26d).

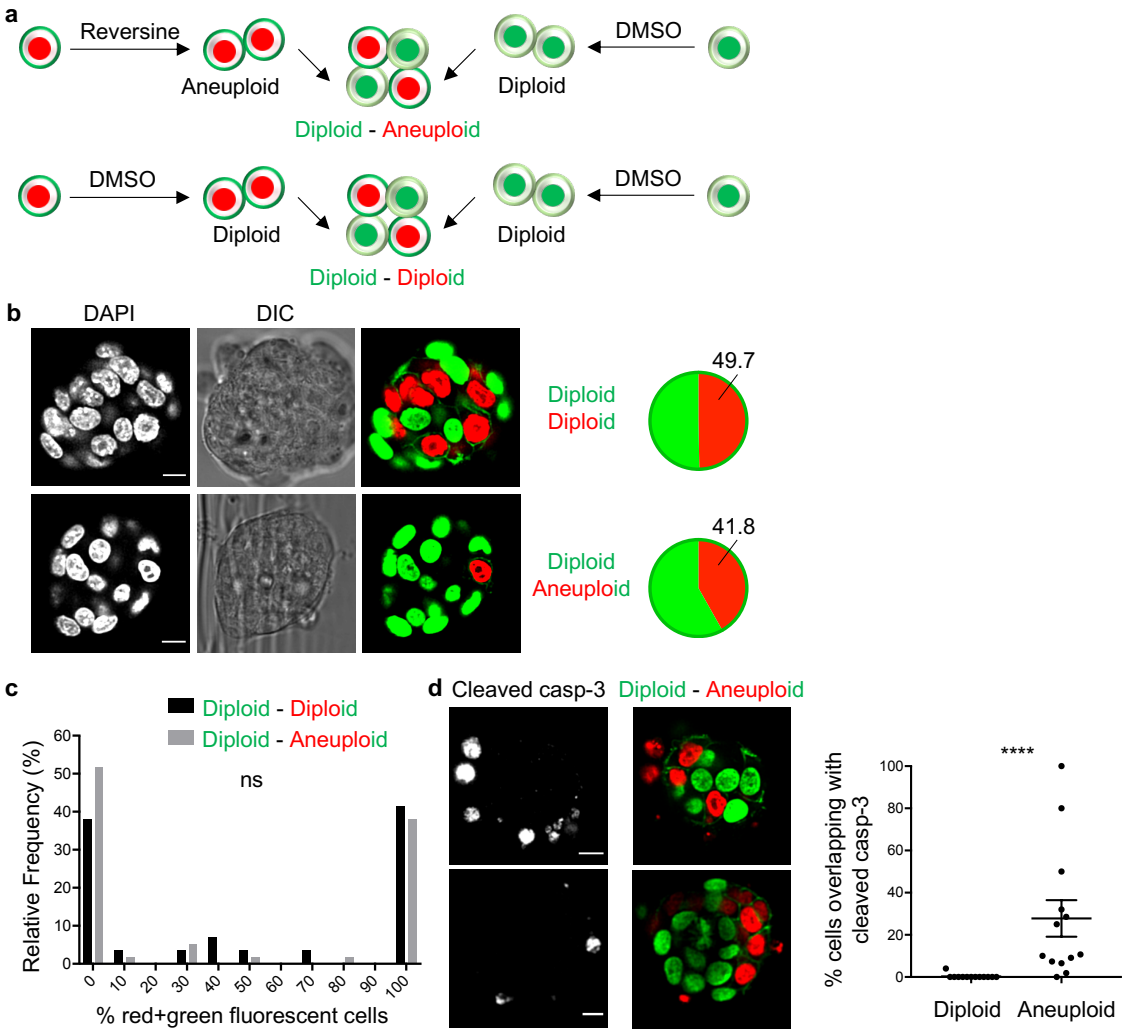

Figure 4.26. Preferential elimination of aneuploid cells in the aneuploid-diploid mouse embryonic stem cells co-culture. (**a**) Schematic for the experimental design where aneuploid (reversine-treated) and diploid (controls) mouse embryonic stem cells were co-cultured in 1:1 ratio to mimic aneuploid-diploid scenario. CAG-GFP plus Cherry Histone (red+green fluorescent) mESCs were used to generate aneuploid cells and Histone H2B-GFP mESCs were used to generate diploid cells. Both types of cells were also co-cultured in 1:1 ratio as diploids to mimic diploid-diploid scenario. (**b**) After 96-hours, the co-cultures were assessed. The composition of the structures obtained, i.e., the average distribution of green and red+green cells was evaluated. In the examples shown, the diploid-diploid structure contained both green and red+green mESCs. In contrast, most of the diploid-aneuploid structure originated from the green diploid mESCs. Scale bars, 10 μm. (**c**) Frequency distribution of red+green mESCs within the structures of diploid(green)-diploid(red+green) and of diploid(green)-aneuploid(red+green) co-cultures. Kolmogorov-Smirnov test was used to compare the frequency distributions for two types of co-cultures and ns = not significantly different. (**d**) Diploid(green)-diploid(red+green) structures obtained after 96-hour co-culture were immunostained for cleaved caspase-3 (to label apoptosis). Scale bars, 10 μm. Diploid-aneuploid n = 13 mESC clumps. Mann-Whitney test was used and ****$p < 0.0001$. Data are mean ± s.e.m. For (**b**) and (**c**), diploid-diploid n = 29 mESC clumps and diploid-aneuploid n = 58 mESC clumps.

5 Discussion I

Bolton *et al.* (2016) recently established that aneuploid mouse embryos and aneuploid cells within diploid-aneuploid mosaic mouse embryos get eliminated by post-implantation stage of development. They also showed that aneuploid cells begin to disappear from the ICM lineage of the diploid-aneuploid mosaic embryos during blastocyst maturation via apoptosis. In Chapter 4, two major questions have been addressed: first, the fate of aneuploid embryos and the fate of aneuploid and diploid cells within diploid-aneuploid mosaic mouse embryos at the peri- and early post-implantation stages of development, and second, the molecular mechanisms that dictate the fate of aneuploid cells during pre- to post-implantation stages of development.

5.1 Merits and limitations of the mouse model for chromosome mosaicism

In order to investigate the above-mentioned questions, mouse model of chromosome mosaicism, as described in Bolton *et al.* (2016), was used. This model uses the drug reversine to induce aneuploidy in mouse embryos during 4- to 8-cell division by inhibiting the key SAC protein Mps1 kinase. Compared to other mouse models of aneuploidy (as described in section 3.3.1), use of Bolton *et al.* (2016) model offers following advantages:

(i) Bolton *et al.* (2016) showed that the effect of reversine on SAC inhibition was immediate and reversible, i.e., SAC function was restored in mouse embryos once reversine was washed out from the culture medium. This enabled the induction of chromosomal errors in mouse embryos during a specific developmental-window, making this model representative of human embryos in which cleavage-stage embryos are highly prone to errors in mitosis (as discussed in section 3.2.1).

(ii) Bolton *et al.* (2016) showed that reversine treatment resulted in chromosome segregation errors, such as lagging chromosomes and the formation of micronuclei, making this model representative of human embryos in which anaphase lagging is speculated to be the main cause of pre-implantation mosaicism (Coonen *et al*., 2004; Daphnis *et al*., 2005; Capalbo *et al*., 2013).

(iii) Bolton *et al.* (2016) showed that reversine treatment resulted in complex mosaic aneuploidy, making this model representative of human embryos (Coonen *et al*., 2004; Daphnis *et al*., 2005; Fragouli *et al.,* 2011; Popovic *et al*., 2018).

However, use of this model also raises following concerns:

(i) Any phenotype revealed in the studies in Chapter 4 could be a consequence of non-specific off-target effects of the drug reversine, independent of chromosome segregation errors or aneuploidy. For instance, Chen *et al.* (2004) showed that prolonged incubation of

lineage-committed myogenic cells in 5 μM reversine led to their dedifferentiation into multipotent progenitor cells and Santaguida *et al.* (2010) showed that reversine can inhibit Aurora B kinase at concentrations higher than 10 μM. In order to circumvent the indirect effects of reversine, it was used at the lowest effective concentration (0.5 μM; as indicated by Santaguida *et al.* (2010) for Mps1 inhibition) and only during short duration of 4- to 8-cell mitotic division. While the above-mentioned concern does not invalidate the findings in Chapter 4, it means that efforts should be made to continue to develop new mouse models of chromosome mosaicism. To this end, attempts were made to induce aneuploidy in early mouse embryos by downregulating Tacc3 and Trf1, individually. Tacc3, a member of the transforming acidic coiled coil family of centrosomal proteins (Burgess *et al*., 2015) and Trf1, telomeric repeat binding factor 1 (Ohishi *et al*., 2014), both have been shown to contribute to proper chromosome segregation. Using cellular systems, these studies show that loss of function mutation in Tacc3 and Terf1 depletion, both lead to aneuploidy induction. Their respective siRNAs were injected at the zygote stage and the chromosome status of injected embryos was characterised by performing metaphase spreads at the 4- to 8-cell division. However, knockdown of both Trf1 and Tacc3 failed to induce aneuploidy in mouse embryos at this stage, despite the high knockdown efficiency of respective siRNAs (data not shown).

(ii) Another problem is that reversine treatment does not induce aneuploidy in 100% of the treated cells and it was not possible to determine which treated cells became aneuploid. This was due to the absence of a live marker for ploidy status of each chromosome in a cell. To this end, attempts were made to label the centromeres in live mouse embryos but were unsuccessful due to the limitations of the imaging technology (Figure 4.1). However, since both metaphase spreads (Figure 4.2) and whole-genome sequencing (Bolton *et al*., 2016) revealed that reversine-treated cells display significantly higher rates of aneuploidy than controls, a comparative approach was adopted for analysis throughout in Chapter 4. It was thus assumed that any significant difference detected between the groups (reversine-treated and controls) could be attributed to true difference between aneuploid and diploid embryos.

(iii) Overall aim of the findings in Chapter 4, obtained using this model, is to expand our understanding of the mechanisms behind subfertility, developmental defects and miscarriages during human pregnancy due to aneuploidy. However, all results using this model need to be interpreted keeping in mind the differences between human and mouse model systems (as described in section 3.1). Overall, mouse offers a valuable model to gain insights into mechanisms used by mammalian systems during development as it overcomes many of the logistical ethical and financial challenges of working with human or larger mammalian species and has several similarities to early human embryo development (as described in section 3.1).

5.2 The peri- and post-implantation fate of aneuploid cells in the mouse epiblast

Bolton *et al*. (2016) showed that on average upto 44% aneuploid cells were preferentially eliminated from the diploid-aneuploid ICM by the late blastocyst stage. In Chapter 4, it was revealed that aneuploid cells continue to undergo preferential elimination from the diploid-aneuploid EPI during peri-implantation and early post-implantation stages of development.

In order to *in vitro* culture embryos continuously from pre- to early post-implantation, several protocols were attempted. Bedzhov *et al*. (2014b) established two *in vitro* culture systems that allowed the conceptuses to develop throughout the implantation stages into egg cylinders *in vitro*. In the first method (5 day long), embryos were recovered at E3.5, zona was removed, and embryos were cultured in IVC1 medium, followed by IVC2 medium (same composition as IVC1 where FBS was replaced with 30% KnockOut serum replacement). In the second method (3 day long), zona-free embryos were recovered at E4.5, mural TE was removed and embryos were cultured in IVC1 medium, followed by IVC2 medium. Conceptuses cultured in both these systems grew to the same size as those developing *in vivo*, displayed the correct morphology and spatial expression of distinct lineage markers. When both of these protocols were employed to *in vitro* culture diploid-diploid and diploid-aneuploid chimeras beyond the blastocyst stage, they showed extremely low post-implantation developmental efficiency (data not shown). Attempts were made to further optimise the protocol using different FBS concentrations and surface coatings with laminin or collagen or fibronectin, but all of them showed low efficiency through peri-implantation development (data not shown). Thus, a novel simplified model to permit EPI rosette transformation during the implantation period was established. In this model, the extra-embryonic TE was removed by immunosurgery and ICM was allowed to develop into post-implantation EPI and PE, enclosing a lumen. However, there is still a pressing need to further optimise or develop a protocol that would allow a more complete investigation of all lineages during peri-implantation and early post-implantation stages. Bolton *et al*., (2016) showed that while aneuploid cells in the fetal lineage are eliminated by apoptosis, those in TE undergo cell cycle arrest. It will be important to investigate if similarly, the fate of aneuploid cells depends on lineage beyond blastocyst stage.

Bolton *et al*. (2016) showed that on average 56% aneuploid cells were remaining in ICM by the end of pre-implantation stage. Using the above-mentioned simplified *in vitro* system, it was revealed that on average 30.3% reversine-treated cells were left in the diploid-aneuploid EPI by early post-implantation stage (Figure 4.8b). Also, diploid-aneuploid chimeras were transferred to pseudo-pregnant mother, recovered 12 hours after implantation and *in vitro* cultured for 36 hours. After 36 hours culture, there were on average 19.67% reversine-treated cells left in the diploid-aneuploid EPI by early post-implantation stage (Figure 4.11c). This

suggested that there is a progressive depletion of aneuploid cells from the EPI beyond blastocyst stage. However, in order to directly demonstrate this finding, aneuploid cells in the chimeras need to be followed uninterrupted in real-time from the early blastocyst to post-implantation stage of development. Also, in order to directly compare the findings from Bolton *et al*. (2016), it will be important to use same combination of genetic backgrounds of the transgenic mice for control and reversine-treated cells as in the paper. However, when all the diploid-aneuploid mosaic chimeras were analysed together, irrespective of the genetic background, it was found using the above-mentioned simplified *in vitro* system that on average 23% reversine-treated cells were left in the EPI by early post-implantation stage (Figure 4.9e). It is possible that the reversine-treated cells left in the diploid-aneuploid EPI by the early post-implantation stage contain well-tolerated aneuploidies or are diploid since not all cells become aneuploid after reversine treatment (Figure 4.2). As distinct aneuploidies show different levels of proliferative disadvantage (Greco *et al*., 2015; Pfau *et al*., 2016), this could account for the variation seen in the timing and extent of the elimination of aneuploid cells.

Live-imaging was adopted to determine the fate of aneuploid cells in real-time during peri-implantation and early post-implantation stages of development of both aneuploid embryos and 1:1 diploid-aneuploid mosaics. It was revealed using transgenic H2B-GFP mouse line that aneuploid cells undergo preferential depletion from the EPI via apoptosis during these stages (Figure 4.7a, 4.12). It would be difficult to carry out similar experiment in humans since there is no live marker for aneuploidy and embryos would also have to be labelled for cell tracking. Bolton *et al*. (2016) found no evidence of increased apoptosis or cellular remnants in the early post-implantation diploid-reversine chimeras. In this study, diploid-reversine chimeras were directly analysed at E7.5 by TdT-mediated dUTP nick end labelling (TUNEL) staining. It is possible that apoptosis might have been missed here since apoptotic debris could already have been removed by neighbouring diploid cells as seen during *in vitro culture* here (Figure 4.12). These findings are consistent with the observations in other chromosome missegregation mouse models: aneuploid embryos from Sycp3-/- females displayed increased apoptosis at E7.0 (Lightfoot *et al*., 2006), Mad2-/- embryos displayed apoptosis at E6.5-7.5 (Dobles *et al*., 2000) and Cenpa-/- lacked a defined ICM at E6.5 (Howman *et al.*, 2000). Lower post-implantation developmental efficiency of aneuploid embryos result (Figure 4.6d) is also consistent with homozygous knockout embryos for several mitotic checkpoint genes or for kinetochore components that show increased chromosome missegregation (Kalistis *et al*., 1998; Dobles *et al*., 2000; Howman *et al*., 2000; Kalistis *et al*., 2000; Putkey *et al*., 2002; Wang *et al*., 2004b). Also, Sancho *et al.* (2013) showed that majority of tetraploid cells were eliminated by apoptosis at E6.5 from chimeras generated using tetraploid ESCs.

5.3 Post-implantation survival of diploid-aneuploid mosaic embryos

Bolton *et al*., (2016) showed that aneuploid embryos underwent complete post-implantation lethality while 1:1 diploid-aneuploid mosaic embryos displayed equivalent post-implantation developmental potential as controls. Similar result was obtained using the above-mentioned simplified *in vitro* system where aneuploid embryos displayed lower post-implantation developmental efficiency compared to controls (Figure 4.6d), while 1:1 diploid-aneuploid chimeras displayed equivalent post-implantation developmental potential as controls (Figure 4.8c). Also, in both set of results (Figure 4.8b and Bolton *et al.*, 2016), post-implantation 1:1 diploid-aneuploid chimeras contained mostly diploid cells in the EPI. This implied that mosaic embryos have the potential to develop into viable diploid pregnancy in the presence of diploid blastomeres. These findings are consistent with the recent papers on the transfer of some mosaic human embryos where diploid-aneuploid mosaics resulted in viable euploid births (Greco *et al*., 2015; Fragouli *et al*., 2017b; Spinella *et al*., 2018; Rubino *et al*., 2018). All of these studies and many others (Li *et al*., 2005; Barbash-Hazan *et al*., 2009, Mantikou *et al*., 2012) talk about the hypothesis for a threshold proportion of diploid to aneuploid cells above which human mosaic embryos can result in viable births, as was also discussed in Bolton *et al*., (2016). It is of worth noting that the critical cell number threshold required for viability could be different in human embryos from that in mouse embryos in light of other developmental differences between them – human embryos implant at day 7 with ~256 cells in the blastocyst while mouse embryos implant at day 4.5 with 164 cells in the blastocyst (Niakan *et al.*, 2012). Besides, reversine treatment can induce very chaotic abnormalities which are not necessarily compatible with the occurrences in human embryos. Therefore, it is important to check if a model with a single specific aneuploidy in diploid-aneuploid mosaic form will produce similar results. Also, clinical outcomes from the transfers described in Greco *et al*. (2015) and Fragouli *et al*. (2017b) indicate that besides the extent of mosaicism, type of aneuploidy affects the IVF success rate as well. Thus, a better understanding of the combined impact of the extent of mosaicism and a specific risk of specific chromosomal abnormality is required to more confidently consider diploid-aneuploid mosaics for uterine transfers in IVF clinics.

Given the highly regulative nature of the mammalian embryo, the above-mentioned finding related to the full developmental potential of diploid-aneuploid mosaics is not unlikely. Using the simplified peri-implantation *in vitro* culture system, the results in Chapter 4 indicate that early diploid-aneuploid mosaic mouse embryos employ two regulative measures to ensure their post-implantation development into healthy diploid embryos (Figure 5.1a): progressive ‘clonal depletion’ of aneuploid cells from the EPI during pre- to post-implantation stages of development via apoptosis (Figures 4.8, 4.9, 4.12a) and over-proliferation of diploid cells in the EPI during peri-implantation stage of development (Figure 4.13g). By early post-

implantation stage, it was found that diploid-aneuploid mosaics had a similar EPI size (total cell number) to diploids (Figure 4.13a-b) despite the depletion of aneuploid cells. In Morris *et al.* (2012a), the number of EPI cells within the blastocyst was correlated with the success of development of embryo to birth. This study determined that a critical minimum of four EPI cells were required for successful post-implantation development. This explains the significance of the presence of diploid cells in ensuring successful post-implantation development of diploid-aneuploid mosaics because it boosts the EPI cell number. Thus, higher the presence of diploid cells in diploid-aneuploid mosaics, higher is their developmental potential as seen in Bolton *et al.* (2016) where 1:1 diploid-aneuploid mosaics had higher post-implantation developmental efficiency than 1:3 diploid-aneuploid mosaics. As the development progresses beyond the blastocyst stage, diploid cells compensate for the loss of aneuploid cells and in this way can regulate the EPI size. It is important to first determine if the over-proliferation of diploid EPI cells in diploid-aneuploid mosaics is dependent on the elimination of aneuploid EPI cells. To this end, it will need to be investigated if diploid EPI cells over-proliferate when diploid-aneuploid mosaics are treated with ZVAD (i.e., apoptosis is inhibited) during peri-implantation stages of development. The over-proliferation of diploid cells in the diploid-aneuploid mosaics during peri-implantation stage of development can be due to two possible reasons. Firstly, the aneuploid EPI cells could be undergoing non-cell autonomous depletion in the diploid-aneuploid mosaics due to cell competition (Kale *et al.*, 2015). This competition in turn could lead to the over-proliferation of 'winner' cells, i.e., diploid EPI cells here (Kucinski *et al.*, 2017). Recently it was shown that tetraploid ESCs undergo apoptotic elimination from mouse ESC-embryo chimeras via mTOR, when surrounded by diploid cells (Bowling *et al.*, 2018). However, tetraploidy and single-chromosome aneuploidy could exhibit different physiological response in a cell since tetraploidy quadruples the whole set of chromosomes, while single-chromosome changes a part of the chromosome set. Thus, tetraploidy will not affect the relative stoichiometry of proteins unlike as expected in the case of single-chromosome aneuploidy, and therefore similar mechanisms of competition-induced elimination might not apply to aneuploidy in the mode that is presented in this thesis. Second possible explanation is that the over-proliferation of diploid EPI cells could be due to the decreased size of the epiblast rather than because they are surrounded by the depleting aneuploid EPI cells, to serve the purpose of regulating the overall EPI size. This observation is in accord with studies showing that half-size embryos, made by separating blastomeres at the 2-cell stage, can undergo compensatory proliferation to increase their size (Rands, 1986).

Since this plasticity is fundamental to successful embryo development, it will be beneficial to investigate the mechanisms employed by diploid cells for size regulation of diploid-aneuploid mosaics. On a cellular level, it will be interesting to track the behavior of diploid cells lying

adjacent to aneuploid cells in mosaics during peri-implantation stages of development. It will help determine if the diploid cells alter their cell cycle lengths to undertake compensatory cell divisions and whether this depends on their position in relation to dying aneuploid cells. On a molecular level, it will be interesting to investigate the involvement of JAK/STAT pathway (Clemente-Ruiz *et al.*, 2016; Kucinski *et al*., 2017) or the coordination between Hippo and mTOR pathways (Tumaneng *et al.*, 2012) in mediating size regulation, as has been demonstrated in *Drosophila*.

Lastly, the above-mentioned result finds clinical significance explaining why blastocyst biopsy can be less detrimental to IVF success rates than cleavage-stage biopsy (Griffin and Ogur, 2018). Firstly, a greater number of cells can be biopsied at the blastocyst stage compared to at the cleavage-stage without affecting embryo viability. Secondly, removal of some cells during cleavage-stage biopsy could significantly alter the overall embryo mosaicism. If more diploid cells are removed compared to aneuploid, it could significantly affect the ability of the remaining embryo to undergo required EPI size regulation and overall development beyond the blastocyst stage. On the other hand, removal of some TE cells during blastocyst biopsy does not alter the EPI cell number. However, it is still unclear as to what extent TE biopsy reflects the overall chromosome constitution of the embryonic lineage. This emphasises the need for non-invasive procedures that can investigate the chromosome constitution of the entire embryo without altering the embryo constitution, as during biopsy.

5.4 Investigating p53-autophagy cascade in aneuploid cells in the epiblast lineage

Next, sections 4.3 and 4.4 explored the molecular mechanisms that describe how aneuploid cells become depleted from the EPI during pre- to post-implantation stages of development. Throughout these sections, the development of aneuploid (whole reversine-treated) and diploid embryos was compared, and it was revealed that p53-induced autophagy is required to eliminate aneuploid cells from the EPI. It will also be interesting to investigate whether aneuploid cells employ similar mechanisms in diploid-aneuploid mosaics.

Aneuploidies of differing chromosomes have been reported to show global and uniform cellular responses including the repression of growth-related genes, the upregulation of energy metabolism and an increased sensitivity to conditions interfering with protein folding (Gasch *et al*., 2000; Torres *et al*., 2007; Tang *et al*., 2011; Sheltzer *et al*., 2012; Stingele *et al*., 2012; Dürrbaum *et al*., 2014). Interestingly, findings from Bonney *et al.* (2015) indicate that aneuploidy-associated phenotypic consequences are caused by copy number changes of a large number of genes not harmful when altered individually. In Chapter 4, using reversine to induce aneuploidy in mouse embryos, the common global effect of aneuploidy on early mouse

embryo development has been determined. Studies in diverse organisms indicate that overall gene transcription and translation levels correlate with gene copy number in aneuploid cells (as described in detail in section 3.4) (Torres *et al*., 2007; Pavelka *et al*., 2010; Stingele *et al*., 2012; Liu *et al*., 2017). Majority of these proteins are components of macromolecular complexes (Stingele *et al*., 2012; Dephoure *et al*., 2014). Aneuploidy perturbs the normal stoichiometry of protein complex subunits, leading to intracellular proteomic imbalance (Dephoure *et al*., 2014; Oromendia and Amon, 2014). Papp *et al.* (2000) demonstrated using yeast that both underexpression and overexpression of protein complex components negatively affects fitness. Thus, it was hypothesized that in reversine-treated mouse embryos, chromosome alterations could lead to transcriptional imbalance that could result in proteomic imbalance and accumulation of misfolded proteins, which could eventually lead to cell death (Figure 5.1b). It was seen that reversine treatment resulted in accumulation of misfolded proteins in early mouse embryos from the 8-cell stage through to the late blastocyst stage (Figure 4.15). This is consistent with the findings in other systems where aneuploidy impairs protein folding (Oromendia *et al*., 2012; Donnelly *et al*., 2014; Aivazidis *et al*., 2017).

As a response to this chronic protein misfolding, the involvement of protein quality control mechanism, autophagy was examined in reversine-treated aneuploid embryos. Aneuploid embryos showed a significant upregulation of autophagy in the EPI at pre- (Figure 4.17) and peri-implantation (Figure 4.22) stages of development. This is consistent with the findings in other systems where aneuploidy upregulates autophagy (Stingele *et al*., 2012; Ohashi *et al*., 2015). It has been shown in human cells that a persistent aneuploid karyotype is required to promote autophagy, same as the case here after reversine treatment (Santaguida *et al*., 2015). Santaguida *et al.* (2015) showed that autophagosomes were not effectively cleared in aneuploid cells, most likely due to lysosomal overload. However, in reversine-treated aneuploid embryos here, there was an increase in the LC3B levels in the EPI after treatment with the lysosomal inhibitor BafA1 (Figure 4.17d), indicating full autophagic flux (Klionsky *et al*., 2016). Furthermore, to check if the entire autophagy flux was involved in the elimination of aneuploid cells, autophagy was inhibited at two different stages: early (autophagosome formation using Atg5 siRNA) and later (lysosome fusion using BafA1). Both treatments attenuated cell death in the ICM of aneuploid embryos from the early to the late blastocyst stages suggesting that the entire autophagic flux is involved (Figure 4.19b-c). In order to further ensure autophagy is not defective in aneuploid cells in the EPI, the Premo™ Autophagy Tandem Sensor RFP-GFP-LC3B Kit (Thermo Fisher Scientific) should be used since it helps monitor different stages of autophagy (as described in Figure 4.16) in real-time. This assay is based on different pH sensitivity of GFP (acid-sensitive) and RFP (acid-insensitive) fluorescent proteins. So, the progression from neutral autophagosome to acidic autolysosome

can be monitored by the loss of GFP fluorescence while RFP stays. It will also be interesting to combine the Premo™ Autophagy Tandem Sensor RFP-GFP-LC3B Kit with SYTOX/nuclear labelling to strengthen above-mentioned findings on the sequence of events by simultaneously imaging apoptosis and autophagy. Inhibition of autophagy did not affect the level of cell death in the EPI of control embryos, consistent with the studies showing that autophagy is not involved in apoptosis during embryo development (Qu *et al.*, 2007; Aburto *et al.*, 2012).

As shown in the model in Figure 5.1b, it was hypothesized that chromosome alterations transcribe into corresponding changes in RNA expression that could then translate into corresponding changes in protein expression, resulting in the accumulation of misfolded proteins and upregulation of protein-degradation pathways like autophagy in early mouse embryo EPI cells, which could eventually lead to their programmed cell death (Figure 5.1b). For future studies, it will be important to check if indeed reversine-induced changes in the DNA copy number transcribe into corresponding changes in RNA expression using mRNA sequencing and if this then translates into corresponding changes in protein expression using quantitave mass spectometry (Gao *et al*., 2017), in the early mouse embryos. The above-mentioned experiments should be done for both specific monosomies and trisomies, that can be obtained using Robertsonian mice (Epstein *et al*., 1985). It will then be important to see in which of these specific aneuploidies, indeed there is an increase in autophagy and whether it leads to the survival or apoptotic cell death of the aneuploid EPI cell after several mitotic divisions. This will help in investigating what is the threshold level of autophagy beyond which it becomes lethal, as hypothesized in the model. It will then be interesting to see if upregulation of autophagy beyond this threshold is sufficient to induce early apoptosis in reversine-treated aneuploid cells, i.e. before the blastocyst maturation, or induce apoptosis of otherwise tolerant aneuploidies. To this end, autophagy can be increased using rapamycin treatment (Klionsky *et al*., 2016) and then the survival of aneuploid cells can be monitored in real-time, using caspase sensor (Bardet *et al*., 2008). In addition to the above, it will be important to check if proteasome machinery is compromised in the reversine-treated EPI of the early mouse embryos, as described in other studies done using aneuploid cellular models (Oromendia *et al*., 2012; Aivazidis *et al*., 2017). To this end, control and reversine-treated blastocysts can be treated with the proteasome inhibitor MG132 (Gleixner *et al*., 2016) and analysed for the further development of the EPI, i.e., developmental efficiency and the EPI size. If indeed proteasome machinery is compromised in the reversine-treated EPI, MG132 treatment will not lead to any significant change in their development, unlike as it should in the controls (Saito *et al.*, 2014). Consequently, it will be important to check if indeed compromising proteasome machinery leads to the upregulation of autophagy in the mouse EPI. To this end, control blastocysts can be treated with MG132 to elicit proteotoxic stress and analysed for the change

in LC3B puncta levels in the EPI at the late blastocyst stage. All these experiments will further support the findings in Chapter 4 and help validate the model shown in Figure 5.1b.

While autophagy generally functions as pro-survival protective pathway (Kenific and Debnath, 2015), it can occasionally lead to cell death (Eisenberg-Lerner *et al*., 2009). Interestingly, Mattiolo *et al.* (2015) showed that at short times of starvation, autophagy sensitized cells to caspase activation and then, apoptosis. It is possible that a similar mechanism is at play in the reversine-treated early mouse embryos. It was shown by Helen Bolton in the Zernicka-Goetz lab, as demonstrated in her PhD thesis, that the ICM lineage of aneuploid embryos, not of diploid embryos, was compromised in culture media containing fewer energy resources beyond the early blastocyst stage (Figure 3.2b). Consistently, metabolic demands of the pre-implantation embryo have been indicated to increase during the blastocoel formation (reviewed in Leese, 2012). This suggests that the pre-implantation aneuploid embryos may have increased energy consumption during blastocyst maturation and experience short time of starvation in standard KSOM. Thus, it can be hypothesized that autophagy induction as a result of proteotoxic and metabolic stress leads to apoptosis of aneuploid cells in EPI during blastocyst maturation. If this is the case, this will further explain the autophagy-mediated low post-implantation developmental efficiency of aneuploid embryos since implantation stage is associated with a burst of proliferation and most likely increased energy requirements.

Aneuploid embryos also showed a significant upregulation of p53 pathway at the late blastocyst stage (Figure 4.18) and p53 pathway downregulation using p53 siRNA attenuated cell death in the ICM of aneuploid embryos during blastocyst maturation (Figure 4.20b). The exact trigger for p53 activation in aneuploid cells is not clear. Findings from Soto *et al.* (2017) suggest whole-chromosome imbalances *per se* are not sufficient to activate p53. Soto *et al.* (2017) proposes that perhaps at high levels of aneuploidy, p53 becomes activated because the stress levels exceed a certain threshold. It is possible that a similar mechanism is employed in the reversine-treated early mouse embryos. As described above, reversine-treated aneuploid embryos may experience short time of starvation and hence metabolic stress during blastocyst maturation and implantation stage, accompanied by proteotoxic stress. Even though Helen Bolton found no evidence of DNA damage or replication stress in the reversine-treated embryos at the blastocyst stage, as demonstrated in her thesis (Figure 3.2), it is worth investigating them in the reversine-treated embryos at the implantation stage. Together these stresses could be sufficient to activate p53 since p53 is stabilized in response to various cellular stimuli (Kastenhuber and Lowe, 2017). Certain p53-driven stress responses could initially instigate a short-term pro-survival program (Humpton and Vousden, 2016) but lead to cell self-destruction once they reach a tipping point (Kastenhuber and Lowe, 2017).

Finally, it was shown that autophagy upregulation is downstream of the p53 pathway in the EPI of aneuploid embryos (Figure 4.21a). Several mechanisms have been shown to be involved in p53-induced autophagy activation such as activation of autophagy by p53 target, DRAM (Damage-regulated autophagy modulator) (Crighton *et al*., 2007) and inhibition of autophagy by bcl-2 during starvation (Pattingre *et al*., 2005). Since reversine-treated aneuploid blastocysts show downregulation in *bcl-2* mRNA levels (Figure 4.18), it will be interesting to explore whether reduced levels of bcl-2 directly upregulate autophagy in aneuploid cells to mediate apoptosis. Conversely, there was no increase in *p53* mRNA when autophagy was depleted in aneuploid late blastocysts (Figure 4.21b). It is worth noting here that *p53* mRNA is not the best measure to investigate p53 pathway since its downstream targets could be post-transcriptionally regulated (Aubrey *et al*., 2018). However, this result was not unexpected given the pre-existing high levels of stress in aneuploid embryos suggesting that, p53 pathway is perhaps already maxed out in reversine-treated aneuploid embryos at the late blastocyst stage.

Overall, findings in Chapter.4 provide a direct evidence that autophagy can be utilized as a defense mechanism to eliminate aneuploid cells from the EPI during late pre-, peri and early post-implantation development of aneuploid embryos (Figure 4.23). While aneuploid embryos are expected to be eliminated at the early post-implantation stage, there was a high incidence of aneuploidy in viable early post-implantation embryos when autophagy was inhibited (Figure 4.24). This indicates that if autophagy is defective or if it does not effectively deplete aneuploid cells, these cells would contribute to the subsequent embryo development and potentially lead to developmental disabilities, such as Down syndrome. It will be helpful to know which aneuploidies are more tolerable during development and the phenotypic effects of specific chromosomal abnormalities. Clinically, it will be of interest to explore whether similar mechanisms extend to human embryos and their role in early pregnancy loss.

5.5 Mouse embryonic stem cell-based model for chromosome mosaicism

Similar to cleavage-stage mouse embryos, reversine treatment was shown to successfully induce higher levels of aneuploidy in mESCs than controls (Figure 4.25). There was some preferential elimination of aneuploid (reversine-treated) mESCs when cultured with diploid mESCs (controls), although not significant (Figure 4.26b-c). There are two possibilities to explain this result. First that the difference between the behaviour of reversine-treated mESCs and control mESCs is not sensitive enough since control mESCs already have high basal levels of aneuploidy (Figure 4.25). Since mESCs are prone to chromosomal aberrations and aneuploidy when maintained in culture for a sustained amount of time (Choi *et al*., 2017), it is

essential to use freshly derived or low passage mESCs as controls in this model (Figure 4.26a). Secondly, it is possible that the small, yet potentially significant difference between naïve reversine-treated and control mESCs become significantly elevated when allowed to differentiate. In embryos, Bolton *et al*. (2016) showed that while some aneuploid cells were preferentially eliminated from the ICM by the late blastocyst stage, the majority (on average 56%) aneuploid cells are eliminated beyond pre-implantation stage of development. Also, Sancho *et al.* (2013) showed that tetraploid ESCs, when co-cultured with diploid mESCs, are preferentially eliminated by apoptosis at the onset of differentiation. So, it will be interesting to investigate the fate of aneuploid mESCs using the model described in Section 4.5 in N2B27 medium rather than in N2B27 2i/LIF medium.

The mESC-based model for chromosome mosaicism developed here showed some evidence of apoptosis in aneuploid cells in diploid-aneuploid co-cultures (Figure 4.26d). It will be interesting to next investigate if the aneuploid mESCs are eliminated by same mechanisms as the mechanisms responsible for eliminating aneuploid cells in mouse embryo EPI (p53-autophagy mediated apoptosis; as revealed in Chapter 4). It will be interesting to compare the findings from this mESC model for chromosome mosaicism to the cellular and molecular mechanisms that dictate the fate of specific aneuploid ES cells (Zhang *et al*., 2016), cultured using similar conditions. This will give further insights into the cellular response of aneuploidy as a combination of uniform, general consequence of aneuploidy and specific responses depending on the genes affected. Lastly, this model can also be applied to study the consequences of aneuploidy in other two extra-embryonic lineages using respective stem cells. Trophoblast stem cells (TSCs) are self-renewing cells characteristic of the post-implantation ExE (Tanaka *et al*., 1998) and extra-embryonic endoderm (XEN) cells are self-renewing cells that represent derivatives of PE lineage (Kunath *et al*., 2005). Furthermore, Sozen *et al*. (2018) recently developed a protocol to generate embryo-like structures *in vitro* using ESCs, TSCs and XEN cells that can be utilized to study the dependency of the fate of aneuploid cells on the crosstalk between different lineages.

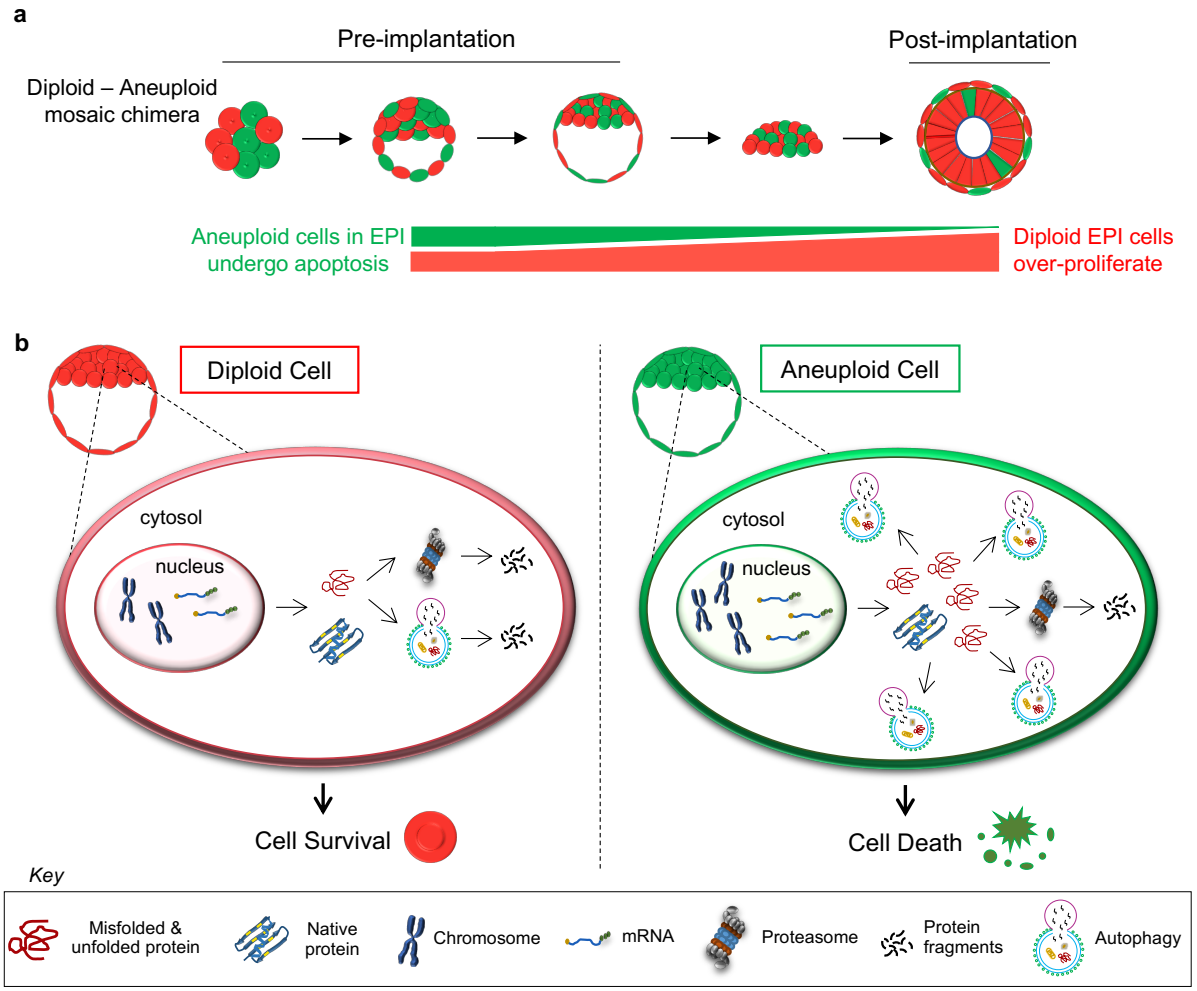

Figure 5.1. Model for the elimination of aneuploid cells from the mouse EPI. (**a**) Aneuploid cells generated at the 4-8 cell stage are progressively depleted from the EPI of the diploid-aneuploid mosaic embryo from the early blastocyst stage to the early post-implantation via apoptosis. Diploid cells in the EPI of same mosaic embryo over-proliferate to compensate for the reduction in overall EPI cell number thereby allowing for successful development. (**b**) In a normal (diploid) cell, cellular protein quality control mechanisms, involving the proteasome machinery and autophagy, degrade misfolded/unfolded proteins to prevent cytotoxicity and promote healthy cell survival (Chen *et al*., 2011). Here, it was hypothesised that in an aneuploid cell in the EPI, gene aberrations are translated into protein aberrations. Chronic protein misfolding after several mitotic divisions upregulates autophagy to an extent where instead of protecting the cell, it leads to cell death. This prevents the aneuploid cell from continuing further in the development of the mouse EPI.

6 Introduction II: 4-cell stage transcriptional heterogeneity in mouse embryo

6.1 'Stochastic' versus 'Biased' models of the first cell fate decision

In Chapter 2, the lineage segregation mechanisms past the polarized 8-cell stage were described. There are two competing models that explain when and how blastomeres initiate the choice between embryonic and extra-embryonic lineage. The two models are: stochastic and biased (Bedzhov *et al*., 2014a). The 'stochastic' model suggests that the differences between blastomeres in the 2-cell, 4-cell and 8-cell embryo are not relevant for lineage segregation. It proposes that the first lineage choice is made at the 16-cell stage or later due to cell position (Tarkowski and Wroblewska, 1967, Dietrich and Hiiragi, 2007). The 'biased' model suggests that the heterogeneity among blastomeres as early as the 2-cell stage bias cell fate decisions. Lineage tracing studies have shown that the animal-vegetal (A-V) axis of the zygote and the order of division of the 2-cell blastomeres can predict the future em-ab axis and embryonic parts of the blastocyst respectively (Gardner, 1997, 2001; Piotrowska *et al*., 2001). Here, the animal pole of the zygote is marked by the second polar body. These results were challenged by studies which showed that there is no specified lineage in 2-cell blastomeres, and mechanical pressure exerted by the ellipsoidal *zona pellucida* specify the em-ab axis of the blastocyst (Kurotaki *et al*., 2007). However, recent mRNA sequencing studies provide further evidence that the 2-cell stage blastomeres have heterogenous gene expression and different developmental potential (Biase *et al*., 2014, 2018; Shi *et al*., 2015, Casser *et al.*, 2017).

Compared to 2-cell stage, there is stronger evidence identifying heterogeneities in the 4-cell embryo and their influence on cell fate. The order and orientation of second cleavage division can result in differences in the developmental properties of 4-cell blastomeres (Piotrowska-Nitsche *et al*., 2005; Piotrowska-Nitsche and Zernicka-Goetz, 2005; Tabansky *et al*., 2013). During 2- to 4-cell division, a blastomere either divide meridionally (M; along the A-V axis of the zygote) or equatorially (E; 90° to the A-V axis of the zygote). 81% of the 4-cell embryos emerge from ME and EM division pattern and have tetrahedral arrangement (Piotrowska-Nitsche and Zernicka-Goetz, 2005). Remaining emerge from MM and EE division pattern and are flat. Of these, EE embryos display severely compromised development (Figure 6.1a) (Piotrowska-Nitsche and Zernicka-Goetz, 2005). The first-dividing 2-cell blastomere of the ME 4-cell embryo shows higher tendency to contribute to embryonic part of the blastocyst (Figure 6.1a) (Piotrowska-Nitsche and Zernicka-Goetz, 2005). The first-dividing 2-cell blastomere of the EM 4-cell embryo can give rise to either the embryonic/abembryonic part of the blastocyst. This tendency is not seen in the MM and EE 4-cell embryos (Piotrowska-Nitsche and Zernicka-

Goetz, 2005). The vegetal blastomere of the 4-cell ME embryo from the second E division shows higher tendency to contribute to mural TE than other blastomeres (Figure 6.1a) (Piotrowska-Nitsche *et al*., 2005). The chimera derived from 4-cell ME blastomeres from the second E division display developmental abnormalities, in contrast to normal development of chimeras derived from 4-cell blastomeres from the first M division (Figure 6.1b) (Piotrowska-Nitsche *et al*., 2005). The chimera derived from 4-cell ME blastomeres from the vegetal blastomeres of the second E division were severely compromised (Piotrowska-Nitsche *et al*., 2005). Coherent with above observations, the progeny of animal and vegetal blastomeres of the 4-cell ME embryo from the second E division showed higher Cdx2 expression in the 8-cell embryo (Jedrusik *et al*., 2008). The 8-cell stage progeny of animal and vegetal blastomeres of the 4-cell EM embryo from the first E division did not show higher Cdx2 expression. Besides the division order and orientation, other hypotheses have been proposed to explain the origin of this early pre-patterning: partitioning error and ZGA (Shi *et al*., 2015), the mechanical effects of sperm entry (Piotrowska and Zernicka-Goetz, 2001) and epigenetic asymmetry between maternal and paternal genomes in the zygote (Takaoka and Hamada, 2014).

There is an increasing amount of recent data identifying specific molecular heterogeneities between the 4-cell blastomeres. The first marker that was heterogenous between 4-cell blastomeres and correlated with cell fate was identified to be histone H3 methylation of specific arginine residues (Torres-Padilla *et al*., 2007). H3R26me, H3R17me and H3R2me are targets of methyltransferase Carm1. At 4-cell stage, the inter-blastomere levels of H3R26me, H3R17me, H3R2me and Carm1 are all correlated, where H3R26me displayed highest heterogeneity (Torres-Padilla *et al*., 2007). Overexpression of Carm1 led to increase in H3R26me levels, upregulated Nanog and Sox2, and predisposed the cell to contribute to ICM (Torres-Padilla *et al*., 2007). In a 4-cell ME embryo, cells with the highest H3R26me levels belonged to M progeny and contributed to the embryonic part and the cell with the lowest H3R26me level belonged to vegetal progeny of E division and contributed to the mural TE (Torres-Padilla *et al*., 2007). This correlates the division order and orientation of 4-cell blastomeres with their heterogenous developmental potential through the involvement of epigenetics (Piotrowska-Nitsche and Zernicka-Goetz, 2005; Torres-Padilla *et al*., 2007). Another chromatin modifier, Prdm14 was found heterogeneous in 4-cell-stage embryos. Prdm14 interacts with Carm1 and its overexpression led to increase in H3R26me and predisposed the cell to contribute to ICM (Burton *et al*., 2013). These epigenetic markers potentially influence the DNA binding dynamics for various lineage-determining transcription factors. For instance, 4-cell blastomeres show distinct Oct4 and Sox2 kinetics (Plachta *et al*., 2011; White *et al*., 2016). Cells with slower Oct4 and Sox2 kinetics, thus increased binding to

DNA-binding sites, contributed mainly to the ICM (Plachta *et al*., 2011; White *et al*., 2016). H3R26me levels and Sox2-DNA binding times correlated within 4-cell blastomeres and Carm1 downregulation reduced the Sox2-DNA binding ability (White *et al*., 2016). Subsequently, Oct4 and Sox2 targets were found to be heterogenous in the 4-cell embryo (Goolam *et al*., 2016). *Sox21* is the most highly heterogenous Oct4 and Sox2 target and is regulated by Carm1 (Goolam *et al*., 2016). Sox21 downregulation led to increased expression of Cdx2 at the 8-cell stage, which biased the cell fate towards TE (Goolam *et al*., 2016). The upstream regulators of Carm1 early heterogeneity are unknown. However, recently, a long noncoding RNA, LincGET was found heterogenous in the 2-cell and 4-cell embryos. It was shown to complex with Carm1 and promote the nuclear localization of Carm1 (Wang *et al*., 2018). Cells with higher levels of LincGET-Carm1 complex were biased towards ICM lineage (Wang *et al*., 2018). Recently it was also shown that the 4-cell heterogeneity is linked to the differential accumulation of CARM1 in nuclear paraspeckles (Hupalowska *et al*., 2018). Together, heterogeneity along LincGET-Carm1/Prdm14-(H3R26me, H3R17me, H3R3me)-Oct4/Sox2-Sox21 axis at the 4-cell stage influences cell fate decisions (Figure 6.1c).

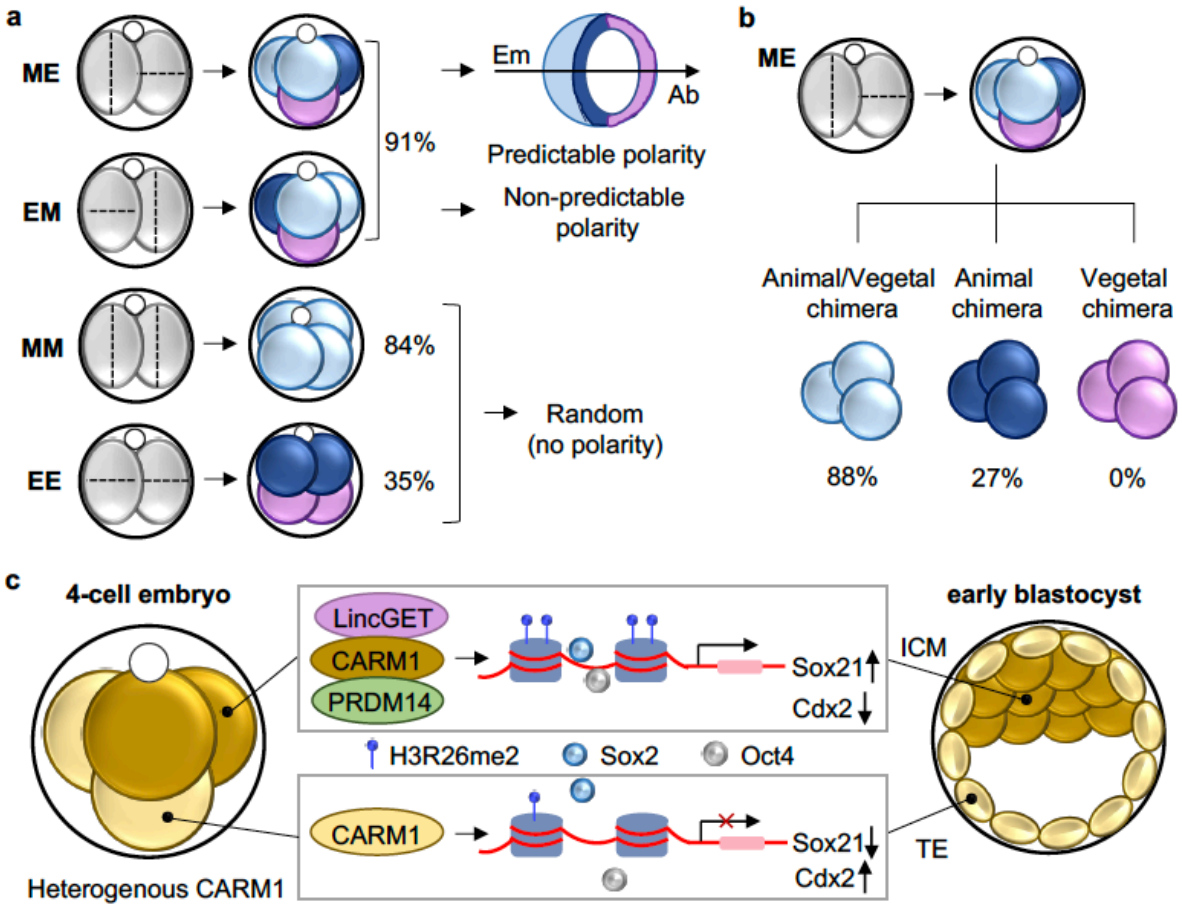

Figure 6.1. 4-cell heterogeneity and cell fate decisions (Adapted from Graham and Zernicka-Goetz, 2016; Chen *et al*., 2018)**.** (**a**) Four possible arrangements of the blastomeres in the 4-cell embryo and

their developmental potential: ME tetrahedral arrangement (first meridional and second equatorial division), EM tetrahedral arrangement (first equatorial and second meridional division), MM flat form (both meridional divisions) and EE flat form (both equatorial divisions). In the ME embryos the earlier dividing 2-cell blastomere tends to contribute to the embryonic (Em) and the later, to the abembryonic (Ab) part of the blastocyst. The vegetal blastomere of the later dividing 2-cell blastomere tends to contribute to the mural TE. (**b**) Chimeras made from 'like' blastomeres from 4-cell ME embryos have different developmental potentials. Animal/vegetal chimeras develop with normal success, while the animal and vegetal chimeras are developmentally compromised. (**c**) Carm1, Prdm14 and LincGET are differentially expressed in 4-cell embryos and regulate the level of histone H3R26 methylation. Higher methylation allows long-lived DNA binding of Oct4 and Sox2. This leads to higher expression of lineage specifiers such as Sox21. Sox21 levels direct cell fate as it is repressor of Cdx2 that differentiates a cell to the TE fate.

The long-lasting debate between two models of the first cell fate decision in mouse embryos may be reconciled. The inter-blastomere differences displayed by early embryos might not be large enough during early stages (2-cell/4-cell) but some of them might get amplified in subsequent divisions to then mediate lineage fates. Thus, while this initial bias could be sufficient to influence cell fate, it is not irreversible. This balance between pre-patterning and regulation will give early cleavage embryos the observed developmental flexibility.

6.2 Transcriptional profiling of pre-implantation mouse embryos

Spatiotemporal transcriptome analysis of the early mouse embryos paves way to obtain significant mechanistic insights into the cell fate decisions. The first studies used microarray technology to explore changes in global gene activity during different stages of mouse pre-implantation development (Hamatani *et al*., 2004; Wang *et al*., 2004a). These studies helped in understanding the zygotic genome activation (Hamatani *et al*., 2004) and the involvement of several conserved signaling pathways including Wnt, BMP, and Notch in pattern formation (Wang *et al*., 2004a). The technique was improved upon to carry out single-cell microarray analysis that allowed the analysis of gene expression in different lineages (Kurimoto *et al*., 2006; Guo *et al*., 2010; Ohnishi *et al*., 2014). The technique was applied to analyse the transcriptomes of single cells in the ICM and identified the differentially expressed genes between the two cell populations: EPI (*Nanog*, *Spic* and *Fgf4*) and PE (*Gata4*, *Gata6*, *Sox17* and *Fgfr2*) (Kurimoto *et al*., 2006). Analysis of 48 genes obtained by single-cell microarray on 500 cells revealed *Id2* and *Sox2* as the earliest markers of outer and inner cells, respectively (Guo *et al*., 2010). Since the development of single cell mRNA sequencing assay for mouse embryos (Tang *et al*., 2009), there have been a shift from the array-based platforms to profile gene expression in early mouse embryos. Single cell mRNA sequencing allows the detection of more genes than microarray and identification of allele specific gene expression and splice

junctions during early mouse embryo development (Tang *et al*., 2009; Tang *et al*., 2011; Xue *et al*., 2013; Deng *et al*., 2014). Another study used mRNA sequencing to identify the differentially expressed genes in inside and outside cells at the 16-cell stage and uncovered a novel role of BMP signalling in pre-implantation development (Graham *et al*., 2014). The single cell mRNA-sequencing is constantly being improved upon. The Smart-Seq protocol (Ramskold *et al*., 2012) was introduced, followed by Smart-Seq2 protocol (Picelli *et al*., 2013; Picelli *et al*., 2014) for better coverage, detection, bias and accuracy. These protocols were used for the analyses of the monoallelic expression in mouse embryos (Deng *et al*., 2014), investigations into inter-blastomere transcriptional differences at the 2-, 4- and 8-cell stages of development (Biase *et al*., 2014; Goolam *et al*., 2016; Biase *et al*., 2018), and a cross-species stage- and lineage-specific analysis of pre-implantation transcriptional features (Boroviak *et al*., 2018). Following new single cell sequencing methods have been recently published: a protocol to analyse both circular and linear RNA (Fan *et al*., 2015), a protocol to sequence both the genome and transcriptome in single cells (Macaulay *et al*., 2015), a protocol to measure single-cell transcriptome repeatedly, known as, MR-seq (Yang *et al*., 2017) and a protocol to combine single-cell RNA-seq with lineage tracing, known as, Rainbow-Seq (Biase *et al*., 2018).

6.3 Project Aims

The mechanisms underlying the lineage segregation in the mouse embryo are still not completely understood. The aim of this chapter was to elucidate how heterogenous *Sox21* expression at the 4-cell stage directs the first cell fate decision. The transcriptome of 4-cell stage wild-type and Sox21 knockout embryos will be compared to identify the novel Sox21 downstream targets. Then, their role in early mouse development will be investigated.

7 Results II: Elucidating the impact of 4-cell stage Sox21 heterogeneity on pre-implantation embryo development

7.1 Sox21 knockout versus wildtype transcriptome

It was previously shown that Sox21 is one of the most heterogeneously expressed genes at the 4-cell stage and that this heterogeneity in Sox21 can bias cell fate decision (Goolam *et al*., 2016). To gain better insight into how Sox21 biases cell fate, Sox21 knockout (KO) and wild-type embryos were RNA-sequenced at the 4-cell stage.

Sox21 KO mice were sourced from the Yumiko Saga lab in Japan (Kiso *et al*., 2009). Two Sox21 KO heterozygous females were received that were bred with Bl6 males to derive a homozygous KO line by Mubeen Goolam in the Zernicka-Goetz lab, as demonstrated in his PhD thesis. It was found that Sox21 homozygous KO mice, although viable, were not as healthy as the wildtype Bl6 mice. They were extremely runty, lethargic, weak, and prone to malocclusion and displayed developmental defects (Mubeen Goolam's PhD Thesis unpublished data). A 2-cell stage chimeric embryo that consisted of one Sox21 KO blastomere and one wildtype blastomere showed a bias in their incorporation into the TE and ICM lineages at the late blastocyst stage. Similar to the phenotype displayed by clonal Sox21 siRNA injection (Goolam *et al*., 2016), Sox21 KO blastomeres were biased towards forming TE (Mubeen Goolam's PhD Thesis unpublished data). This further emphasised that heterogenous Sox21 expression at the 4-cell stage can bias cell fate and clonal contribution to embryonic and extra-embryonic lineages.

To investigate the downstream targets of Sox21, four Sox21 KO embryos and four wildtype embryos were collected by Mubeen Goolam at the 4-cell stage and then subjected to library preparation using the Smart-Seq2 single-cell RNA-sequencing protocol (Picelli *et al*., 2013; Picelli *et al*., 2014). Extrinsic spike-in RNA-molecules were added to each embryo's lysate prior to cDNA conversion, amplification and library preparation (similar to as described in Goolam *et al*., 2016). All the samples were consistent for the total number of reads, fraction of mapped reads and fraction of reads mapped to spikes (Figure 7.1a-c). Interestingly, the fraction of mitochondrial reads was twice as high in Sox21 KO (Figure 7.1d), which might suggest a higher level of stress for cells in the KO embryos. Overall, all the samples passed the quality check and the libraries were sequenced (similar to as described in Goolam *et al*., 2016). Principal component analysis was applied to the log-transformed normalised read counts of the union of 5,000 most highly expressed genes from each sample. The principal component analysis of these embryos indicated that Sox21 KO and wildtype embryos

separated along the first principal component (Figure 7.1e), suggesting a substantial variation between Sox21 KO and wildtype 4-cell stage embryos. Next, genes that were differentially expressed between the wildtype and Sox21 KO 4-cell stage embryos were identified. Using adjusted p-value for the differential expression test < 0.1, 512 genes were found to be differentially expressed between the wildtype and Sox21 KO embryos. Of these, 233 genes were highly downregulated and 279 genes were highly upregulated in Sox21 KO embryos compared to the wildtype. This indicates that the expression pattern of Sox21 at the 4-cell stage can affect the expression of a lot of other genes at the 4-cell stage which can potentially bias cell fate.

The RNA-sequencing and mapping was carried out by Lia Chappell in the lab of Thierry Voet at the Sanger Institute (Hinxton). The quality assessment and differential expression analysis was carried out by Antonio Scialdone in the lab of John Marioni at the EMBL-EBI.

7.2 Functional siRNA screen in the pre-implantation mouse embryo

7.2.1 Selection of candidate genes

Recent studies have shown that Oct4 and Sox2 have heterogenous activity (Plachta *et al*., 2011; White *et al*., 2016) and that Oct4 and Sox2 targets have highly heterogenous expression (Goolam *et al*., 2016) at the 4-cell stage. Also, Sox21 is a Sox2 target (Chakravarthy *et al*., 2011; Kuzmichev *et al*., 2012) that also displays binding of Oct4 (Chakravarthy *et al*., 2011). So, it was reasoned that the downstream targets for Sox21 should also be Oct4 and/or Sox2 targets. Out of 512 differentially expressed genes between the wildtype and Sox21 KO embryos, Oct4 and/or Sox2 targets were determined (using protocol as described in Goolam *et al*., 2016). 25 differentially expressed Oct4 and/or Sox2 targets were identified of which 12 genes were highly upregulated and 13 genes were highly downregulated in Sox21 KO embryos compared to the wildtype embryos (Figure 7.1f). Some of these genes showed highly heterogenous expression at the 4-cell stage (determined using protocol as described in Goolam *et al*., 2016) including *Cldn4*, *Sars*, *Klf5*, *Ckb*, *Tdgf1*, *Slc25a36* and *Runx1t1*. The analysis related to testing differentially expressed genes for Oct4 and Sox2 target enrichment, and identification of highly heterogenous genes were carried out by Antonio Scialdone.

The mRNA expression profiles of the list of genes mentioned in Figure 7.1f was examined at the oocyte, zygote, 2-cell, 4-cell, 8-cell, 16-cel and 32-cell stages (Figure 7.2). The single-cell RNA-sequencing data previously generated in the Zernicka-Goetz lab was used to generate their expression profiles. Since the mRNA expression for Sox21 through pre-implantation developmental stages peaked at the 4-cell stage (Goolam *et al*., 2016), we assumed that its downstream targets should also follow a similar profile. We looked for genes where the mRNA

expression dramatically changed from the 2- to 4-cell stage and then reversed from the 4- to 8-cell stage. The genes that were selected included *Ncl*, *Klf2*, *Tdgf1*, *Ppp2r5c*, *Cdca7*, *Ift52*, *Slc25a36*, *Sec24a*, *Hikeshi*, *Fbxo36* and *Taf12*. From this list, *Klf2*, *Slc25a36* and *Tdgf1* were chosen for functional siRNA screening based on their known functions. Klf2 had been shown to be critical to sustain the naïve pluripotent state of ESCs (Yeo *et al*., 2014; Qiu *et al*., 2015). The depletion of Slc25a36 in mESCs had been shown to cause the downregulation of pluripotency markers including *Oct4*, *Sox2* and upregulation of trophoblast-associated markers including *Cdx2*, *Eomes* (Lim *et al*., 2008). The depletion of Tdgf1/Cripto in mESCs had been shown to reduce their self-renewal, cause the downregulation of pluripotency markers including *Oct4*, *Nanog* and cause the upregulation of trophoblast-associated markers including *Cdx2*, *Eomes*, *Gata3* (Fiorenzano *et al*., 2016). It was also noted that the expression for *Klf2*, *Slc25a36* and *Tdgf1* peaked at the 4-cell stage (Figure 7.2), similar to Sox21 expression profile (Goolam *et al*., 2016).

To determine the functional significance of *Klf2*, *Slc25a36* and *Tdgf1* genes, loss-of-function studies were carried out. To reduce each target gene, a mixture of three specific siRNAs was injected into the embryos at the zygote stage which were then allowed to develop until the 8-cell stage (Figure 7.3a). The embryos were then analyzed by qRT-PCR. Klf2 siRNA injection reduced *Klf2* mRNA to 20% relative to embryos injected with control siRNA (Figure 7.3b). Tdgf1 siRNA injection reduced *Tdgf1* mRNA to 22% relative to embryos injected with control siRNA (Figure 7.3c). Slc25a36 siRNA injection did not reduce *Slc25a36* mRNA levels relative to embryos injected with control siRNA (Figure 7.3d). Due to the inefficiency of Slc25a36 siRNA, it was not used further to study the function of Slc25a36 in the pre-implantation mouse development. Klf2 and Tdgf1 siRNAs were sufficient to knockdown the mRNA expression of respective target genes and were therefore used further in functional studies.

Interestingly, besides peaking at the 4-cell stage (Figure 7.4a-c), mRNA for *Klf2* and *Tdgf1* genes were enriched in inside cells compared to outside cells at the 32-cell stage, similar to *Sox21* mRNA (determined using the previously available single-cell RNA-sequencing dataset generated in the Zernicka-Goetz lab) (Figure 7.4d-f). Moreover, Tdgf1 mRNA and protein had been shown to be enriched in ICM at E3.5 and in EPI at E4.5 (Fiorenzano *et al*., 2016). Klf2 mRNA has also been found to be expressed exclusively in pre-implantation mouse EPI cells (Guo *et al*., 2010; Boroviak *et al*., 2018). Thus, *Klf2* and *Tdgf1* were identified as the genes of interest to be studied further in the context of pre-implantation mouse embryogenesis.

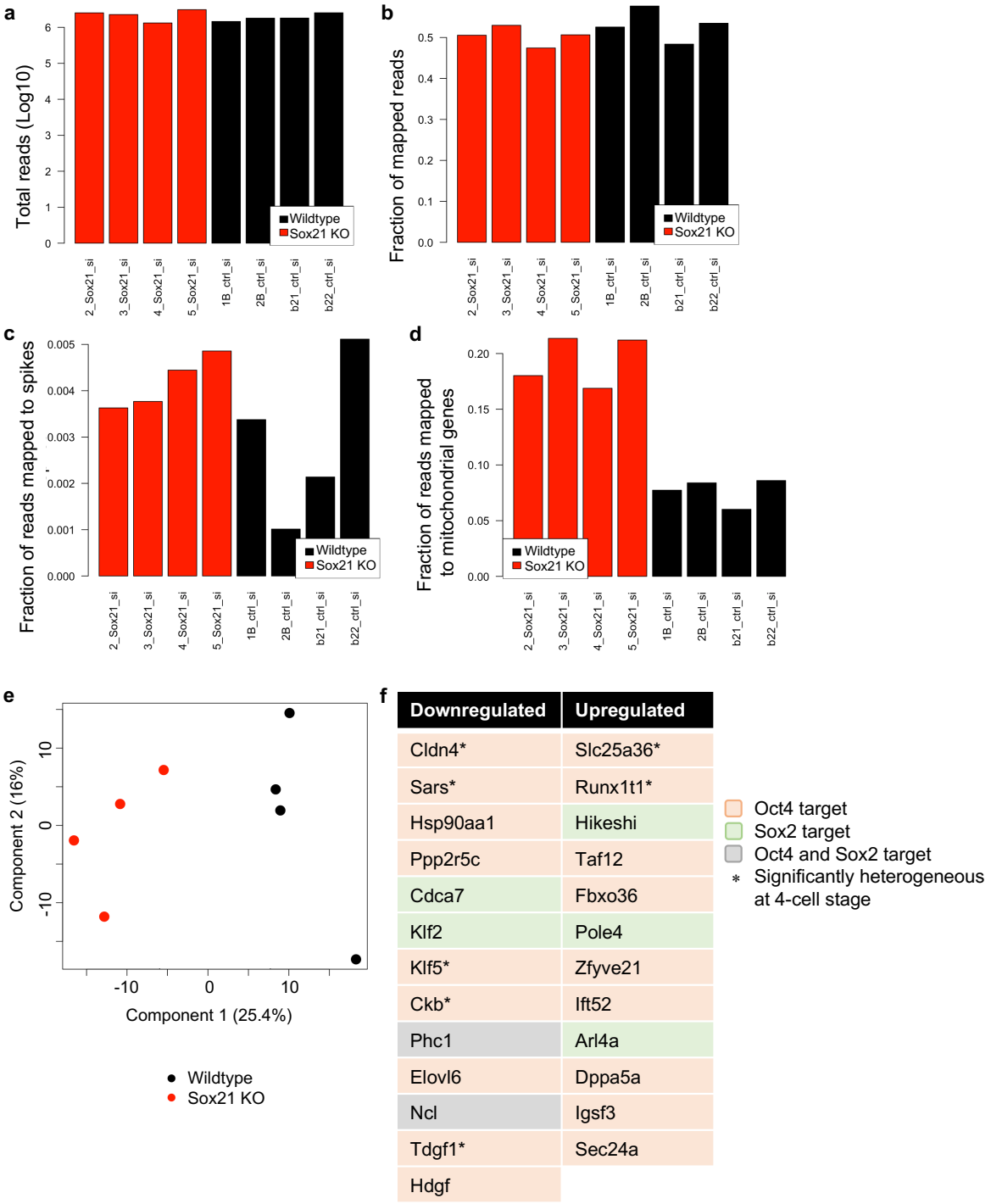

Downregulated	Upregulated
Cldn4*	Slc25a36*
Sars*	Runx1t1*
Hsp90aa1	Hikeshi
Ppp2r5c	Taf12
Cdca7	Fbxo36
Klf2	Pole4
Klf5*	Zfyve21
Ckb*	Ift52
Phc1	Arl4a
Elovl6	Dppa5a
Ncl	Igsf3
Tdgf1*	Sec24a
Hdgf	

Figure 7.1. Sox21 knockout versus wildtype transcriptome. Four Sox21 knockout (KO) and four wildtype 4-cell stage embryos were RNA-sequenced and compared. To assess the quality of library of each embryo, (**a**) total number of reads, (**b**) fraction of mapped reads, (**c**) fraction of reads mapped to spikes and (**d**) fraction of reads mapped to mitochondrial genes, was measured. The black bar-plots are for wildtype and the red bar-plots are for Sox21 KO embryos. (**e**) Principal component analysis of the gene expression patterns of Sox21 KO and wildtype embryos. The percentage of variance explained by each principal component is indicated in parentheses. (**f**) List of genes that are differentially expressed (highly downregulated and highly upregulated) in Sox21 KO embryos compared

to in wildtype 4-cell stage embryos and are also Oct4 and/or Sox2 targets. Adjusted p-value < 0.1 for these genes. The level of differential expression decreases from top to bottom of the list.

Figure 7.2. Expression profile of highly differentially expressed genes in Sox21 KO versus wild type embryos. Sox21 KO and wildtype 4-cell stage embryos were RNA-sequenced and compared. 13 highly downregulated and 12 highly upregulated genes in Sox21 KO embryos compared to in wildtype 4-cell stage embryos were obtained. Their mRNA expression profiles are shown here from the oocyte to the 32-cell stage. Data are shown as mean for each stage. These genes are also Oct4 and/or Sox2 targets and adjusted p-value for the differential expression test < 0.1.

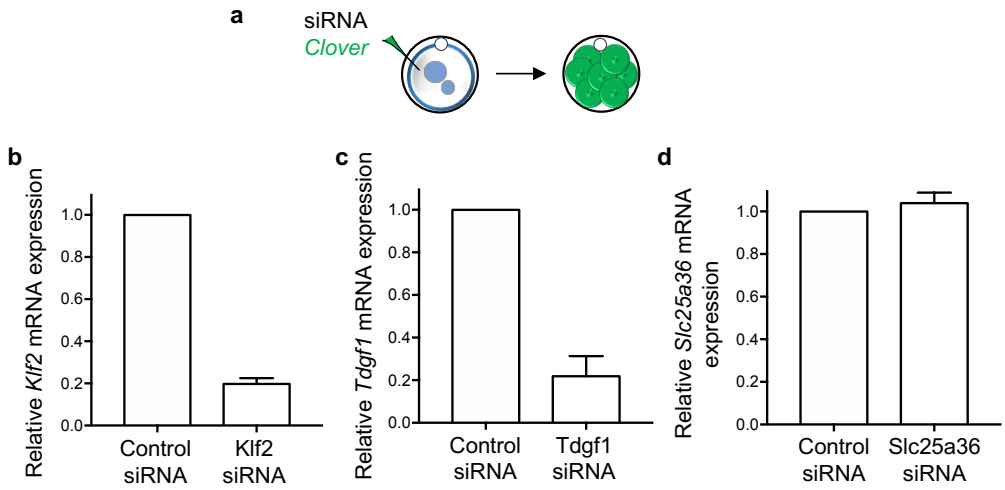

Figure 7.3. Klf2, Tdgf1 and Slc25a36 siRNA efficiency. (**a**) Zygotes were injected with siRNA and mRNA was assessed at the 8-cell stage using qRT-PCR (relative to the control siRNA-injected embryos). (**b**) *Klf2* mRNA expression levels in control siRNA-injected and Klf2 siRNA-injected embryos. Control siRNA n = 51 embryos, Klf2 siRNA n = 37 embryos. (**c**) *Tdgf1* mRNA expression levels in control siRNA-injected and Tdgf1 siRNA-injected embryos. Control siRNA n = 15 embryos, Tdgf1 siRNA n = 10 embryos. (**d**) *Slc25a36* mRNA expression levels in control siRNA-injected and Slc25a36 siRNA-injected embryos. Control siRNA n = 9 embryos, Slc25a36 siRNA n = 12 embryos.
For all the graphs, data are mean ± s.e.m.

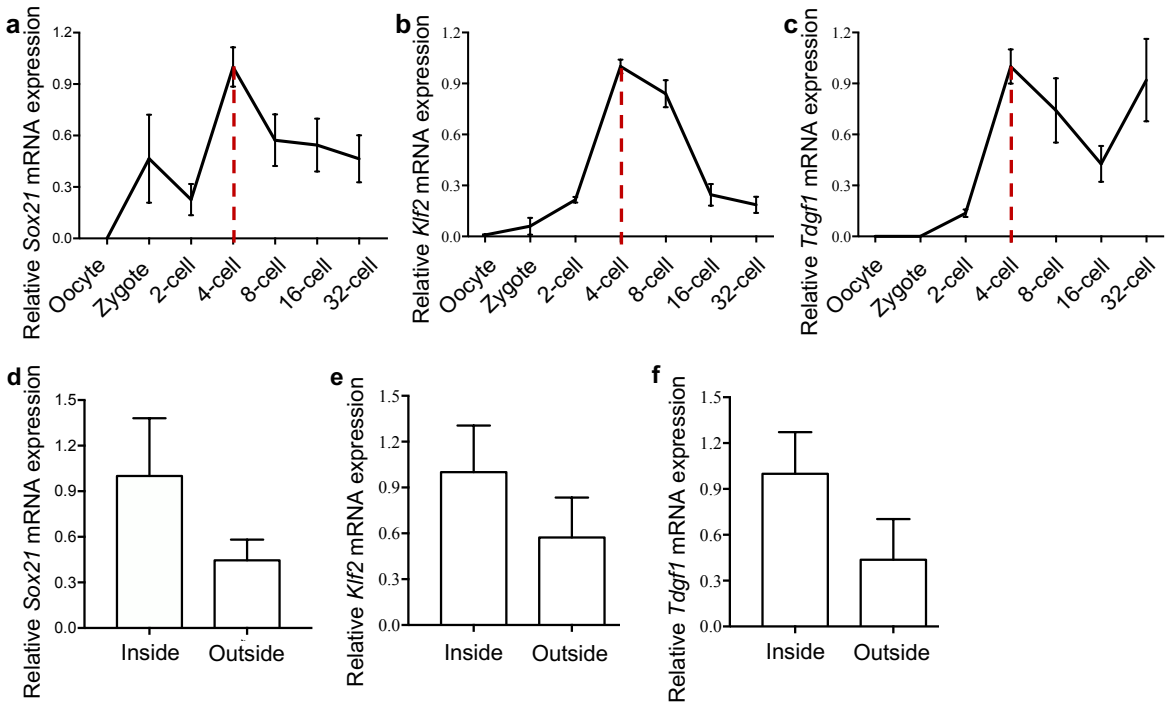

Figure 7.4. *Klf2*, *Tdgf1* and *Sox21* mRNA expression during pre-implantation stages. Relative mRNA expression profiles from the oocyte to the 32-cell stage of *Sox21* (**a**), *Klf2* (**b**) and *Tdgf1* (**c**) (relative to the mean 4-cell stage mRNA expression levels). Red line points the 4-cell stage expression levels. Relative mRNA expression levels of *Sox21* (**d**), *Klf2* (**e**) and *Tdgf1* (**f**) in inside and outside cells at the 32-cell stage (relative to the mean inside cells mRNA expression levels).
For all the graphs, data are mean ± s.e.m.

7.2.2 Effect of Klf2 and Tdgf1 knockdown on lineage specification

To investigate the function of Klf2 and Tdgf1 in pre-implantation development, their expression was reduced within the embryo using respective siRNAs (Figure 7.3b-c) and the effect on lineage specification was examined.

To induce clonal depletion of Klf2, Klf2 siRNA was injected into one blastomere of 2-cell stage embryos, along with the injection marker *Gap-RFP* mRNA (Figure 7.5a). The embryos were cultured until the late blastocyst stage (E4.5) and were assessed for the contribution of injected clone to the TE (marked by Cdx2), EPI and PE (marked by Sox17) lineages. Klf2 siRNA-injected clone of cells contributed 19% more cells to the TE compared to control siRNA-injected clone of cells (Figure 7.5b-c). Accordingly, there was significant decrease in the contribution of Klf2 siRNA-injected clone of cells to EPI and PE lineages (Figure 7.5b-c). To induce clonal depletion of Tdgf1, Tdgf1 siRNA was injected into one blastomere of 2-cell stage embryos, along with the injection marker *Clover* mRNA (Figure 7.6a). The embryos were cultured until E4.5 and were assessed for the contribution of injected clone to the TE (marked

by Cdx2), EPI and PE (marked by Sox17) lineages. Tdgf1 siRNA-injected clone of cells contributed 15% more cells to the TE compared to control siRNA-injected clone of cells (Figure 7.6b-c). Accordingly, there was significant decrease in the contribution of Tdgf1 siRNA-injected clone of cells to EPI and PE lineages (Figure 7.6b-c). Also, there was no change in the average total cell number in the Klf2 siRNA-injected (Figure 7.5d) and Tdgf1 siRNA-injected (Figure 7.6d) half of the embryos compared to that of control siRNA-injected. Overall, these results indicated that heterogenous expression of Klf2 and Tdgf1 can bias cell fate at the blastocyst stage. Similar to the cells with lower Sox21 levels, cells with lower Klf2 and Tdgf1 levels showed a significantly lower tendency to contribute to pluripotent ICM lineages.

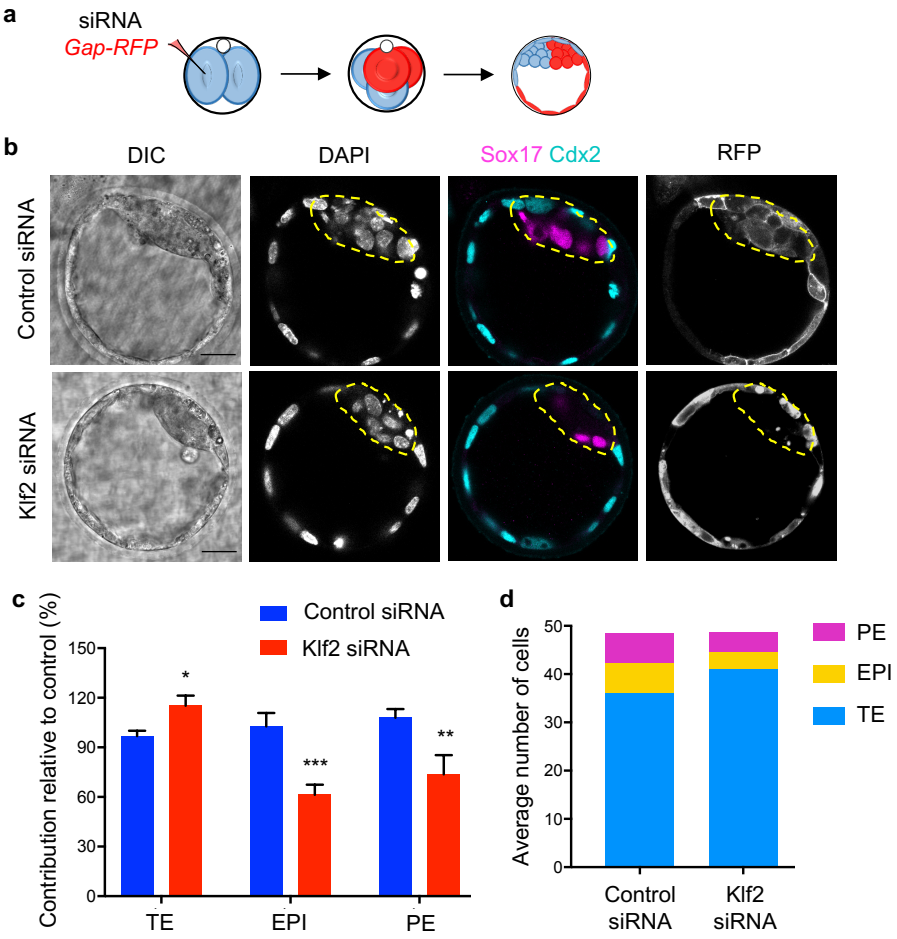

Figure 7.5. Effect of Klf2 knockdown on lineage specification. (**a**) Klf2 siRNA or control siRNA was injected into one blastomere of 2-cell stage embryos, along with *Gap-RFP* mRNA. The embryos were cultured until the late blastocyst stage (E4.5). (**b**) The embryos were immunostained for Cdx2, Sox17, RFP and DAPI to assess all three lineages: TE (Cdx2-positive cells), EPI (DAPI-positive, Sox17-negative, Cdx2-negative cells) and PE (Sox17-positive cells). Scale bars, 20 μm. Yellow lines indicate the ICM. (**c**) Relative contribution of the injected clone of cells was assessed in all three lineages (relative to the contribution of non-injected clone). Student's t-test with Welch's correction was used for TE and *$p < 0.05$. Student's t-test was used for EPI and ***$p < 0.001$. Mann-Whitney test was used for

PE and **p < 0.01. Data are mean ± s.e.m. (**d**) Average cell numbers for each lineage in the injected half of the embryo. For (**b**), (**c**) and (**d**), Control siRNA n = 16 embryos, Klf2 siRNA n = 26 embryos.

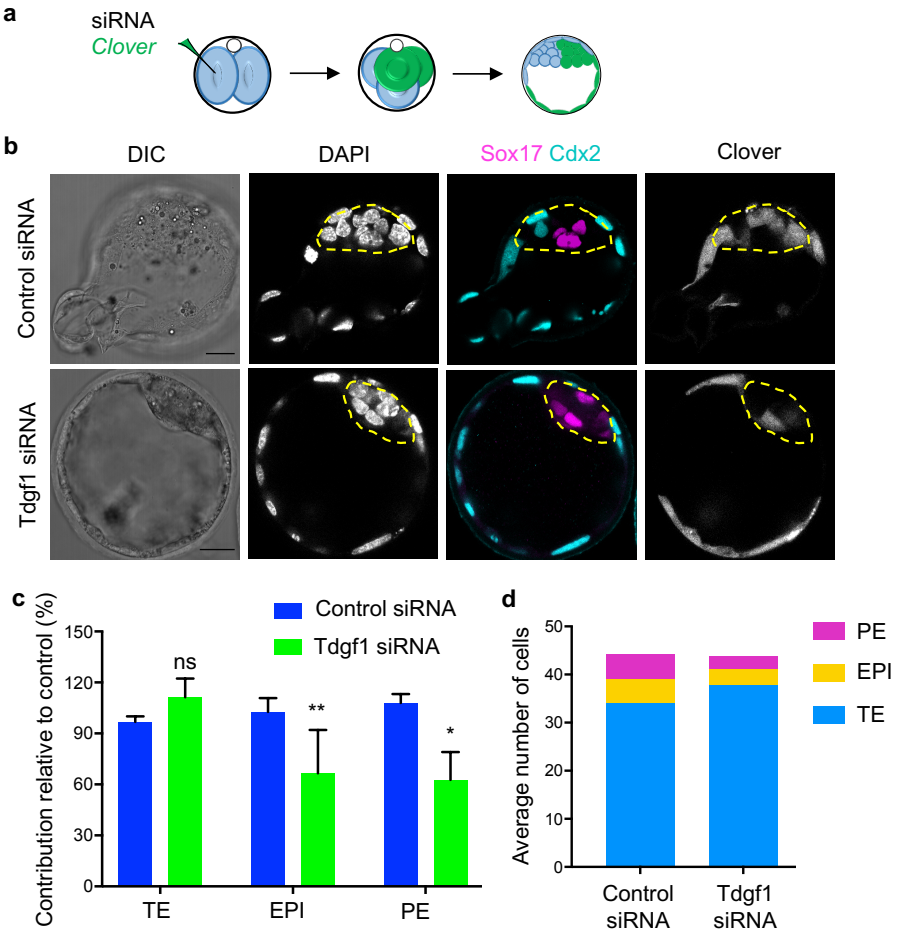

Figure 7.6. Effect of Tdgf1 knockdown on lineage specification. (**a**) Tdgf1 siRNA or control siRNA was injected into one blastomere of 2-cell stage embryos, along with *Clover* mRNA. The embryos were cultured until the late blastocyst stage (E4.5). (**b**) The embryos were immunostained for Cdx2, Sox17 and DAPI to assess all three lineages: TE (Cdx2-positive cells), EPI (DAPI-positive, Sox17-negative, Cdx2-negative cells) and PE (Sox17-positive cells). Scale bars, 20 μm. Yellow lines indicate the ICM. (**c**) Relative contribution of the injected clone of cells was assessed in all three lineages (relative to the contribution of non-injected clone). Student's t-test with Welch's correction was used for TE and PE, *p < 0.05 and ns = not significantly different. Mann-Whitney test was used for EPI and **p < 0.01. Data are mean ± s.e.m. (**d**) Average cell numbers for each lineage in the injected half of the embryo. For (**b**), (**c**) and (**d**), Control siRNA n = 15 embryos, Tdgf1 siRNA n = 12 embryos.

7.2.3 Effect of Klf2 and Tdgf1 knockdown on Cdx2 expression

It was shown in Goolam *et al*. (2016) that the levels of Sox21 expression affect expression of the transcription factor Cdx2. The cells with lower Sox21 have higher levels of Cdx2 protein by the late 8-cell stage (Goolam *et al*., 2016). The bias of blastomeres with lower Sox21 towards the TE is potentially because of this ability of Sox21 to regulate Cdx2, since Cdx2 is

required for correct differentiation into TE (Strumpf *et al*., 2005). Since results in section 7.2.2 show that cells with lower Klf2 and Tdgf1 levels contribute less towards pluripotent ICM progeny, it was next investigated if Klf2 and Tdgf1 might also be able to regulate the expression of Cdx2 in the embryo, similar to the regulation of Cdx2 expression by Sox21.

To this end, Klf2 siRNA was injected into the zygotes which were allowed to develop to the early-to-mid 8-cell stage (when Cdx2 starts to be expressed). The embryos were then analyzed by qRT-PCR for Cdx2. Klf2 siRNA injection increased *Cdx2* mRNA level by 33% relative to embryos injected with control siRNA (Figure 7.7a). Similarly, Tdgf1 siRNA was injected into the zygotes and embryos were analyzed by qRT-PCR at the 8-cell stage. Tdgf1 siRNA injection increased *Cdx2* mRNA level by 56% relative to embryos injected with control siRNA (Figure 7.7b). These results indicate that cells with lower Klf2 or Tdgf1 levels are likely to express higher Cdx2 and are thus predisposed to differentiate first to give the TE. Next, it will be important to confirm if cells with lower Klf2 or Tdgf1 levels express higher levels of Cdx2 protein using immunofluorescence.

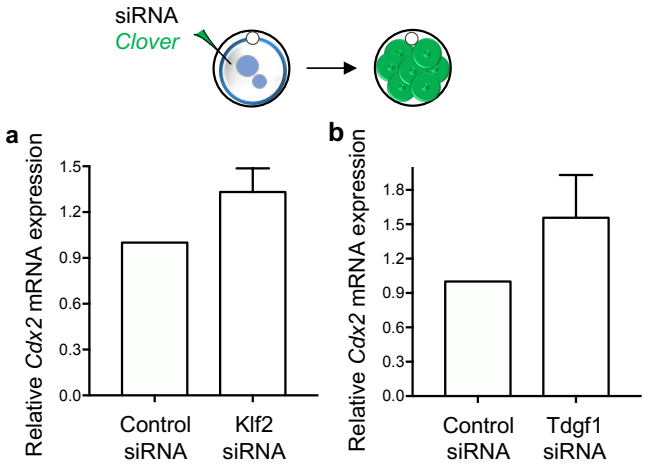

Figure 7.7. Effect of Klf2 and Tdgf1 knockdown on *Cdx2* mRNA expression at the 8-cell stage. Zygotes were injected with siRNA and mRNA was assessed at the 8-cell stage using qRT-PCR for *Cdx2* mRNA expression levels (relative to the control siRNA-injected embryos). (**a**) Control siRNA-injected and Klf2 siRNA-injected embryos were compared. Control siRNA n = 26 embryos, Klf2 siRNA n = 20 embryos. (**a**) Control siRNA-injected and Tdgf1 siRNA-injected embryos were compared. Control siRNA n = 25 embryos, Tdgf1 siRNA n = 21 embryos. For both the graphs, data are mean ± s.e.m.

7.3 Downstream targets of Sox21 - Klf2 and Tdgf1

7.3.1 Effect of Sox21 on Klf2 and Tdgf1 expression at the 4-cell stage

It was found from the RNA-sequencing data that both *Klf2* and *Tdgf1* genes were downregulated in Sox21 KO 4-cell stage embryos compared to wildtype (Figure 7.8a-b). The

Klf2 mRNA levels dropped to 40% and *Tdgf1* mRNA levels dropped to 35% in Sox21 KO compared to in wildtype 4-cell embryos (Figure 7.8a-b). The same was confirmed by downregulating Sox21 using Sox21 siRNA (same siRNA as used in Goolam *et al*., 2016). A mixture of three Sox21 siRNAs was injected into the embryos at the zygote stage which were then allowed to develop until the 4-cell stage (Figure 7.8c). The embryos were then analyzed by qRT-PCR. Sox21 siRNA injection reduced *Klf2* mRNA level to 62% and *Tdgf1* mRNA level to 55% relative to embryos injected with control siRNA (Figure 7.8d-e).

Alternatively, the effect of Sox21 overexpression on the expression of *Klf2* and *Tdgf1* was also determined. To this end, zygotes were injected with mRNA encoding Sox21 and were allowed to develop until the 4-cell stage (Figure 7.8f). First, the effectiveness of *Sox21* mRNA in upregulating Sox21 was tested by fixing the injected embryos at the 4-cell stage and immunostaining them for Sox21. Injection of *Sox21* mRNA resulted in an increase in the Sox21 protein expression at the 4-cell stage (Figure 7.8g). To check the effect of Sox21 overexpression on *Klf2* and *Tdgf1* expression, the injected embryos were analyzed by qRT-PCR at the 4-cell stage. *Sox21* mRNA injection increased *Klf2* mRNA level by 23% and *Tdgf1* mRNA level by 29% relative to embryos injected with control mRNA (Figure 7.8h-i). Together, these results indicate that Sox21 can regulate *Klf2* and *Tdgf1* genes in the 4-cell embryo.

7.3.2 Rescue of Sox21 siRNA phenotype by Klf2 and Tdgf1 co-overexpression

Above results suggested that Klf2 and Tdgf1 could be downstream targets of Sox21 because of two reasons: (1) reduction and overexpression of Sox21 resulted in a respective downregulation and upregulation of *Klf2* and *Tdgf1* mRNA expression (section 7.3.1); and (2) reducing Klf2 and Tdgf1 can phenocopy the Sox21 siRNA phenotype (section 7.2). To functionally test whether Klf2 and Tdgf1 act downstream of Sox21 to eventually bias the cell fate choice within the blastocyst, the Sox21 siRNA phenotype was examined with simultaneous Klf2 and Tdgf2 overexpression. To this end, one blastomere of a 2-cell stage embryo was injected with control siRNA or Sox21 siRNA or Sox21 siRNA + *Klf2* mRNA + *Tdgf1* mRNA (Figure 7.9a). In all the groups, *Gap-RFP* mRNA was co-injected to visualise injected clone of cells. The embryos were cultured until the late blastocyst stage (E4.5) and were assessed for the contribution of injected clone to the TE (marked by Cdx2), EPI and PE (marked by Sox17) lineages. As expected, Sox21 siRNA-injected clone of cells showed bias towards the TE lineage and showed decreased contribution to both EPI and PE lineages, compared to control siRNA-injected clone of cells (Figure 7.9b-c). The Sox21 siRNA-injected clone of cells that were co-injected with *Klf2* mRNA + *Tdgf1* mRNA, however, had very similar levels of contribution to all three lineages, compared to control siRNA-injected clone of cells (Figure 7.9b-c). Thus, these results indicated that *Klf2* mRNA + *Tdgf1* mRNA can rescue the

bias in cell fate choice after Sox21 siRNA, providing evidence that they act downstream of Sox21. It will be more insightful to study the effect of simultaneous Klf2 and Tdgf2 overexpression on Sox21 KO embryos, rather than Sox21 siRNA-injected embryos.

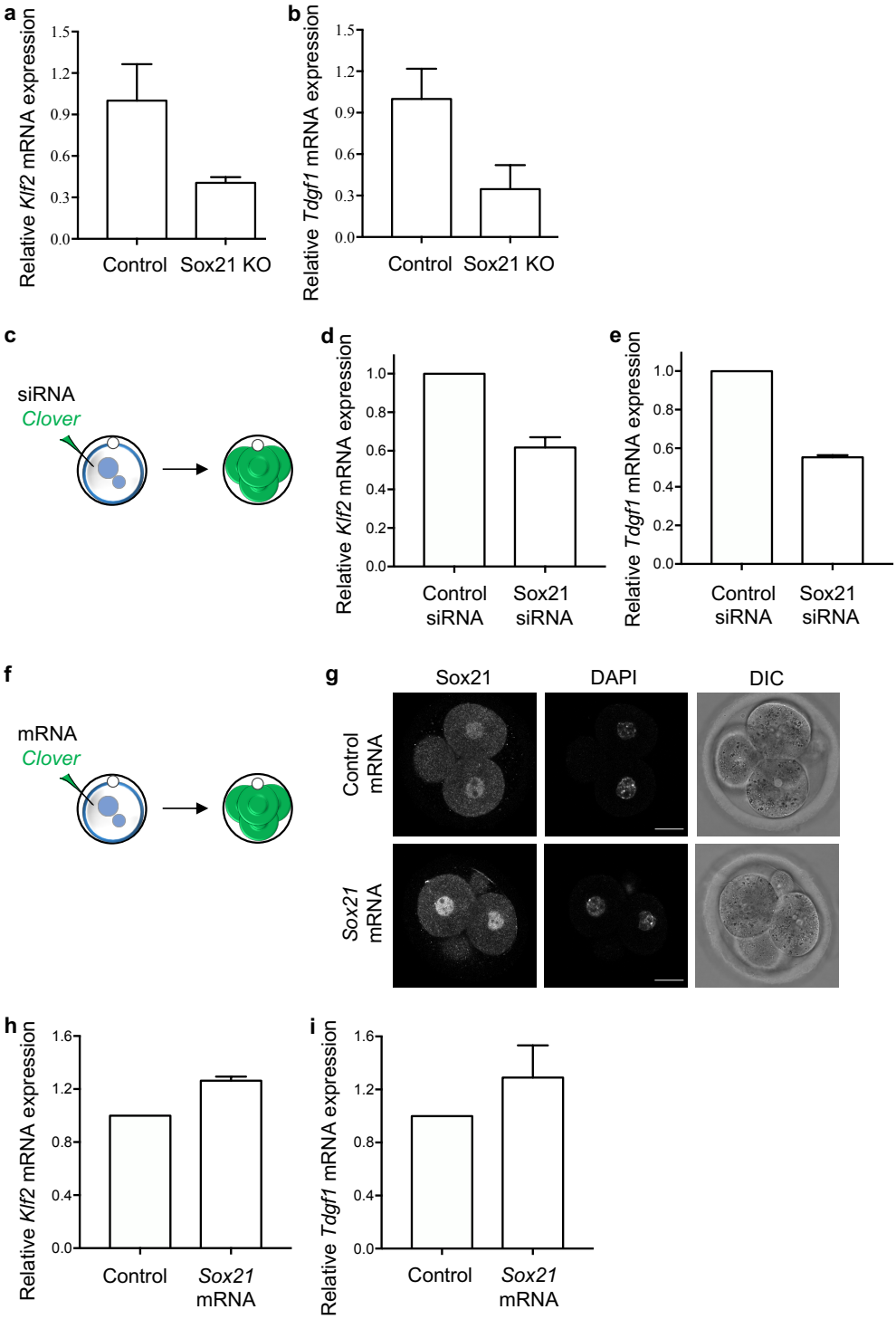

Figure 7.8. Effect of Sox21 on *Klf2* and *Tdgf1* mRNA expression at the 4-cell stage. *Klf2* (**a**) and *Tdgf1* (**b**) mRNA expression levels (relative to the mean 4-cell stage mRNA expression levels in controls) in Sox21 KO and control embryos, determined using RNA-sequencing. Control n = 4 embryos,

Sox21 KO n = 4 embryos. (**c**) Zygotes were injected with siRNA and mRNA was assessed at the 4-cell stage using qRT-PCR for (**d**) and (**e**). *Klf2* (**d**) and *Tdgf1* (**e**) mRNA expression levels in control siRNA-injected and Sox21 siRNA-injected embryos (relative to the control siRNA-injected embryos). Control siRNA n = 20 embryos, Sox21 siRNA n = 20 embryos. (**f**) Zygotes were injected with mRNA and analyzed at the 4-cell stage using immunostaining for (**g**) or using qRT-PCR for (**h**) and (**i**). (**g**) Immunostaining of Sox21 in control mRNA-injected and *Sox21* mRNA-injected 4-cell embryos. Scale bars, 20 μm. Control mRNA n = 4 embryos, *Sox21* mRNA n = 6 embryos. *Klf2* (**h**) and *Tdgf1* (**i**) mRNA expression levels in control mRNA-injected and *Sox21* mRNA-injected embryos (relative to the control mRNA-injected embryos). For (**h**) and (**i**), Control mRNA n = 12 embryos, *Sox21* mRNA n = 12 embryos. For all the graphs, data are mean ± s.e.m.

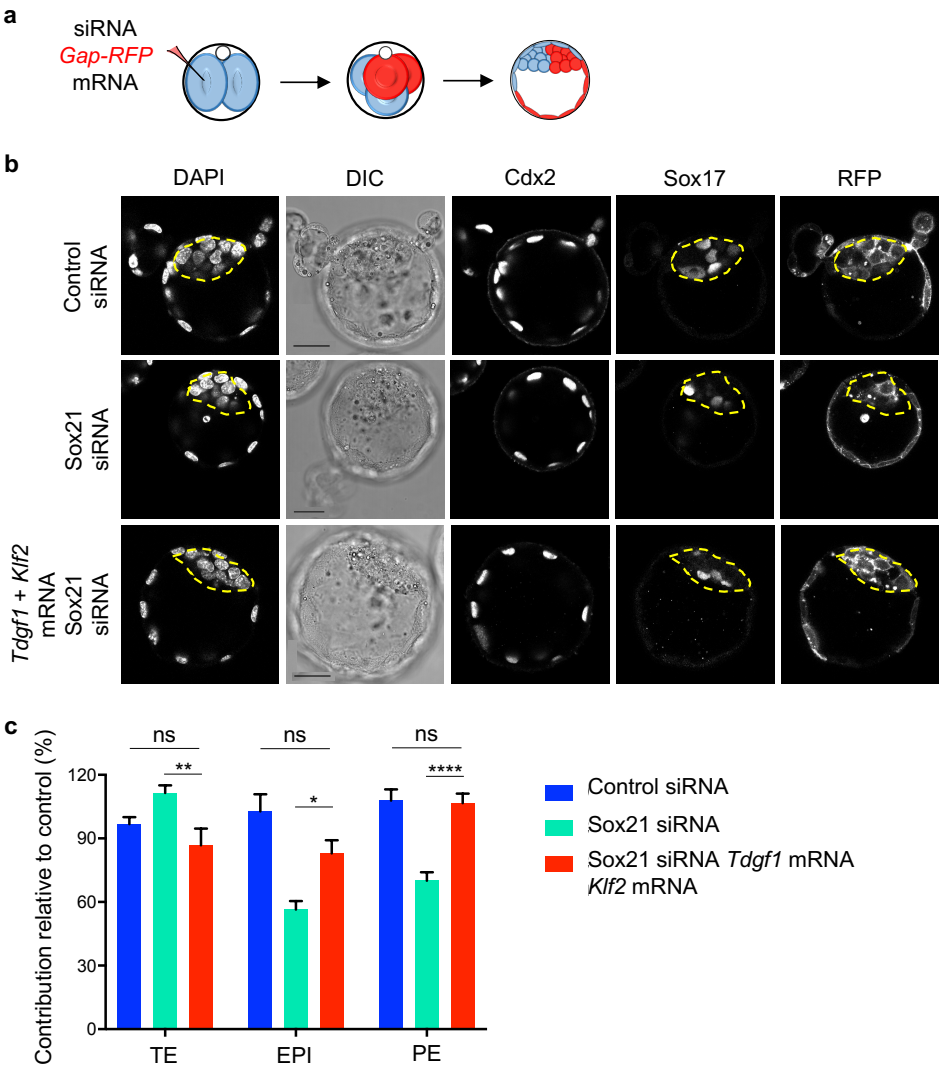

Figure 7.9. Rescue of Sox21 siRNA phenotype by *Klf2* and *Tdgf1* mRNA. (**a**) Sox21 siRNA or control siRNA was injected into one blastomere of 2-cell stage embryos, along with *Gap-RFP* mRNA and/or *Klf2* mRNA plus *Tdgf1* mRNA. The embryos were cultured until the late blastocyst stage. (**b**) The embryos were immunostained for Cdx2, Sox17, RFP and DAPI to assess all three lineages: TE (Cdx2-positive cells), EPI (DAPI-positive, Sox17-negative, Cdx2-negative cells) and PE (Sox17-positive

cells). Scale bars, 30 μm. Yellow lines indicate the ICM. (**c**) Relative contribution of the injected clone of cells was assessed in all three lineages (relative to the contribution of non-injected clone). Data are mean ± s.e.m. and ns = not significantly different. One-way ANOVA test was used for TE and EPI, **p < 0.01 and *p < 0.05. Kruskal-Wallis test was used for PE and ****p < 0.0001. Control siRNA n = 16 embryos, Sox21 siRNA n = 12 embryos, Sox21 siRNA *Klf2* mRNA *Tdgf1* mRNA n = 12 embryos.

7.4 Effect of Carm1 upregulation on Klf2 and Tdgf1 expression

It was shown by Torres-Padilla *et al*. (2007), Goolam *et al.* (2016) and White *et al.* (2016) that Carm1 inhibition has a significant effect on pluripotency within the blastocyst. It was also shown that Sox21 expression is significantly affected when Carm1 activity is altered - inhibition of Carm1 led to a complete loss of Sox21 protein and conversely, Carm1 overexpression led to a significant upregulation of *Sox21* mRNA (Goolam *et al*., 2016). Other pluripotency regulators, including Sox2 and Nanog, were also shown upregulated after Carm1 overexpression. It was decided to test whether Klf2 and Tdgf1 might also be regulated by Carm1 in the embryo.

To this end, zygotes were injected with mRNA encoding Carm1 and were allowed to develop until the early-to-mid 8-cell stage (Figure 7.10a). First, the effectiveness of *Carm1* mRNA in upregulating Carm1 was tested by fixing the injected embryos at the 8-cell stage and immunostaining them for Carm1. Numerous bright foci were identified in the nucleus after Carm1 immunostaining of the embryos. Injection of *Carm1* mRNA resulted in an increase in the Carm1 protein expression (increase in the number of foci) at the 8-cell stage (Figure 7.10b). To check the effect of Carm1 overexpression on *Klf2* and *Tdgf1* expression, the injected embryos were analyzed by qRT-PCR at the 8-cell stage. *Carm1* mRNA injection significantly increased *Klf2* mRNA level by 68% (Figure 7.10c). However, *Tdgf1* mRNA levels were not affected by Carm1 overexpression (Figure 7.10d). This suggests that Carm1 can regulate Klf2, but not Tdgf1 in the embryo.

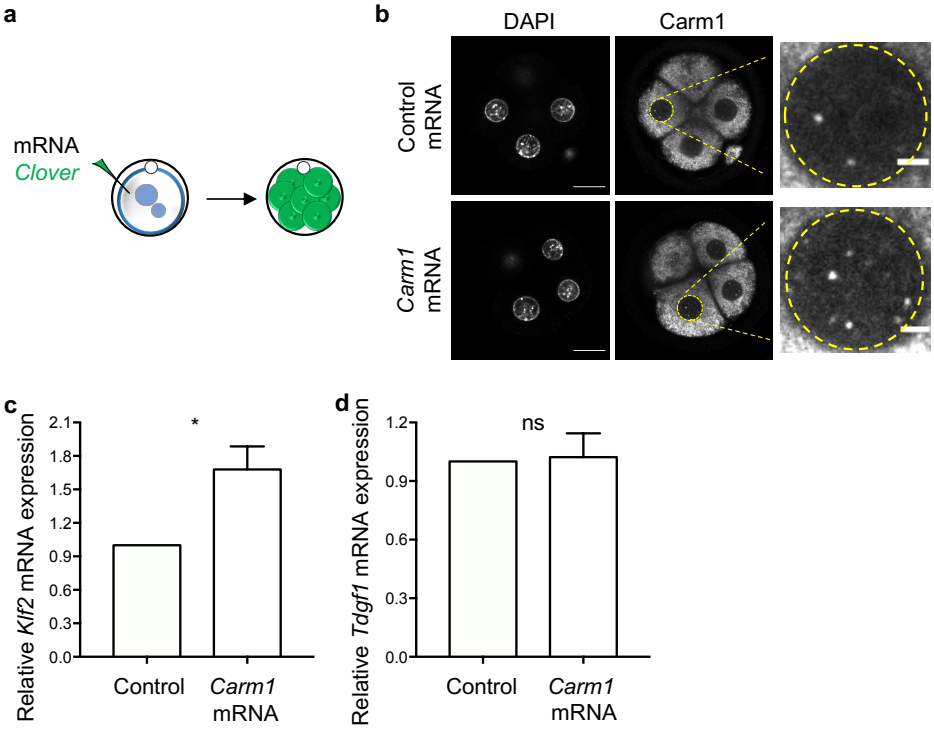

Figure 7.10. Effect of Carm1 overexpression on *Klf2* and *Tdgf1* mRNA expression at the 8-cell stage. (**a**) Zygotes were injected with mRNA and analyzed at the 8-cell stage using immunostaining for (**b**) or using qRT-PCR for (**c**) and (**d**). (**b**) Immunostaining of Carm1 in control mRNA-injected and *Carm1* mRNA-injected 8-cell embryos. Scale bars, 20 μm. The yellow circles mark the magnified nuclear regions, scale bars, 3 μm. Control mRNA n = 14 embryos, *Carm1* mRNA n = 12 embryos. *Klf2* (**c**) and *Tdgf1* (**d**) mRNA expression levels in control mRNA-injected and Carm1 mRNA-injected embryos (relative to the control mRNA-injected embryos). For (**c**), Mann-Whitney test was used and *p < 0.05. Control mRNA n = 33 embryos, *Carm1* mRNA n = 28 embryos. For (**d**), Mann-Whitney test was used and ns = not significantly different. Control mRNA n = 43 embryos, *Carm1* mRNA n = 40 embryos. For both the graphs, data are mean ± s.e.m.

8 Discussion II

The work in Chapter 7 sought to investigate into the 'biased' model of the first cell fate decision with a focus on how Sox21 heterogeneity at the 4-cell stage can predict cell fate. The findings presented in this chapter suggest that Klf2 and Tdgf1 are two important downstream targets of Sox21. These genes were identified by comparing the transcriptome of Sox21 KO and wildtype 4-cell stage embryos. Then, the role of Klf2 and Tdgf1 in mediating cell fate choice due to heterogeneous Sox21 4-cell expression was investigated. Klf2 and Tdgf1 were considered possible downstream targets of Sox21 because both of them were downregulated in Sox21 KO embryos compared to wildtype (Figure 7.8a-b) and had similar mRNA expression profiles to Sox21 during pre-implantation stages of development (Figure 7.4a-c). Also, similar to *Sox21* mRNA (Figure 7.4d), mRNAs for *Klf2* and *Tdgf1* were expressed more in inner cells than outside cells at the 32-cell stage, respectively (Figure 7.4e-f), hinting at their possible role within the inner cells. While mRNA expression levels are not a guarantee that same differences get translated on the protein expression levels, the above-mentioned criteria, combined with their known function in the available literature were used to pick relevant genes. In mESCs, both Klf2 and Tdgf1 have been shown to inhibit the TE determinants, such as Cdx2, and are directly involved in sustaining their ground state pluripotency (Qiu *et al*., 2015; Fiorenzano *et al*., 2016). Also, Fiorenzano *et al*. have shown that Tdgf1 deficiency in mESCs attenuates their restriction to embryonic lineage. Using this, the functional significance of Klf2 and Tdgf1 was elucidated in early mouse development. Since, the co-overexpression of these genes rescued Sox21 siRNA phenotype (Figure 7.9), it validates the criteria used to narrow down the gene list. Since, both of these genes showed, previously unknown, mouse pre-implantation phenotype (Figure 7.5, 7.6), it suggests that this dataset can be utilized further to find novel molecular players in the pre-implantation mouse development. Also, this further supports the previous Goolam *et al.* (2016) studies that first reported that Sox21 heterogeneity at the 4-cell stage is not random but is functionally relevant to subsequent development. Overall, more sample numbers will be required to consolidate the results in this chapter. However, the phenotype shown by Klf2 and Tdgf1 knockdown in the blastocyst formation are consistent with the findings in mESCs, where these genes positively regulate pluripotency (Qiu *et al*., 2015; Fiorenzano *et al*., 2016).

Klf2 is a member of 'Klf' family proteins which have highly conserved C_2H_2-type three zinc finger domains at the C-terminal that allow them to bind to GC-rich sites and 5'-CACC-3' motifs in promoters and enhancers of the genes they regulate (McConnell and Yang, 2010). Since Klf proteins have highly variable N-terminal sequences, they can interact uniquely with specific binding partners, giving them functional diversity and specificity (McConnell and Yang, 2010).

Klf2 is predominantly expressed in lungs and some expression is also seen in spleen, heart and skeletal muscle (Anderson *et al*., 1995). Klf2 has been shown to be involved in mediating various functions, including, late-stage lung development (Wani *et al*., 1999), T-cell survival and migration (Kuo *et al*., 1997; Carlson *et al*., 2006), vascular development (Novodvorsky and Chico, 2014), skeletal muscle regeneration (Manoharan *et al*., 2019), inhibitor of adipocyte differentiation (Wu *et al*., 2005), and erythropoiesis (Basu *et al*., 2005). Klf2-/- mice die *in utero* between E11.5 and E13.5 and have retarded growth, craniofacial abnormalities, abdominal bleeding, and severe intraembryonic haemorrhaging (Basu *et al*., 2005). Despite its significance in the blastocyst formation (Figure 7.5), successful development of mice lacking Klf2 until E11.5 could be because of two possible reasons. Firstly, there could be maternal contribution of Klf2, sufficient to take embryos successfully through early stages of development. Since Basu *et al.* (2005) generated Klf2-/- mice by times mating between Klf2+/- male and Klf2+/- female, maternal contribution of Klf2 is likely. Secondly, Klf2 could be part of a functionally redundant mechanism. Given the highly regulative nature of mouse embryo, it is likely that other members from the 'Klf' family could functionally compensate for Klf2 loss to ensure successful development. Klf2, Klf4 and Klf5 have been shown to share overlapping functions in maintaining self-renewal of mESCs via activation of naïve pluripotency TFs (Jiang *et al.*, 2008; Yamane *et al*., 2018). It will be interesting to investigate if there are changes in *Klf4* and *Klf5* levels after knocking down *Klf2* at the 4-cell stage, and to investigate the effect of triple knockdown for Klf2, Klf4 and Klf5 on the blastocyst formation.

Tdgf1/Cripto is a member of epidermal growth factor (EGF)-Cripto/Fibroblast Growth factor related ligand (FRL1)/Cryptic (CFC) family proteins. Structurally, it is a cell membrane-bound protein containing signal peptide for extracellular secretion at the N-terminus, a modified EGF-like domain, a cysteine-rich CFC-motif and a short hydrophobic domain at the C-terminus for glycosylphosphatidylinositol (GPI) modification (Minchiotti *et al*., 2002). In mouse embryos, Tdgf1 expression is seen in ICM at E3.5 in a salt-and-pepper fashion and restricts to EPI at E4.5 (Fiorenzano *et al*., 2016). By E6.75, Tdgf1 expression localizes to primitive streak and forming mesoderm (Ding *et al*., 1998). At E8.0, Tdgf1 expression is seen in cardiac progenitors (Ding *et al*., 1998) and at E9.5, its expression is restricted to the outflow region of the heart (Johnson *et al*., 1994). Tdgf1 null mice die by E7.5 due to defects in anterior-posterior axis organization and formation of mesoderm derivatives such as somites and cardiac tissue (Ding *et al*., 1998). Besides its role in axial organization and cardiogenesis in embryos, Tdgf1 is a regulator of both mESCs and mEpiSCs (EPI stem cells; similar to primed pluripotent early post-implantation mouse EPI). Tdgf1 is involved in their self-renewal, metabolic reprogramming in mESCs-mEpiSCs transition, and restricting ESC differentiation towards embryonic lineage (Fiorenzano *et al*., 2016). Furthermore, Tdgf1 has been shown to function

as oncogene during tumorigenesis, driving proliferation, migration, invasion, and stimulating angiogenesis (Klauzinska *et al*., 2014). Similar to its role in EPI undergoing gastrulation, Tdgf1 facilitates epithelial-mesenchymal transition in cancer stem cells, contributing to cancer progression (Klauzinska *et al*., 2014). Tdgf1 interacts with various signalling pathways to drive the above-mentioned processes. Most importantly, it functions as coreceptor for the transforming growth factor-β family proteins including Nodal and Activins (Minchiotti *et al*., 2002; Klauzinska *et al*., 2014; Fiorenzano *et al*., 2016).

Using the above-mentioned criteria, Klf2 and Tdgf1 were selected to test for their functional significance in lineage segregation by knocking them down individually using siRNAs. Clonal knockdown of Klf2 as well as Tdgf1 biased the clones towards a TE cell fate (Figure 7.5, 7.6). Also, Klf2 and Tdgf1 knockdown led to Cdx2 upregulation at the 8-cell stage (Figure 7.7), similar to the effect of Sox21 downregulation on Cdx2. This is consistent with the findings in mESCs, where Sox21, Klf2 and Tdgf1 repress Cdx2 (Kuzmichev *et al*., 2012; Qiu *et al*., 2015; Fiorenzano *et al*., 2016). It will be interesting to also investigate if clonal Klf2 and Tdgf1 depletion result in clonal elevation of Cdx2 protein at the 8-cell stage, and consequently, if these clones of cells undergo more symmetric divisions compared to asymmetric divisions. Finally, Klf2 and Tdgf1 proved to be downstream of Sox21 as they rescued the bias in cell fate choice when co-overexpressed in Sox21 reduced blastomeres. To investigate further the relationship between Klf2, Tdgf1 and Sox21 during mouse pre-implantation development, it will be interesting to investigate the effect of the following clonal perturbations on lineage segregation: Klf2 mRNA with Sox21 siRNA, Tdgf1 mRNA with Sox21 siRNA, Klf2 mRNA with Tdgf1 siRNA, and Tdgf1 mRNA with Klf2 siRNA. Also, it is likely that besides Klf2 and Tdgf1, other genes are downstream of Sox21 at the 4-cell stage. To identify the network of genes through which Sox21 mediates cell bias, the list of differentially regulated Oct4/Sox2 targets in Sox21 KO embryos generated here could be fully investigated.

Since findings from Goolam *et al.* (2016) suggested that the heterogenous Carm1 activity at the 4-cell stage could regulate Sox21 heterogeneity, it was next considered that Carm1 might also be regulating Klf2 and Tdgf1. Here, it was found that Carm1 upregulation resulted in an increase in *Klf2* mRNA (Figure 7.10c) but did not affect *Tdgf1* mRNA (Figure 7.10d). A possible reason for this could be that Klf2 is a Sox2 target while Tdgf1 is an Oct4 target (Figure 7.1f). Goolam *et al.* (2016) showed that Carm1 upregulation resulted in an increase in *Sox2* mRNA but did not affect *Oct4* mRNA. Also, White *et al*. (2016), showed that Carm1 downregulation reduced the DNA-binding accessibility of Sox2 but did not affect Oct4-DNA binding at the 4-cell stage. However, it does not exclude the possibility that Carm1 might indirectly affect Oct4

activity and Tdgf1. Together, it can be hypothesized that heterogeneity along Carm1-Oct4/Sox2-Sox21-Klf2/Tdgf1 axis at the 4-cell stage influences cell fate decisions (Figure 8.1).

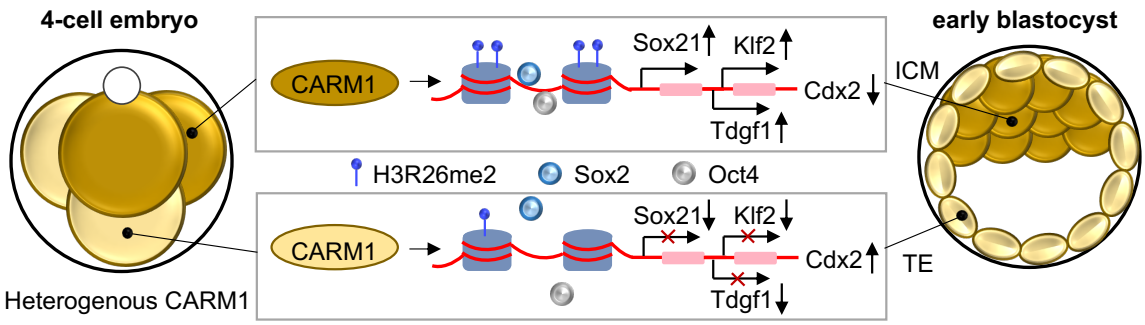

Figure 8.1. Model for the role of Sox21 4-cell heterogeneity in cell fate decisions (Adapted from Figure 6.1)**.** Carm1 is differentially expressed in 4-cell embryos and regulate the level of histone H3R26 methylation. Higher methylation allows long-lived DNA binding of Oct4 and Sox2. This leads to higher expression of Sox21, which leads to higher expression of its downstream targets such as Klf2 and Tdgf1. Klf2 and Tdgf1 levels direct cell fate by repressing Cdx2 such that cells with lower Klf2 or Tdgf1 levels at the 4-cell stage show lower tendency to contribute to pluripotent ICM lineages.

While Goolam *et al.* (2016) have demonstrated the significance of Sox21 in the pre-implantation embryo development, Sox21 KO mice are viable (Kiso *et al*., 2009) and show correct lineage specification (Mubeen Goolam's PhD Thesis unpublished data). Since mouse embryo development is highly regulative, one of the possible explanations is that Sox21 is part of a functionally redundant mechanism. It could be hypothesized that some other factor compensates for the loss of Sox21 at the 4-cell stage. The dataset generated in this study to identify downstream targets for Sox21 can also be utilized to mine genes that could compensate and have a functional overlap with Sox21. It will be interesting to investigate the role of *Slc25a36* and *Runx1t1* genes in Sox21 KO embryos since they were both upregulated in Sox21 KO 4-cell embryos compared to wildtype, and both were identified as Oct4 targets and significantly heterogenous at the 4-cell stage (Figure 7.1f). Also, Slc25a36 has been shown to maintain the pluripotent state of mESCs (Xin *et al*., 2019). *Dppa5a*, although not significantly heterogenous at the 4-cell stage, is another interesting Oct4 target that was upregulated in Sox21 KO embryos compared to wildtype (Figure 7.1f). Dppa5a has been shown to regulate Nanog in human pluripotent stem cells as well as increase the reprogramming efficiency to obtain induced pluripotent stem cells (Qian *et al*., 2016).

Overall, the results described in Chapter 7 gave further insight into the 'biased' model of cell fate decision and revealed novel molecular players in the formation of the blastocyst.

9 Concluding Remarks

Mouse embryo employs several regulative and adaptive mechanisms at various stages of development to prepare itself for successful development beyond implantation. The work in this thesis has been divided into two major sections, aimed at understanding better such mechanisms: (1) the first section attempted to characterize the mechanisms used by early mouse embryo to ensure only the chromosomally fit cells proceed through the post-implantation development in the embryonic lineage; (2) the second section extended our understanding of the 'biased' model of the first cell fate decision and identified novel factors that bias cell fate specification.

In Chapter 4, the mouse model for chromosome mosaicism, previously developed by the Zernicka-Goetz lab (Bolton *et al.*, 2016), was utilized to investigate the fate of chromosomally abnormal cells in mouse embryos. The fate of aneuploid cells was investigated specifically in the embryonic lineage in both aneuploid embryos and 1:1 diploid-aneuploid mosaic chimeras during pre-, peri- and early post-implantation stages of development. Using time-lapse imaging, it was revealed that aneuploid cells were progressively depleted from the diploid-aneuploid mosaic EPI during blastocyst maturation via apoptosis. The same result was found in the case of aneuploid pre-implantation EPI using pan-caspase pharmacological inhibition. Then, to investigate the fate of remaining aneuploid cells within the embryonic lineage beyond the blastocyst stage, a 72-hour *in vitro* culture method was developed that recapitulated the development of the EPI from the late blastocyst to early post-implantation stages without interruption. Using this culture system, it was found that aneuploid embryos displayed lower post-implantation developmental efficiency and had significantly fewer cells remaining in the EPI lineage than diploids after 72 hours. The time-lapse imaging of labelled aneuploid cells (from H2B-GFP transgenic mice) and cleaved caspase-3 immunostaining together indicated the involvement of apoptosis in the elimination of aneuploid cells from aneuploid EPI beyond blastocyst stage. The same culture system was used to monitor the fate of aneuploid and diploid cells in diploid-aneuploid mosaics beyond blastocyst stage. Interestingly, unlike aneuploid embryos, diploid-aneuploid mosaics displayed equivalent post-implantation developmental efficiency and had similar number of cells in the EPI as diploid-diploid chimeras after 72-hour *in vitro* culture. When composition of the EPI of the diploid-aneuploid mosaics was analysed at the end of the 72-hour *in vitro* culture, it was found that aneuploid cells were preferentially eliminated. The time-lapse imaging indicated the involvement of apoptosis in the elimination of aneuploid cells from the diploid-aneuploid mosaic EPI beyond blastocyst stage. On the other hand, diploid cells in the diploid-aneuploid mosaic EPI displayed preferentially increased proliferation during peri-implantation stage. Thus, elimination of aneuploid cells and

simultaneous over-proliferation of diploid cells allowed successful post-implantation development of diploid-aneuploid mosaics with mostly diploid cells succeeding in the EPI. However, it will be beneficial to employ a live marker of ploidy status of each chromosome in a cell for the future experiments, since reversine does not induce aneuploidy in 100% of the treated cells. Also, it will be benefical to develop an *in vitro* culture system, using which the mouse embryos can be cultured uninterrupted from pre- to post-implantaiton stages with all the lineages intact. Together, these will allow to determine the precise fate of aneuploid cells in all lineages and the level of depletion at different stages of early development. Overall, the findings in Chapter 4 provide direct evidence for the 'clonal depletion' hypothesis, where the anueploid clone in the EPI undergoes depletion by apoptosis. Since, the over-proliferation of diploid EPI cells is key to the successful post-implantation development of diploid-aneuploid mosaics, it is important to investigate further two outstanding questions: (i) what is the threshold proportion of diploid to aneuploid cells in mosaics, above which they can result in viable births; and (ii) the mechanisms employed by diploid cells for size regulation in diploid-aneuploid mosaic EPI. The mouse model of chromosome mosaicism using reversine used in this thesis can be used to gather insights on both these questions. Besides, it will be important to also use some specific monosomy and trisomy mouse lines to investigate the critical cell number threshold required for viability. Lastly, it is worth noting that human aneuploid embryos have been reported to display high levels of cellular fragmentation (Chavez *et al*., 2012), unlike reversine-treated aneuploid mouse embryos. However, the hypothesis that the human embryo responds to lagging chromosomes by forming a cellular fragment, remains speculative. Therefore, there is still a pressing need for further research on the animal models that share greater similarities with the human such as cows or rhesus macaques.

Next, the mechanisms triggering this apoptosis of aneuploid cells in the embryonic lineage were investigated in aneuploid embryos during pre- and peri-implantation stages of development. Since, aneuploidy was induced using reversine, global cellular responses of aneuploidy were assessed in the early mouse embryos, especially in the EPI lineage. Elevated levels of heat shock protein 70 indicated chronic misfolding in pre-implantation aneuploid embryos. Consequently, autophagy and p53 pathway were upregulated in aneuploid late blastocysts. For future experiments, it will be interesting to investigate if proteotoxic stress and metabolic stress induced by aneuploidy are sufficient for this upregulation of p53 and autophagy. The functional significance of upregulated autophagy and p53 pathway was determined using loss-of-function studies. Disruption of autophagy and p53 pathway, separately, resulted in a significant reduction in the number of dying cells in the ICM of aneuploid embryos. Furthermore, depletion of p53 pathway resulted in a significant decrease in autophagy in the aneuploid EPI. So, these results indicated that p53-autophagy cascade

eliminated aneuploid cells from the ICM during blastocyst maturation. However, how p53 upregulates autophagy in the aneuploid EPI cells remains unanswered. Similar to pre-implantation stage, peri-implantation stage aneuploid EPI also displayed upregulated autophagy. Finally, when autophagy was inhibited from the early blastocyst to the early post-implantation stage, autophagy-inhibited aneuploid embryos displayed equivalent post-implantation developmental efficiency and had similar number of cells in the EPI lineage as diploids. Together, this elucidated that autophagy eliminates aneuploid cells from the EPI from pre- to post-implantation stages. Even though autophagy was inhibited at two different stages, using Atg5 siRNA and BafA1, to check if the entire autophagy flux was involved in the elimination of aneuploid cells, it is important to validate it further. This can be done by combining Premo™ Autophagy Tandem Sensor RFP-GFP-LC3B Kit with caspase sensor and following the embryo development in real-time, both during blastocyst maturation as well as during implantation. Furthermore, it is essential to investigate the threshold level of autophagy, beyond which it gets lethal for the EPI in the early mouse embryo. Overall, this is the first study to establish a direct link between autophagy and apoptosis in the development of aneuploid mammalian embryos. This is also the first study to provide direct evidence that autophagy can be utilized as a defence mechanism in the EPI to get rid of abnormal cells during the early stages of mouse embryo development. In the future, it will be important to investigate whether the cellular response of reversine-induced aneuploidy is also seen in the case of specific aneuploidies and to understand what the other phenotypic effects of specific aneuploidies are. It will also be of future interest to explore whether similar mechanisms extend to human embryos, thereby further increasing our understanding of early pregnancy loss.

In Chapter 7, transcriptome of Sox21 KO and wildtype 4-cell stage embryos was compared. A list of 25 differentially expressed Oct4 and/or Sox2 target genes were identified. Of these, Klf2 and Tdgf1 were explored further as candidate downstream targets of Sox21 due to three reasons: (1) similar mRNA expression profiles to Sox21 profile during pre-implantation stages of mouse embryo development and mRNA enrichment in inside cells at the 32-cell stage, (2) their downregulation after Sox21 knockdown/KO and upregulation after Sox21 overexpression at the 4-cell stage, and (3) their known functions in sustaining mESCs' naïve pluripotency, similar to known Sox21 function. Clonal depletion of Klf2 and Tdgf1, individually, biased the cells away from the pluripotent ICM lineages. Similar to the effect of Sox21 depletion, this was due to Cdx2 upregulation after Klf2 and Tdgf1 depletion. Finally, co-overexpression of Klf2 and Tdgf1 was successful in rescuing the the bias in cell fate choice after Sox21 depletion. This suggested that Klf2 and Tdgf1 are important Sox21 downstream targets that can influence lineage segregation at the blastocyst stage. However, it is important to perform the experiments in Chapter 7 with more sample numbers since these are preliminary findings. In

addition, it will be important to explore the mechanistic relationship between LincGET, Carm1, Sox21, Klf2 and Tdgf1. It is also important to investigate if the genes involved in 4-cell hetereogeneity such as Sox21, Klf2, Tdgf1 are dispensable for successful pre-implantation development because there is a compensatory mechanism at play or because they are only required to create an initial bias that can then get amplied as the embryo develops and mediate lineage fates. This will shed further light on the balance between pre-patterning and regulation in the early cleavage-stage mouse embryos.

Overall, findings from Chapters 4 and 7 allow us to understand the mechanisms through which transcriptional and chromosomal heterogenetities in the early cleavage-stage embryos affect the overall number of cells within each lineage as the embryo develops. In this thesis, it is shown that while transcriptional heterogeneity at the 4-cell stage affects the number of cells within each lineage by significantly affecting the lineage segregation (Chapter 7), chromosomal heterogeneity, i.e. aneuploidy, has been shown to do the same by affecting the survival of the lineages already segregated (Chapter 4). Both of the mechanisms are key to developmental plasticity of the early mammalian system and to the success of post-implantation embryo development. However, more experiments are needed to better understand how early mouse embryo adapts to transcriptional and chromosomal heterogenetities. It will be interesting to introduce aneuploidy at the 2-4 cell division instead of 4-8 cell division to obtain chromosomal heterogeneity at the 4-cell stage, and then follow the pre-implantation development of the embryo to see if aneuploidy impacts lineage segregation or the survival of segregated lineages in this case. This will allow us to understand two aspects of early mouse embryo development: (i) does the mechanistic response of mouse embryos to heterogeneities depends on the stage of development at which the heterogeneity was introduced; and (ii) do mouse embryos have similar mechanisms to handle different kinds of heterogeneities introduced at the same stage of development. Further, if aneuploidies introduced during the 2-4 cell division do affect lineage segregation, it will be interesting to see if the aneuploid cell that goes to the epiblast lineage shows higher levels of Carm1 and Sox21. However, if aneuploidies introduced during the 2-4 cell division show similar phenotype to as when introduced during the 4-8 cell division (Chapter 4), it will be interesting to suppress the apoptosis by overexpressing bcl2 to see if now aneuploidy affect lineage segregation. Besides, since early cleavage stage human embryos display both transcriptional heterogeneity (Shi *et al*., 2015) and aneuploidy, it will be interesting to explore if the two kinds of heterogeneities have similar cause, or if the transcriptional hetereogeneity causes aneuploidy. Together, the results shown in this thesis and the above-mentioned future experiments will bring us closer to understanding the first few days of our lives.

10 Materials and Methods

Pre-implantation embryo collection and culture

This research has been carried out following regulations of the Animals (Scientific Procedures) Act1986 - Amendment Regulations 2012 - reviewed by the University of Cambridge Animal Welfare and Ethical Review Body (AWERB). Animals were maintained in the Animal Facility of Gurdon Institute at 12:12 light cycle and provided with food and water *ad libitum*. 4- to 6-week-old F1 (C57Bl/6 x CBA) females were injected with 10 IU of pregnant mare's serum gonadotrophin (PMSG, Intervet) and, 48 hours later, with 10 IU of human chorionic gonadotrophin (hCG, Intervet). These super-ovulated mice were then mated with F1 (C57Bl/6 x CBA) males or, where indicated, with Histone H2B-GFP or mT/mG males. 2-cell stage embryos were recovered in M2 medium supplemented with 4mg/ml BSA. Zygotes were recovered in M2 medium supplemented with 1mg/ml hyaluronidase to get rid of cumulus cells. After collection, embryos were cultured in drops of KSOM media (Millipore) under mineral oil (Biocare Europe) in 37 °C and 5% CO_2.

Drug treatments

Reversine (Cayman Chemicals), Z-VAD-FMK (Enzo Life Sciences), Bafilomycin A1 (Sigma-Aldrich) and Rapamycin (Millipore) were dissolved in dimethylsulfoxide (DMSO) (Sigma-Aldrich). For pre-implantation embryos, these drugs were used at following final concentrations in KSOM respectively: 0.5 μM (1:2000), 20 μM (1:1000), 160.6 nM (1:800) and 400 nM (1:2500). For 72-hour *in vitro* peri-implantation culture of ICMs, Bafilomycin A1 was used at 1 nM in IVC1. Control embryos were incubated in the equivalent DMSO concentration. SYTOX Orange nucleic acid stain (Life technologies) was used to analyze cell death in the embryo. It was dissolved in DMSO and used according to manufacturer's instructions. Doxycycline (Clontech) was dissolved in water at 1 mg/ml concentration and colcemid (Cayman chemical) was dissolved in DMSO at 1 mg/ml concentration.

Generation of chimeric embryos

The zona pellucida of 8cell stage embryos was removed by treatment with acidic Tyrode's solution (Sigma-Aldrich). Two types of mosaic chimeras were created at the 8-cell stage.

Single chimera: The embryos were incubated in Ca^{2+}/Mg^{2+}-free M2 for 5 min and then disaggregated into individual blastomeres by gentle pipetting. Four control and four control/reversine-treated blastomeres were aggregated together in M2 to get an 8-cell chimera.

Double chimera: A control and a reversine-treated embryo were aggregated together in M2 to get a 16-cell chimera.
The chimeras were cultured in drops of KSOM media under mineral oil in 37 °C and 5% CO_2.

Pre-implantation time-lapse imaging

Embryos for live imaging were transferred to glass-bottom dishes (MatTek) and cultured within the individual interstices of a finely weaved nylon mesh (Plastok). Imaging was performed using a spinning disk confocal microscopy system (3i Intelligent Imaging Innovations) in 37 °C and 5% CO_2 and SlideBook software. The images were captured every 10-20 min in 65 μm stacks of 2.0-2.5 μm intervals.

Immnunosurgery

The zona pellucida was removed at the late blastocyst stage. Embryos/chimeras were exposed to 20% rabbit anti-mouse whole serum (Sigma-Aldrich) in M2 medium for 30 min at 37 °C. Next, they were incubated for with 20% guinea pig complement serum (Sigma-Aldrich) in M2 medium for 30 min at 37 °C. The damaged TE was removed by pipetting the embryos in M2.

Peri-implantation embryo *in vitro* culture and time-lapse imaging

To culture embryos through the pre- to post-implantation transition, the immunosurgery was performed at the late blastocyst stage. Two different protocols were used to culture them further. Both the protocols were developed by Francesco Antonica in Zernicka-Goetz's lab.
With Matrigel: 20 µl drop of ice-cold growth factor-reduced Matrigel (BD Biosciences) was placed in a well of a µ-Slide 8-well ibiTreat (Ibidi) dish and embryos were mouth pipetted inside the Matrigel drop. The dish was incubated for 5 min at 37 °C to allow the Matrigel to solidify. Then, 300 µl of prewarmed IVC1 medium was added to the well.
Without Matrigel: Micromesh (Microsurfaces) was placed in the centre of the glass-bottom dish. The, the dish was rinsed for 5 min with anti-adherence rinsing solution (Stemcell Technologies). Embryos were cultured within the individual interstices of the mesh in IVC1 medium under mineral oil.
In both the cases, imaging was performed using a spinning disk confocal microscope in 37 °C and 5% CO_2. The images were captured every 20 min in 50-90 μm stacks of 2.5 μm intervals.

IVC1 medium constitution: Advanced DMEM F12 (Thermo Fisher Scientific), 20% v/v heat-inactivated FBS (Stem Cell Institute), GlutaMAX (Thermo Fisher Scientific), 25 U/ml penicillin–25 µg/ml streptomycin (Thermo Fisher Scientific), 1 × ITS-X (Thermo Fisher

Scientific), 8 nM β-oestradiol (Sigma-Aldrich), 200 ng/ml progesterone (Sigma-Aldrich) and 25 μM *N*-aceyl-L-cysteine (Sigma-Aldrich)

Embryo transfers and post-implantation recovery and time-lapse imaging

Chimeras at the E3.5 blastocyst stage were transferred into the uterine horn of pseudo-pregnant females that had been mated with vasectomized males. The uterine transfers were performed by Bill Mansfield in the Animal Facility of Gurdon Institute. Early post-implantation embryos (E5.0) were dissected from the maternal decidua and recovered into M2 medium. For live imaging, chimeras were transferred to glass-bottom dishes and cultured in drops of prewarmed IVC medium (Advanced DMEM F12, 20% v/v heat-inactivated FBS, GlutaMAX, penicillin-streptomycin, 1 × ITS-X) under mineral oil for 36 hours. Imaging was performed using a spinning disk confocal microscopy system in 37 °C and 5% CO_2. The images were captured every 10 min in 70 μm stacks of 2.0 μm intervals. Post-implantation embryos were recovered with the help of Meng Zhu, Christos Kyprianou and Antonia Weberling in Zernicka-Goetz's lab.

siRNA preparation

For each target gene, three predesigned siRNAs (Qiagen) were supplied. They were mixed together in equal proportions. For control, AllStars Negative Control (Qiagen) siRNA was used. Lyophilized siRNAs were dissolved in nuclease-free water at 20 μM concentration and stored in -80 °C. The siRNA sequences are in Supplementary Table 10.1.

Table 10.1 Sequences of siRNAs used

Gene	siRNA1	siRNA2	siRNA3
sox21	CCCGGTTTGTATGTACATAGA	TACTCTGATTGTACTGTTGAA	TTGTATGTACATAGATGTATA
tdgf1	CACAGTGAATCCCTAATGTTA	ATGGAGGTACTGGGAATTTAA	CACGGAGATCTTGGCTGCTAA
p53	CCGGGTGGAAGGAAATTTGTA	ACCGCCGTACAGAAGAAGAAA	TGGAGAGTATTTCACCCTCAA
atg5	ATGGTTCTAGATTCAATAATA	CAGAAGGTTATGAGACAAGAA	ACAGTTTGTATTTCTGATTAA
slc25a36	AACGTCTACAATTAAACTCTA	TCCAATCTATTTGGAGACCAA	AAGGTATTTGCTGCAATACTA
klf2	CACGGATGAGGACCTAAACAA	ATGACCGATTGTATTTCTATA	CTGCGGCAAGACCTACACCAA

Preparation of constructs and mRNA

In order to make mRNAs for injections, pRN3P was used as the vector for all DNA constructs (Zernicka-Goetz *et al*., 1997). DNA constructs to prepare *Carm1*, *Clover*, *Gap-RFP* and *Gap-GFP* mRNAs for injection were already available in the Zernicka-Goetz lab. DNA constructs to prepare *CENPA-Zsgreen*, *Sox21*, *Klf2* and *Tdgf1* mRNAs were constructed. To prepare construct pRN3P-CENPA-Zsgreen, CENPA was PCR-amplified from mouse embryonic stem cell complementary DNA (cDNA) and cloned into pRN3P-Zsgreen vector (already available in

the Zernicka-Goetz lab), downstream of Zsgreen. To prepare construct pRN3P-Sox21, Sox21 cDNA was obtained from Thermo Fisher Scientific (MMM1013-202798743) and cloned into pRN3P vector. To prepare construct pRN3P-Klf2, Sox21 was PCR-amplified from pMXs-Klf2 (Addgene plasmid #50786) and cloned into pRN3P vector. To prepare construct pRN3P-Tdgf1, Tdgf1 cDNA was obtained from Dharmacon (MMM1013-202805617) and cloned into pRN3P vector. Primer sequences for preparing constructs are in Supplementary Table 10.2. The insert was PCR-amplified using Phusion High-Fidelity PCR (Thermo Fisher Scientific) - HF buffer was used to amplify CENPA and Tdgf1; GC buffer was used to amplify Sox21 and Klf2. The ligation was performed using T4 DNA ligase (Roche), followed by transformation into DH5-α *E. coli* (Stratagene). Positive clones were verified using sequencing before mRNA preparation.

To prepare mRNA, each DNA construct was linearized. KpnI-HF (New England Biolabs) was used to linearise pRN3P-CENPA-Zsgreen and pRN3P-Tdgf1; SbfI-HF (New England Biolabs) was used to linearise pRN3P-Sox21 and SfiI (New England Biolabs) was used to linearise other constructs. The mMessage mMachine T3 kit (Ambion, AM1348) was used to *in vitro* transcribe, according to the manufacturer's instructions. The mRNA was dissolved in nuclease-free water and stored in -80 °C.

Table 10.2 Sequences of primers used for preparing constructs

Primer	Sequence - (5' to 3')
CENPA-BamHI Fw	ATGCGGATCCAGAAGGCTTAGGGAAGGCG
CENPA-XbaI Rev	ATCGTCTAGAGAGTGGGCAGACCTCTGTG
Sox21-EcoRI Fw	ATGCGAATTCATGTCCAAGCCTGTGGACCAC
Sox21-BamHI Rev	CGTAGGATCCTCATAGCGCGGCAGCGTAG
Klf2-BamHI Fw	ATGCGGATCCAATGGCGCTCAGCGAGCCTATC
Klf2-XbaI Rev	ATGCTCTAGACTACATGTGTCGCTTCATGTGCAAGG
Tdgf1-EcoRI Fw	ATGCGAATTCATGGGGTACTTCTCATCCAG
Tdgf1-BamHI Rev	CGTAGGATCCACATGACACCTATACTTTCATATCT

Microinjection

siRNAs were used at a final concentration of 12 μM for microinjection. For microinjection, synthetic mRNAs were used at a final concentration of: 400 ng/μl *CENPA-Zsgreen*, 400 ng/μl *Carm1*, 500 ng/μl *Clover*, 300 ng/μl *Gap-RFP*, 100 ng/μl *Gap-GFP*, 50 ng/μl *Sox21*, 50 ng/μl *Klf2* and 60 ng/μl *Tdgf1*. Microinjection of embryos was performed in M2 medium under mineral oil on a glass slide with a depression using a Femtojet Microinjector system

(Eppendorf). Negative capacitance was used to facilitate membrane penetration. For Atg5 siRNA and p53 siRNA injections, *Gap-GFP* mRNA was used as an injection marker to confirm successful injection. For other experiments, injection marker used has been shown in the respective illustrations. Injected embryos were cultured finally in KSOM.

Quantitative real-time PCR (qRT-PCR)

Total RNA was extracted using the Arcturus PicoPure RNA Isolation Kit and qRT–PCR was performed using the Power SYBR Green RNA-to-CT 1-Step Kit (Life Technologies) and a StepOne Plus Real-time PCR machine (Applied Biosystems). The following program was used: 30 min 48 °C (reverse-transcription) followed by 10 min 95 °C followed by 45 cycles of 15 s 95 °C (denaturing) and 1 min 60 °C (annealing and extension). The ddCT method (Livak and Schmittgen, 2001) was used to determine relative levels of mRNA expression, with Gapdh as an endogenous control. Primer sequences are in Supplementary Table 10.3.

Table 10.3 Sequences of primers used for qRT-PCR

Gene	Forward Sequence - (5' to 3')	Reverse Sequence - (5' to 3')
gapdh	AGAGACGGCCGCATCTTC	CCAATACGGCCAAATCCGT
atg5	GGATGGGACTGCAGAATGACAG	AGCTTCTGGATGAAAGGCCG
lc3b	TTATAGAGCGATACAAGGGGGAG	CGCCGTCTGATTATCTTGATGAG
cyclin G1	TTTTATTTGGCTGTGAAAGCGAC	AGGTCTGAAACCGTGAACCTAT
p53	GTCACAGCACATGACGGAGG	TCTTCCAGATGCTCGGGATAC
p21	CCTGGTGATGTCCGACCTG	CCATGAGCGCATCGCAATC
p62	AGGATGGGGACTTGGTTGC	TCACAGATCACATTGGGGTGC
bcl2	GCTACCGTCGTGACTTCGC	CCCCACCGAACTCAAAGAAGG
tdgf1	CAGTGCGTTTGAATTTGGACC	GCACGAACTGGAAAGACCGA
klf2	CTCAGCGAGCCTATCTTGCC	CACGTTGTTTAGGTCCTCATCC
cdx2	AAACCTGTGCGAGTGGATG	TCTGTGTACACCACCCGGTA
slc25a36	GACACGCTGGTGCATCTGTT	CTACTCGGTTCACACTGGCT

Immunofluorescence and imaging

Embryos/mESCs were fixed in 4% PFA for 20 min at room temperature. They were then permeabilized, washed in PBST (0.1% Tween 20 (Sigma-Aldrich) in PBS) and incubated in blocking solution at 4 °C for 4 hours and then with primary antibodies in blocking solution for overnight at 4 °C. They were then washed in PBST and incubated with secondary antibodies in blocking solution for 1 hour, washed again and incubated with DAPI (Thermo Fisher Scientific) for 5 min. For antibodies, anti-LC3B and anti-Carm1, embryos were fixed in ice-cold

100% Methanol (Sigma-Aldrich) for 20 min at -20 °C. Confocal imaging was carried out using Leica SP5 (LAS AF software) inverted confocal microscope.
For pre-implantation embryos: Permeabilization was for 20 min in 0.5% Triton X-100 (Sigma-Aldrich) in PBS and blocking solution was 3% BSA (Sigma-Aldrich) in PBST
For peri- or post-implantation embryos/ICMs or mESCs: Permeabilization was for 15 min in 0.3% Triton X-100 (Sigma-Aldrich) in PBS and blocking solution was 10% FBS in PBST.

Primary antibodies used: mouse anti-Cdx2 (Biogenex, MU392-UC, 1:200), goat anti-Sox17 (R&D Systems, AF1924, 1:200), mouse anti-Oct3/4 (Santa Cruz Biotechnology, 5279, 1:200), goat anti-Gata4 (Santa Cruz Biotechnology, 1237, 1:200), rat anti-Podocalyxin (R&D Systems, MAB1556, 1:500), goat anti-Sox21 (R&D Systems, AF3538, 1:100), rabbit anti-RFP (Rockland, 600-401-379, 1:500), rat anti-GFP (Nacalai Tesque, 04404-84, 1:1000), mouse anti-HSP70 (Proteintech, 66183, 1:50), rabbit anti-p62 (Proteintech, 55274, 1:100), rabbit anti-phospho-p38 (Cell Signaling, 4631, 1:200), rabbit anti-cenpa (Cell Signaling, 2048, 1:100), rabbit anti-phospho-Histone H3 (Millipore, 06-570, 1:200), rabbit anti-cleaved caspase-3 (Cell Signaling, 9664, 1:200), rabbit anti-LC3B (Cell Signaling, 2775, 1:200) and mouse anti-Carm1 (Cell Signaling, 12495, 1:200).
Secondary antibodies used (1:400 each): Alexa Fluor 568 Donkey anti-Goat (A-11057, Thermo Fisher Scientific), Alexa Fluor 488 Donkey anti-Mouse (A-21202, Thermo Fisher Scientific), Alexa Fluor 568 Donkey anti-Mouse (A-10037, Thermo Fisher Scientific), Alexa Fluor 647 Donkey anti-Mouse (A-31571, Thermo Fisher Scientific), Alexa Fluor 568 Donkey anti-Rabbit (A-10042, Thermo Fisher Scientific) and Alexa Fluor 647 Donkey anti-Rabbit (A-31573, Thermo Fisher Scientific).

Image processing

All images and movies were exported to ImageJ software for processing.
To measure relative fluorescence intensity for phospho-p38, the nuclear region was extracted using ImageJ ROI function for phospho-p38 and DAPI channels, their intensities measured using ImageJ measure function and relative intensity calculated using formula: $I_{nuclear}$(phospho-p38) / $I_{nuclear}$(DAPI).
To measure relative fluorescence intensity for cytosolic HSP70, the nuclear region was extracted for HSP70 and DAPI channels and entire embryo was extracted for HSP70, their intensities measured and relative intensity calculated using formula: [I_{embryo}(HSP70) - $I_{nuclear}$(HSP70)] / $I_{nuclear}$(DAPI).
To quantify LC3B and p62 puncta, the embryo was extracted using ImageJ ROI function, the image was processed to black pixels over a white background using ImageJ Threshold function followed by ImageJ Analyze Particles function to count the number of puncta.

For all the above-mentioned quantifications, embryo groups within the same experiment were imaged during the same session with identical imaging parameters.
Cell counting was performed manually.

Metaphase Spreads

Embryos/mESCs were cultured in 0.1 μg/ml colcemid for 12 hours to arrest them in metaphase. Hypotonic solution: 1% sodium citrate (Sigma-Aldrich) and Carnoy's fixative: 3:1 methanol : glacial acetic acid (Sigma-Aldrich).

8- to 16-cell embryos were incubated for 10min in pre-warm hypotonic solution and fixed for 30 min in Carnoy's fixative.

ICMs embedded in Matrigel were incubated in Cell Recovery Solution (Corning) for 20 min at 4 °C and then taken out of Matrigel using pipetting. They were incubated for 10 min in pre-warm hypotonic solution and fixed for 30 min in Carnoy's fixative.

mESCs were trypsinized and collected in a tube, incubated for 10 min in 5 ml pre-warm hypotonic solution. Then, they were centrifuged at 500 r.p.m. for 5 min and incubated for 10 min in 5 ml Carnoy's fixative. Fixation step was repeated two more times and finally, the cells were resuspended in 1 ml fixative.

Embryos were mouth-pipetted on clean SuperFrost Plus Slide (Thermo Fisher Scientific). 100 μl mESCs were were dropped on the clean slide. Slides were air-dried and mounted with ProLong® Gold Antifade Mountant with DAPI (Life Technologies). Spreads were analysed using Leica SP5 inverted confocal microscope.

Mouse embryonic stem cell culture

mESCs were maintained on gelatinized plates in N2B27 2i/LIF medium at 37 °C and 5% CO_2 and the medium were changed daily. They were routinely passaged, once they became confluent. For passage, cells were exposed to 0.05% trypsin-EDTA (Thermo Fisher Scientific) at 37 °C for 2 min. FC medium was added to neutralize the trypsin and cells were centrifuged at 1,000 r.p.m. for 5 min. The mESC lines used were: Histone-GFP mESCs (provided by Lorenzo Orietti from the Zernicka-Goetz lab) and CAG-GFP plus Cherry Histone mESCs (provided by Gianluca Amadei from the Zernicka-Goetz lab).

N2B27 2i/LIF medium constitution: 1:1 mix of DMEM F12 (Thermo Fisher Scientific) and neurobasal A (Thermo Fisher Scientific) supplemented with 1% v/v B27 (Thermo Fisher Scientific), 0.5% v/v N2 (homemade), 100 μM β-mercaptoethanol (Thermo Fisher Scientific), penicillin–streptomycin, GlutaMAX, 1 μM MEK inhibitor PD0325901 (Stem Cell Institute), 3 μM GSK3 inhibitor CHIR99021 (Stem Cell Institute) and 10 ng ml^{-1} LIF (Stem Cell Institute). N2 supplement contained DMEM F12 medium, 2.5 mg/ml insulin (Sigma-Aldrich), 10 mg/ml Apo-transferrin (Sigma-Aldrich), 0.75% bovine albumin fraction V

(Thermo Fisher Scientific), 20 µg/ml progesterone, 1.6 mg/ml putrescine dihydrochloride (Sigma-Aldrich) and 6 µg/ml sodium selenite (Sigma-Aldrich).
FC medium constitution: DMEM (Thermo Fisher Scientific), 15% FBS, penicillin–streptomycin, GlutaMAX, MEM non-essential amino acids (Thermo Fisher Scientific), sodium pyruvate (Thermo Fisher Scientific) and 100 µM β-mercaptoethanol.

Mouse embryonic stem cell mosaicism model

CAG-GFP plus Cherry Histone mESCs were treated with 0.5 µM reversine or equivalent concentration DMSO in N2B27 2i/LIF medium for 16 hours. Histone-GFP mESCs were treated with equivalent DMSO concentration. 5,000 CAG-GFP plus Cherry Histone mESCs and 5,000 Histone-GFP mESCs were counted using haemocytometer and mixed. The 1:1 mixture was then seeded onto gelatin-coated µ-Slide 8-well ibiTreat dishes for co-culture. The cells were co-cultured in N2B27 2i/LIF medium supplemented with 0.5 µg/ml doxycycline for 4 days at 37 °C and 5% CO_2.

Statistical analysis

The statistical tests used are indicated in the corresponding figure legends. In all cases, the two-tailed version of the test was used. Qualitative data was analysed using Fisher's exact test. Normality of quantitative data was first assessed using D'Agostino's K-squared test. To determine statistical significance when the data was normally distributed, Student's t-test was used to compare two experimental groups of equal variances or Student's t-test with Welch's correction was used to compare two experimental groups of significantly different variances or one-way ANOVA test was used to compare more than two experimental groups. To determine statistical significance when the data was not normally distributed, Mann-Whitney test was used to compare two experimental groups or Kruskal-Wallis test with a Dunn's multiple comparison test was used to compare more than two experimental groups. Kolmogorov-Smirnov test was used to compare two frequency distributions. Linear regression was used to determine if the two slopes were significantly different from each other. Statistical analysis was performed using Prism (GraphPad) software.

References

Aburto, M. R. *et al.* Early otic development depends on autophagy for apoptotic cell clearance and neural differentiation. *Cell Death Dis.* **3(10)**, e394 (2012).

Aiken, C. E. *et al*. The direct measurement of embryogenic volume and nucleo-cytoplasmic ratio during mouse pre-implantation development. *Reproduction* **128**, 527-535 (2004).

Aivazidis, S. *et al.* The burden of trisomy 21 disrupts the proteostasis network in Down syndrome. *PLoS ONE* **12(4)**, e0176307 (2017).

Almeida, P. A. and Bolton, V. N. The relationship between chromosomal abnormality in the human preimplantation embryo and development *in vitro*. *Reprod. Fertil. Dev.* **8(2)**, 235-241 (1996).

Ambartsumyam, G. and Clarke, A. T. Aneuploidy and early human embryo development. *Hum. Mol. Genet.* **17**, R10-R16 (2008).

Anani, S. *et al*. Initiation of Hippo signaling is linked to polarity rather than to cell position in the pre-implantation mouse embryo. *Development* **141**, 2813-2824 (2014).

Anderson, K. P. *et al.* Isolation of a gene encoding a functional zinc finger protein homologous to erythroid Kruppel-like factor: identification of a new multigene family. *Mol. Cell Biol.* **15**, 5957–5965 (1995).

Anding**,** A**.** L**.** and Baehrecke**,** E**.** H**.** Autophagy in Cell Life and Cell Death**.** *Curr. Top. Dev. Biol.* **114**, 67-91 *(*2015).

Aplin, J. D. and Ruane, P. T. Embryo-epithelium interactions during implantation at a glance. *J. Cell Sci.* **130**, 15-22 (2017).

Aubrey, B. J. *et al.* How does p53 induce apoptosis and how does this relate to p53-mediated tumour suppression? *Cell Death Differ.* **25(1)**, 104-113 (2018).

Avilion, A. A. *et al.* Multipotent cell lineages in early mouse development depend on SOX2 function. *Genes Dev.* **17**, 126-140 (2003).

Baart, E. B. *et al.* FISH analysis of 15 chromosomes in human day 4 and 5 preimplantation embryos: the added value of extended aneuploidy detection. *Prenat. Diagn.* **27**, 55-63 (2007).

Baart, E. B. *et al.* Preimplantation genetic screening reveals a high incidence of aneuploidy and mosaicism in embryos from young women undergoing IVF. *Hum. Reprod.* **21**, 223-233 (2006).

Baffero, G. M. *et al.* Confined placental mosaicism at chorionic villous sampling: risk factors and pregnancy outcome. *Prenat. Diagn.* **32(11)**, 1102-1108 (2012).

Bany, B. M. and Cross, J. C. Post-implantation mouse conceptuses produce paracrine signals that regulate the uterine endometrium undergoing decidualization. *Dev. Biol.* **294**, 445–456 (2006).

Barbash-Hazan, S. *et al.* Preimplantation aneuploid embryos undergo self-correction in correlation with their developmental potential. *Fertil. Steril*. **92**, 890-896 (2009).

Barcroft, L. C. *et al.* Aquaporin proteins in murine trophectoderm mediate transepithelial water movements during cavitation. *Dev. Biol.* **256**, 342-354 (2003).

Bardet, P.-L. *et al.* A fluorescent reporter of caspase activity for live imaging. *Proc. Natl. Acad. Sci. U. S. A.* **105(37)**, 13901-13905 (2008).

Bartek, J. and Lukas, J. DNA damage checkpoints: from initiation to recovery or adaptation. *Curr. Opin. Cell Biol.* **19**, 238-245 (2007).

Basak, S. *et al.* Steroids modulate the expression of alpha4 integrin in mouse blastocysts and uterus during implantation. *Biol. Reprod.* **66**, 1784–1789 (2002).

Basile, N. *et al.* The use of morphokinetics as a predictor of implantation: a multicentric study to define and validate an algorithm for embryo selection. *Hum. Reprod.* **30(2)**, 276-283 (2015).

Basu, P. *et al.* KLF2 is essential for primitive erythropoiesis and regulates the human and murine embryonic beta-like globin genes *in vivo*. *Blood* **106**, 2566–2571 (2005).

Bedzhov, I. and Zernicka-Goetz, M. Self-organizing properties of mouse pluripotent cells initiate morphogenesis upon implantation. *Cell* **156**, 1-13 (2014).

Bedzhov, I. *et al*. Developmental plasticity, cell fate specification and morphogenesis in the early mouse embryo. *Philos. Trans. Royal Soc. B* **369**, 20130538 (2014a).

Bedzhov, I. *et al*. *In vitro* culture of mouse blastocysts beyond the implantation stage. *Nat. Protocols* **9(12)**, 2732-2739 (2014b).

Ben-Nagi, J. *et al.* The first ongoing pregnancy following comprehensive aneuploidy assessment using a combined blastocenetesis, cell free DNA and trophectoderm biopsy strategy. *J. Reprod. Infertil*. **20(1)**, 57-62 (2019).

Biase, F. H. *et al.* Cell fate inclination within 2-cell and 4-cell mouse embryos revealed by single-cell RNA sequencing. *Genome Res.* **24,** 1787-1796 (2014).

Biase, F. H. *et al.* Rainbow-Seq: Combining cell lineage tracing with single-cell RNA sequencing in preimplantation embryos. *iScience* **7**, 16-29 (2018).

Bielanska, M. *et al.* Chromosomal mosaicism throughout human preimplantation development *in vitro*: incidence, type, and relevance to embryo outcome. *Hum. Reprod.* **17(2),** 413-419 (2002).

Bischoff, M. *et al.* Formation of the embryonic-abembryonic axis of the mouse blastocyst: relationships between orientation of early cleavage divisions and pattern of symmetric/asymmetric divisions. *Development* **135**, 953-962 (2008).

Bolton, H. *et al.* Mouse model of chromosome mosaicism reveals lineage-specific depletion of aneuploid cells and normal developmental potential. *Nat. Commun.* **7(11165)** (2016).

Bonney, M. E. *et al.* Aneuploid proliferation defects in yeast are not driven by copy number changes of a few dosage-sensitive genes. *Genes & Dev.* **29**, 898-903 (2015).

Boroviak, T. *et al.* Single cell transcriptome analysis of human, marmoset and mouse embryos reveals common and divergent features of preimplantation development. *Development* **145(21)**, dev167833 (2018).

Boroviak, T. *et al.* The ability of inner-cell-mass cells to self-renew as embryonic stem cells is acquired following epiblast specification. *Nat. Cell Biol.* **16(6),** 516–528 (2014).

Boué, J. *et al.* Retrospective and prospective epidemiological studies of 1500 karyotyped spontaneous human abortions. *Teratology* **12(1)**, 11-26 (1975).

Bowling, S. *et al.* P53 and mTOR signalling determine fitness selection through cell competition during early mouse embryonic development. *Nat. Commun.* **9**, 1763 (2018).

Burgess, S. G. *et al.* Aurora-A-Dependent Control of TACC3 Influences the Rate of Mitotic Spindle Assembly. *PLoS Genet.* **11(7)**, e1005345 (2015).

Burton, A. *et al.* Single-cell profiling of epigenetic modifiers identifies PRDM14 as an inducer of cell fate in the mammalian embryo*. Cell Rep.* **5**, 687-701 (2013).

Capalbo, A. *et al.* Correlation between blastocyst morphology, euploidy and implantation: an observational study in two centers involving 956 screened blastocysts. *Hum. Reprod.* **29(6)**, 1173-1181 (2014).

Capalbo, A. *et al.* Sequential comprehensive chromosome analysis on polar bodies, blastomeres and trophoblast: insights into female meiotic errors and chromosomal segregation in the preimplantation window of embryo development. *Hum. Reprod.* **28(2)**, 509-518 (2013).

Carbone L. and Chavez, S. L. Mammalian preimplantation chromosomal instability: species comparison, evolutionary considerations, and pathological correlations. *Syst. Biol. Reprod. Med.* **61(6)**, 321-335 (2015).

Carlson, C. M. *et al.* Kruppel-like factor 2 regulates thymocyte and T-cell migration. *Nature* **442**, 299–302 (2006).

Casser, E. *et al.* Totipotency segregates between the sister blastomeres of two-cell stage mouse embryos. *Scientific reports* **7(1)**, 8299 (2017).

Chakravarthy, H. *et al.* Rapid activation of the bivalent gene Sox21 requires displacement of multiple layers of gene-silencing machinery. *FASEB J.* **25**, 206-218 (2011).

Chambers, I. *et al.* Functional expression cloning of Nanog, a pluripotency sustaining factor in embryonic stem cells. *Cell* **113**, 643-655 (2003).

Charles, J. E. Mouse monosomies and trisomies as experimental systems for studying mammalian aneuploidy. *Trends Genet.* **1**, 129-134 (1985).

Chavez, S. L. *et al*. Dynamic blastomere behaviour reflects human embryo ploidy by the four-cell stage. *Nat Commun.* **3**, 1251 (2012).

Chazaud, C. *et al.* Early lineage segregation between epiblast and primitive endoderm in mouse blastocysts through the Grb2-MAPK pathway. *Dev. Cell* **10**, 615-624 (2006).

Chen, B. *et al.* Cellular Strategies of Protein Quality Control. *Cold Spring Harb. Perspect. Biol.* **3(8)**, a004374 (2011).

Chen, Q. *et al.* Tracing the origin of heterogeneity and symmetry breaking in the early mammalian embryo. *Nat Commun.* **9(1)**, 1819 (2018).

Chen, S. *et al.* Dedifferentiation of lineage-committed cells by a small molecule. *J. Am. Chem. Soc.* **126**, 410-411.

Choi, J. *et al.* Prolonged Mek1/2 suppression impairs the developmental potential of embryonic stem cells. *Nature* **548(7666)**, 219-223 (2017).

Clemente-Ruiz, M. *et al*. Gene dosage imbalance contributes to chromosomal instability-induced tumorigenesis. *Dev. Cell* **36**, 290–302 (2016).

Coates, A. *et al.* Optimal euploid embryo transfer strategy, fresh versus frozen, after preimplantation genetic screening with next generation sequencing: a randomized controlled trial. *Fertil. Steril.* **107(3)**, 723-730 e3 (2017).

Cockburn, K. and Rossant, J. Making the blastocyst: lessons from the mouse. *J. Clin. Invest.* **120(4)**, 995-1003 (2010).

Cohen, G. M. Caspases: the executioners of apoptosis. *Biochem. J.* **326**, 1-16 (1997).

Coonen, E. *et al.* Anaphase lagging mainly explains chromosomal mosaicism in human preimplantation embryos. *Hum. Reprod.* **19**, 316-324 (2004).

Coppola, G. *et al.* Use of cross-species in-situ hybridization (ZOO-FISH) to assess chromosome abnormalities in day-6 in-vivo- or in-vitro-produced sheep embryos. *Chromosome Res.* **15(3)**, 399-408 (2007).

Cortezzi, S. S. *et al.* Secretome of the preimplantation human embryo by bottom-up label-free proteomics. *Anal. Bioanal. Chem.* **401(4)**, 1331-1339 (2011).

Crighton, D. *et al.* DRAM links autophagy to p53 and programmed cell death. *Autophagy* **3(1)**, 72-74 (2007).

Cross, J. C. *et al.* Trophoblast functions, angiogenesis and remodelling of the maternal vasculature in the placenta. *Mol. Cell Endocrinol.* **187**, 207-212 (2002).

Curlej, J. *et al.* Occurrence of chromosomal aneuploidy in rabbit oocytes and embryos at different developmental stages. *Zygote* **18**, 203-207 (2010).

Daphnis, D. D. *et al.* Detailed FISH analysis of day 5 human embryos reveals the mechanisms leading to mosaic aneuploidy. *Hum. Reprod.* **20**, 129-137 (2005).

Daughtry, B. L. *et al.* Single-cell sequencing of primate preimplantation embryos reveals chromosome elimination via cellular fragmentation and blastomere exclusion. *Genome Res.* **29(3)**, 367-382 (2019).

Deglincerti, A. *et al.* Self-organization of the *in vitro* attached human embryo. *Nature* **533(7602)**, 251-254 (2016).

Delhanty, J. D. *et al.* Detection of aneuploidy and chromosomal mosaicism in human embryos during preimplantation sex determination by fluorescent in situ hybridisation, (FISH). *Hum. Mol. Genet.* **2**, 1183-1185 (1993).

Deng, Q. *et al.* Single-cell RNA-seq reveals dynamic, random monoallelic gene expression in mammalian cells. *Science* **343**, 193-196 (2014).

Dephoure, N. *et al.* Quantitative proteomic analysis reveals posttranslational responses to aneuploidy in yeast. *Elife* **3**, e03023 (2014).

Desai, N. *et al.* Analysis of embryo morphokinetics, multinucleation and cleavage anomalies using continuous time-lapse monitoring in blastocyst transfer cycles. *Reprod. Biol. Endocrinol*. **12**, 54 (2014).

Dietrich, J. E. and Hiiragi, T. Stochastic patterning in the mouse pre-implantation embryo. *Development* **134**, 4219-4231 (2007).

Diez-Juan, A. *et al.* Mitochondrial DNA content as a viability score in human euploid embryos: less is better. *Fertil. Steril.* **104(3)**, 534-541 e1 (2015).

Ding, J. *et al.* Cripto is required for correct orientation of the anterior-posterior axis in the mouse embryo. *Nature* **395**, 702–707 (1998).

Dobles, M. *et al.* Chromosome missegregation and apoptosis in mice lacking the mitotic checkpoint protein Mad2. *Cell* **101**, 635-645 (2000).

Dodgson, S. E. *et al*. The pleiotropic deubiquitinase Ubq3 confers aneuploidy tolerance. *Genes Dev.* **30**, 2259-2271 (2016).

Donnelly, N. *et al.* HSF1 deficiency and impaired HSP90-dependent protein folding are hallmarks of aneuploid human cells. *EMBO J.* **33(20)**, 2374-2387 (2014).

Ducibella, T. and Anderson, E. Cell shape and membrane changes in the eight-cell mouse embryo: prerequisites for morphogenesis of the blastocyst. *Dev. Biol.* **47**, 45-58 (1975).

Ducibella, T. *et al.* The preimplantation mammalian embryo: characterization of intercellular junctions and their appearance during development. *Dev. Biol.* **45**, 231-250 (1975).

Duncan, E. J. *et al.* The role of HSP70 and its co-chaperones in protein misfolding, aggregation and disease. *Subcell. Biochem.* **78**, 243–273 (2015).

Dupont, C. *et al.* Incidence of chromosomal mosaicism in morphologically normal nonhuman primate preimplantation embryos. *Fertil. Steril*. **93(8)**, 2545-2450 (2010).

Dürrbaum, M. *et al.* The deregulated microRNAome contributes to the cellular response to aneuploidy. *BMC Genomics* **19(1)**, 197 (2018).

Dürrbaum, M. *et al.* Unique features of the transcriptional response to model aneuploidy in human cells. *BMC Genomics* **15**, 139 (2014).

Eisenberg-Lerner, A. *et al.* Life and death partners: apoptosis, autophagy and the cross-talk between them. *Cell Death Differ.* **16**, 966–975 (2009).

El-Deiry, W. S. Regulation of p53 downstream genes. *Semin. Cancer Biol.* **8(5)**, 345-357 (1998).

Evans, M. J. and Kaufman, M. H. Establishment in culture of pluripotential cells from mouse embryos. *Nature* **292**, 154–156 (1981).

Fabian, D. *et al.* Apoptotic process during mammalian preimplantation development. *Theriogenology* **64**, 221-231 (2005).

Fan, X. *et al.* Single-cell RNA-seq transcriptome analysis of linear and circular RNAs in mouse preimplantation embryos. *Genome Biology* **16**, 148 (2015).

Fierro-Gonzalez, J. C. *et al*. Cadherin-dependent filopodia control preimplantation embryo compaction. *Nat. Cell Biol*. **15**, 1424-1433 (2013).

Fiorentino, F. *et al.* Development and validation of a next-generation sequencing-based protocol for 24-chromosomeaneuploidy screening of embryos. *Fertil. Steril.* **101(5)**, 1375-1382 (2014).

Fiorenzano, A. *et al*. Cripto is essential to capture mouse epiblast stem cell and human embryonic stem cell pluripotency. *Nat. Commun.* **7**, 12589 (2016).

Fragouli, E. *et al.* Altered levels of mitochondrial DNA are associated with female age, aneuploidy, and provide an independent measure of embryonic implantation potential. *PLoS Genet.* **11(6)**, e1005241 (2015a).

Fragouli, E. *et al.* Analysis of implantation and ongoing pregnancy rates following the transfer of mosaic diploid-aneuploid blastocysts. *Hum. Genet.* **136(7)**, 805-819 (2017b).

Fragouli, E. *et al.* Clinical implications of mitochondrial DNA quantification on pregnancy outcomes: a blinded prospective non-selection study. *Hum. Reprod.* **32(11)**, 2340-2347 (2017b).

Fragouli, E. *et al.* Cytogenetic analysis of human blastocysts with the use of FISH, CGH and aCGH: scientific data and technical evaluation, *Hum. Reprod.* **26(2)**, 480-490 (2011).

Fragouli, E. *et al.* The developmental potential of mosaic embryos. *Fertil. Steril.* **104(3)**, e96 (2015b).

Fritz, B. *et al.* Cytogenetic analyses of culture failures by comparative genomic hybridisation (CGH)-Re-evaluation of chromosome aberration rates in early spontaneous abortions. *Eur. J. Hum. Genet.* **9**, 539-547 (2001).

Frum, T. *et al.* HIPPO signalling resolves embryonic cell fate conflicts during establishment of pluripotency *in vivo*. *eLife* **7**, e42298 (2018).

Gao, Y. *et al*. Protein Expression Landscape of Mouse Embryosduring Pre-implantation Development. *Cell Reports* **21**, 3957–3969 (2017).

Gardner, R. L. The early blastocyst is bilaterally symmetrical and its axis of symmetry is aligned with the animal-vegetal axis of the zygote in the mouse. *Development* **124**, 289-301 (1997).

Gardner, R. L. Specification of embryonic axes begins before cleavage in normal mouse development. *Development* **128**, 839-847 (2001).

Gasch, A. P. *et al.* Further support for aneuploidy tolerance in wild yeast and effects of dosage compensation on gene copy-number evolution. *Elife*. **5**, e14409 (2016).

Gasch, A. P. *et al.* Genomic expression programs in the response of yeast cells to environmental changes. *Mol. Biol. Cell* **11(12)**, 4241-4257 (2000).

Gearhart, J. D. *et al.* Autosomal aneuploidy in mice: generation and developmental consequences. *Brain Res. Bull.* **16(6)**, 789-801 (1986).

Gianaroli, L. *et al.* Blastocentesis: a source of DNA for preimplantation genetic testing. Results from a pilot study. *Fertil. Steril.* **102(6)**, 1692-1699 e6 (2014).

Gleixner, A. M. *et al.* Astrocytes surviving severe stress can still protect neighboring neurons from proteotoxic injury. *Mol. Neurobiol*. **53**, 4939-4960 (2016).

Glenister, P. H. *et al.* Incidence of chromosome anomalies in first-cleavage mouse embryos obtained from frozen-thawed oocytes fertilized *in vitro*. *Gamete Research* **16**, 205-216 (1987).

Goolam, M. *et al.* Heterogeneity in Oct4 and Sox2 Targets Biases Cell Fate in 4-Cell Mouse Embryos. *Cell* **165(1)**, 61–74 (2016).

Graham, S. J. *et al.* BMP signalling regulates the pre-implantation development of extra-embryonic cell lineages in the mouse embryo. *Nat. Commun.* **5**, 5667 (2014).

Greco, E. *et al.* Healthy Babies after Intrauterine Transfer of Mosaic Aneuploid Blastocysts. *N. Engl. J. Med.* **373(21)**, 2089-2090 (2015).

Griffin, D. K. and Ogur, C. Chromosomal analysis in IVF: just how useful is it? *Reproduction* **156(1)**, F29-F50 (2018).

Guo, G. *et al.* Resolution of cell fate decisions revealed by single-cell gene expression analysis from zygote to blastocyst. *Dev. Cell* **18**, 675-685 (2010).

Hadjantonakis, A. K. and Papaioannou, V. Dynamic *in vivo* imaging and cell tracking using a histone fluorescent protein fusion in mice. *BMC Biotechnol.* **4**, 33 (2004).

Halevy, T. *et al.* Molecular Characterization of Down Syndrome Embryonic Stem Cells Reveals a Role for RUNX1 in Neural Differentiation. *Stem Cell Rep.* **7(4)**, 777-786 (2016).

Hamatani, T. *et al*. Dynamics of global gene expression changes during mouse preimplantation development. *Dev. Cell* **6**, 117-131 (2004).

Handyside, A. H. PGD and aneuploidy screening for 24 chromosomes by genome-wide SNP analysis: seeing the wood and the trees. *Reprod. Biomed. Online* **23(6)**, 686-691 (2011).

Hans, F. and Dimitrov, S. Histone H3 phosphorylation and cell division. *Oncogene* **20**, 3021-3027 (2001).

Hardy, K. Cell death in the mammalian blastocyst. *Mol. Hum. Reprod.* **3(10)**, 919-925 (1997).

Harper, J. C. *et al.* Mosaicism of autosomes and sex chromosomes in morphologically normal, monospermic preimplantation human embryos. *Prenat. Diagn.* **15**, 41-49 (1995).

Hashimoto, S. *et al.* Selection of high-potential embryos by culture in poly(dimethylsiloxane) microwells and time-lapse imaging. *Fertil. Steril.* **97**, 332-337 (2012).

Hassold, T. and Hunt, P. To err (meiotically) is human: the genesis of human aneuploidy. *Nat. Rev. Genet.* **2(4)**, 280-291 (2001).

Hassold, T. *et al.* A cytogenetic study of 1000 spontaneous abortions. *Ann. Hum. Genet.* **44**, 151-178 (1980).

Heard, E. Recent advances in X-chromosome inactivation. *Curr. Opin. Cell Biol.* **16(3)**, 247–255 (2004).

Hertig, A. T. *et al.* Thirty-four fertilized human ova, good, bad and indifferent, recovered from 210 women of known fertility. *Pediatrics* **23(1)**, 202-211 (1959).

Hillman, N. *et al*. The effect of spatial arrangement on cell determination during mouse development. *J. Embryol. Exp. Morph.* **28**, 263-278 (1972).

Hirate, Y. *et al.* Polarity-dependent distribution of angiomotin localizes Hippo signaling in preimplantation embryos. *Curr. Biol.* **23(13)**, 1181-1194 (2013).

Hirota, T. *et al*. Fertile offspring from sterile sex chromosome trisomic mice. *Science* **357**, 932–935 (2017).

Hodes-Wertz, B. *et al.* Idiopathic recurrent miscarriage is caused mostly by aneuploid embryos. *Fertil. Steril.* **98(3)**, 675-680 (2012).

Hornak, M. *et al.* A high incidence of chromosome abnormalities in two-cell stage porcine IVP embryos. *J. Appl. Genet.* **56(4)**, 515-523 (2015).

Hornak, M. *et al.* Aneuploidy detection in pigs using comparative genomic hybridization: from the oocytes to blastocysts. *PLoS One* **7**, e30335 (2012).

Howman, E. V. *et al*. Early disruption of centromeric chromatin organization in centromere protein A (Cenpa) null mice. *Proc. Natl. Acad. Sci. U. S. A.* **97**, 1148-1153 (2000).

Huettel, B. *et al.* Effects of Aneuploidy on Genome Structure, Expression, and Interphase Organization in Arabidopsis thaliana. *PLoS Genet.* **4(10)**, e1000226 (2008).

Humpton, T. J. and Vousden, K. H. Regulation of Cellular Metabolism and Hypoxia by p53. *Cold Spring Harb. Perspect. Med.* **6(7)**, a026146 (2016).

Hupalowska, A. *et al*. CARM1 and paraspeckles regulate pre-implantation mouse embryo development. *Cell* **175**, 1902-1916 (2018).

Hyafil, F. *et al.* A cell surface glycoprotein involved in the compaction of embryonal carcinoma cells and cleavage stage embryos. *Cell* **21**, 927-934 (1980).

Inoue, M. *et al.* Autonomous trisomic rescue of Down syndrome cells. *Lab Invest.* **99(6)**, 885-897 (2019).

Ishikawa, K. *et al.* Post-translational dosage compensation buffers genetic perturbations to stoichiometry of protein complexes. *PLoS Genet.* **13(1)**, e1006554 (2017).

Iwasaki, S. *et al.* Developmental changes in the incidence of chromosome anomalies of bovine embryos fertilized *in vitro*. *J. Exp. Zool.* **261(1)**, 79-85 (1992).

Jacobs, P. A. *et al.* A cytogenetic survey of 11,680 newborn infants. *Ann. Hum. Genet.* **37**, 359-376 (1974).

James, R. M. *et al.* Restricted distribution of tetraploid cells in mouse tetraploid←→diploid chimaeras. *Dev. Biol.* **167**, 213-226 (1995).

Janssen, A. *et al.* Chromosome segregation errors as a cause of DNA damage and structural chromosome aberrations. *Science* **333(6051)**, 1895-1898 (2011).

Jedrusik, A. *et al.* Role of Cdx2 and cell polarity in cell allocation and specification of trophectoderm and inner cell mass in the mouse embryo. *Genes Dev.* **22**, 2692-2706 (2008).

Jiang, J. *et al.* A core Klf circuitry regulates self-renewal of embryonic stem cells. *Nat. Cell Biol.* **10**, 353–360 (2008).

Johnson, D. S. *et al*. Comprehensive analysis of karyotypic mosaicism between trophectoderm and inner cell mass. *Mol. Hum. Reprod.* **16**, 944-949 (2010).

Johnson, M. H. and Maro, B. The distribution of cytoplasmic actin in mouse 8-cell blastomeres. *J. Embryol. Exp. Morph.* **82**, 97-117 (1984).

Johnson, M. H. and McConnell, J. M. Lineage allocation and cell polarity during mouse embryogenesis. *Semin. Cell Dev. Biol.* **15**, 583-597 (2004).

Johnson, M. H. and Ziomek, C. A. Cell interactions influence the fate of mouse blastomeres undergoing the transition from the 16- to the 32-cell stage. *Dev. Biol.* **95**, 211-218 (1983).

Johnson, S. E. *et al.* Expression of epidermal growth factor family gene members in early mouse development. *Dev. Dyn.* **201**, 216–226 (1994).

Kale, A. *et al.* Apoptotic mechanisms during competition of ribosomal protein mutant cells: roles of the initiator caspases Dronc and Dream/Strica. *Cell Death Differ.* **22(8)**, 1300–1312 (2015).

Kalitsis, P. *et al.* Bub3 gene disruption in mice reveals essential mitotic spindle checkpoint function during early embryogenesis. *Genes Dev.* **14**, 2277-2282 (2000).

Kalitsis, P. *et al.* Targeted disruption of mouse centromere protein C gene leads to mitotic disarray and early embryo death. *Proc. Natl. Acad. Sci. U. S. A.* **95**, 1136-1141 (1998).

Kalousek, D. K. and Dill, F. J. Chromosomal mosaicism confined to the placenta in human conceptions. *Science* **221**, 665-667 (1983).

Kang, M. *et al.* Lineage establishment and progression within the inner cell mass of the mouse blastocyst requires FGFR1 and FGFR2. *Dev. Cell* **41(5)**, 496-510 (2017).

Kastenhuber, E. R. and Lowe, S. W. Putting p53 in Context. *Cell* **170(6)**,1062-1078 (2017).

Kenific, C. M. and Debnath, J. Cellular and metabolic functions for autophagy in cancer cells. *Trends Cell Biol*. **25(1)**, 37-45 (2015).

Kerr, J. F. R. *et al.* Apoptosis: a basic biological phenomenon with wide-ranging implications in tissue kinetics. *Br. J. Cancer* **26**, 239–257 (1972).

Kiessling, A. A. *et al.* Genome-wide microarray evidence that 8-cell human blastomeres over-express cell cycle drivers and under-express checkpoints. *J. Assist. Reprod. Genet.* **27(6)**, 265-276 (2010).

Kiso, M. *et al.* The disruption of Sox21-mediated hair shaft cuticle differentiation causes cyclic alopecia in mice. *Proc. Natl. Acad. Sci. U. S. A.* **106**, 9292-9297 (2009).

Klauzinska, M. *et al.* The multifaceted role of the embryonic gene Cripto-1 in cancer, stem cells and epithelial-mesenchymal transition. *Semin. Cancer Biol*. **29**, 51-58 (2014).

Klionsky, D. J. *et al.* Guidelines for the use and interpretation of assays for monitoring autophagy (3rd edition). *Autophagy* **12(1),** 1-222 (2016).

Kono, K. *et al*. Inhibition of RHO-ROCK signalling enhances ICM and suppresses TE characteristics through activation of Hippo signaling in the mouse blastocyst. *Dev. Biol.* **394**, 142-155 (2014).

Korotkevich, E. *et al*. The apical domain is required and sufficient for the first lineage segregation in the mouse embryo. *Dev. Cell* **40**, 235-247 e237 (2017).

Koutsourakis, M. *et al.* The transcription factor GATA6 is essential for early extraembryonic development. *Development* **126**, 723-732 (1999).

Krupa, M. *et al.* Allocation of inner cells to epiblast vs primitive endoderm in the mouse embryo is biased but not determined by the round of asymmetric divisions (8→16- and 16→32-cells). *Dev. Biol.* **385**, 136-148 (2014).

Kucinski, I. *et al.* Chronic activation of JNK JAK/STAT and oxidative stress signalling causes the loser cell status. *Nat. Commun.* **8,** 136 (2017).

Kunath, T. *et al.* Imprinted X-inactivation in extra-embryonic endoderm cell lines from mouse blastocysts. *Development* **132(7)**, 1649–1661 (2005).

Kuo, C. T. *et al.* LKLF: a transcriptional regulator of single-positive T cell quiescence and survival. *Science* **277**, 1986–1990 (1997).

Kurimoto, K. *et al.* An improved single-cell cDNA amplification method for efficient high-density oligonucleotide microarray analysis. *Nucleic Acids Res.* **34**, e42 (2006).

Kurotaki, Y. *et al.* Blastocyst axis is specified independently of early cell lineage but aligns with the ZP shape. *Science* **316**, 719-723 (2007).

Kuzmichev, A. N. *et al.* Sox2 acts through Sox21 to regulate transcription in pluripotent and differentiated cells. *Curr. Biol.* **22(18)**, 1705-1710 (2012).

Kuznyetsov, V. *et al*. Evaluation of a novel non-invasive preimplantation genetic screening approach. *PLoS ONE* **13(5)**, e0197262 (2018).

Leese, H. J. Metabolism of the preimplantation embryo: 40 years on. *Reproduction* **143(4)**, 417-427 (2012).

Letourneau, A. *et al*. Domains of genome-wide gene expression dysregulation in Down's syndrome. *Nature* **508**, 345-352 (2014).

Leung, C. Y. and Zernicka-Goetz, M. Angiomotin prevents pluripotent lineage differentiation in mouse embryos via Hippo pathway-dependent and -independent mechanisms. *Nat. Commun.* **4**, 2251 (2013).

Lightfoot, D. A. *et al.* The fate of mosaic aneuploid embryos during mouse development. *Dev. Biol.* **289**, 384-394 (2006).

Lim, C. Y. *et al.* Sall4 regulates distinct transcription circuitries in different blastocyst-derived stem cell lineages. *Cell Stem Cell* **3(5)**, 543-554 (2008).

Li, M. *et al.* Fluorescence in situ hybridization reanalysis of day-6 human blastocysts diagnosed with aneuploidy on day 3. *Fertil. Steril.* **84(5)**, 1395-1400 (2005).

Li, M. *et al.* The ATM-p53 pathway suppresses aneuploidy-induced tumorigenesis. *Proc. Natl. Acad. Sci. U. S. A*. **107(32)**, 14188-14193 (2010).

Liu, L. *et al.* Evaluation of the developmental competence and chromosomal compliment of mouse oocytes derived from in-vitro growth and maturation of preantral follicles. *J. Assist. Reprod. Genet.* **25**, 107-113 (2008).

Liu, Y. *et al.* Systematic proteome and proteostasis profiling in human Trisomy 21 fibroblast cells. *Nat. commun.* **8(1)**, 1212 (2017).

Livak, K. J. and Schmittgen, T. D. Analysis of relative gene expression data using real-time quantitative PCR and the 2(-Delta Delta C(T)) Method. *Methods* **25**, 402-408 (2001).

Li, Y. *et al.* Entosis allows timely elimination of the luminal epithelial barrier for embryo implantation. *Cell Reports* **11**, 358-365 (2015).

Macaulay, I. C. *et al.* G&T-seq: parallel sequencing of single-cell genomes and transcriptomes. *Nat. Methods* **12**, 519-522 (2015).

Machtinger, R. and Racowsky, C. Morphological systems of human embryo assessment and clinical evidence. *Reprod. Biomed. Online* **26**, 210-221 (2013).

Mackay, G. E. and West, J. D. Fate of tetraploid cells in 4n←→2n chimeric mouse blastocysts. *Mech. Dev.* **122**, 1266-1281 (2005).

Macklon, N. S. *et al.* Conception to ongoing pregnancy: the 'black box' of early pregnancy loss. *Hum. Reprod. Update* **8(4)**, 333–343 (2002).

Magli, M. C. *et al.* Chromosome mosaicism in day 3 aneuploid embryos that develop to morphologically normal blastocysts *in vitro*. *Hum. Reprod.* **15**, 1781-1786 (2000).

Magli, M. C. *et al.* Paternal contribution to aneuploidy in preimplantation embryos. *Reprod. Biomed. Online* **18(4)**, 536-542 (2009).

Magli, M. C. *et al.* Preimplantation genetic testing: polar bodies, blastomeres, trophectoderm cells, or blastocoelicfluid? *Fertil. Steril.* **105(3)**, 676-683 e5 (2016).

Mains, L. M. *et al.* Identification of apolipoprotein A1 in the human embryonic secretome. *Fertil. Steril.* **96(2)**, 422-427 e2 (2011).

Maitre, J. L. *et al*. Asymmetric division of contractile domains couples cell positioning and fate specification. *Nature* **536**, 344-348 (2016).

Maitre, J. L. *et al*. Pulsatile cell-autonomous contractility drives compaction in the mouse embryo. *Nat. Cell Biol*. **17**, 849-855 (2015).

Makarevitch, I. *et al.* Profiling expression changes caused by a segmental aneuploid in maize. *BMC Genomics* **9**, 7 (2008).

Manoharan, P. *et al.* KLF2 in Myeloid Lineage Cells Regulates the Innate Immune Response during Skeletal Muscle Injury and Regeneration. *iScience* **17**, 334–346 (2019).

Mantikou, E. *et al.* Molecular origin of mitotic aneuploidies in preimplantation embryos. *Biochim. Biophys. Acta* **1822**, 1921-1930 (2012).

Mao, R. *et al.* Primary and secondary transcriptional effects in the developing human Down syndrome brain and heart. *Genome Biol*. **6(13)**, R107 (2005).

Martin, G. R. Isolation of a pluripotent cell line from early mouse embryos cultured in medium conditioned by teratocarcinoma stem cells. *Proc. Natl Acad. Sci. USA* **78(12)**, 7634–7638 (1981).

Matiolo, P. *et al.* Autophagy exacerbates caspase-dependent apoptotic cell death after short times of starvation. *Biochem. Pharmacol.* **98(4)**, 573-586 (2015).

Ma, W.-ge *et al.* Estrogen is a critical determinant that specifies the duration of the window of uterine receptivity for implantation. *Proc. Natl Acad. Sci. USA* **100**, 2963–2968 (2003).

McClintock B. A Cytological and Genetical Study of Triploid Maize. *Genetics* **14(2)**, 180-222 (1929).

McConnell, B. B. and Yang, V. W. Mammalian Krüppel-Like Factors in Health and Diseases. *Physiol. Rev.* **90**, 1337–1381 (2010).

McCoy, R. C. *et al*. Common variants spanning PLK4 are associated with mitotic-origin aneuploidy in human embryos. *Science* **348(6231)**, 235-238 (2015a).

McCoy, R. C. *et al*. Evidence of selection against complex mitotic-origin aneuploidy during preimplantation development. *PLoS Genet.* **11(10)**, e1005601 (2015b).

McDole, K. *et al*. Lineage mapping the pre-implantation mouse embryo by two-photon microscopy, new insights into the segregation of cell fates. *Dev. Biol*. **355**, 239-249 (2011).

McReynolds, S. *et al.* Lipocalin-1: a potential marker for noninvasive aneuploidy screening. *Fertil. Steril.* **95(8)**, 2631-2633 (2011).

Melihac, S. M. *et al.* Active cell movements coupled to positional induction are involved in lineage segregation in the mouse blastocyst. *Dev Biol.* **331**, 210-221 (2009).

Mertzanidou, A. *et al.* Microarray analysis reveals abnormal chromosomal complements in over 70% of 14 normally developing human embryos. *Hum. Reprod,* **28**, 256-264 (2013).

Minchiotti, G. *et al.* Role of the EGF-CFC gene cripto in cell differentiation and embryo development. *Gene* **287(1-2)**, 33-37 (2002).

Miner, J. H. *et al.* Compositional and structural requirements for laminin and basement membranes during mouse embryo implantation and gastrulation. *Development* **131(10)**, 2247–2256 (2004).

Molkentin, J. D. *et al.* Requirement of the transcription factor GATA4 for heart tube formation and ventral morphogenesis. *Genes Dev.* **11**, 1061-1072 (1997).

Molotkov, A. *et al.* Distinct requirements for FGFR1 and FGFR2 in primitive endoderm development and exit from pluripotency. *Dev. Cell* **41**, 511-526 (2017).

Morris, S. A. *et al.* Developmental plasticity is bound by pluripotency and the Fgf and Wnt signaling pathways. *Cell Reports* **2**, 756-765 (2012a).

Morris, S. A. *et al.* Dynamics of anterior-posterior axis formation in the developing mouse embryo. *Nat. Commun.* **3**, 673 (2012b).

Morris, S. A. *et al*. Origin and formation of the first two distinct cell types of the inner cell mass in the mouse embryo. *Proc. Natl. Acad. Sci. USA* **107**, 6364-6369 (2010).

Mort, R.L. *et al*. Fucci2a: a bicistronic cell cycle reporter that allows Cre mediated tissue specific expression in mice. *Cell Cycle* **13**, 2681-2896 (2014).

Mulla, W. A. *et al.* Aneuploidy as a cause of impaired chromatin silencing and mating-type specification in budding yeast. *Elife* **6**, e27991 (2017).

Munne, S. Chromosome abnormalities and their relationship to morphology and development of human embryos. *Reprod. Biomed. Online* **12(2)**, 234-253 (2006).

Munne, S. *et al.* Improved detection of aneuploid blastocysts using a new 12-chromosome FISH test. *Reprod. Biomed. Online* **20**, 92-97 (2010).

Munne, S. *et al.* Self-correction of chromosomally abnormal embryos in culture and implications for stem cell production. *Fertil. Steril.* **84**, 1328-1334 (2005).

Muzumdar, M. D. *et al.* A global double-fluorescent Cre reporter mouse. *Genesis* **45**, 593–605 (2007).

Nagy, H. *et al.* Manipulating the mouse embryo.(2003).

Niakan, K. K. *et al.* Human pre-implantation embryo development. *Development* **139**, 829-841 (2012).

Niakan, K. K. *et al.* Sox17 promotes differentiation in mouse embryonic stem cells by directly regulating extraembryonic gene expression and indirectly antagonizing self-renewal. *Genes Dev.* **24**, 312-326 (2010).

Nichols, J. and Smith, A. Naive and Primed Pluripotent States. *Cell Stem Cell* **4(6)**, 487–492 (2009).

Niklaus, M. *et al.* Expression analysis of LC3B and p62 indicates intact activated autophagy is associated with an unfavourable prognosis in colon cancer. *Oncotarget* **8(33)**, 54604-54615 (2017).

Nishioka, N. *et al*. Tead4 is required for specification of trophectoderm in pre-implantation mouse embryos. *Mech. Dev.* **125**, 270-283 (2008).

Nishioka, N. *et al.* The Hippo signaling pathway components Lats and Yap pattern Tead4 activity to distinguish mouse trophectoderm from inner cell mass. *Dev. Cell* **16(3)**, 398–410 (2009).

Niwa, H. *et al*. Interaction between Oct3/4 and Cdx2 determines trophectoderm differentiation. *Cell* **123**, 917-929 (2005).

Northrop, L. E. *et al.* SNP microarray-based 24 chromosome aneuploidy screening demonstrates that cleavage-stage FISH poorly predicts aneuploidy in embryos that develop to morphologically normal blastocysts. *Mol. Hum.Reprod.* **16**, 590-600 (2010).

Novodvorsky, P. and Chico, T. J. The role of the transcription factor KLF2 in vascular development and disease. *Prog. Mol. Biol. Transl. Sci.* **124**, 155-188 (2014).

Ohashi, A. *et al.* Aneuploidy generates proteotoxic stress and DNA damage concurrently with p53-mediated post-mitotic apoptosis in SAC-impaired cells. *Nat. Commun.* **6**, 7668 (2015).

Ohishi, T. *et al.* TRF1 ensures the centromeric function of Aurora-B and proper chromosome segregation. *Mol. Cell Biol*. **34(13)**, 2464-2478 (2014).

Ohnishi, Y. *et al.* Cell-to-cell expression variability followed by signal reinforcement progressively segregates early mouse lineages. *Nat. Cell Biol.* **16**, 27-37 (2014).

Oromendia, A. B. and Amon, A. Aneuploidy: implications for protein homeostasis and disease. *Dis. Model Mech*. **7(1)**, 15-20 (2014).

Oromendia, A. B. *et al.* Aneuploidy causes proteotoxic stress in yeast. *Genes Dev.* **26**, 2696–2708 (2012).

O'Sullivan, D. M. *et al*. Staurosporine advances interblastomeric flattening of the mouse embryo. *Zygote* **1**, 103-112 (1993).

Palermo, G. D. *et al.* The human sperm centrosome is responsible for normal syngamy and early embryonic development. *Rev. Reprod.* **2,** 19-27 (1997).

Palermo, G. *et al.* The human zygote inherits its mitotic potential from the male gamete. *Hum. Reprod.* **9(7),** 1220-1225 (1994).

Papp, B. *et al.* Dosage sensitivity and the evolution of gene families in yeast. *Nature* **424**, 194–197 (2003).

Parr, E. L. *et al.* Apoptosis as the mode of uterine epithelial cell death during embryo implantation in mice and rats. *Biol. Reprod.* **36**, 211–225 (1987).

Passerini, V. *et al.* The presence of extra chromosomes leads to genomic instability. *Nat. Commun*. **7**, 10754 (2016).

Pattingre, S. *et al.* Bcl-2 antiapoptotic proteins inhibit Beclin 1-dependent autophagy. *Cell* **122(6)**, 927-939 (2005).

Pavelka, N. *et al.* Aneuploidy confers quantitative proteome changes and phenotypic variation in budding yeast. *Nature* **468(7321)**, 321-325 (2010).

Payer, B. and Lee, J. T. X chromosome dosage compensation: How mammals keep the balance. *Annu. Rev. Genet.* **42**, 733-772 (2008).

Pfau, S. J. *et al.* Aneuploidy impairs hematopoietic stem cell fitness and is selected against in regenerating tissues *in vivo*. *Genes Dev*. **30(12)**, 1395-1408 (2016).

Picelli, S. *et al.* Full-length RNA-seq from single cells using Smart-seq2. *Nat. Protocols* **9**, 171-181 (2014).

Picelli, S. *et al.* Smart-seq2 for sensitive full-length transcriptome profiling in single cells. *Nat. Methods* **10**, 1096-1098 (2013).

Picton, H. M. *et al.* Association between amino acid turnover and chromosome aneuploidy during human preimplantation embryo development *in vitro*. *Mol. Hum. Reprod.* **16**, 557-569 (2010).

Piotrowska, K. and Zernicka-Goetz, M. Role of sperm in spatial patterning of the early mouse embryo. *Nature* **409(6819)**, 517–521 (2001).

Piotrowska, K. *et al.* Blastomeres arising from the first cleavage division have distinguishable fates in normal mouse development. *Development* **128**, 3739–3748 (2001).

Piotrowska-Nitsche, K. and Zernicka-Goetz, M. Spatial arrangement of individual 4-cell stage blastomeres and the order in which they are generated correlate with blastocyst pattern in the mouse embryo. *Mech. Dev.* **122**, 487–500 (2005).

Piotrowska-Nitsche, K. *et al.* Four-cell stage mouse blastomeres have different developmental properties. *Development* **132**, 479–490 (2005).

Plachta, N. *et al.* Oct4 kinetics predict cell lineage patterning in the early mammalian embryo. *Nat. Cell Biol.* **13**, 117-123 (2011).

Plusa, B. *et al.* Distinct sequential cell behaviours direct primitive endoderm formation in the mouse blastocyst. *Development* **135(18)**, 3081–3091 (2008).

Popovic, M. *et al.* Chromosomal mosaicism in human blastocysts: the ultimate challenge of preimplantation genetic testing? *Hum. Reprod.* **33(7)**, 1342–1354 (2018).

Porter, A. G. and Jänicke, R. U. Emerging roles of caspase-3 in apoptosis. *Cell Death Differ.* **6(2)**, 99-104 (1999).

Pratt, H. P. *et al*. Compaction of the mouse embryo: an analysis of its components. *J. Embryol. Exp. Morph.* **70**, 113-132 (1982).

Putkey, F. R. *et al.* Unstable kinetochore-microtubule capture and chromosomal instability following deletion of CENP-E. *Dev. Cell* **3**, 351-365 (2002).

Qian, X. *et al.* DPPA5 Supports Pluripotency and Reprogramming by Regulating NANOG Turnover. *Stem Cells* **34(3)**, 588-600 (2016).

Qiu, D. *et al.* Klf2 and Tfcp2l1, Two Wnt/β-Catenin Targets, Act Synergistically to Induce and Maintain Naive Pluripotency. *Stem Cell Rep*. **5(3)**, 314-322 (2015).

Qu, X. *et al.* Autophagy gene-dependent clearance of apoptotic cells during embryonic development. *Cell* **128(5)**, 931-946 (2007).

Ramskold, D. *et al.* Full-length mRNA-Seq from single-cell levels of RNA and individual circulating tumor cells. *Nat. Biotechnol.* **30**, 777-782 (2012).

Rancati, G. *et al.* Aneuploidy underlies rapid adaptive evolution of yeast cells deprived of a conserved cytokinesis motor. *Cell* **135(5)**, 879-893 (2008).

Rands, G. F. Size regulation in the mouse embryo. II. The development of half embryos. *J. Embryol. Exp. Morphol.* **98**, 209-221 (1986).

Reeve, W. J. D. and Kelly, F. P. Nuclear position in the cells of the mouse early embryo. *J. Embryol. Exp. Morph.* **75**, 117-139 (1983).

Rubino, P. *et al.* Embryos classified as low-grade mosaic (<50%) after preimplantation genetic screening (PGS) by means of high resolution next-generation screening (hr-NGS), can have the same competence of producing healthy newborns as euploid embryos. *Fertil. Steril.* **109(3)**, e46-e47 (2018).

Saito, K. *et al.* Degradation of estrogen receptor α in activated blastocysts is associated with implantation in the delayed implantation mouse model. *Mol. Hum. Reprod.* **20(5)**, 384–391 (2014).

Samarage, C. R. *et al*. Cortical tension allocates the first inner cells of the mammalian embryo. *Dev. Cell* **34**, 435-447 (2015).

Sancho, M. *et al*. Competitive interactions eliminate unfit embryonic stem cells at the onset of differentiation. *Dev. Cell* **26(1)**, 19-30 (2013).

Santaguida, S. *et al.* Aneuploidy-induced cellular stresses limit autophagic degradation. *Genes Dev.* **29(19)**, 2010-2021 (2015).

Santaguida, S. *et al.* Dissecting the role of MPS1 in chromosome biorientation and the spindle checkpoint through the small molecule inhibitor reversine. *J. Cell Biol.* **190**, 73-87 (2010).

Santos, M. A. *et al.* The fate of the mosaic embryo: chromosomal constitution and development of Day 4, 5 and 8 human embryos. *Hum. Reprod.* **25**, 1916-1926 (2010).

Seli, E. *et al.* Noninvasive metabolomic profiling as an adjunct to morphology for noninvasive embryo assessment in women undergoing single embryo transfer. *Fertil. Steril.* **94(2)**, 535-542 (2010).

Siegel, J. J. and Amon, A. New insights into the troubles of aneuploidy. *Annu. Rev. Cell Dev. Biol.* **28**, 189–214 (2012).

Shahbazi, M. N. *et al.* Self-organization of the human embryo in the absence of maternal tissues. *Nat Cell Biol.* **18(6)**, 700-708 (2016).

Shamonki, M. I. *et al.* Proof of concept: preimplantation genetic screening without embryo biopsy through analysis of cell-free DNA in spent embryo culture media. *Fertil. Steril.* **106(6)**, 1312-1318 (2016).

Sheltzer, J. M. *et al.* Transcriptional consequences of aneuploidy. Proc. Natl. Acad. Sci. U. S. A. **109(31),** 12644-12649 (2012).

Sheth, B. *et al.* Differentiation of the epithelial apical junctional complex during mouse preimplantation development: a role for rab13 in the early maturation of the tight junction. *Mech. Dev.* **97**, 93-104 (2000).

Shi, J. *et al.* Dynamic transcriptional symmetry-breaking in pre-implantation mammalian embryo development revealed by single-cell RNA-seq. *Development* **142**, 3468-3477 (2015).

Shi, W. *et al.* Methylation reprogramming and chromosomal aneuploidy in *in vivo* fertilized and cloned rabbit preimplantation embryos. *Biol. Reprod.* **71**, 340-347 (2004).

Silber, S. *et al.* Chromosomal abnormalities in embryos derived from testicular sperm extraction. *Fertil. Steril.* **79(1)**, 30-38 (2003).

Simões-Sousa, S. *et al.* The p38α Stress Kinase Suppresses Aneuploidy Tolerance by Inhibiting Hif-1α. *Cell Rep*. ***25*(3)**, 749–760 e6 (2018).

Singh, K. *et al.* Secondary trisomics and telotrisomics of rice: origin, characterization, and use in determining the orientation of chromosome map. *Genetics* **143(1)**, 517-529 (1996).

Smyth, N. *et al.* Absence of basement membranes after targeting the LAMC1 gene results in embryonic lethality due to failure of endoderm differentiation. *J. Cell Biol.* **144(1)**, 151–160 (1999).

Soto, M. *et al.* Consequences of genomic diversification induced by segregation errors. *Trends Genet.* **35**, 4 (2019).

Soto, M. *et al.* p53 Prohibits Propagation of Chromosome Segregation Errors that Produce Structural Aneuploidies. *Cell Rep.* **19(12)**, 2423-2431 (2017).

Sozen, B. *et al.* Self-assembly of embryonic and two extra-embryonic stem cell types into gastrulating embryo-like structures. *Nat. Cell Biol.* **20**, 979-989 (2018).

Spinella, F. *et al.* Extent of chromosomal mosaicism influences the clinical outcome of *in vitro* fertilization treatments. *Fertil. Steril.* **109(1)**, 77-83 (2018).

Stephens, L. E. *et al.* Deletion of beta 1 integrins in mice results in inner cell mass failure and periimplantation lethality. *Genes Dev.* **9(15)**, 1883–1895 (1995).

Stephenson, R. O. *et al*. Disorganized epithelial polarity and excess trophectoderm cell fate in preimplantation embryos lacking E-cadherin. *Development* **137**, 3383-3391 (2010).

Steptoe, P. C. and Edwards, R. G. Birth after the reimplantation of a human embryo. *Lancet* **2**, 366 (1978).

Stingele, S. *et al.* Global analysis of genome, transcriptome and proteome reveals the response to aneuploidy in human cells. *Mol. Syst. Biol.* **8**, 608 (2012).

Stirparo, G. G. *et al.* Integrated analysis of single-cell embryo data yields a unified transcriptome signature for the human pre-implantation epiblast. *Development* **145 (3)**, dev158501 (2018).

Storchova, Z. The causes and consequences of aneuploidy in eukaryotic cells. Aneuploidy in Health and Disease. *InTech* (2012).

Strumpf, D. *et al.* Cdx2 is required for correct cell fate specification and differentiation of trophectoderm in the mouse blastocyst. *Development* **132**, 2093-2102 (2005).

Suwińska, A. *et al.* Blastomeres of the mouse embryo lose totipotency after the fifth cleavage division: expression of Cdx2 and Oct4 and developmental potential of inner and outer blastomeres of 16- and 32-cell embryos. *Dev. Biol.* **322(1)**, 133-144 (2008).

Tabansky, I. *et al.* Developmental bias in cleavage-stage mouse blastomeres. *Curr. Biol.* **23**, 21-31 (2013).

Takaoka, K. and Hamada, H. Origin of cellular asymmetries in the preimplantation mouse embryo: a hypothesis. *Phil. Trans. R. Soc. B* **369**, 20130536 (2014).

Tanaka, S. *et al.* Promotion of Trophoblast Stem Cell Proliferation by FGF4. *Science* **282(5396)**, 2072–2075 (1998).

Tang, F. *et al.* Deterministic and stochastic allele specific gene expression in single mouse blastomeres. *PLoS One* **6**, e21208 (2011b).

Tang, F. *et al.* mRNA-Seq whole-transcriptome analysis of a single cell. *Nat. Methods* **6**, 377-382 (2009).

Tang, Y.-C. *et al.* Identification of aneuploidy-selective antiproliferation compounds. *Cell* **144**, 499-512 (2011a).

Tarkowski, A. K. and Wroblewska, J. Development of blastomreres of mouse eggs isolated at the 4- and 8-cell stage. *J. Embryol. Exp. Morph.* **18**, 155-180 (1967).

Tarkowski, A. K. Experiments on the development of isolated blastomeres of mouse eggs. *Nature* **184**, 1286-1287 (1959).

Tarkowski, A. K. Mouse chimaeras developed from fused eggs. *Nature* **190**, 857-860 (1961).

Thompson, S. L. and Compton, D. A. Proliferation of aneuploid human cells is limited by a p53-dependent mechanism. *J. Cell Biol.* **188**, 369–381 (2010).

Torres, E. M. *et al.* Effects of aneuploidy on cellular physiology and cell division in haploid yeast. *Science* **317**, 916–924 (2007).

Torres-Padilla, M. E. *et al*. Histone arginine methylation regulates pluripotency in the early mouse embryo. *Nature* **445**, 214-218 (2007).

Treff, N. R. and Scott, R. T. Jr. Four-hour quantitative real-time polymerase chain reaction-based comprehensive chromosomescreening and accumulating evidence of accuracy, safet y, predictive value, and clinical efficacy. *Fertil. Steril.* **99(4)**, 1049-1053 (2013).

Treff, N. R. *et al.* Accurate single cell 24 chromosome aneuploidy screening using whole genome amplification and single nucleotide polymorphism microarrays. *Fertil. Steril.* **94(6)**, 2017-2021 (2010).

Tumaneng, K. *et al.* Organ size control by Hippo and Tor pathways. *Curr. Biol.* **22(9)**, R368–R379 (2012).

Turner, K. J. *et al.* Karyomapping for simultaneous genomic evaluation and aneuploidy screening of preimplantation bovine embryos: The first live-born calves. *Theriogenology* **125**, 249-258 (2019).

Ulloa Ullo, C. M. *et al.* The blastocyst production rate and incidence of chromosomal abnormalities by developmental stage in in vitro produced porcine embryos. *J. Reprod. Dev.* **54(1)**, 22-29 (2008).

Van Echten-Arends, J. *et al.* Chromosomal mosaicism in human pre-implantation embryos: a systematic review. *Hum. Reprod. Update* **17**, 620- 627 (2011).

Vanneste, E. *et al.* Chromosome instability is common in human cleavage- stage embryos. *Nat. Med.* **15**, 577-583 (2009).

Vázquez-Diez, C. *et al.* Micronucleus formation causes perpetual unilateral chromosome inheritance in mouse embryos. *Proc. Natl. Acad. Sci. U. S. A*. **113(3)**, 626-631 (2016).

Vera-Rodriguez, M. *et al.* Prediction model for aneuploidy in early human embryo development revealed by single-cell analysis. *Nat. Commun*. **6**, 7601 (2015).

Viuff, D. *et al*. Bovine embryos contain a higher proportion of polyploid cells in the trophectoderm than in the embryonic disc. *Mol. Reprod. Dev.* **62**, 483-438 (2002).

Viuff, D. *et al*. Chromosome aberrations in in vitro-produced bovine embryos at days 2-5 post-insemination. *Biol. Reprod.* **63**, 1143-1148 (2000).

Voullaire, L. *et al.* Chromosome abnormalities identified by comparative genomic hybridization in embryos from women with repeated implantation failure. *Mol. Hum. Reprod.* **8(11)**, 1035-1041 (2002).

Wang, J. *et al.* Asymmetric Expression of LincGET Biases Cell Fate in Two-Cell Mouse Embryos. *Cell* **175(7)**, 1887-1901 e18 (2018).

Wang, Q. *et al*. BUBR1 deficiency results in abnormal megakaryopoiesis. *Blood* **103**, 1278-1285 (2004b).

Wang, Q. T. *et al*. A genome-wide study of gene activity reveals developmental signaling pathways in the preimplantation mouse embryo. *Dev. Cell* **6**, 133-144 (2004a).

Wang, W.-H. *et al*. Limited recovery of meiotic spindles in living human oocytes after cooling–rewarming observed using polarized light microscopy. *Hum. Reprod.* **16(11)**, 2374-2378 (2001).

Wani, M. A. *et al.* Lung Kruppel-like factor, a zinc finger transcription factor, is essential for normal lung development. *J. Biol. Chem.* **274**, 21180–21185 (1999).

Wells, D. and Delhanty, J. D. Comprehensive chromosomal analysis of human preimplantation embryos using whole genome amplification and single cell comparative genomic hybridization. *Mol. Hum. Reprod,* **6**, 1055-1062 (2000).

Wells, D. *et al.* Clinical utilisation of a rapid low-pass whole genome sequencing technique for the diagnosis of aneuploidy in human embryos prior to implantation. *J. Med. Genet*. **51(8)**, 553-562 (2014).

White, M. D. *et al*. Long-lived binding of Sox2 to DNA predicts cell fate in the four-cell mouse embryo. *Cell* **165**, 75-87 (2016).

Wicklow, E. *et al*. HIPPO pathway members restrict SOX2 to the inner cell mass where it promotes ICM fates in the mouse blastocyst. *PLoS Genetics* **10**, e1004618 (2014).

Williams, B. R. *et al*. Aneuploidy affects proliferation and spontaneous immortalization in mammalian cells. *Science* **322(5902)**, 703-709 (2008).

Wilton, L. Preimplantation genetic diagnosis for aneuploidy screening in early human embryos: a review. *Prenat. Diagn.* **22**, 512-518 (2002).

Wong, C. C. *et al.* Non-invasive imaging of human embryos before embryonic genome activation predicts development to the blastocyst stage. *Nat. Biotechnol.* **28**, 1115-1121 (2010).

Wu, G. *et al.* Totipotency in the mouse. *J. Mol. Med. (Berl.)* **95(7)**, 687–694 (2017).

Wu, J. *et al.* The KLF2 transcription factor does not affect the formation of preadipocytes but inhibits their differentiation into adipocytes. *Biochemistry* **44**, 11098–11105 (2005).

Xin, Y. *et al. Slc25a36* modulates pluripotency of mouse embryonic stem cells by regulating mitochondrial function and glutathione level. *Biochem. J.* **476(11)**, 1585-1604 (2019).

Xue, Z. *et al.* Genetic programs in human and mouse early embryos revealed by single-cell RNA sequencing. *Nature* **500**, 593-597 (2013).

Xu, J. *et al.* Noninvasive chromosome screening of human embryos by genome sequencing of embryo culture medium for *in vitro* fertilization. *Proc. Natl. Acad. Sci. U. S. A*. **113(42)**, 11907-11912 (2016).

Yamanaka, Y. *et al.* Cell and molecular regulation of the mouse blastocyst. *Dev. Dyn.* **235(9)**, 2301–2314 (2006).

Yamane, M. *et al.* Overlapping functions of Krüppel-like factor family members: targeting multiple transcription factors to maintain the naïve pluripotency of mouse embryonic stem cells. *Development* **145(10)**, dev162404 (2018).

Yang, L. *et al.* MR-seq: measuring a single cell's transcriptome repeatedly by RNA-seq. *Sci. Bull.* **62(6)**, 391-398 (2017).

Yang, S. H. *et al.* Effect of morphokinetics and morphological dynamics of cleavage stage on embryo developmental potential: A time-lapse study. *Taiwan J. Obstet. Gynecol.* **57(1)**, 76-82 (2018).

Yang, Z. *et al.* Selection of single blastocysts for fresh transfer via standard morphology assessment alone and with array CGH for good prognosis IVF patients: results from a randomized pilot study. *Mol. Cytogenet.* **5(1)**, 24 (2012).

Yeo, J. C. *et al.* Klf2 is an essential factor that sustains ground state pluripotency. *Cell Stem Cell* **14(6)**, 864-872 (2014).

Ying, Q. *et al.* The ground state of embryonic stem cell self-renewal. *Nature* **453(7194)**, 519–524 (2008).

Yuan, L. *et al.* Female germ cell aneuploidy and embryo death in mice lacking the meiosis-specific protein SCP3. *Science* **296**, 1115-1118 (2002).

Zenzes, M. T. *et al.* Chromosome status of untransferred (spare) embryos and probability of pregnancy after *in-vitro* fertilisation. *Lancet* **340**, 391-394 (1992).

Zernicka-Goetz, M. *et al.* Following cell fate in the living mouse embryo. *Development* **124**, 1133-1137 (1997).

Zernicka-Goetz, M. Fertile offspring derived from mammalian eggs lacking either animal or vegetal poles. *Development* **125**, 4803-4808 (1998).

Zhang, A. *et al.* Global Analysis of Gene Expression in Response to Whole-Chromosome Aneuploidy in Hexaploid Wheat. *Plant Physiol*. **175(2)**, 828-847 (2017).

Zhang, Y. *et al.* Expression in Aneuploid *Drosophila* S2 Cells. *PLoS Biol.* **8(2),** e1000320 (2010).

Zhan, Q. *et al.* Direct Unequal Cleavages: Embryo Developmental Competence, Genetic Constitution and Clinical Outcome. *PLoS One* **11(12)**, e0166398 (2016).

Zhao, X. *et al.* Single-cell RNA-seq reveals a distinct transcriptome signature of aneuploid hematopoietic cells. *Blood* **130(25)**, 2762-2773 (2017).

Zheng, H. *et al.* Application of next-generation sequencing for 24-chromosome aneuploidy screening of human preimplantation embryos. *Mol. Cytogenet*. **8**, 38 (2015).

Zhu, J. *et al.* Cellular Stress Associated with Aneuploidy. *Dev. Cell* **44(4)**, 420-431 (2018).

Zhu, M. *et al*. Actomyosin polarisation through PLC-PKC triggers symmetry breaking of the mouse embryo. *Nat. Commun.* **8(1),** 921 (2017).

Zimmerman, R. S. *et al.* Development and validation of concurrent preimplantation genetic diagnosis for single gene disorders and comprehensive chromosomal aneuploidy screening without whole genome amplification. *Fertil. Steril.* **105(2)**, 286-294 (2016).

Ziomek, C. A. and Johnson, M. H. The roles of phenotype and position in guiding the fate of 16-cell mouse blastomeres. *Dev. Biol.* **91**, 440-447 (1982).

Appendix I: Original manuscript in preparation

Singla, S., Iwamoto-Stoh, L. K., Zhu, M. and Zernicka-Goetz, M. Autophagy-mediated apoptosis eliminates aneuploid cells in a mouse model of chromosome mosaicism. *Nat. Commun.* (2020, accepted).